Advanced Tracking and Image Registration Techniques for Intraoperative Radiation Therapy

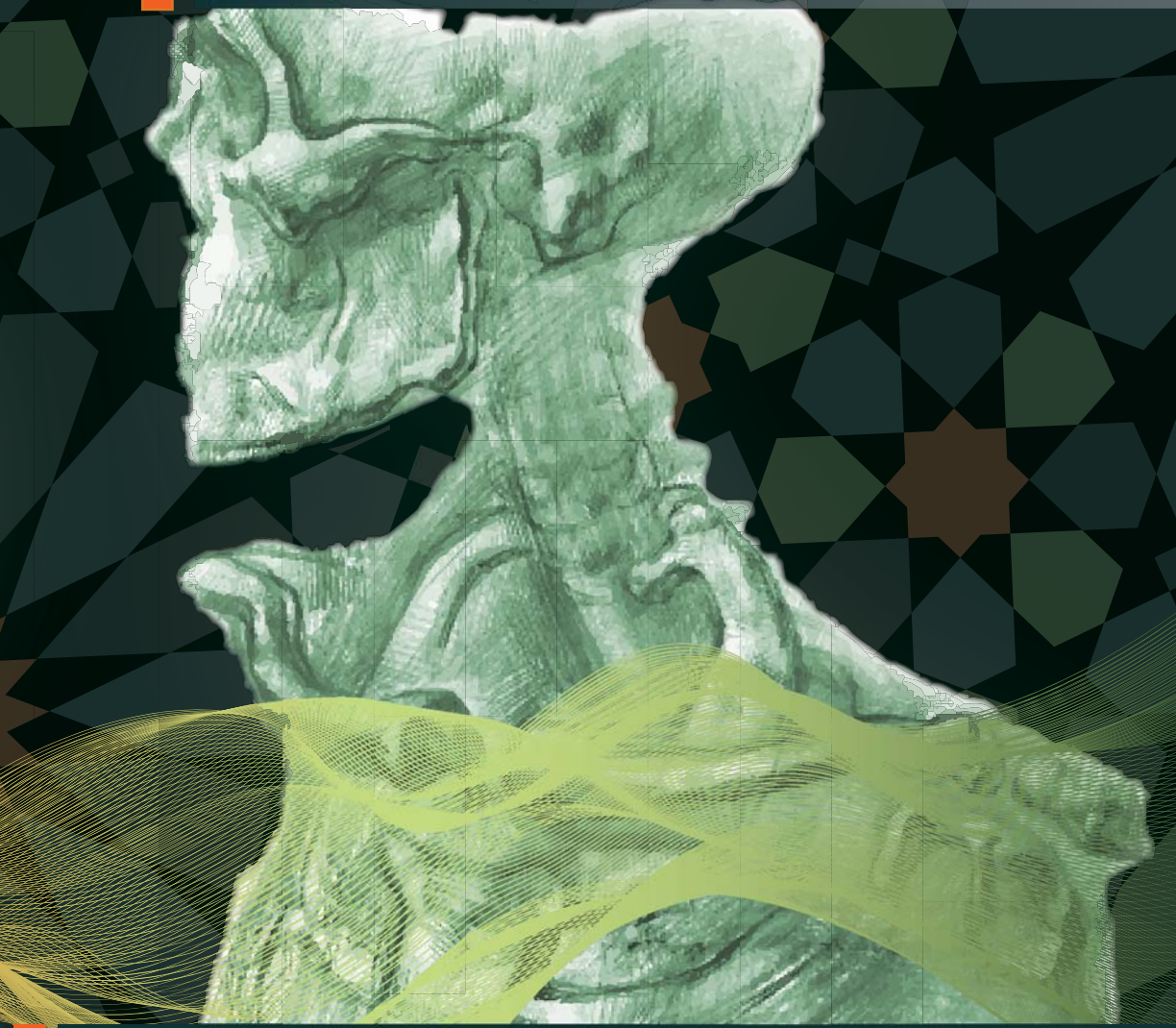

PhD Thesis

Marinetto Carrillo
Eugenio Daniel

Universidad Carlos III de Madrid

TESIS DOCTORAL

Advanced Tracking and Image Registration Techniques for Intraoperative Radiation Therapy

Autor:

Eugenio Daniel Marinetto Carrillo

Directores:

Javier Pascau González-Garzón

Felipe Ángel Calvo Manuel

Tutor:

Javier Pascau González-Garzón

DEPARTAMENTO DE BIOINGENIERÍA E INGENIERÍA AEROESPACIAL

Madrid, 12 de mayo de 2017

II

TESIS DOCTORAL

Advanced Tracking and Image Registration Techniques for Intraoperative Radiation Therapy

Autor: *Eugenio Daniel Marinetto Carrillo*

Directores:

Javier Pascau González-Garzón

Felipe Ángel Calvo Manuel

Firma del Tribunal Calificador:

Firma

Presidente:		
Vocal:		
Secretario:		

Calificación:

Madrid, 12 de mayo de 2017

Para Marinetto

El derecho surgido, con fuente en un sujeto,
acaecido en un segundo ocurre en manera
que queda implícita la conferencia de reciprocidad
que ese derecho otorga, por extensión,
equitativamente a ambas partes

Pablo de Justo, 2016

Agradecimientos

Dado que es la parte más leída de cualquier tesis, estos párrafos están escritos en plata a propósito. Sin hipérboles. Sin cinismo. Pero con todo el cariño que os tengo a cada uno aquí nombrado y a algún olvidado. Gracias a todas las que formasteis, formáis y formaréis parte de mí.

A mis tutores. A **Javi**, por darme la oportunidad de participar de su proyecto investigador desde muy temprano. Por aguantar mis discusiones, mi evolución escritora-científica y confiar en mi labor. Por escucharme, lidiarme, asediarme, retarme y fomentarme. Y por lo que aún te queda lidiar. A **Felipe**, por los ánimos incansables, por su sonrisa siempre a la espera de novedades, por educarme en el plano médico y por su reguero de docencia improvisada. Te mereciste estar aquí porque ya estuviste desde el principio. A **Manolo**, por permitirme formar parte del equipo durante tantos años, darme la oportunidad de formarme en el LIM y por sus sabias lecciones de casi todo.

A todo el equipo de Oncología Radioterápica. A **Mercedes**, por su disponibilidad infinita y buen hacer. A **J. Serrano**, por el trato humano, el colegueo y su maravillosa capacidad de asombro y colaboración. A los oncólogos pediátricos **Dr. Ruiz** y el **Dr. Fernández** del Hospital Virgen de las Nieves de Granada, porque con esta tesis os puedo devolver un poquito de lo que me habéis cedido. A los colaboradores del departamento de Robótica de la UC3M. A **Juan** por exhaustivas revisiones y docencia. A **Santiago** por su paciencia y capacidad resolutiva.

A mis Padres, por ser los mejores patrocinadores y mecenas del mundo. A mamá, por no dejar de querer a su niño malo y cuidarme siempre. A papá, por

apoyarme incluso a escondidas y porque merecías estar aquí para presenciar esto que es casi tan tuyo, como mío.

A mi Familia. A mis hermanas **Marisa** y **Paloma**, por saber ver lo bueno de la oveja rara de la familia. A **Eva**, por venir. A **Helena**, por mirarme siempre con asombro y orgullo, por seguirme y aprender a volar sola para convertirse en una persona de la que siempre me siento orgulloso como padrino. A mi abuelo **Carrillo**, por enseñarme el lado bueno de la vida y regalarme cartas. A mi abuelo **Marinetto**, por enseñarme el lado duro de la vida y quitarme las cartas. A mi abuela **María** (Aguilar), por calmarme en mis tormentas y nunca olvidarse de mí. A mi abuela **María** (Ortega), por haber luchado tanto por quedarte y porque aún te puedo tocar entre tus hijos. A mis **tías** y **tíos**, por no cansaros de preguntar cuándo iba a terminar, apoyarme y quererme en mi idiosincrasia. A mis **primas** y **primos** porque sois únicos y os quiero sin cambiaros. A **Encarna** y **Jorge** (mis padres adoptivos), por quererme, acogerme, comprenderme, valorarme y celebrarme. Porque os merecéis mucho más que estas frases y estar en este párrafo junto al resto.

A todos mis compañeros del LIM. A **Paula** por la sencillez, la dulzura, el cariño, los raticos, los cafés, Tailandia… Por sus torpezas encantadoras y porque siempre la recordaré con la lluvia corriendo por sus mejillas. A **Cris**, por las *cerdomonas*. Por su sinceridad, apoyo constante y por enseñarme tantísimo. Por la complicidad y por creer en mí. Por los pájaros besucones, estoy muy orgulloso de ti. A **Marta**, por ser oasis, refugio y lanza. Por aprenderse cada nombre, escuchar con el tacto y estar en cada etapa. A **Susanna** (y **Otto**), por aparecer. Por ayudarme a entenderme con luz o sin ella y no perder su esencia tras mil cambios vitales. A **Sisni**, por cubrirme, celebrarme, ayudarme y compartirme. Por abrirme sus diferentes mundos y por formar especialmente parte de esto. Por todo lo que aún te debo y por ser un referente. A **Esther**, por los disfraces, los abrazos, las cenas, las cervezas y por guardarme siempre un hueco allá donde la encuentre. Por valorarme y quererme. Por entenderme. A **Kenia**, por la confianza y el amor. Por los cafés y las filosofías mañaneras. A **Joost**, por sus consejos, valoración profesional y mantenerme a flote en la última etapa de esta tesis. A **Yasser**, por las historias cubanas y su carisma, te seguiré admirando siempre. A **David** (Neuro), por tener más ganas que yo siempre de ver terminado este libro. A **María** (de la Jara, Ji) por comenzar como alumna, por sus verdades y sus abrazos. A **Diego**, porque me ha encantado verte crecer todo este tiempo. A **Pedro**, por sus EugeÑos, sus risas escondidas y su visión particularmente pulcra del trabajo científico. A **Menchu**, porque vales mucho y te lo dicen poco; por tus górdicas y frikismo entrañable. A **Esther** (Chema 2),

por adaptarte a este grupo de locos, querernos y disfrutarnos. A **Elena** (Calidad), por su extrarradio maravilloso. A **Elena** (Martino), por su curiosidad incansable. A **Henar** y **Nico**. A **Xandra**, por su capacidad de ver la vida a su antojo. A **Yolanda**, por deslomarse cada día por muchos otros. A **Carmen**, porque merecías estar aquí. A Juan (**Abascal**) por las discusiones matemáticas tan enriquecedoras. A **Ángela**, por la complicidad, los daikiris y por no dejar de creer en ella misma. A Cristina **Santamarta**, por enseñarme MRI y la importancia del tamaño de gantry. A **Edu**, por saber de electricidad. A **Asier**, por no perder la esperanza y ser un colgado más. A **Ana**, por su capacidad de salir a flote siempre. A **Trajana**, por millones de cosas que no da tiempo a listar. A **Pajarito**, por cada vuelo. A **David** (Brasil), por descubrirse y ser un gran compañero de aventuras varias y de variedades. A **Roberto**, por pintar mi tesis en tres dimensiones. A **Estíbaliz**, por acogerme como friki de categoría 'A' y comprenderme. A **Eva**, porque nunca pierdas ese toque tan característico que te hace especial y única. A **Chema**, por ser un segundo tutor, regalarme su tiempo enseñándome y darme las contraseñas. A María (**La Calle**) por la especial dulzura y forma de ver la vida, ser una impoluta profesional y mejor amiga. A **Fidel**, por hacerte pequeño cuando ya eres muy grande, traerme un poco de Andalucía y entender siempre mi humor. ¡Porque ni Lagartija, ni Suricato, ni Hurón supieron que calzas un 46 de corazón! A **Gema**, por las risas, el azúcar y los piropos de *rolemodel*. A **Juanolas**, por dejarme que lo respete y tratarme de rey. A **Natalia**, por acompañarme parte del camino y descubrir juntos tutorías imprevistas. A **Iván**, por ser mi confidente, mi consejero, mi amigo, cuidarme de que no me quede sin aire, por quererme tal cual vengo, por cada experimento, por los ponys, los US y los abrazos largos. A **Laura**, por conectar tan rápido, por su capacidad resolutiva y por hacerme ver que lo humano es lo correcto. A **Gonzalo** (Montoya), por enseñarme tantas cosas sin que él mismo sepa que lo hace. A **Gonzalo**, por sus divertidas noches entre cuerdas. A **Marina**, por el chiste de la vela. A **Marco**, por sus sabias palabras en los momentos más oportunos. A **Rocío**, por tus ganas infinitas de aprender y tus ánimos. A **Mónica**, por pillarme el puntito de humor sarcástico. A **David** y **Alonso**, por hacerme sentir orgullo como docente y formar parte de esto. A **Marisa**, por segmentarme, por su confianza y genial trato y por llevar siempre un llamador de ángeles. A **Arrate**, por valorarme como profesional y persona y verme como un igual en el que confía. A **Juanjo**, por mandarme a Brasil. A **Chus**, por ser una gran profesora y sonreír siempre. A **Imke**, por ser una entusiasta de los aéreos. A **Santi**, por hacerse fuerte en su humildad. A **Lanillos**, por su música interna. A Santi **Reig**, por enseñarme la calma, por su esquina de paz donde me frustré tantas veces

para terminar viendo a la musa mustela. A los **técnicos** del BiiG de Leganés, por acogerme sin reparos y ayudarme. A **Paco**, por enseñarme desde el cuidado animal, primeros auxilios como lecciones importantes de vida. A **Fernando**, por cuidar de cosas importantes sin dudarlo ni un segundo.

A mis amigas y amigos. A **María** (Ostias Hey!) – tendría que escribir otra tesis tan solo de agradecimientos para poder explicarlo todo: Teka Nilme. A **Pedrito**, por mantenerse Nildo siempre y reservarme cada 24 de diciembre. A **Mariazel**, mi primera ratuna, por acompañarme tanto tiempo, no dejar de enseñarme nunca y saber ver al soñador incansable. A **Marta**, por las series con galletas, la nieve, los perros, el vino… Por enseñarme que enfadarse es gratis y me puedo coger todo lo que quiera. Mi ying. A Carlos (**Lombao**), por su generosidad constante. Por cuidarme en todo momento y aparecer cuando más lo necesito. Por ser muleta, consejero y amigo. A **Espe**, por tantas cosas compartidas. Por su visión espléndida de la vida y su lucha constante ante cualquier imprevisto. A **Anita**, por no desaparecer (te la devuelvo). Por ser hermana, compañera y amiga. A **Beita**, por descubrirnos y por su sentido de la justicia que me sigue dando lecciones. A **Bego**, por tu entereza y perseverancia mezcladas con dulzura e implacable inteligencia. A **Víctor** Bohórquez, por no desaparecer nunca, por conocer cada rincón de mi persona y haber crecido conmigo en territorios hostiles entre juegos y sonrisas. A **Chechi**, por su fortaleza y naturalidad, sus noches de chicas y su cariño. A **Outi**, por acogerme entre el frío y hacerme descubrir lo cálido tan lejos. A mi **Torri**, por encontrarnos con solo pensarlo y por lo que nos queda que intuyo, será grande. A **Isaac**, porque sin él no habrían sido posibles muchas cosas. Por la literatura, las charlas, Garfunkel and Oates, arepas, discusiones filosóficas y noches de polos al calor de abrazos que dejan huella. A **Juanito**, porque con él la risa fluye sin miedos. Por volver siempre y tenernos para lo que sea. Por ser, estar y no parecer. Por Sakura, el Dolce Prima y cada chiste hasta llorar. A **Celia**, porque nunca se rinde y la quiero cerca. A **Jandro**, por las picsas, las risas y los Tarazonas. Por su forma auténtica de vivirse y buscarse. Por dejarme acompañarlo y ser una muleta espléndida en un año dedicado a Saturno. A **Luis**, por enseñarme a ver que la vida es súper guay, que las cosas bonitas se toman con calma. Por las películas y cumbias. Por ser paz y retorno. Por estar. A **Nando**, por acogerme en un país extraño y entregármelo como regalo. Por inyectar esperanza y valorarme como lo hace. A **Carl**, por valorar el resto de páginas y su especial manera de mirarme, indeed. A Laura **Pina**, por descubrirme que la cordura está sobrevalorada y lo especial y bonito en cada enfermedad mental que a todos nos acompaña. A **Karen** (La China Bonita), por su ayuda infinita para obtener una portada decente

y por acogerme entre cervezas y bailes sin juzgar ni un solo instante. A **Mera**, por arroparme en mi llegada a Madrid y dejarme robarle de vez en cuando a Ana. A **Pyter**, por su visión especial de las cosas y su fe inquebrantable en mi futuro. A **Violín**, por mantenerse cerca siempre y dejarme descubrirla entre tanto teatro. A **Karol**, porque lejos, aquí te tengo. A **Lobohemio** (sí). A **Camino** y **Rocky**, por como son y mantener viva esta relación. A Luis (**Yaya**).

A mis Primas. A **Joselítico**, por tu incansable capacidad de ponerle chispa a la vida de cualquiera. A Borja, por su resilencia, gran maestra para los que te rodeamos. A **Pablo**, por enseñarme en cada frase (o sentencia), mirarme y comunicarse sin palabras. Por quedarte y formar parte. A **Reque**, por compartir tantos años y aprendernos juntos. Por valorar lo que de verdad importa y sobreponerlo a todo. A **Edu**, por su tenacidad envidiable, su maravilloso humor y su lucha, de la que me siento muy orgulloso tan solo estando cerca. A **Pedro**, por ser mi doctora preferida. Por las cabañas y aventuras y por los buenismos que me contrarrestan. A **Llabrés**, por tu apoyo y cariño inagotables. A **José Luis**, por comerte más de la mitad de esta tesis a mi lado. Por tu apoyo, paciencia y cariño. Por abrirme tu mundo sin condiciones y regalarme tantas cosas que aún conservo. Por dejarme seguir ahí y por quererme tanto. **A mis niñas de Motril**. A **Mónica**, por la conexión instantánea y el futuro ligado. A **Esther**, porque estando lejos, siempre la siento cerca. A mi **Nere**, porque un abrazo tuyo lo cura todo. A **Noe**, por ser la cabeza fría entre tanta demente. A **Paloma**, porque mirarte es viajar a muchos mundos lejanos. A **Encarni**, por intentarlo incansable, siempre. A **Isaac**, por ser mi rolemodel particular y una más de este equipo. A **Femi**, por ser tan jodidamente enorme. **A mis perdidos**. A **Rober**, por no juzgarme. A **Julio** por vigilar a Pyter. A **Barby**, por acordarte siempre. A **Ana** por pedirme colacao. A **Cubo**, por las noches Bio, las risas, pipas y cerves. A **Sergio**, por advertirme de Saturno. A **Libertad**, porque me nace. A **Lucía**, mi pirámide. A Angelines (**Little Angels**) porque sin ella mi vida sería un desastre. A **Marimar** por encontrarte. **A Baltimoreanish.** A **Alex e Isabel**, por lo cuqui. A **Isabel** (Sevillana) porque sin ella, Bmore no tiene ni puñetera gracia. A **Usama** y **Mariana**, por acogerme siempre. A **Bea**, por conectar tan rápido y ser un referente de humanidad. A **Caty**, por su apoyo, confianza y por darme fuerzas para seguir adelante en jornadas de doce horas. A **Víctor** (Graná), porque te lo mereces en tu grandeza humilde. A **David**, por su incansable superación y cariño. A **Giorgina**, **María**, **David** y **Bernat**, por las compras, la guitarra y los patines. A **Iván**, por acogerme y tener guardado siempre un trocito de Andalucía para mí. A **Genaro**, por su espíritu. **A mis pequeños**. A **Sarcasmo**, por escucharme lo más interno. A **Pancho**, por esperar siempre un abrazo. A **Mari**

Pili (mi primera rata). **A mis circenses.** A **Carmen** por los sonidos que podemos crear juntos. A **Eva** por darme ánimo para terminar esto desde un trapecio. A **Inés** porque nunca nada más bonito voló más alto. A **Jaime** por su entereza, ánimos y cariño. A **Juan**, por su capacidad para animar cada día sin descanso. A **Laura**, por la conexión ingenieril colgados de las telas. A **Valentina** por dejarse subir la adrenalina juntos. A **Fer**, por tu nobleza. A **Ana**, por enseñarme cada figura, en el trape y en la vida. A **Rafa**, por 'pesao' pero cuqui. A **Sara**, por ayudarme a rediseñar la casa y tirar platos al suelo. A **Iván**, por descubrirme que las cosas pueden ser lo mismo y a la vez no tener nada que ver. Y al excelentísimo Roberto **Gasca**, por valorar el esfuerzo con tanto humor que crea un espacio único de trabajo.

Acknowledgments

To **Jeff** Siewerdsen, for the opportunity to work in his lab and teach me with care and diligence. To **Wojciech** Zbijewski, for the trust and let me share not only science. To **Web**, for opening his house and peppers to this little strange and every shared meal. To **Amir**, for being a great buddy and reminds me of what really matters. To **Ali**, for being my coding-role-model, trust me and help me in every step. To **Ja**, for the hugs and making the lab nicer every day. To **Grace**, for being the spice of every morning. To **Tharindu**, for being a true friend and trust me unquestioningly. To **Hao**, **Steven**, **Sarah**, **Qian** and **Michael**, for welcoming me on every secret santa and celebrating every arriving to the lab. To **Leslie**, for your pizza decoration.

To **Anders**, for every after-work time and baseball. To **Antje**, for the coffees and moments. To **Anouk**, for the Sunday's brunch, tees, laughs and shared black humor. To **Garnett**, for your morning muffins, opera nights and being the best landlord ever.

To **Tiia**, for opening me her house's door. To Veronika, for make me check the title again, and again. To **Cindy** of Samoa, my princess, for being my mom abroad, trust me driving on the left, opening me her world and heart and for keeping in touch. To **Rasmus** Aagaard, for letting me use his illustration in this cover.

TABLE OF CONTENTS

Abstract

Intraoperative electron radiation therapy (IOERT) is a technique used to deliver radiation to the surgically opened tumor bed without irradiating healthy tissue. Treatment planning systems and mobile linear accelerators enable clinicians to optimize the procedure, minimize stress in the operating room (OR) and avoid transferring the patient to a dedicated radiation room. However, placement of the radiation collimator over the tumor bed requires a validation methodology to ensure correct delivery of the dose prescribed in the treatment planning system. In this dissertation, we address three well-known limitations of IOERT: applicator positioning over the tumor bed, docking of the mobile linear accelerator gantry with the applicator and validation of the dose delivery prescribed. This thesis demonstrates that these limitations can be overcome by positioning the applicator appropriately with respect to the patient's anatomy.

The main objective of the study was to assess technological and procedural alternatives for improvement of IOERT performance and resolution of problems of uncertainty. Image-to-world registration, multicamera optical trackers, multimodal imaging techniques and mobile linear accelerator docking are addressed in the context of IOERT.

IOERT is carried out by a multidisciplinary team in a highly complex environment that has special tracking needs owing to the characteristics of its working volume (i.e., large and prone to occlusions), in addition to the requisites of accuracy. The first part of this dissertation presents the validation of a commercial multicamera optical tracker in terms of accuracy, sensitivity to miscalibration, camera occlusions and detection of tools using a feasible surgical setup. It also proposes an automatic miscalibration detection protocol that satisfies the IOERT requirements of automaticity and speed. We show that the multicamera tracker is suitable for IOERT navigation and demonstrate the feasibility of the miscalibration detection protocol in clinical setups.

Image-to-world registration is one of the main issues during image-guided applications where the field of interest and/or the number of possible anatomical localizations is large, such as IOERT. In the second part of this dissertation, a registration algorithm for image-guided surgery based on line-shaped fiducials (line-based registration) is proposed and validated. Line-based

registration decreases acquisition time during surgery and enables better registration accuracy than other published algorithms.

In the third part of this dissertation, we integrate a commercial low-cost ultrasound transducer and a cone beam CT C-arm with an optical tracker for image-guided interventions to enable surgical navigation and explore image-based registration techniques for both modalities.

In the fourth part of the dissertation, a navigation system based on optical tracking for the docking of the mobile linear accelerator to the radiation applicator is assessed. This system improves safety and reduces procedure time. The system tracks the prescribed collimator location to solve the movements that the linear accelerator should perform to reach the docking position and warns the user about potentially unachievable arrangements before the actual procedure. A software application was implemented to use this system in the OR, where it was also evaluated to assess the improvement in docking speed.

Finally, in the last part of the dissertation, we present and assess the installation setup for a navigation system in a dedicated IOERT OR, determine the steps necessary for the IOERT process, identify workflow limitations and evaluate the feasibility of the integration of the system in a real OR. The navigation system safeguards the sterile conditions of the OR, clears the space available for surgeons and is suitable for any similar dedicated IOERT OR.

Resumen

La Radioterapia Intraoperatoria por electrones (RIO) consiste en la aplicación de radiación de alta energía directamente sobre el lecho tumoral, accesible durante la cirugía, evitando radiar los tejidos sanos. Hoy en día, avances como los sistemas de planificación (TPS) y la aparición de aceleradores lineales móviles permiten optimizar el procedimiento, minimizar el estrés clínico en el entorno quirúrgico y evitar el desplazamiento del paciente durante la cirugía a otra sala para ser radiado. La aplicación de la radiación se realiza mediante un colimador del haz de radiación (aplicador) que se coloca sobre el lecho tumoral de forma manual por el oncólogo radioterápico. Sin embargo, para asegurar una correcta deposición de la dosis prescrita y planificada en el TPS, es necesaria una adecuada validación de la colocación del colimador. En esta Tesis se abordan tres limitaciones conocidas del procedimiento RIO: el correcto posicionamiento del aplicador sobre el lecho tumoral, acoplamiento del acelerador lineal con el aplicador y validación de la dosis de radiación prescrita. Esta Tesis demuestra que estas limitaciones pueden ser abordadas mediante el posicionamiento del aplicador de radiación en relación con la anatomía del paciente.

El objetivo principal de este trabajo es la evaluación de alternativas tecnológicas y procedimentales para la mejora de la práctica de la RIO y resolver los problemas de incertidumbre descritos anteriormente. Concretamente se revisan en el contexto de la radioterapia intraoperatoria los siguientes temas: el registro de la imagen y el paciente, sistemas de posicionamiento multicámara, técnicas de imagen multimodal y el acoplamiento del acelerador lineal móvil.

El entorno complejo y multidisciplinar de la RIO precisa de necesidades especiales para el empleo de sistemas de posicionamiento como una alta precisión y un volumen de trabajo grande y propenso a las oclusiones de los sensores de posición. La primera parte de esta Tesis presenta una exhaustiva evaluación de un sistema de posicionamiento óptico multicámara comercial. Estudiamos la precisión del sistema, su sensibilidad a errores cometidos en la calibración, robustez frente a posibles oclusiones de las cámaras y precisión en el seguimiento de herramientas en un entorno quirúrgico real. Además, proponemos un protocolo para la detección automática de errores por

calibración que satisface los requisitos de automaticidad y velocidad para la RIO demostrando la viabilidad del empleo de este sistema para la navegación en RIO.

Uno de los problemas principales de la cirugía guiada por imagen es el correcto registro de la imagen médica y la anatomía del paciente en el quirófano. En el caso de la RIO, donde el número de posibles localizaciones anatómicas es bastante amplio, así como el campo de trabajo es grande se hace necesario abordar este problema para una correcta navegación. Por ello, en la segunda parte de esta Tesis, proponemos y validamos un nuevo algoritmo de registro (LBR) para la cirugía guiada por imagen basado en marcadores lineales. El método propuesto reduce el tiempo de la adquisición de la posición de los marcadores durante la cirugía y supera en precisión a otros algoritmos de registro establecidos y estudiados en la literatura.

En la tercera parte de esta tesis, integramos un transductor de ultrasonido comercial de bajo coste, un arco en C de rayos X con haz cónico y un sistema de posicionamiento óptico para intervenciones guiadas por imagen que permite la navegación quirúrgica y exploramos técnicas de registro de imagen para ambas modalidades.

En la cuarta parte de esta tesis se evalúa un navegador basado en el sistema de posicionamiento óptico para el acoplamiento del acelerador lineal móvil con aplicador de radiación, mejorando la seguridad y reduciendo el tiempo del propio acoplamiento. El sistema es capaz de localizar el colimador en el espacio y proporcionar los movimientos que el acelerador lineal debe realizar para alcanzar la posición de acoplamiento. El sistema propuesto es capaz de advertir al usuario de aquellos casos donde la posición de acoplamiento sea inalcanzable. El sistema propuesto de ayuda para el acoplamiento se integró en una aplicación software que fue evaluada para su uso final en quirófano demostrando su viabilidad y la reducción de tiempo de acoplamiento mediante su uso.

Por último, presentamos y evaluamos la instalación de un sistema de navegación en un quirófano RIO dedicado, determinamos las necesidades desde el punto de vista procedimental, identificamos las limitaciones en el flujo de trabajo y evaluamos la viabilidad de la integración del sistema en un entorno quirúrgico real. El sistema propuesto demuestra ser apto para el entorno RIO manteniendo las condiciones de esterilidad y dejando despejado el campo quirúrgico además de ser adaptable a cualquier quirófano similar.

List of Abbreviations and acronyms

2D	:	Two-Dimmensional
3D	:	Three-Dimmensional
AAPM	:	American Association of Physicist in Medicine
AICP	:	Anisotropic ICP
API	:	Application Programming Interface
AT	:	Acoustic Tracker
CBCT	:	Cone-Beam Computerized Tomography
CE	:	Conformité Européenne
CI	:	Confidence Interval
CNR	:	Contrast-to-noise Ratio
CPD	:	Coherent Point Drift
CT	:	Computerized Tomography
DH	:	Denavit-Hartenberg
DNA	:	Deoxyribonucleic Acid
DoF	:	Degree of Freedom
EBRT	:	External Beam Radiation Therapy
EM	:	Expectation-Maximization
EMT	:	Electromagnetic Tracker
FDA	:	U. S. Food & Drug Administration
FLE	:	Fiducial Localization Error
FOV	:	Field Of View
FWHM	:	Full-Width at Half-Maximum
GMM	:	Gaussian Mixture Model
GUI	:	General User Interface
HDR-IORT	:	High-Dose Rate Intraoperative Radiation Therapy
ICP	:	Iterative Closest Point

IGI	:	Image-guided Interventions
IGS	:	Image-guided Surgery
IGSTK	:	Image-Guided Surgery Toolkit
IOERT	:	Intraoperative Electron Radiation Therapy
IORT	:	Intraoperative Radiation Therapy
IPE	:	In-Plane Error
IR	:	Infrared
ISIORT	:	International Society of Intraoperative Radiation Therapy
ITK	:	Insight Toolkit
LBR	:	Line-based Registration
LED	:	Light-Emitting Diode
LINAC	:	Linear Accelerator
LS	:	Least Squares
MIND	:	Modality-independent neighborhood descriptors
MITK	:	Medical Imaging Interaction Toolkit
MRI	:	Magnetic Resonance Imaging
MT	:	Mechanical Tracker
NCC	:	Normalized Cross Correlation
NMI	:	Normalized Mutual Information
OR	:	Operating Room
PCA	:	Principal Component Analysis
PIB	:	Percutaneous Imag-guided Biopsy
Plus	:	Public software Library for UltraSound imaging research
PMMA	:	Polymethylmethacrylate
PSF	:	Point Spread Function
RFA	:	Radiofrequency Ablation
rms	:	Root Mean Square
ROI	:	Regiton of Interest
RT	:	Radiation Therapy
SDK	:	Software Development Kit
SLSQP	:	Sequential Least SQuares Programming
SSD	:	Sum of Squared differences

std	:	Standard Deviation
TARGIT	:	Targeted Intraoperative Radiotherapy
TE	:	Tracking Error
TNM	:	Classification of Malignant Tumors
ToF	:	Time of Flight
TPS	:	Treatment Planning System
TRE	:	Target Registration Error
UICC	:	Union for International Cancer Control
URTC	:	Unified Real-Time Communications
US	:	Ultrasound
VTK	:	Visualization Toolkit
WHO	:	World Health Organization

1

Introduction

The first historical reported description of cancer appeared in the Edwin Smith Papyrus (1600 BC, attributed to Imhotep) from Ancient Egypt. This medical text was probably a manual of military surgery and contains the description of 48 cases of injuries. Specifically, it describes different types of cancer as well as removal procedures by cauterization [1]–[3] (Fig. 1.1). Hippocrates (ca. 460 BC – ca. 370 BC) was the first that coined the term *karkinos* (*carcinos*, Greek word for a crab or crayfish), referring to several forms of cancer. Hippocrates noted the appearance of the cut surface of a solid malignant tumor, with "*the veins stretched on all sides as the animal the crab has its feet, whence it derives its name*"[4]). Celsus (ca. 25 BC - 50 AD) translated *karkinos* into cancer, the Latin word for crab or crayfish.

Specifically, cancer refers to any one of many diseases characterized by the development of abnormal (tumor) cells in a multistage process that generally progresses from a pre-cancerous lesion to a malignant tumor under uncontrolled cell proliferation. Cancer generation or carcinogenesis is directly related to the DNA (deoxyribonucleic acid) damage that could result from errors of DNA repair mechanisms. If those mutations, whatever their cause, are not repaired, they can impede normal cell functioning. In fact, if gene mutations are accumulated into genes related to apoptosis or cell proliferation, repair mechanisms could become uncontrolled and produce a tumor that might pervade to nearby tissues or to distant organs (metastasis) making them dysfunctional [5].

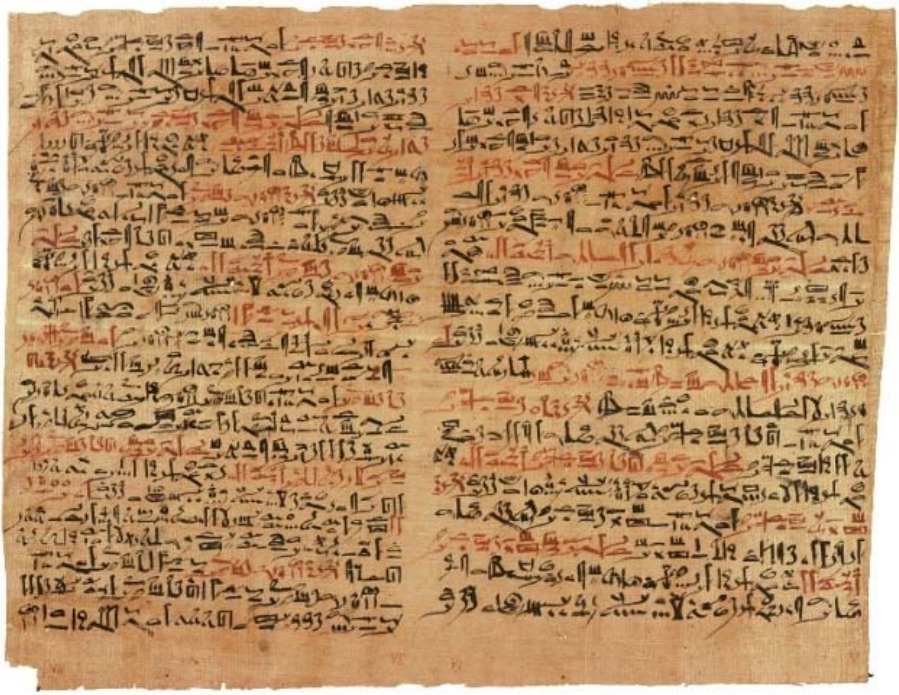

Figure 1.1: Plates vi & vii of the Edwin Smith Papyrus at the Rare Book Room, New York Academy of Medicine.

According to the World Health Organization, cancer is the second leading cause of death globally (Fig. 1.2) and accounted for 8.8 million deaths in 2015 with a growing tendency: the number of new cases is expected to rise about 70% in the next two decades. The most common causes of cancer mortality are cancers of the lung and liver (Fig. 1.3). The estimated total annual cost of cancer in 2010 was at approximately US$ 1.16 trillion and its major risk factors are tobacco use, alcohol use, unhealthy diet, and physical inactivity. Hence, an important area of research focuses on the early detection since cancer is more likely to respond to effective treatment and can result in a greater probability of surviving, less morbidity, and less expensive treatment when treatment starts shortly after disease onset [6].

In 1943, Pierre Denoix [7] devised a staging system called Classification of Malignant Tumors (TNM) in order to describe the stage of a cancer using alphanumeric codes. In this system, T describes the original tumor size or local

extension (primary lesion), N the involved nearby lymph nodes and M the distant metastasis. Currently, this system is used in clinical practice for oncological evolution and patient survival estimation depending on the cancer

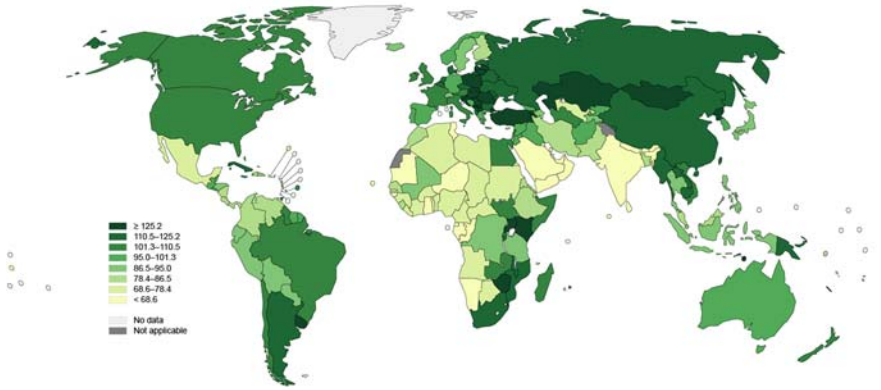

Figure 1.2: Estimated age-standardized rates of deaths all cancers excluding non-melanoma skin cancer worldwide (Courtesy of GLOBOCAN, WHO, 2012).

type (original affected organ) and its given TNM stage. Nowadays, TNM is maintained by the Union for International Cancer Control (UICC) providing a global consensus for tumor classification and standardization [8].

Well-known techniques for tumor treatment can be classified into radiotherapy (use of ionizing radiation), chemotherapy (use of drugs) and surgery. Surgical tumor resection is often the treatment of choice for the patient. However, depending on the TNM classification, some tumors present better prognosis with a different treatment approach. Specifically, when a patient presents metastasis of a solid primary tumor, the chosen treatment is usually a systemic approach (i.e., cytotoxic chemotherapy) since metastasis are induced by hematogeneous spread and tend to be numerous. In 1995, Hellman and Weichselbaum proposed an intermediate staging for metastasis classification (TNM, revision 7) named oligometastasis —a state in which the patient shows distant relapse (recurrence) in only a limited number of regions [9], [10]. In such a scenario, metastatic evolution could be organ-selective and size-limited, which could make local therapies more appropriated for treating these type of lesions [8], [11]. This highlights the importance for local control of tumor recurrence with a high metastatic risk (i.e., after a resection surgery, where tumor margins could be compromised) for the patient's survival. Commonly, (neo-) post-

adjuvant chemo/radiotherapy techniques are used to control the recurrence and/or to reduce the volume of the tumor before and after the surgical treatment approach.

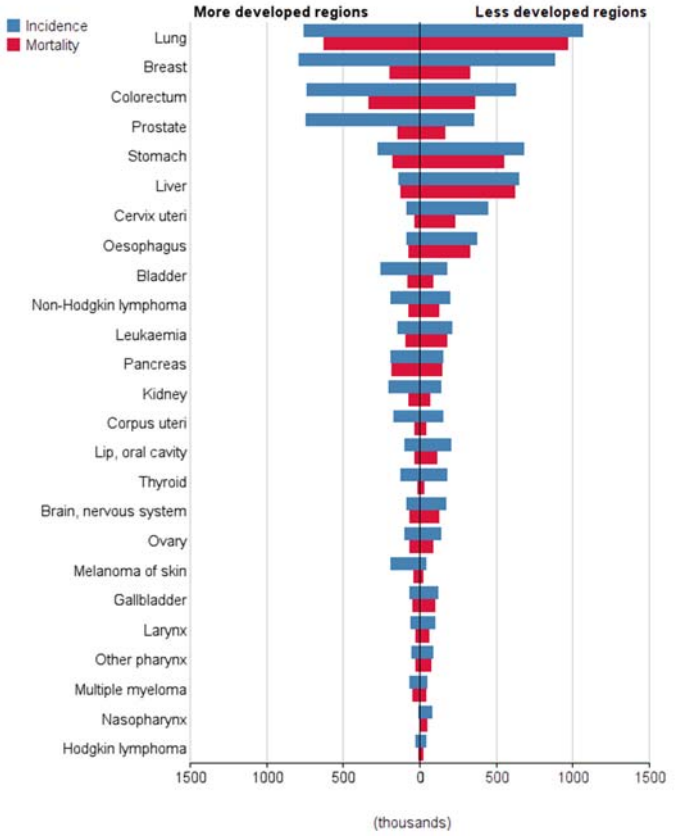

Figure 1.3: Incidence and mortality for different cancer localizations (Courtesy of GLOBOCAN, WHO, 2012).

1.1 Intraoperative Irradiation

Radiation therapy (RT) refers to the application of radiation with enough energy to remove tightly bound electrons from atoms' orbit and create ionized (charged) atoms. This radiation is called ionizing radiation and can be produced

in the form of different particles as photons (X- or gamma rays) or electrons. In particular, the interaction of biological tissues with this kind of radiation ionizes the present water molecules and produces free radicals that could react with the DNA structure. Thus, this reaction can modify the DNA chain. In fact, if the accumulated radiation dose in the tissue is sufficient, cell destruction could be achieved by mitotic catastrophe or apoptosis.

The key point of using ionizing radiation for cancer treatment is based on the administration of enough dose on the tumor cell to eliminate it while simultaneously protecting the healthy tissues. Since radiosensitivity (susceptibility of cells, tissues or organs to the harmful effect of ionizing radiation) is higher for cancer cells than healthy tissue, radiotherapy is classically administered using a time-fractioning scheme that allows time for the healthy tissue to recover from the DNA damage and accumulates injury on the target cancer cells [12], [13]. The most common radiotherapy technique is known as External Beam Radiotherapy (EBRT) that irradiates the tumor by means of a photon beam from different directions to accumulate dose on the cancer tissue while minimizing the irradiated healthy anatomy.

One main characteristic of this medical specialty is the heavy dependence on modern technology and the intensive coordination and collaboration between members of the procedure team to achieve a successful treatment outcome. The radiotherapy team consists of radiation oncologists, medical physicists and radiation therapy technologists: all professionals characterized by widely differing educational backgrounds and one common link —the need to understand the basic elements of radiation physics, and the interaction of ionizing radiation with human tissue in particular [14].

Radiotherapy has demonstrated a favorable effect on local recurrence [15]. In fact, the likelihood of obtaining local control improves when higher doses are administered. However, in order to deliver a high dose, a very precise control on dose distribution must be ensured to protect the healthy surrounding tissue from radiation [16]. Following this idea, specific techniques such as the Intraoperative Radiation Therapy (IORT) have been developed enabling a high-dose treatment under safe conditions.

1.1.1 Rationale and History of Intraoperative Irradiation

Intraoperative radiation therapy (IORT) refers to the radiation delivery at the time of a tumor resection over the tumor bed. These techniques allow for

the precise application of a high dose on the tumor bed and have demonstrated an improvement on tumor local control even for minimal microscopic residual disease [15], [17]. It is necessary to consider the post-surgical phenomenon of the "accelerated repopulation", where the first phases of neoplastic cellular growth follow an exponential-type course. IORT may avoid the problem of the "accelerated repopulation" on the irradiated area. With the administration of a high dose in a single fraction in the IORT, the reduction of the cell survival rate is achieved with smaller total dose (half to one third) in comparison to that achieved with conventional fractionated treatment (i.e., 15 Gy of IORT is equivalent to giving 30-45 Gy of fractionated external beam irradiation [18]). However, a potential disadvantage is the higher risk of late effects, such as fibrosis in late responding tissues like nerves [16]. In some particular cases, IORT becomes a better treatment option for malignancies with a high propensity for local recurrence which are located near critical organs that prohibit delivery of an adequate EBRT dose [19].

Figure 1.4 depicts the history of IORT and the current clinical studies. IORT pioneering description was performed in Barcelona (Spain) in 1905 [20] (graphically documented, Fig. 1.5). The first IORT patient treated in a stablished hospital program was in 1960 at the University of Tokyo using Cobalt 60 to produce the irradiation. In the early 1960s Betatron (a device that produces an electron beam) was employed at the same university reporting the first treatments using electrons. Later, in 1976, Howard University performed its first IOERT treatment followed by the Massachusetts General Hospital in 1978. During the 1980's, the community interest on IORT grew and IOERT programs were initiated in many European, American and Japanese hospitals. Until then, IOERT was performed using EBRT-dedicated linear accelerators (LINAC) to produce the radiation beam. Recently (late 90's), mobile-linear-accelerators were introduced as dedicated units that could be moved into the operating room (OR) and avoid transferring the anesthetized patient during surgery to the EBRT

Intraoperative Radiation Therapy

Brief History

1905 — First Pioneering Description | Barcelona Spain

1960 — First Patient Treated with Cobalt 60 | University Tokyo

1965 — Betatron installed in OR | University Tokyo

1976 — First IOERT world treatment | Howard University

1978 — First IOERT treatment | Mass General Hospital

1979 — IOERT + Large-field Surgery Feasible | National Cancer Institute USA

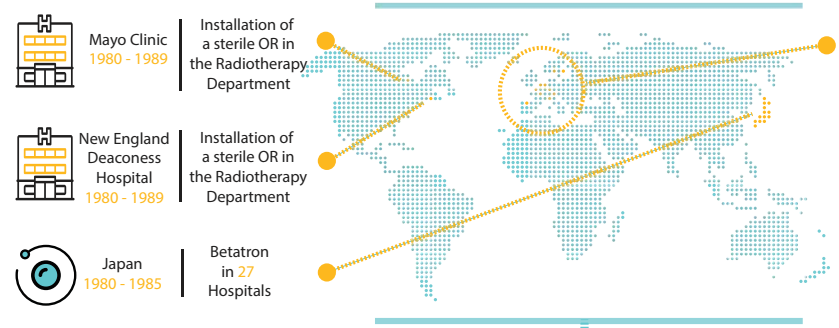

Mayo Clinic 1980 - 1989 | Installation of a sterile OR in the Radiotherapy Department

New England Deaconess Hospital 1980 - 1989 | Installation of a sterile OR in the Radiotherapy Department

Japan 1980 - 1985 | Betatron in 27 Hospitals

IOERT Program
High-Energy Electron Beam or Orthovoltage

Caen (France)	1983
Pamplona (Spain)	1984
Inssbruck (Austria)	1984
Lyon (France)	1985
Milan (Italy)	1985
Munchen (Germany)	1986
Brussels (Belgium)	1987
Groningen (Holland)	1988
Oslo (Norway)	1990
Stockholm (Sweden)	1990

1997 — Mobetron
Mobile Electron Linear Accelerator
Intraop

1998 — Foundation of International Society of Intraoperative Radiation Therapy ISIORT

1999 — Book
Intraoperative Irradiation: Techniques and Results
Springer (1st edition)

1999 — Intrabeam
Mobile Low-energy X-ray phontons
Zeiss

1999 — Novac 7
Mobile Electron Linear Accelerator
New RT

2011 — Liac
Mobile Electron Linear Accelerator
Sordina

1991 - 2016 — Clinical Studies

2011 — Book
Intraoperative Irradiation: Techniques and Results
Springer (2nd edition)

Clinical IORT Studies

Type

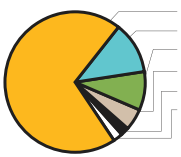

70 %	Breast
12 %	Pancreas
9 %	Sarcoma
5 %	Spine
2 %	Ovary
2 %	Rectum

Phase Study

29 %	Phase 1
52 %	Phase 2
12 %	Phase 3
7 %	Phase 4

Current Status

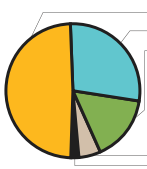

49 %	Recruiting
28 %	Completed
16 %	Active not recruiting
5 %	Terminated
2 %	Finished

Figure 1.4: Infographic of the Intraoperative Radiation Therapy History. Current clinical IORT studies (down).

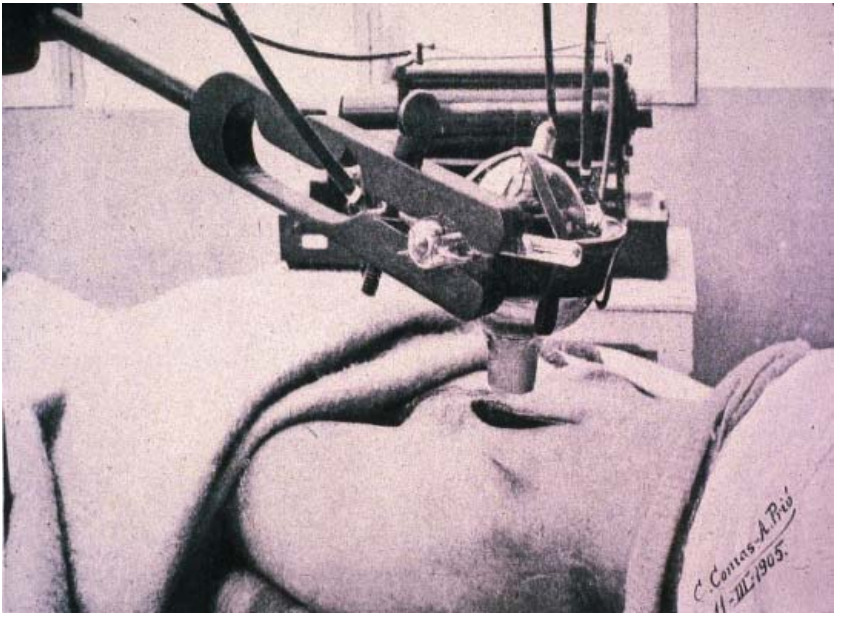

Figure 1.5: Photographic document of the case report during roentgen treatment. Notice in the right-lower corner of the figure the note with the picture date: March 11th 1905 [20]

LINAC room. These new technologies made the logistics and setting up of IOERT programs easier and cheaper for hospitals and clinics [21], [22]. At the same time, the first clinical studies focusing on a wide variety of cancer types were initiated. Finally, in 1998 the International Society of Intraoperative Radiation Therapy (ISIORT) was founded with the aim of promoting biological, translational and clinical research and dissemination of IORT scientific knowledge.

IORT can be delivered using electrons (IOERT), brachytherapy catheters (high-dose rate IORT, HDR-IORT) [15] or low energy X-rays (50 kV, soft X-rays) (targeted intraoperative radiotherapy, TARGIT) [23]. These methods have evolved with similar philosophies, attempting to achieve higher effective radiation doses in the tumor bed while limiting the dose to healthy tissues.

HDR-IORT delivers photon irradiation using a remotely controlled afterloader. An Ir-192 source attached by cable to the afterloader is propelled into hollow catheters embedded in a surface applicator. The advantages of HDR-IORT include the increased flexibility of the applicators (Fig. 1.6) which allows easy treatment of nearly all complex surfaces and the ability to treat large fields with minimal dosimetric inhomogeneity. Once the tumor resection surgery is finished, the applicator is placed over the tumor bed and the radiation seeds are positioned inside the catheters. The treatment time is usually 30 to 45 minutes, depending on the size of the tumor bed [19]. Portable HDR brachytherapy devices using molds and flaps are able to adapt the dose distribution to curve volumes in the target regions [16].

Figure 1.6: The Harrison-Anderson-Mick (H.A.M.) applicator facilitates the delivery of superficial high-dose rate intraoperative radiation treatments of advanced cancers via remote afterloading [19].

On the other hand, IOERT uses electron radiation to deliver the dose over the tumor bed. In particular, this technique is able to deliver a high dose in a shorter time (10-15 min) and treats deeper risk or residual cancer volumes (up to 1.0 cm) compared to other techniques. However, a linear accelerator (LINAC) device is needed to produce the beam under safety conditions that imply specific considerations from a radiation-safety point of view. In this approach, the radiation applicator is a cylinder that is attached (docked) to the LINAC's gantry to collimate the electron beam towards the target tumor bed. Depending on the

shape and size of the tumor bed, the bevel angle and the diameter of the applicator can be adapted to the surgical resection needs.

Dose-distribution characteristics are different for HDR-IORT and for IOERT. Figure 1.7 shows the differences between the depth-dose distribution for IOERT and HDR-IORT techniques. The dose is usually prescribed at 1 cm from the plane of catheters (0.5 cm from the applicator surface). The dose at the surface is higher for HDR-IORT. However, the dose at depth (for example, at 2 cm) is greater and more homogeneous for IOERT (usual surface applicator with a null bevel angle). The depth–dose advantage of IOERT over HDR-IORT is demonstrated for tumor residual of at least 0.5 cm depth [16], [19].

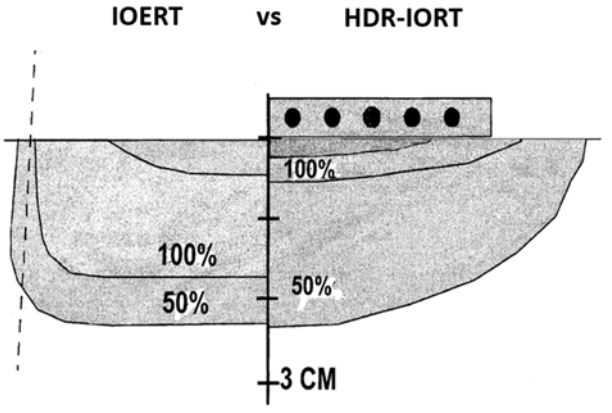

Figure 1.7: Differences between depth-dose distribution in electron (intraoperative electron radiation, IOERT, left) and brachytherapy (high-dose rate intraoperative radiation, HDR-IORT, right) [16].

In some cases, IOERT can be used in combination with fractionated EBRT. A common technique is to employ an IOERT boost before and/or after the resection surgery and thereafter fractionated EBRT sessions. The excellent long-term results achieved with EBRT plus IOERT boost techniques for breast, gynecologic, head and neck and other cancer sites support the concept of this combined approach since good local control is achieved with relatively low morbidity to dose-limiting normal tissues [16]. Moreover, the IOERT-EBRT combination can improve the therapeutic ratio for various reasons: (1) decrease the volume of the irradiation boost field by direct tumor visualization and appositional treatment, (2) exclude all or part of the dose-limiting sensitive

structures by operative mobilization or shielding and use of appropriate beam energies and (3) increase the total effective dose [16]. All these well-known advantages make IOERT a useful technique to treat a great variety of tumors and address the problem of the local cancer recurrence.

Although IOERT has demonstrated to be effective for local control of certain cancer types, the general criteria for the proper selection of patients are:

- when surgery alone does not achieve acceptable local control (i.e., microscopic residual disease or greater after maximal resection);
- when EBRT doses needed for adequate local control after subtotal resection or no resection would exceed normal tissue tolerance (60–70 Gy for microscopic residual, 70–90 Gy for gross residual or unresected disease);
- when IOERT plus EBRT technique would result in a more suitable therapeutic ratio between cure and complications;
- when there is no evidence of distant metastases or peritoneal seeding;
- when IOERT as well as other treatment modalities of partial breast irradiation may be an alternative to the traditional postoperative radiotherapy after conservative surgery in some selected cases, or when used as a boost technique in the treatment of initial-stage breast cancer; and when there are no distant metastases [16], [18].

When a high dose is being administered to a patient in a short period of time an important concern is the radiobiological effect limiting the opportunity for sublethal damage repair by healthy tissue, and thus increasing the risk for complications [19]. For instance, IOERT doses of 25–30 Gy can be administered to patients in which no (or limited) EBRT is planned, but who present a higher risk of nerve intolerance [16]. In comparison to fractionated EBRT, the most common toxicities reported include peripheral neuropathy, ureteral obstruction, and sexual and urinary dysfunction [24].

Furthermore, since the electron beam travels only in a straight line and the applicator has a limited diameter, IOERT cannot be feasible when the tumor bed is poorly accessible. In such cases, HDR-IORT is more adequate at the expense of considerably increasing the procedure time, which is not always possible [16], [25].

1.1.2 Multidisciplinary aspects of intraoperative electron radiation therapy

During IOERT performance the radiation oncologist is the maximum responsible of the prescription and execution of the treatment. However, to achieve a successful outcome, a multidisciplinary collaboration between the surgeon, anesthetist, medical physics experts, radiation technologists and nursing personnel is required. This multidisciplinary characteristic of IOERT puts a high demand on quality assurance programs as well as new attitudes and approaches for patient safety [26]–[28]. In that sense, the development of training programs for all levels of personnel is essential, as well as a clear definition of the different roles and technical procedures during the IOERT execution. This emphasized the need for procedural documentation in order to optimize the program when it is to be started in a medical center [28]–[31]. In fact, some authors have focused on the optimization process evaluating the risk factors and involved agents that are related to this specific procedure [27], [32]. Figure 1.8 depicts the processes in intraoperative radiation therapy showing the complexity and multidisciplinary characteristics of the procedure.

One main concern is the noticeable empirical characteristic of the IOERT performance since a great number of parameters must be decided in situ by the oncologist such as field size, beam energy, protections, applicator size and bevel. For this reason, image-based treatment planning systems (TPS), which are like the ones employed for EBRT planning, were developed. These provide a simulation of the therapy results in advance using a preoperative CT scan of the patient. TPS enable the oncologist, outside the stress of the OR, to settle the procedure parameters. Moreover, the TPS is useful for the important process documentation. A commercial example of TPS for IORT procedures is radiance [33], that obtained the CE certificate in 2011 and FDA approval in 2015 for clinical use, which also denotes the growing research tendency in the IOERT domain (Fig. 1.9).

Processes leading to an IOERT treatment

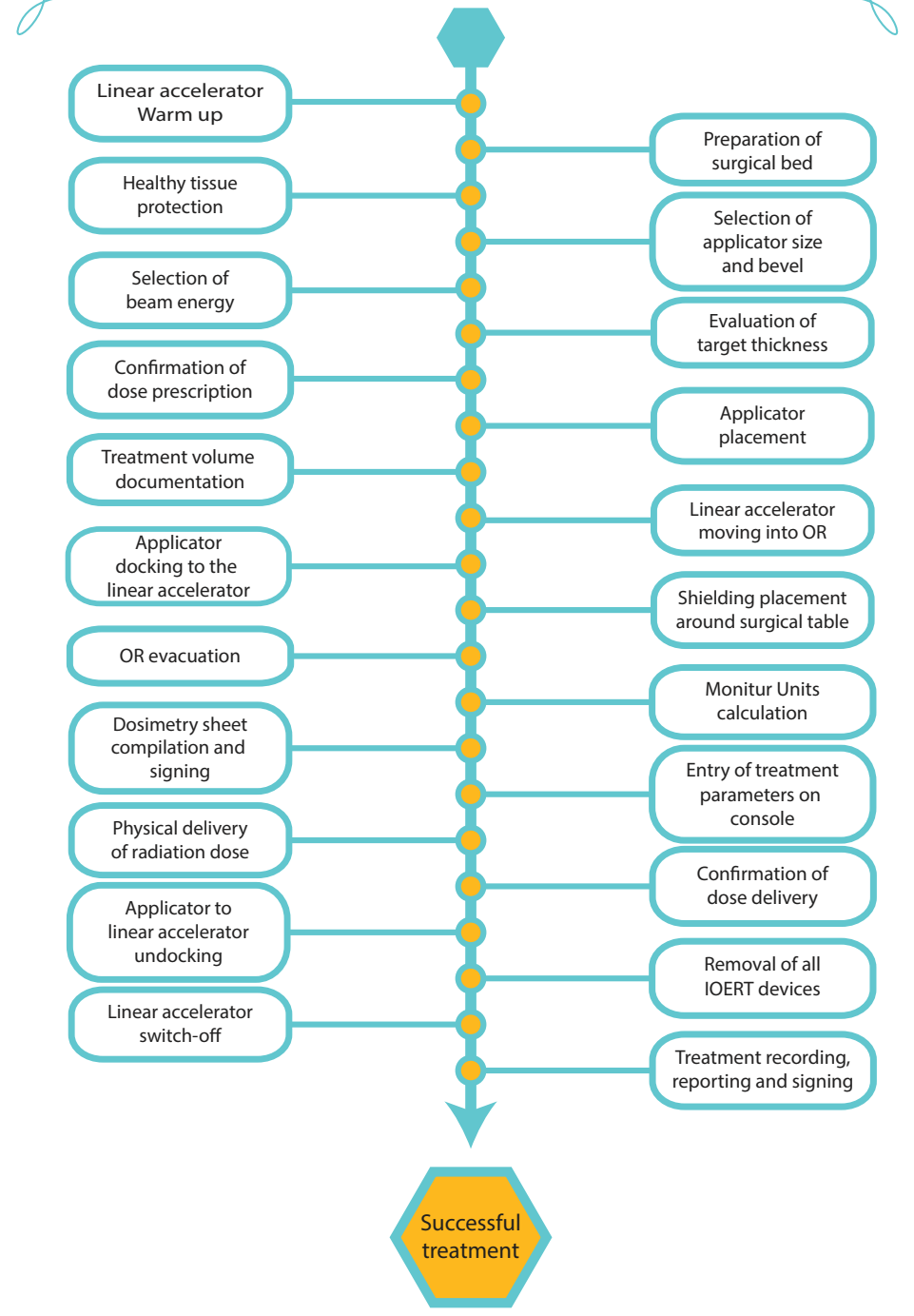

Figure 1.8: Subprocess of the IOERT. **OR** = operating room.

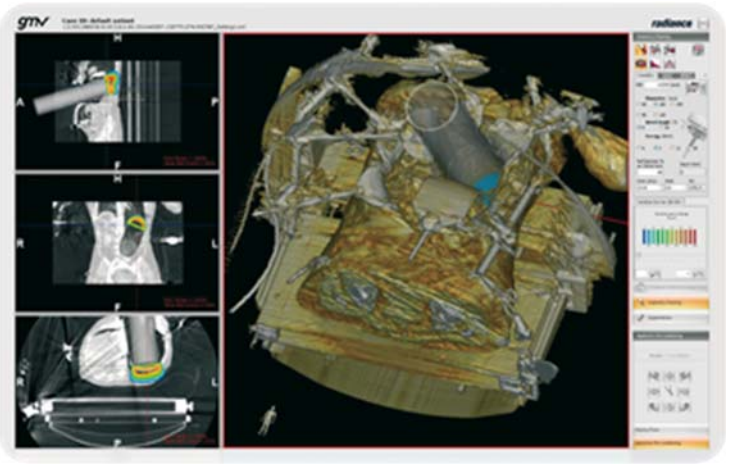

Figure 1.9: IOERT treatment planning system (TPS) radiance. A simulation of the IOERT procedure over a CT image of the patient, showing the radiation dose distribution and affected tissues.

Commonly, IOERT preplanning on the TPS is performed using a preoperative CT image. But the important contribution of TPS to IOERT also created new challenges. Since the IOERT parameters are decided prior to the procedure, a validation process to ensure the prescribed treatment is needed. In fact, due to surgical findings for preplanned cases, a clinical approach could require updating the treatment parameters (i.e., change the size of the applicator because the surgical incision is smaller than predicted during the treatment planning). Such cases would demand re-estimation of the delivered dose which is not feasible for reasons of safety and time in most of cases. Nevertheless, to perform the dose distribution simulation in the TPS, the positioning of the applicator related to the patient's anatomy must be known in advance and inputted properly into the software, either for treatment simulation or documentation purposes. Some authors tried to overcome this problem using intraoperative imaging (i.e., ultrasound imaging, US) to determine the distance between the tumor bed and the radiation applicator in order to confirm the prescribed dose [34].

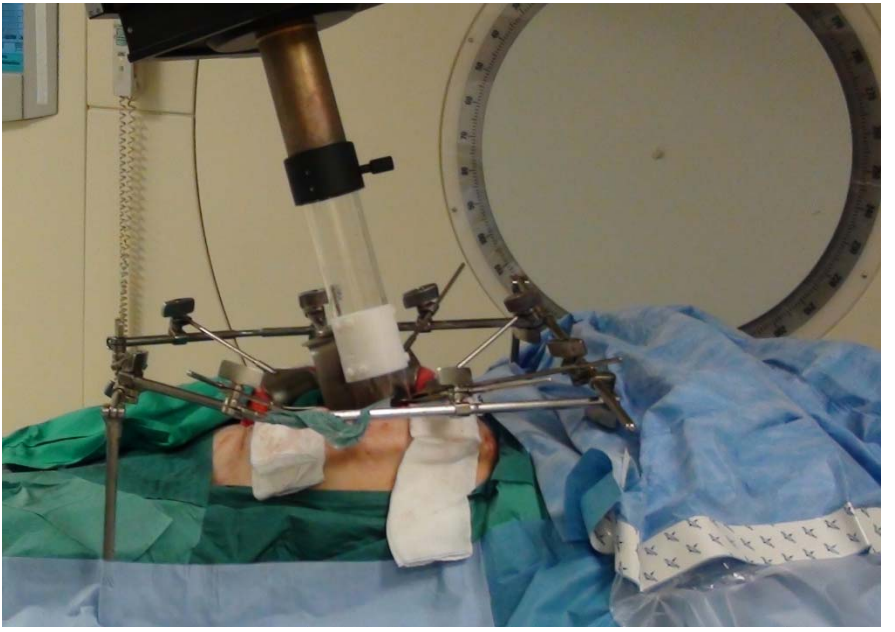

Figure 1.10: IOERT procedure on a non-dedicated linear accelerator.

1.1.3 Mobile Linear Accelerators

The first IOERT clinical experiences were carried out with non-dedicated linear accelerators that were commonly used for EBRT (Fig. 1.10). To perform IOERT treatment during the surgical procedure, the patient had to be transported to the shielded linear accelerator room where specifically-designed applicators were used to collimate the electron beam towards the tumor bed. However, patient transfer during surgery involved technical problems that oncology departments overcame with dedicated or semi-dedicated linear accelerators that could be available close to the operating room.

Mobile linear accelerators have improved the availability of IOERT from the perspective of cost-effective alternatives. These new technologies are quite compact and operate only in the electron mode (up to 10-12 MeV), so they are safe to use in almost any existing OR and can be moved from one OR to another [9]. This reason makes the logistics and setting up of IOERT program easier and cheaper for hospitals and clinics [21], [22]. Examples of commercial devices are

LIAC (Sordina IORT Technology, Aprilia, Italy), NOVAC-7/11 (Sordina IORT Technology, Aprilia, Italy), and Mobetron (IntraOp Medical Corporation, Sunnyvale, CA, USA) [16], [35]. Specifically, the LIAC and NOVAC models are robotic devices with a reduced weight, compared with conventional linear accelerators. The beam collimation system is similar in both systems and consists of different polymethylmethacrylate (PMMA) applicators with diameters ranging from 3 to 10 cm, flat-ended or beveled up to 45° [9].

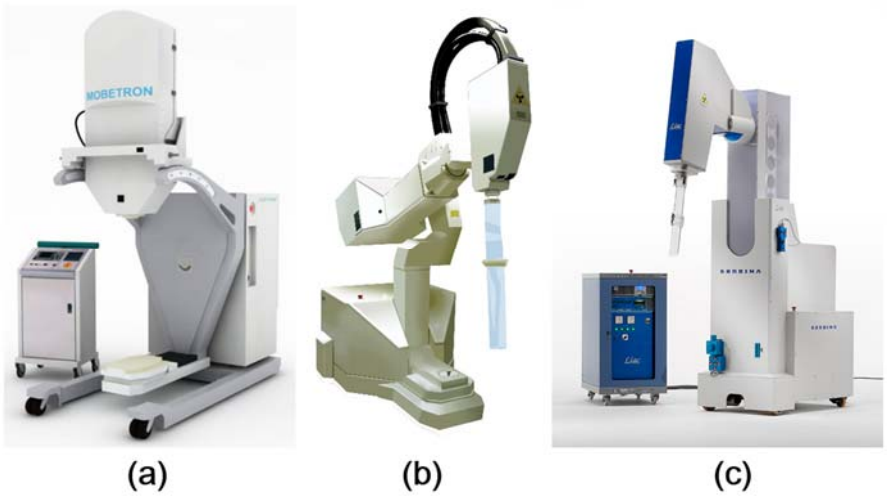

Figure 1.11: Commercial mobile linear accelerators. **(a)** Mobetron [22]. **(b)** NOVAC 7 [198]. **(c)** LIAC 12 [199].

Safe delivery of the correct dose is a key concern when using mobile accelerators. The procedure starts with the placement of the IOERT applicator (collimator) into the surgical area (i.e., inside the patient's anatomy). The angle, location, bevel and diameter of the applicator are decided by the radiation oncologist prior to delivery. The applicator is generally fixed to the patient's bed, thus ensuring that radiation is delivered to the prescribed location, and the mobile accelerator is moved to dock the applicator to the radiation beam output (gantry). This task is critical for IOERT procedures [36] because the applicator could deviate from its current position during docking, thus altering the distribution of the dose delivered. As Beddar and colleagues suggest in [21], "the geometric accuracy of treatment delivery using a mobile unit will depend solely on the accuracy of the docking". In a typical clinical scenario, this task is time-consuming owing to safety requirements and the limited degrees of freedom

(DoF) of the gantry. In order to facilitate docking, some commercial devices provide various DoFs to adapt the beam trajectory to the prescribed applicator location and, optionally, dedicated guiding systems. Docking techniques can be divided into two main groups: hard and soft docking.

In **hard docking** (used for example by the NOVAC-7 and LIAC systems), the electron applicator is divided into two parts: at the time of IOERT, when applicator parameters have been chosen, the upper part is directly connected and fixed to the gantry of the mobile linear accelerator, typically by a nurse under sterile conditions, while the lower part is placed in contact with the tumor bed to be irradiated by the radiation oncologist. Then, the therapist moves the machine towards the patient, simultaneously aligning and minimizing the distance between the two components of the applicator. Once this procedure is complete, the two parts are then firmly connected to guarantee the precise alignment of the radiation beam axis. For safety reasons, and in order to prevent potential injury to the patient, it is mandatory for the therapist to select all rotational and translational movements of the machine [9]. The time needed for the docking procedure to complete depends on the application and can take up to ~15 min [37] .

In **soft docking**, the machine is decoupled from the applicator to ensure the patient's safety in the event of an uncontrolled movement of the machine. The difficulty then arises as to how to align the central axis of the linear accelerator with that of the applicator and set the correct treatment distance. This requires an optical or mechanical alignment system. Many soft-docking systems have been described in the literature [22], [36], [38], [39]. The technique used in Mobetron was evaluated in terms of accuracy of the dose delivered and time consumed in [37] and [36]. In terms of treatment accuracy, angular displacements were found to be critical for ensuring dose distribution flatness (maximum energy value) and symmetry. Furthermore, docking time was slightly reduced to 10 minutes (mean) using Mobetron soft docking guidance system.

(a) (b)

Figure 1.12: IOERT in a dedicated OR using a mobile linear accelerator (LIAC 12). **(a)** Linear accelerator docked to the radiation applicator. **(b)** Shielding panels surrounding the patients during actual radiation delivery.

1.2 Image-guided surgery

Image-guided interventions (IGI or image-guided surgery, IGS) are medical procedures in which the position of surgical tools or therapeutic devices is displayed to the clinical expert in situ to facilitate decision making process during the clinical intervention. This approach has been implemented in neurosurgical, orthopedic, cardiovascular or radiation oncology interventions, with the main purpose of improving performance, speed and security of the clinical procedures. Advances in medical imaging, techniques and computing power has expanded this field notably in the last decades [40].

Main advantages of IGI are: improved understanding of surgical anatomy, potentially faster operating time and decreased physicians' workload and stress. IGI solutions can also be used for training and educational purposes. Thus, IGI improves surgical outcome and has decreased the need for revision surgery. Even experienced surgeons seem to benefit from the improved anatomic

orientation and situational awareness offered by IGS and subjectively equate this with less-apparent surgical risk [41].

Modern image-guided intervention techniques have been employed for approximately 20 years, and all use preoperative data, usually in the form of tomographic images combined with some tracking technology to relate these images to the patient (image-to-world registration). IGI require the localization (tracking) of surgical tools or therapeutic devices, the registration of the pose information to the preoperative data, the display of tools position regarding preoperative data, and the evaluation of possible differences between the intraoperative and preoperative findings.

The first documented surgical procedure using imaging for guidance dates to 1895, a mere eight days after Roentgen's first paper on X rays was published. Dr. John Hall-Edwards in Birmingham, England, used the new technique of X-ray imaging to guide the removal of an industrial sewing needle from a woman's hand [40]. The success, and symbolism, of this procedure opened the way for a shift in a long-last paradigm in medicine: the use of medical imaging solely as a diagnostic tool [42].

In oncology, the first applications of IGI were focused on obtaining tumor tissue for histologic diagnosis by percutaneous image-guided biopsy (PIB). Currently, this procedure is well-established, safe and widely used for obtaining tissue samples with few complications and high diagnostic yield, making it the preferable alternative for the clear majority of biopsies. Furthermore, it reduces costs, hospital length of stay and associated anxiety for patients. IGI is also used in other cancer-related procedures. For instance, in EBRT, IGI is employed for patient set-up verification, gating of the radiation beam based on organ/respiratory motion and the assessment of the IORT-HDR brachytherapy seed placement [43]–[48].

1.2.1 Tracking devices

The main component of any image-guided system is the tracking device that determines the localization of the surgical or therapeutic tools in the space [40]. Tracking technologies can be classified in mechanical, acoustic, electromagnetic and optical trackers depending on their tracking principle.

Mechanical trackers

Mechanical trackers (MT) are based on rigid mounting frames that are fixedly attached to the patient's anatomy and allow the guidance of surgical tools to reach the target tissue. One of the first reported MT was introduced by Horsley and Clarke [49]. They attached a metallic frame (later to be known as a stereotactic frame) to a monkey's head and used external markers to assign a coordinate system for the animal's brain (Fig. 1.13). In order to display the surgical position simultaneously on three orthogonal preoperative CT planes, Galloway and colleagues [50], [51] developed an articulated arm designed exclusively for assistance during neurosurgery procedures.

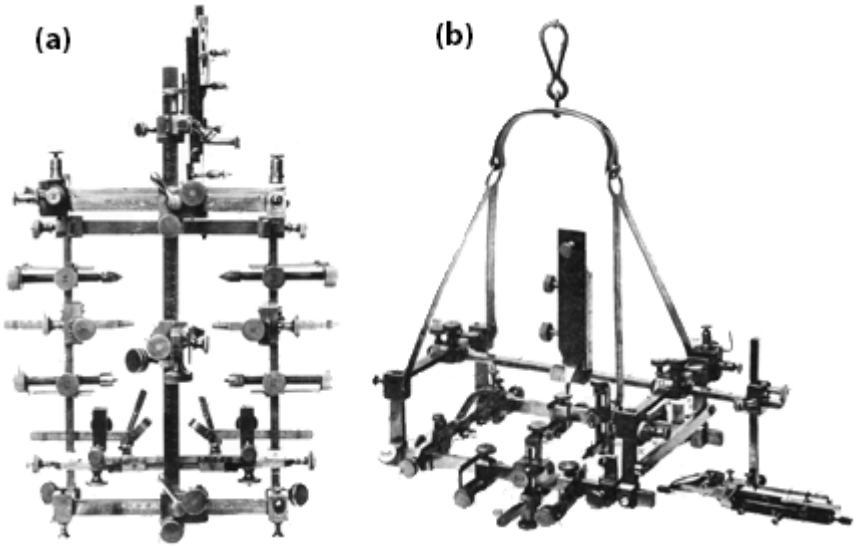

Figure 1.13: Clarke's stereotaxic apparatus for directing an insulated needle by graduated movement in three planes. **(a)** Top and **(b)** side elevations [49].

Acoustic trackers

Despite the valuable contribution of MT systems for certain surgical procedures, the intrusive effect of these systems forced researchers to develop handier technologies [40], [50]. The first attempt to overcome the MT constrains was reported by David Roberts's lab at Dartmouth [52], [53]. In 1993, Roberts

and his colleagues could locate the target within the operative field on a tomographic image in real time by means of a spark-gap sonic localization

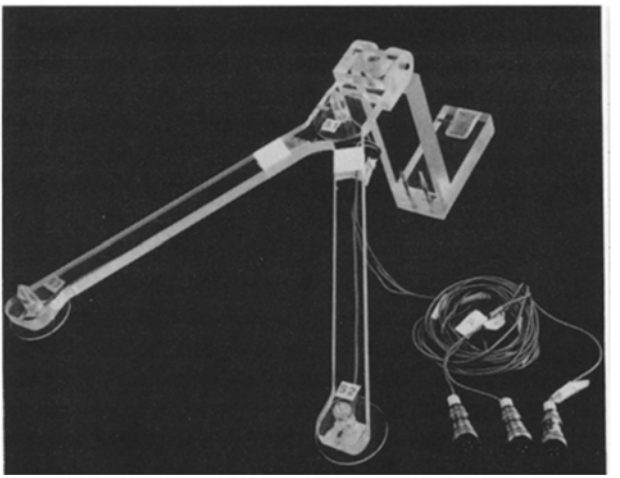

Figure 1.14: The Plexiglas bracket with a nonlinear array of three spark gaps. This component of the acoustic localization system attaches to the operating microscope in David Roberts's work [53].

(acoustic tracker, AT) system attached to the operating microscope (Fig. 1.14). Acoustic trackers estimate the tools positions by measuring the time it takes for a sound wave to travel from the transmitter to the receivers in a similar manner as ultrasound imaging (US) works. However, they are very dependent on the working volume (noise, reflections, etc.) and are quite inaccurate for certain surgical applications.

Electromagnetic trackers

Electromagnetic trackers (EMT) create a pulsed magnetic field over the working volume (tracking volume). Small sensors (solenoids) are attached to the tracked tools and measure the magnetic field which is different depending on the localization. The main advantage of these systems is the sensor coils size (less than 0.5 mm in diameter and 8 mm in length) that can be embedded in the surgical tools allowing tracking inside the individual's body. However, they are very sensitive to metallic objects in the working volume that could distort and

compromise the accuracy of the system. Commercially available products include trackSTAR and driveBAY from Northern Digital Inc. (Shelburne, USA).

Optical trackers

Optical trackers use cameras surrounding the working area to determine the position of surgical devices through various visualization techniques. These systems enable higher accuracy and a larger tracked volume than other technologies [54], [55]. However, they need a clear line-of-sight between the tracked object and the detecting cameras, which is not always possible (e.g., when tools such as catheters and probes are tracked inside the patient). In these

Figure 1.15: Commercial optical trackers. **(a)** fusionTrack [200]. **(b)** Polaris Spectra and Vicra [106].

situations electromagnetic trackers are better suited [40], [56]. Commercially available optical systems include fusionTrack (Atracsys Inc., Puidoux, Switzerland) and Polaris (NDI Inc., Ontario, Canada) (Fig. 1.15).

Both commercial systems share a common constraint, namely, that they use a single pair of tracking cameras. Given that their working volume is limited and

they are prone to occlusions in specific surgical scenarios, performance and accuracy are often affected [57], [58]. A higher number of cameras would enlarge the working volume and improve accuracy, thus enabling the system to overcome this limitation [54], [57], [59].

OptiTrack optical tracker

OptiTrack [60] is an optical tracking system based on infrared cameras that enables objects to be located in the surgical space, much in the same way as Polaris or fusionTrack. The number of tracking cameras and their spatial configuration are flexible (i.e., they can be modified depending on the requirements of the application). This characteristic makes it possible to track very different environments, such as a complete operating room (OR), with almost no restrictions on working volume. The main advantages of the system are the accuracy of tracking (submillimeter level, according to the manufacturer) and its robustness against camera occlusions. Optical systems including more than two cameras (hereinafter referred to as multicamera systems) lead to data redundancy and ensure a clear line-of-sight. Consequently, OptiTrack could be more suited to environments that are prone to occlusions than 2-camera trackers. In fact, some studies have examined the use of this tracker for IGS applications [61]–[63].

1.2.2 Image-to-world registration

In the most common clinical scenario, preoperative images must be registered (aligned) with the patient's position on the operating table. This alignment process, named registration, is an essential component for all IGI since it enables correspondence between the image and the tracker system. Thus, registration allows navigation of surgical instruments. In the context of image-guided surgery, this issue is widely known as image-to-world registration. If the estimation of the registration parameters is not sufficiently accurate, errors will occur while the position of the instrument is displayed over the image, with the result that guidance «could be worse than useless», as Fitzpatrick and colleagues suggest in [64]. In order to estimate the geometric transformation between the two coordinate systems (image and tracker), it is necessary to record the position of matching reference locations in both geometries. The data acquired enable the registration algorithm to estimate the best transformation between both coordinate systems (image and tracking). However, the spatial position obtained

for those references has limited accuracy owing to poor resolution (in the image space), tracking system localization error and user interaction (in the world/tracker space). This effect is called fiducial localization error (FLE) and is a well-known source of errors during image-guided procedures. Reports reviewing studies of registration can be found in [65], [66].

Registration can be classified into rigid or nonrigid registration. In rigid registration, deformations of the two registered geometries (preoperative image and tracker) are not allowed and only translations and rotations are permitted. On the other hand, nonrigid registration techniques attempts to deform the two geometrical spaces to perform the alignment. Although this is an area of active research with considerable progress made over the last decade, currently available nonrigid registration techniques lack the robustness required for clinical practice and have only been applied in very limited trials to date [40]. Current commercial IGS only use rigid registration, while nonrigid registration continues to be a major research topic of discussion.

Image-to-world registration is based on two approaches. One uses markers or fiducials that are attached to the patient's body (fiducial-based registration); the other avoids the use of fiducials by capturing position data from homologous anatomical surfaces or structures [64]. The fiducial-based registration approach typically uses small point-like fiducials attached to the patient's skin or to a bony structure to compute the correspondence between the image and the tracking system coordinates. It is assumed that only rigid transformations occur between image acquisition and surgery [64]. In this context, the estimation of the geometric rigid transformation becomes a least-square fitting problem in which the three-dimensional positions of fiducials are aligned (registered) in both spaces. Ideally, this match will show no error. However, in a real-world situation, FLE results in a mismatch that causes the actual position of a tracked instrument to be erroneously displayed on the image space during navigation. The localization error of tools or anatomical structures inside the surgical-guidance region is known as target registration error (TRE), which is a common figure of merit for registration evaluation purposes. The relationship between FLE and TRE has been analyzed in several studies [64], [67], [68], which show that both metrics are statistically independent, thus underlining the importance of TRE as a measurement of registration accuracy.

The second registration approach is to use a fiducial-free approximation, in which devices such as surface scanners or time-of-flight (ToF) cameras are used to acquire position data from the patient's surface and structures [69], [70]. These

devices usually collect a greater amount of position data in the world space (tracker coordinate system) more quickly than the classical fiducial-based approach. In fiducial-free approximation, the more information is collected, the better accuracy (lower TRE) is expected during registration, because TRE depends on the number of fiducials used [68]. However, one-to-one correspondence between fiducials is no longer available, and least squares fitting is not adequate for estimating registration parameters. The iterative closest point (ICP) algorithm is a common solution when the point cloud must be matched with no knowledge of point-to-point correspondence [71]. Many variants have been proposed to overcome the known limitations of ICP, which become relevant for specific applications [70], [72]–[74].

In the last few decades, the field of IGS technology has improved with more accurate trackers, compact systems, user-friendly interfaces and more precise registration algorithms and techniques. These features have contributed enormously to the increased utilization and acceptance of IGS in the clinical setting. However, the great number of components that form an IGS system also requires a quality control in order to perform a safe and accurate guidance of surgical tools and devices in clinical use.

2

Motivation and objectives

2.1 Motivation

The main objective in radiation therapy is to ensure therapeutic quality by providing state of the art technical equipment and procedures, maintaining a safe application of radiation for patients, personnel and environment and minimizing uncertainties in the therapeutic procedures. IOERT overcomes many of the technical difficulties by applying a high radiation dose directly to the surgically opened tumor bed, without irradiating healthy tissue in front of the target, using mobile or fixed linear accelerators to deliver the radiation dose. However, the noticeable complexity of IOERT introduces some uncertainties that must be addressed for a more accurate and safe procedure [16], [27], [28], [35], [75].

Nowadays, IOERT dosimetry planning is carried out with the availability of treatment planning systems that address the important challenge of the estimation of the dose distribution on a pre-surgical CT scan. Despite this very valuable improvement, a large number of physical preparations and quality assurance measures are needed and must be adapted to the IOERT workflow of each individual case. Major issues have been discussed in three reports and guidelines by the American Association of Physicist in Medicine (AAPM) [76], [77] and the Italian Instituto Superiore di Sanità [78]. Nevertheless, the uncertainty of the correct and safe dose delivery inside the operating room is a key concern not yet solved in the literature. Differences between the prescribed

and the surgical applicator localization are commonly due to: the manual applicator placement by the radiation oncologist, the docking misalignment of the applicator and the mobile linear accelerator (because of the limited degrees of freedom of commercial linear accelerators) or the need for a re-planning inside the OR due to the surgical findings. Any of these reasons may lead to dosimetry deviations from the prescribed dose which cannot be fully assessed by surgeon and radiation oncologist. This problem motivates the research on better approaches for the assessment of dosimetric planning in the OR [36], [79]–[82].

Some authors have already reported the use of ultrasound imaging during breast IOERT in order to ensure the correct placement of the protection just behind the tumor bed, its alignment with the radiation applicator and treatment of the prescribed tumor bed depth [34], [83], [84]. Despite this valuable enhancement, US imaging is not suitable for dose distribution estimation which may be required during the procedure re-planning (if needed). Moreover, the cost of a dedicated US device could be an important limitation that motivates the research on new commercially available low-cost US probes for this application. Other intraoperative imaging techniques such as the Cone-Beam CT C-arm could be used in this context for accurate dose delivery estimation [85]–[87]. Although these two imaging approaches seem to combine useful information for IOERT procedures, registration techniques are needed for the fusion of both modalities.

Image-guided approaches could overcome those described limitations providing a validation method for the prescribed treatment and enable a procedure re-planning during the surgery by means of the applicator tracking — relating the surgical patient's anatomy to the applicator. A similar solution may aid during the docking of the mobile linear accelerator. Furthermore, the combination of US and CBCT modalities under an image-guided system could enhance the procedure performance noticeably if both images are registered.

The use of an image-guided approach implies a registration process (image-to-world registration) of the patient's anatomy to the imaging studies. This strategy could provide the applicator position regarding the prescribed procedure (pre-surgical CT scan) and the surgical imaging studies (US or CBCT C-arm) for assessment purposes. Image-to-world registration has been addressed commonly in the literature by means of fiducial-based rigid registration in surgical environments. However, in order to achieve an accurate registration, the number of fiducials must be very large which may increase

substantially the time required for localizing all fiducials in the OR. This could be a safety issue for most of IOERT procedures. This encourages specific registration schemes that could fulfill the particular requirements of this surgical procedure.

On the other hand, IOERT is carried out by a multidisciplinary team in a very complex environment that has special tracking needs due to its working volume characteristics —large and prone-to-occlusions- in addition to the accuracy requisites [27]. Commercial medical trackers do not satisfy all these requirements, though. A possible approach is to use a multicamera optical tracking system that could lead to a larger working volume while preserving the accurate positioning of the tracked tools. Nonetheless, assessments of multicamera trackers for the surgical environment are limited in the literature.

This research work is linked to a broader strategy designed for the reduction of uncertainties and quality improvement in IOERT, providing better data to prove evidence of the therapeutic benefit of IOERT. For this reason, a main characteristic of this work is the strong collaboration of different actors (technical and clinical) during the development of each research piece. Furthermore, with the main objective of producing translational research that could actually be transferred to the clinical environment, this thesis was carried out in close collaboration with GMV (Tres Cantos, Madrid, Spain), that developed the IOERT treatment planning system in collaboration with the Biomedical Imaging and Instrumentation Group (Universidad Carlos III de Madrid - Hospital General Universitario Gregorio Marañón, Madrid, Spain), Sordina (Aprilia, Italy) that produces mobile linear accelerators for IOERT and the Oncology Department of the Hospital General Universitario Gregorio Marañón (Madrid, Spain).

2.2 Objectives

The main objective of this thesis is to explore technological and procedural alternatives to improve the IOERT performance and address the described uncertainty problems. In particular, image-to-world registration, multicamera optical trackers, multimodal imaging techniques and the mobile linear accelerator docking are revisited in the IOERT context through the following objectives:

1. To evaluate a commercial multicamera optical tracker in terms of accuracy, sensitivity to miscalibration, camera occlusions and detection of tools using a feasible surgical setup; and propose an automatic miscalibration detection protocol that satisfies the IOERT requirements of automaticity and speed.
2. To develop a new, robust, accurate and fast image-to-world alternative approach for image-guided interventions.
3. To study the integration of a commercial low-cost ultrasound transducer and cone beam CT C-arm for image-guided interventions that combines surgical navigation and to explore registration techniques for both modalities.
4. To develop a navigation solution based on optical tracking for the docking of the mobile linear accelerator to the radiation applicator, improving safety and reducing procedure time.
5. To propose and assess the installation setup of a navigation system in a dedicated OR, to determine the required steps in the IOERT process tree, to identify the workflow limitations and to evaluate the feasibility of the integration in a real OR.

OBJECTIVES

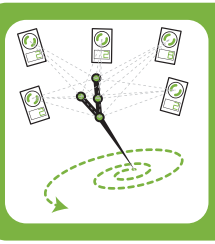

1

Multicamera Tracker Evaluation

To evaluate a commercial multicamera optical tracker in terms of accuracy, sensitivity to miscalibration, camera occlusions and detection of tools using a feasible surgical setup; and propose an automatic miscalibration detection protocol that satisfies the IOERT requirements of automaticity and speed.

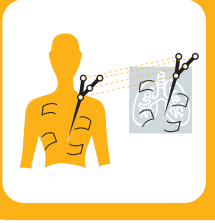

2

Image-to-World Registration

To develop a new robust, accurate and fast image-to-world alternative approach for image-guided interventions.

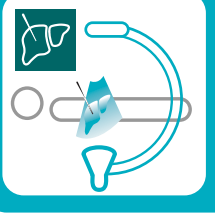

3

Needle Guidance: Ultrasound & CBCT C-arm

To study the integration of a commercial low-cost ultrasound transducer and cone beam CT C-arm for image-guided interventions that combines surgical navigation and to explore registration techniques for both modalities.

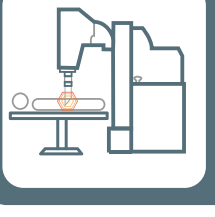

4

Liac Docking guidance

To develop a navigation solution based on optical tracking for the docking of the mobile linear accelerator to the radiation applicator, improving safety and reducing procedure time.

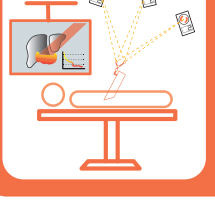

5

Image-guided IOERT

To propose and assess the installation setup of a navigation system in a dedicated OR, determine the required steps in the IOERT process tree, identify the workflow limitations and evaluate the feasibility of the integration in a real OR.

2.3 Outline of the document

The present document is organized into twelve chapters. Chapter 1 introduces the IOERT state of the art and the image-guided applications. Chapter 2 presents the motivation and objectives of the work. Chapters 3 to 7 describe the research work of this thesis where each objective is addressed. In Chapter 3, the multicamera optical tracker is evaluated in terms of accuracy and calibration reliability. In Chapter 4 a new image-to-world registration schema is proposed for the IOERT environment. In Chapter 7 an image-guided system for needle-based procedures that combines US and CBCT images is presented. Chapter 6 describes a new approach for the aid of the mobile linear accelerator docking. In Chapter 7 the clinical evaluation of a navigator system for the IOERT applicator placement is described and discussed in twelve patients.

Chapter 8 presents a global discussion together with the main conclusions and contributions of this thesis and some possible lines of future work. In Chapter 9 a summary of the software contributions developed during this work is depicted. In Chapter 10 the publications derived from this thesis are presented. Chapter 11 lists all the references of this work. Finally, Chapter 12 contains some useful material for readers such as summaries of each main chapter (3 to 7).

3

Multicamera Optical Tracker Assessment for Image-Guided Surgery Applications

3.1 Introduction

Current commercial optical trackers for image-guided applications use a single pair of tracking cameras such as Polaris (NDI Inc., Ontario, Canada) and fusionTrack (Atracsys Inc., Puidoux, Switzerland). Hence, their working volume is limited and they are prone to occlusions in specific surgical scenarios, which often affects their performance and accuracy [57], [58]. Optitrack multicamera optical tracker [60] would enlarge the working volume and improve accuracy, thus enabling the system to overcome this limitation thanks to the flexible number of cameras and their spatial configuration. To our knowledge, there are no commercial multicamera trackers offering accurate tracking for IGS [54], [57], [59].

However, multicamera systems require a calibration process for every single application. This step is time-consuming and must be carried out under very specific conditions: a clear working volume, specific calibration tools and finely tuned camera parameters (illumination, threshold and exposure). Ensuring suitable tracking accuracy depends on the quality of calibration. Therefore, the feasibility of OptiTrack could be threatened if the calibration process must be performed regularly in the OR, where access is limited and a sterile environment is essential prior to a surgical procedure. OptiTrack has been used for tracking

purposes in several fields [88]–[91]. Nevertheless, few studies have examined the use of this tracker for IGS applications [61], [63]. In particular, for IOERT procedures, static accuracy is the main point of interest, and dynamic accuracy (real-time tracking) is not a key issue.

When a navigation system is evaluated for IGS, the principal concern is the tracking error of the system in the image geometrical space [40], [92], [93]. Several error sources may influence the correct three-dimensional location of surgical tools [94]. Common factors that affect the accuracy of IGS navigation include image-to-world registration outcome [95], [96], the technical specifications of the cameras, non-optimal design of rigid bodies [97], [98], the use of different marker sizes and the distance between the markers and the sensors [93]. OptiTrack, in particular, is affected by camera calibration, which is performed in advance and provides the location of each tracking camera in space [99]. The role of these factors in optical trackers for IGS has been widely assessed in the literature [92], [99]–[101]. However, most studies are subject to limitations and focus mainly on a specific IGS application of interest [56], [93], [102]–[104]; hence, it is difficult to extrapolate their results to other applications or compare systems from different manufacturers [93].

One common limitation during assessment is the use of another tracker as the gold standard for the evaluation of accuracy and the assumption that the chosen gold standard is sufficiently accurate [56], [103], [105]. Although the studies cited here provide very valuable information, a true gold standard is needed for further evaluation so that independent measurements of tracking accuracy can be provided. In addition, not all published studies provide measurements that consider the spatial dependency of the accuracy value on the position inside the working volume. Some authors and manufacturers provide the accuracy of trackers in terms of distance to cameras (i.e., NDI specifications [106]). However, these studies are usually made for a fixed spatial camera configuration, which cannot match the requirements of a multicamera optical tracker. A key aspect of assessment of multicamera optical trackers is the effect of occlusions on tracking accuracy. When the line-of-sight requirement is not ensured for some of the cameras, multicamera trackers are still able to track the objects owing to the data redundancy of the remaining non-occluded cameras. It is very important to consider the dependency of accuracy on the number of occluded cameras to ensure a fair assessment. Finally, also important is the use of a tracked tool during the acquisition of assessment data that includes a set of optical markers in a fixed geometrical configuration (rigid-body). Some studies have demonstrated the dependency of accuracy on the markers' spatial

configuration that could lead to amplification of the tracking error and bias the assessment [97], [98].

The number of image-guided applications using OptiTrack is increasing because of its advantages, such as the flexible number of cameras, robustness against occlusions and a configurable spatial distribution that adapts to several scenarios with application-specific requirements. Nonetheless, the literature contains no extensive studies of the system that demonstrate accuracy in terms of camera occlusions, tracked tools used and the temporal reliability of calibration using a gold standard with significantly higher accuracy than the system we evaluate here.

3.2 Objective

The purpose of this study was to evaluate an OptiTrack 8-camera optical tracker in terms of accuracy, sensitivity to miscalibration, camera occlusions and detection of tools using a feasible clinical setup. We performed an exhaustive evaluation, showing detailed measures of accuracy and performance under occlusions with different tracked tools. A very accurate robotic arm is used as a gold standard. We also propose and validate a protocol to detect miscalibration of these systems that was tested on a real clinical setting in terms of sensitivity to miscalibrations and temporal reliability.

3.3 Material and Methods

3.3.1 Optical tracker

The tracker we evaluated consists of a set of 8 OptiTrack Flex13 cameras (1280 x 1024 image resolution, 4.8 x 4.8 μm pixel size and a frame rate in the range of 30-120 frames per second). Each camera had a 5.5-mm F#1.8 lens and an 800-nm infrared (IR) long pass filter with a horizontal and vertical field of view (FOV) of 56 and 46 degrees, respectively. Flex13 cameras illuminate the scene with a light-emitting diode (LED) ring composed of 28 LEDs (850 nm) with adjustable brightness (Fig 3.1 a).

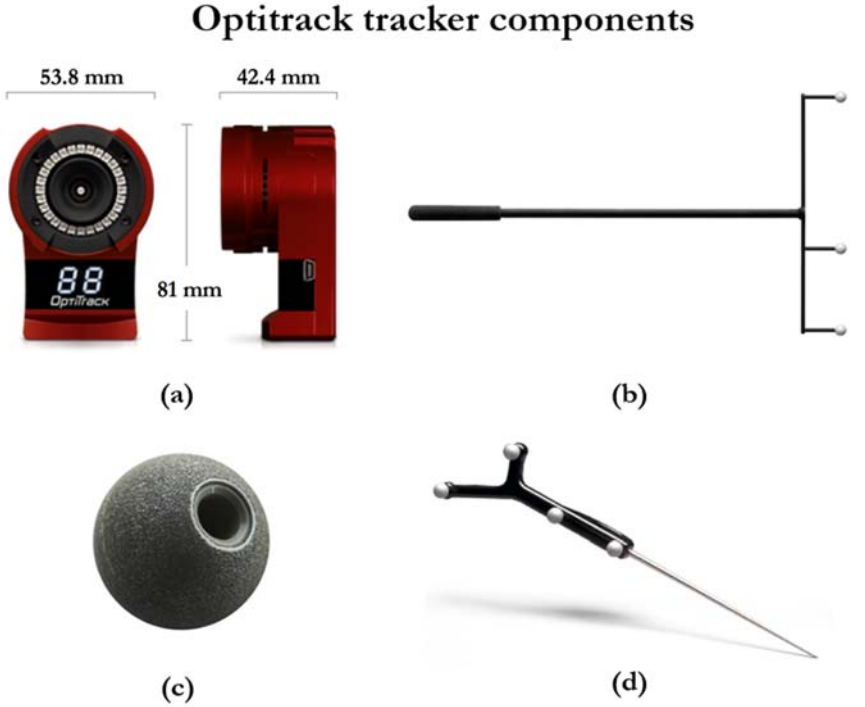

Figure 3.1: (a) OptiTrack Flex13 camera **(b)** Optiwand calibration tool **(c)** Reflective marker of 11.5 mm radius. **(d)** Rigid-body pointer tool (NDI, Ontario,

Depending on the application, the cameras are arranged around the working volume and connected to a USB hub to be controlled using the manufacturer's software. The system calculates the position of passive retro-reflective markers (Fig. 3.1 c), which are small spheres coated with IR reflective material. Several marker diameter sizes are offered by the manufacturer depending on the specific application. In the present study, we used an 11.5-mm diameter marker from NaturalPoint (7/16" hard model [60]) for all experimental setups because it is the manufacturer's recommended size for the OR tracking volume studied. All the tools were built using the same marker size.

The position of the tracked tools is obtained in real time using a forward projection approach [107] and acquired using the manufacturer's application programming interface (API). Reflective markers are positioned in a unique geometric form known as a rigid body (an unmistakable shape in any orientation) that is identified by the cameras to determine the tool's position and orientation. The simplest rigid-body must be composed of at least three reflective markers, between which distances and angles are fixed with respect to each other.

The multicamera tracker must be calibrated in advance to know the relative position of each camera in the space and the optical lens parameters (e.g., focal length, optical aberrations). Calibration requires a specially designed tool (Optiwand, Fig 3.1 b), which is provided by the manufacturer. This tool consists of three aligned markers with fixed positions (Fig 3.1 b). The calibration procedure starts by moving the calibration tool along the working volume. As the system knows the spatial configuration of the tool's markers, relative positions of the cameras can be computed by using the projections of the markers for several acquired spatial locations of this rigid body. These samples must be acquired over the whole working volume, and their number will determine the quality and accuracy of the calibration. When enough samples have been acquired, the system software (TrackingTools) calculates the best calibration parameters from the available set of calibration samples in the least-squares (LS) sense.

Multicamera tracking is based on the projection of reflective markers into each camera detection plane (Fig. 3.2 a4). This projection (Fig. 3.2 a5) is collected for each camera. Using the calibration parameters, the expected projection (Fig. 3.2 a3) can be computed from the location of the 3-dimensional marker (Fig. 3.2 a2). In an ideal case, the current marker projection (Fig. 3.2 a5) will perfectly match the expected projection (Fig. 3.2 a3). However, under non-ideal conditions, this match is not perfect and differs between collected and expected

projections. This absolute difference is known as projection error (Fig. 3.2 a6). Similarly, when a pair of cameras detects a projected marker, the system estimates the three-dimensional location as the intersection of the rays that join each camera plane and the marker. Again, under ideal conditions, all projection rays collide at the true marker location (Fig. 3.2 a2). Nevertheless, owing to the projection error (different on each camera), the estimated (Fig. 3.2 a7) and the true marker location (Fig. 3.2 a2) are not coincident. This absolute difference is

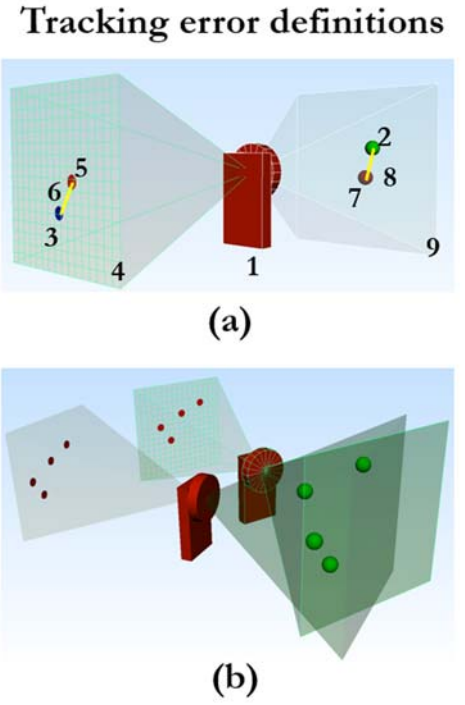

Figure 3.2: (a) Tracking error definitions. **(a1)** Optical tracking camera, **(a2)** reflective marker true position, **(a3)** true projection on **(a4)** camera plane, **(a5)** expected projection from calibration, **(a6)** camera projection error, **(a7)** marker location estimate, **(a8)** marker tracking error within **(a9)** camera acquisition range. **(b)** Two cameras imaging 4 retro-reflective targets. Target locations are determined from a forward projection of the target images on the camera image plane. Targets lie at the intersection of the projected rays (R. Gooch, 1998, [15]).

known as tracking error (tracking error, Fig. 3.2 a8), which determines the tracking accuracy of the tracker system.

Immediately after calibration, the projection error (Fig. 3.2 a6) is expected to be under a certain small threshold. When a miscalibration occurs on one camera, the projection error and the tracking error (Fig. 3.2 a8) increase accordingly. For a setup case formed by 2 optical cameras, if a miscalibration on 1 of the cameras is large enough, the camera system will not detect the three-dimensional location of the marker.

It is important to detect miscalibration during IGS procedures. Two-camera optical commercial trackers are commonly calibrated in advance by the manufacturer. The Polaris system includes a software tool for testing camera calibration before tracking which warns the user if miscalibration is detected. If a miscalibration occurs in a multicamera tracking system after calibration, the tracking error induced by this camera could be compensated by the remaining (well-calibrated) cameras. However, this condition could lead to a loss of accuracy. Even so, there is no established protocol for controlling the reliability of the calibration for multicamera optical trackers.

3.3.2 Evaluation of the tracker calibration

The number and position of the cameras are selected by the user depending on the application requirements for multicamera trackers. In our case, large working volume, high accuracy and robustness against occlusions are mandatory requirements for the location of the IOERT radiation collimator. Eight Flex13 cameras where installed in the IOERT operating room at Hospital Gregorio Marañón to cover the large working volume that includes the surgical table. This setup (hereinafter referred to as 'OR scenario') allows surgeons to navigate procedures for different anatomical targets without modifying the cameras' spatial configuration (Fig. 3.3).

In the OR scenario, miscalibrations can occur during real procedures, since moving the surgical light (Fig. 3.3 c) could deviate some cameras from the calibrated position. Therefore, we proposed a new miscalibration detection protocol and studied its sensitivity and feasibility. On the other hand, with the intention of minimizing the periodicity of calibration in the OR scenario, the temporal reliability of the calibration was also assessed.

Miscalibration detection protocol

The protocol proposed for detection of miscalibration is based on the projection error and consists of the following steps. First, we place a unique reflective marker into the working volume. This marker must be detected by each camera on the projection plane (Fig. 3.2 a4) individually. Once the marker is fixed and visible, its three-dimensional location is recorded for a specific time using the complete calibrated system. Marker location is then reacquired using all possible combinations of two cameras to cover the complete system. Finally, the three-dimensional location of the marker acquired using each camera pair is compared with the location acquired using all the cameras to estimate tracking error.

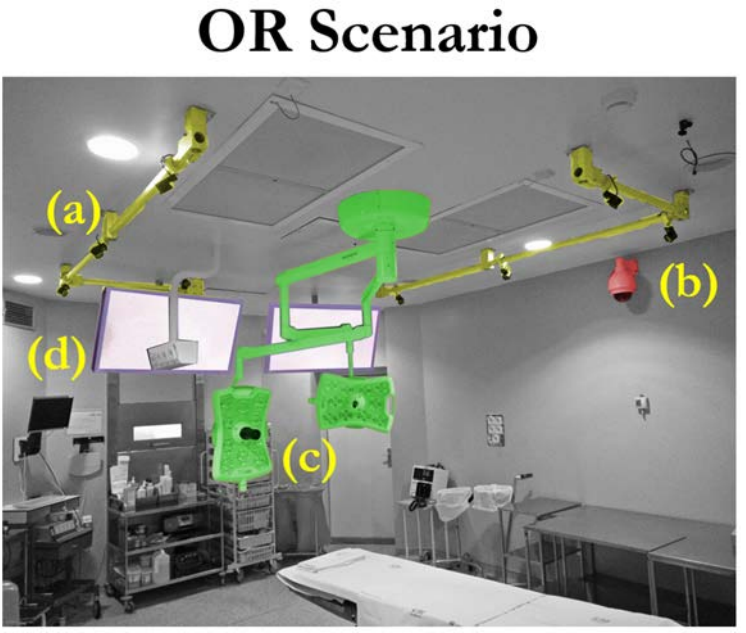

Figure 3.3: OR scenario: Distribution of cameras in Hospital Gregorio Marañón (Madrid) used for navigation of the IOERT applicator. **(a)** Tracker structure with 8 Flex13 cameras. **(b)** Video camera. **(c)** Surgical lights. **(d)** Navigation screens.

If an individual pair includes a miscalibrated camera, the 3-dimensional marker location acquired will be significantly different from the location

provided by the system when all the available cameras are used. This is expected, since the miscalibration produces a more pronounced tracking error (Fig. 3.2 a8) on a single pair. Furthermore, if the miscalibration is large enough, this camera pair will not report visible markers in its working volume, whereas the complete system will. Therefore, differences in the location of markers could be used as a metric of miscalibration. In order to determine the sensitivity of this miscalibration metric and its feasibility, we designed two experimental setups in the OR scenario.

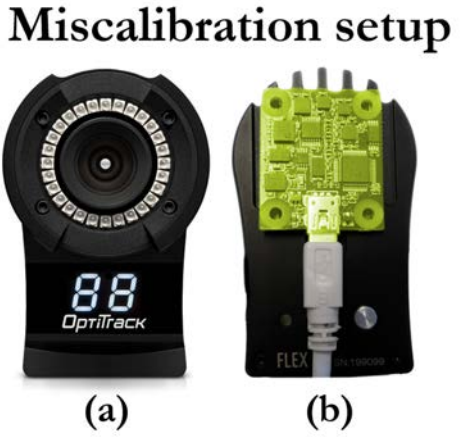

Figure 3.4: Phidget orientation sensor attached to an OptiTrack camera. **(a)** Front part of OptiTrack Flex 13 camera. **(b)** Phidget 3/3/3 attached to the camera back.

Miscalibration sensitivity study

For this sensitivity study, we used one camera pair (for tracking) and an orientation sensor (to measure miscalibration).

A two-camera system (Flex13) was calibrated using the calibration tool according to the manufacturer's instructions (~3000 samples of the Optiwand tool position were tracked by each camera). A reflective marker was placed at a fixed point in the system working volume at ~1.5 m from the cameras. An inclinometer (orientation sensor) was attached to the back of one camera to provide rotation measurements. The sensor used was the PhidgetSpatial

Precision 3/3/3 (Phidgets Inc., Alberta, Canada), which combines the functionality of a 3-axis compass, a 3-axis gyroscope, and a 3-axis accelerometer and provides an accurate estimation of orientation (Fig. 3.4 b). The gyroscope resolution is 0.02 degrees/s in both the X and the Y axes and 0.013 degrees/s in the Z axis. The sensor was connected via USB to a computer in order to measure changes in the orientation of the camera to which it is attached.

We acquired the three-dimensional position of the marker ($N_{cal} = 5000$ samples) using the calibrated tracker and computed the mean calibrated marker location ($\boldsymbol{p}_{\boldsymbol{\mu}}^{\boldsymbol{cal}}$). We then slightly rotated the camera manually to cause a miscalibration. This manual rotation was performed around the mounting screw of the camera. We used the rotation sensor to measure the rotation produced and acquired ($N_{\alpha} = 5000$) samples of the marker position. We repeated the acquisition of the three-dimensional marker location using the tracker API 10 (M) times and computed the mean and standard deviation of the tracking error (Eq. 3.1). This procedure was repeated three times, increasing the camera rotation each time.

Sensitivity was evaluated in terms of the tracking error ($\widehat{TE}$ Eq. 3.1) and rotation value (α). The miscalibration threshold was defined as the maximum rotation value (α_{th}) before the tracker software reported no markers in the working volume (Eq. 3.1).

$$\widehat{TE}(\alpha) = \sqrt{\frac{1}{N_{\alpha}} \sum_{i=1}^{N_{\alpha}} \left\| \boldsymbol{p}_{\boldsymbol{i}}^{\boldsymbol{\alpha}} - \boldsymbol{p}_{\boldsymbol{\mu}}^{\boldsymbol{cal}} \right\|^2} \quad \textbf{(3.1),}$$

where $\widehat{TE}(\alpha)$ is the tracking error for a miscalibration of α degrees, $\boldsymbol{p}_{\boldsymbol{i}}^{\boldsymbol{\alpha}}$ the i-th sample (of $N_{\alpha} = 5000$) location of the marker acquired with the tracker under a miscalibration of α degrees and $\boldsymbol{p}_{\boldsymbol{\mu}}^{\boldsymbol{cal}}$ the mean marker location acquired using the calibrated system ($\alpha = 0^{\text{º}}$).

Feasibility study of the miscalibration detection protocol

To demonstrate the feasibility of the proposed miscalibration detection protocol, we calibrated the multicamera system installed in the OR (eight Flex13

cameras) following the manufacturer's instructions. After calibration, a reflective marker was placed in a fixed position inside the working volume of the tracker. First, we acquired ($N = 1000$ samples) the position using the calibrated 8-camera system and each possible camera pair ((i,j), $\binom{8}{2} = 28$ camera pairs). We repeated the acquisition of the marker location using each possible camera pair, while one, two, three and four cameras were miscalibrated by manually rotating the camera (~1 degree) around its mounting screw. Miscalibrated cameras were chosen at random. The tracking error of each camera pair was estimated as (Eq. 3.2).

$$\widehat{TE}_{(i,j)} = \sqrt{\frac{1}{N}\sum_{k=1}^{N}\left\|\boldsymbol{p}_{(i,j)k} - \overline{\boldsymbol{p}}_{\boldsymbol{\mu}}\right\|^2} \quad \textbf{(3.2),}$$

where $\widehat{TE}_{(i,j)}$ is the estimated tracking error for the camera pair (i,j), $\boldsymbol{p}_{(i,j)k}$ is the k-th marker location (of N samples) acquired using the camera pair (i,j) and $\overline{\boldsymbol{p}}_{\mu}$ is the mean marker location acquired using the 8-camera system at the beginning of the experiment.

Calibration temporal reliability study

We performed another experiment in the OR scenario in order to evaluate the temporal reliability of calibration. For that purpose, we analyzed the estimated tracking error over time using the eight-camera tracker setup installed in the OR. To ensure constant conditions, the experiment was specifically scheduled over a period of 5 days when the OR scenario was not used for any other purpose.

On the first day, we calibrated the tracking system and slightly rotated (around the mounting screw) a random camera manually to cause a miscalibration. Then, during the following 5 days, the position of a single steady marker inside the working volume was acquired every four hours using the 8-camera system and for each possible camera pair (28 pairs). We acquired 1000 samples of the marker every time and studied the tracking error (Eq. 3.2) over time.

3.3.3 *Evaluation of the accuracy and occlusions*

In order to determine the true accuracy of the 8-camera tracker configuration installed in the OR, we designed a second scenario (hereinafter referred as the 'robotic scenario'). We measured the tracking error on a single marker with/without occlusions and using different tracked tools inside the working volume.

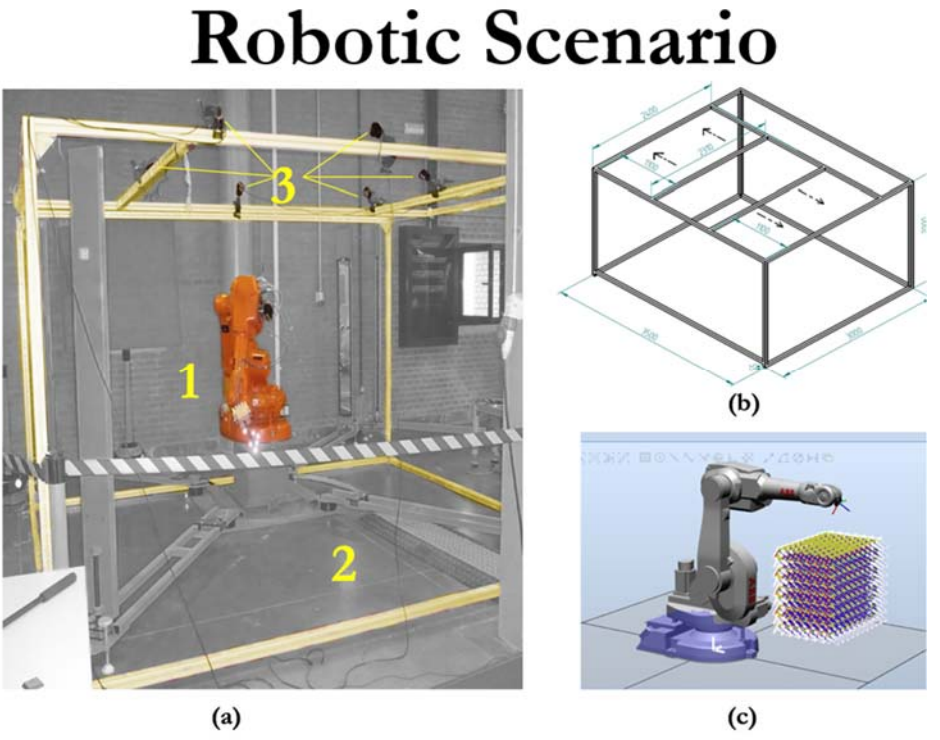

Figure 3.5: Robotic scenario **(a)** Experimental setup for optical tracker accuracy assessment. **(a1)** ABB Robot, **(a2)** metallic structure simulating OR camera holders, **(a3)** OptiTrack Flex 13 cameras. **(b)** Metallic structure diagram (all measurements are in mm; arrows mean that the piece is movable). **(c)** Programmed robot path over the working volume.

To provide a location gold standard during acquisition, we used an ABB IRB 1600 industrial robotic arm (ABB Inc., Zürich, Switzerland) with a 1.2-m reach and 6 kg of maximum load at the tip. This robot has a position repeatability

error of 0.02 mm (Fig. 3.5 a1). This accuracy is one order of magnitude higher than the optical tracker assessed (submillimeter, as specified by the manufacturer).

We built a metal structure (Fig. 3.5 a2, b) to mount the cameras in a spatial configuration similar to that installed in the OR scenario. The metal structure was placed over the reaching zone of the robot arm and cameras were attached to it (Fig. 3.5 a3). During the experiments, the tip of the arm moved along a 50-mm step path covering the whole working volume (300 × 500 × 400 mm) (Fig. 3.5 c). As tracker accuracy is spatially dependent, it was not expected to be constant inside the whole working volume.

We designed 2 experiments for the robotic scenario. In the first one we studied the accuracy of the system under occlusions using a single reflective marker attached to the robot arm tip. During the second, we studied the tracking accuracy using different tools with their corresponding rigid bodies.

Static tracking accuracy assessment

A single marker was attached to the robot tip and robotically moved to cover the whole working volume Ω (300 × 500 × 400mm) in 50-mm (g_t) steps (Fig. 3.5 c). For each position, 1000 ($N_{samples}$) samples of the 3-dimensional position of the marker using the 8 calibrated cameras were acquired. The mean marker location for each point ($\overline{\boldsymbol{p}}_k$) was computed (Eq. 3.3). This acquisition was repeated ($k = 1, 2, \dots, M$) 10 times.

$$\overline{\boldsymbol{p}}_k = \frac{\sum_i^{N_{samples}} p_i}{N_{samples}} \tag{3.3}$$

Straight comparison of the optical tracker ($\overline{\boldsymbol{p}}_k$) and the robot positions ($\boldsymbol{r}_k$) is not possible, since the tracker and robot geometrical spaces are not registered. To overcome this limitation, a point-based registration from the robot ($\boldsymbol{r}_k$) to the tracker ($\overline{\boldsymbol{p}}_k$) working volume locations could be performed. However, owing to registration errors, this approach could distort our evaluation, since the tracker accuracy is expected to be spatially dependent. To avoid registration dependency, we computed the root mean square (rms) distance of each point

($d(\overline{\boldsymbol{p}}_k)_{rms}$) to the closest neighbors ($\boldsymbol{n}(\overline{\boldsymbol{p}}_k)$) for the tracker acquisition data (Eq. 3.4).

$$d(\overline{\boldsymbol{p}}_k)_{rms} = \sqrt{\frac{1}{N_{neighbors}} \sum_{j}^{N_{neighbors}} \left\| \overline{\boldsymbol{p}}_k - \boldsymbol{n}_j(\overline{\boldsymbol{p}}_k) \right\|^2} \quad \textbf{(3.4),}$$

where $\overline{\boldsymbol{p}}_k$ is the mean location point provided by the tracker, $N_{neighbors}$ the number of closest neighbors and $\boldsymbol{n}_j(\overline{\boldsymbol{p}}_k)$ is the j-th neighbor location of $\overline{\boldsymbol{p}}_k$. Inside the working volume studied (Fig. 3.5 c), each measured point has 6 neighbors ($N_{neighbors}$). For points placed at the studied working volume sides/corners, the number of available neighbors is four and three, respectively. Ideally, $d(\overline{\boldsymbol{p}}_k)_{rms} - g_t = 0$. Given the limited accuracy of the tracker, this condition is not fulfilled.

As explained above, the robot moves the marker inside the working volume using a step size (g_t) of 50 mm with very high precision (± 0.02 mm). We estimated the spatially dependent tracking error ($\widehat{TE}$, Eq. 3.5)) at point $\boldsymbol{p}$ by comparing the point distances provided by the tracker ($d(\overline{\boldsymbol{p}}_k)_{rms}$) with the gold standard distance (g_t) for all M experiment repetitions. Note that this figure of merit is spatially dependent and registration-independent.

$$\widehat{TE}(\boldsymbol{p}) = \sqrt{\frac{1}{M} \sum_{k}^{M} \| d(\overline{\boldsymbol{p}}_k)_{rms} - g_t \|_k^2} \quad \textbf{(3.5)}$$

To study the system accuracy under occlusions, we used the same setup with 8 cameras and a single reflecting marker. We acquired marker location data with one, two, three, four and five occluded cameras. To simulate occlusions, we covered the camera lens with an opaque coating. For the one occluded camera case, we occluded each (of 8) cameras separately. We estimated the tracking error over the working volume ($\widehat{TE}$, Eq. 3.5) and performed 10 repetitions ($M = 10$) for each single occluded camera. For the remaining cases studied (two, three, four and five occluded cameras), we were unable to run all possible (210) occlusion setups because of time limitations. Instead, we randomly chose the occluded camera group. On each number of occluded

cameras, we repeated 15 acquisitions ($M = 15$, thus avoiding group repetition) and estimated the tracking error ($\widehat{TE}$, Eq. 3.5).

Study of accuracy of tracked tools

For our image-guided applications in the OR, we usually track four different tools. To study tracking accuracy, we repeated the previous accuracy assessment using different rigid bodies instead of a single marker with no occlusions in the robotic scenario. We used an in-house pointer with 6 markers (BiiG Pointer, Fig. 3.6 a), the NDI Polaris pointer (four markers, Fig. 3.6 c), a configurable rigid body (OptiTrack, four markers, Fig. 3.6 d) and an in-house tracked IOERT collimator (four markers Fig. 3.6 b). Each tool was attached to the robot tip and moved inside the working volume. We estimated the tracking error within the working volume ($\widehat{TE}$ Eq. 3.5) using each tool ($M = 5$ repetitions). Pivot locations of the rigid-bodies were tracked (Fig. 3.6 P). In the case of the pointers (Fig. 3.6 a and c, P), the pivot is placed at the tip of the tool. The configurable

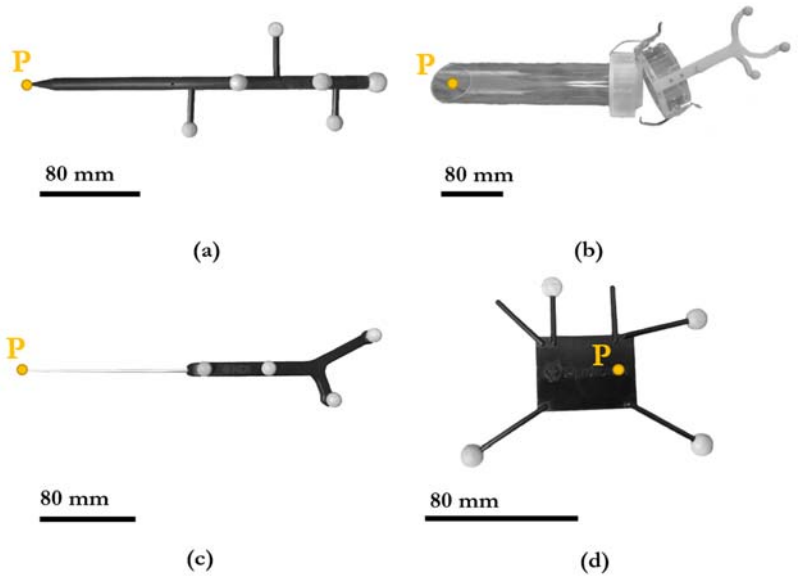

Figure 3.6: Rigid-body tools. **(a)** BiiG pointer. **(b)** IOERT applicator tool. **(c)** NDI Polaris Pointer. **(d)** NaturalPoint Marker Set: 14 mm X-Base. **(P)** Tracked pivot point.

OptiTrack rigid body uses the centroid of the markers as a pivot (Fig. 3.6 d, P). Finally, the IOERT applicator rigid body has the pivot point at the centroid of the IOERT collimator bevel (Fig. 3.6 b, P). For clarify, in Figure 3.7 a summary of the different studies and used scenarios is depicted.

Summary of Material and Methods

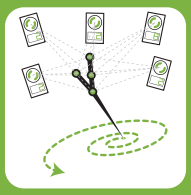

MATERIAL

Description of Optitrack Flex13

METHODS

Calibration Evaluation

OR Scenario

Miscalibration Detection Protocol

Miscalibration sensitivity study

Miscalibration setup

Miscalibration detection protocol feasibility study

Temporal calibration reliability study

Accuracy & Occlusions Evaluation

Robotic Scenario

Occlusions accuracy study

Tools accuracy study

Figure 3.7: Summary of Material and Methods section

3.4 Results

3.4.1 Evaluation of the tracker calibration

Miscalibration sensitivity study

Miscalibration sensitivity study results are summarized in Figure 3.8. The 'x' axis shows the mean and standard deviation of the produced camera rotation (α, miscalibration). The 'y' axis shows the mean and standard deviation of the

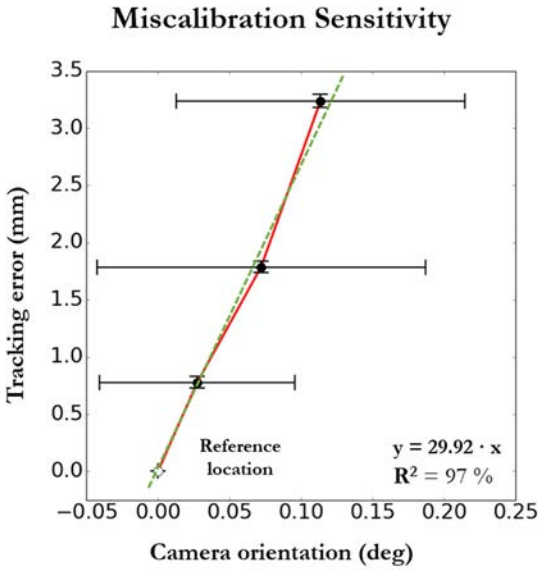

Figure 3.8: Tracking error (mean and standard deviation for the 10 repetitions) for four different orientations (mean and standard deviation for the 10 repetitions) of a miscalibrated camera using a 2-camera OptiTrack tracker. Sensitivity: 29.92 mm/deg (R2 = 97%, CI = [0.94,1.00]).

estimated tracking error $\widehat{TE}$, (Eq. 3.1). Table 1 shows the data points of Fig. 3.8. Note that for the case where the system is calibrated ($\alpha = 0º$), the angle measured is null because no rotation has been made on any of the cameras. As described above, we performed four manual miscalibrations, although only three are shown in Fig 3.8. The last miscalibration caused OptiTrack to report no

markers inside the working volume (Table 3.1), indicating that the maximum miscalibration (i.e., α_{th}) is below ~0.2 deg rotation. According to the results, miscalibrations higher than α_{th} lead the system to report no markers inside the working volume for a two-camera setup. Furthermore, it is remarkable that the tracking error increases more than 3 mm for a rotation greater than 0.1 degrees. The estimated sensitivity was 29.92 mm/deg (R^2 = 97%, CI = [0.94, 1.00]).

Miscalibration setup	Tracked Marker	Tracking error (mm) [mean ± std]	Camera orientation (deg) [mean ± std]
First	Yes	0.78 ± 0.07	0.03 ± 0.09
Second	Yes	1.79 ± 0.11	0.07 ± 0.09
Third	Yes	3.24 ± 0.10	0.11 ± 0.10
Forth	No	-	0.16 ± 0.09

Table 3.1: Tracking error (mean and standard deviation for the 10 repetitions) for four different orientations (mean and standard deviation for the 10 repetitions) of a miscalibrated camera using a 2-camera OptiTrack tracker.

Study of the feasibility of the miscalibration detection protocol

The results of the study of the feasibility of the miscalibration detection protocol are shown in Fig. 3.9. For each experimental case—with a different number of miscalibrated cameras—the estimated tracking error (Eq. 3.2) of each camera pair is plotted. Most pairs containing a miscalibrated camera reported no tracked marker in their working volume. However, some of the miscalibrated pairs were still able to track the marker. For example, in Fig. 3.9 b, where camera '6' was miscalibrated, pairs 5-6 and 6-7 preserved their tracking ability but showed higher tracking errors (> 30 mm). As for the calibrated pairs, the tracking error is noticeably smaller (depicted in blue).

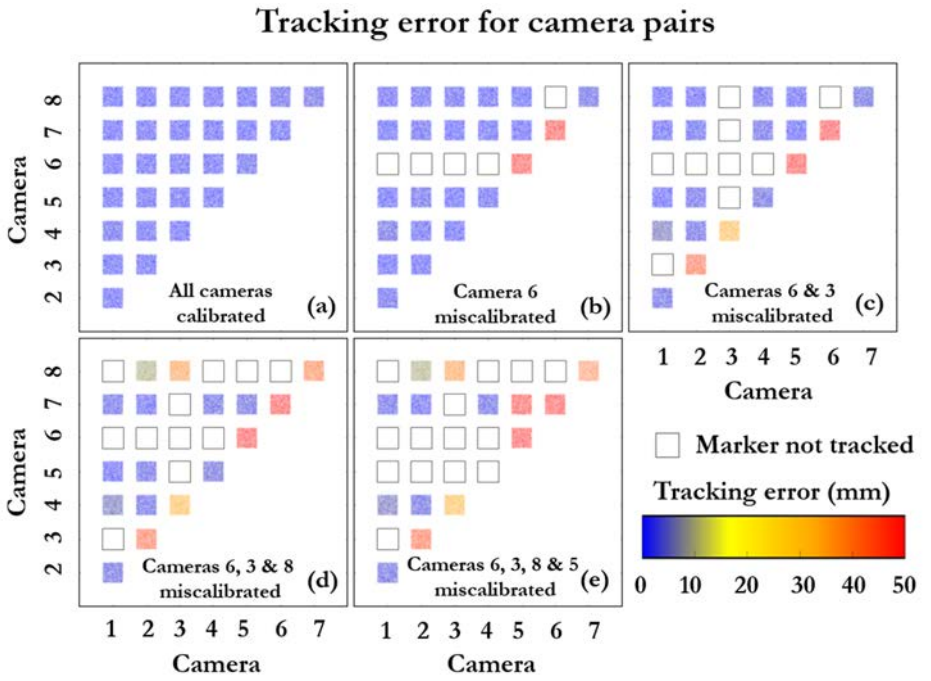

Figure 3.9: Difference in 3D position of the marker with respect to the initial reference location for different numbers of miscalibrated cameras. **(a)** All cameras calibrated. **(b)** Camera number 6 miscalibrated. **(c)** Cameras 6 and 3 miscalibrated. **(d)** Cameras 6, 3 and 8 miscalibrated. **(e)** Cameras 6, 3, 8 and 5 miscalibrated.

Calibration: temporal reliability study

In Figure 3.10, the tracking error of each camera pair is shown over time (5 days). Red lines correspond to the results for camera pairs containing the miscalibrated camera. We miscalibrated this camera on purpose at the beginning of the experiment (Fig. 3.10 a). The lines in blue (Fig. 3.10) represent the calibrated camera pairs. As expected, the tracking error is larger for the miscalibrated pairs (up to ~3.5 mm) and smaller for the calibrated pairs (~1.5 mm). The green zone corresponds to the estimated tracking error from the acquisitions of the system comprising all 8 cameras. This value is always below

0.5 mm, which represents the variability of tracking over time and is consistent with the manufacturers' specification accuracy (Table 3.2).

Table 3.2 shows the tracking error (mean and standard deviation) over time for the 8-camera system, the calibrated pairs and the miscalibrated pairs. Tracking errors for the miscalibrated camera pairs increase in comparison with the calibrated pairs, as does the use of the complete system for tracking. Note also the decrease in the tracking error when single camera pairs are used (mean

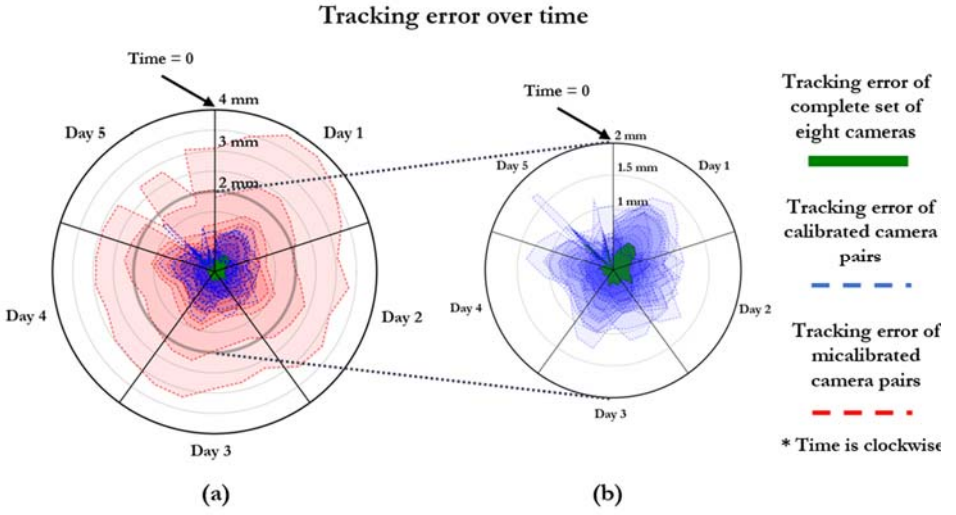

Figure 3.10: Tracking error over time. **(a)** Results for all cameras (green), miscalibrated camera pairs (red) and calibrated camera pairs (blue). **(b)** Detail of the results for the calibrated camera pairs.

Miscalibration setup	Tracking error (mm) [mean ± std]
Complete set of eight cameras	0.25 ± 0.26
Calibrated camera pairs	0.57 ± 0.26
Miscalibrated camera pairs	1.41 ± 0.80

Table 3.2: Tracking error over time mean and standard deviation (std) for the complete system (8 cameras), the calibrated pairs and the miscalibrated pairs.

0.57 mm) compared with the multicamera system comprising the 8 cameras (mean 0.25 mm).

3.4.2 Evaluation of the accuracy and occlusions

Assessment of static tracking accuracy

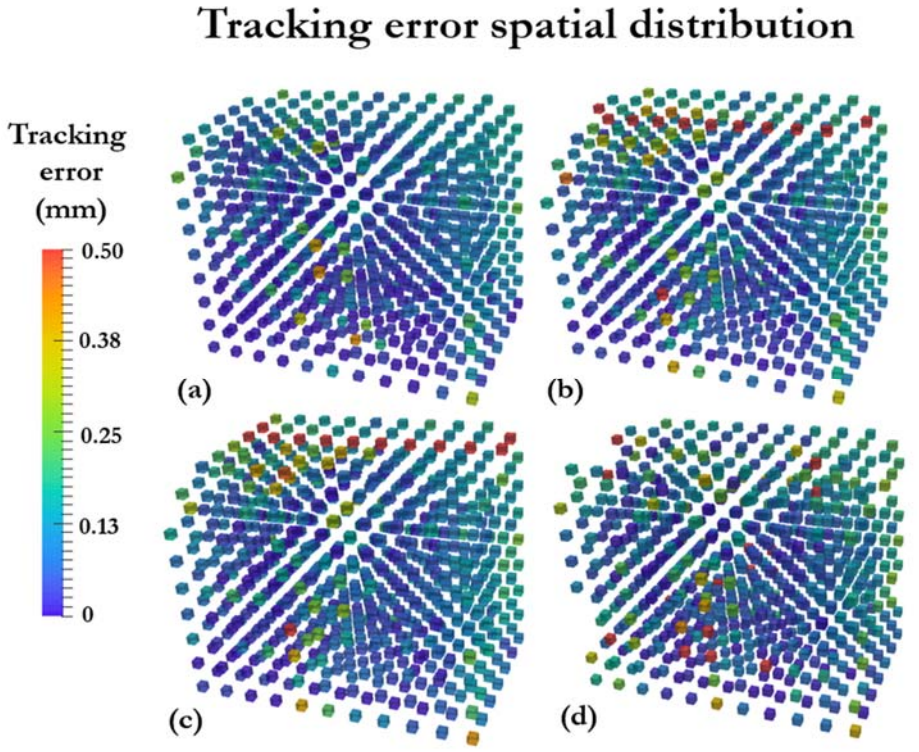

Figure 3.11: Tracking error (Eq. 3.4) on different acquisitions **(a to d)** of an 8-camera system (Flex13 OptiTrack) with no occlusion installed in the robotic scenario.

Figure 3.11 shows the results for the accuracy study with no occlusions in four different acquisitions in the complete working volume. As we can see, the tracking error is almost constant in all the inner part of the volume. Points with higher errors are concentrated at the edges of the volume. Figure 3.12 shows the

tracking error within the whole working volume (300 × 500 × 400 mm) and for two smaller inner volumes (200 × 400 × 300 mm and 100 × 200 × 100 mm).

Number of Occluded Cameras	Tracking Error (mm)						
	Central Statistics			Percentiles			
	Mean	Standard Deviation	Mean rms	50	75	95	99
5	1.65	5.07	5.33	0.11	0.11	0.11	0.11
4	1.18	2.99	3.21	0.12	0.12	0.12	0.12
3	0.94	2.49	2.66	0.11	0.11	0.11	0.11
2	0.82	2.31	2.45	0.10	0.10	0.10	0.10
1	0.55	1.84	1.92	0.10	0.10	0.10	0.10
0	0.24	1.05	1.08	0.08	0.08	0.08	0.08

Table 3.3: Tracking error (Eq. 3.4, within the studied working volume) for different numbers of occluded cameras in the Flex 13 8-camera system.

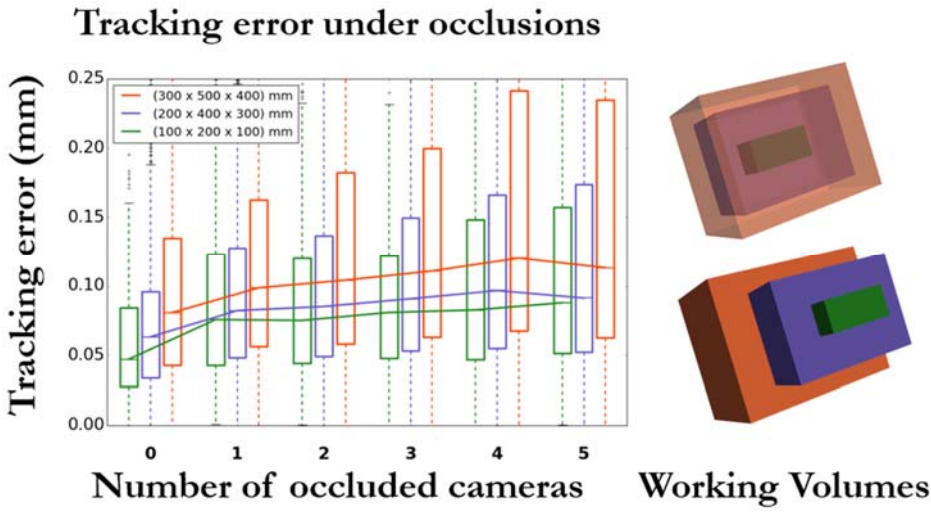

Figure 3.12: Tracking error (Eq. 3.4, within the studied working volume) for different numbers of occluded cameras and different subvolumes.

We found that tracking error increased with the number of occluded cameras. We also found that the higher tracking errors were produced at the outer part of the working volume, since the smaller subvolumes show lower maximum error.

Table 3.3 summarizes the results of the study of occlusion accuracy. As expected, tracking error in the working volume increases with the number of cameras occluded (Eq. 3.4). In cases of non-occlusion, the tracking error for the complete volume (mean 0.24 mm) is comparable to the result of the calibration reliability study (mean 0.25 mm). Nevertheless, in the calibration reliability study, the tracking error was analyzed at a single location inside the working volume (mean tracking error was reported), while in the case of non-occlusion, the reported value corresponds to the complete studied volume (300 × 500 × 400 mm). On the other hand, the results also showed the spatial tracking error dependency (Fig. 3.11). The median tracking error value decreases in the inner part of the working volume (Figure 3.12).

Tracking accuracy of the tools

Figure 3.13 and Table 3.4 show the results for the tracking accuracy of the tools. Here, the tracking error over the tracking volume is summarized for each tool. There is a clear difference between the tracking error produced when using

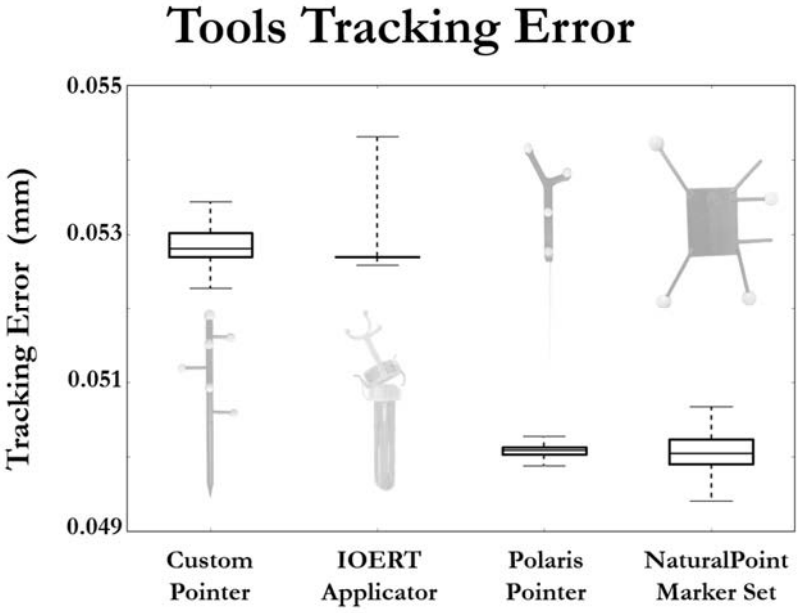

Figure 3.13: Tracking Error (Eq. 3.4) on the working volume for different tracking tools.

Tool	Tracking Error (mm) [mean ± std]	Tracking Error (mm) [min, max]
Custom Pointer	0.0593 ± 0.0338	[0.0523, 0.3936]
IOERT Applicator	0.0527 ± 0.0001	[0.0526, 0.0543]
Polaris pointer tip	0.0501 ± 0.0001	[0.0497, 0.0506]
NaturalPoint Marker Set	0.0501 ± 0.0003	[0.0494, 0.0510]

Table 3.4: Tracking error (Eq. 3.4, mean and standard deviation) on the working volume for the four studied tools.

the commercial tools (Polaris pointer and Natural Point marker set) and the in-house tools. However, the tracking difference in tracking error is small, ~0.03 mm. It is also noteworthy that the tracking error was dramatically smaller for rigid bodies than for a single marker (results from Fig. 3.12 using 8 cameras). This is expected, since the location of the tools is computed from several tracked markers and the system uses the spatial configuration of the markers to compensate for single-marker tracking errors. In fact, using a four-marker rigid body seems to reduce tracking error by an order of magnitude. This tracking error is almost constant over the whole working volume (Table 3.4), with a low spatial dependency of the tracking accuracy for all tools (Table 3.4, third column).

3.5 Discussion and Conclusion

We performed an exhaustive assessment of the accuracy of the OptiTrack tracking system for IGS applications. To our knowledge, this is the first study to assess the tracking accuracy of the OptiTrack system using Flex 13 cameras. We studied the system's sensitivity to miscalibration in terms of tracking error. Moreover, we also proposed and validated a new miscalibration detection protocol in a surgical environment that satisfies the requirements of automaticity and speed, both of which are essential in an IGS navigation scenario. Furthermore, we assessed the reliability of calibration over time, analyzed the spatial distribution of tracking accuracy for a single marker and studied camera occlusions using a well-characterized gold standard (i.e., a robotic arm with μm

accuracy). Finally, we assessed the dependence of accuracy on different tools used during IOERT collimator guidance.

We found that the system had a miscalibration sensitivity of ~30 mm/deg and a maximum rotation threshold of 0.16 ± 0.09 degrees. Our experiment confirmed the dependence of tracking accuracy on calibration quality. Even though this value was estimated from a system comprising 2 cameras, the reported sensitivity highlighted the relevance of calibration quality in an IGS scenario based on OptiTrack. It is also noteworthy that the sensitivity of calibration is directly proportional to the camera marker distance, since resolution of the sensor is directly related to projection error [93]. Hence, for larger working volumes (larger marker-to-sensor distances), the loss of accuracy for a constant miscalibration rotation could be larger than that reported.

Our miscalibration detection protocol proved to be feasible for clinical use. A non-experienced user can evaluate calibration using a single marker in the working area and detect which cameras deviated from the calibrated orientation. Multicamera tracker setups are prone to miscalibration owing to factors associated with manual installation (e.g., screws, mounting) and OR factors (e.g., surgical lamps manipulation that could hit the installed cameras on the OR's ceiling). We assume that the tracking software (provided by the manufacturer) does not identify miscalibrations during real-time tracking. This could lead to a loss of accuracy if the information gathered from a miscalibrated camera is used to solve the three-dimensional location of a marker. Furthermore, if occlusions occur with the well-calibrated cameras, the expected loss of accuracy could be even worse. Nevertheless, the high sensitivity observed in the first experiment (Sec. 3.3.2, *Miscalibration sensitivity study*) ensures that even very small miscalibrations (~0.16 degrees, Table 1) are detected, thus supporting our protocol for pre-surgical assessment of tracking, which could ensure that the IGS tracking setup is both accurate and reliable.

As for temporal reliability, the accuracy of the system seems to be constant over 5 consecutive days (tracking error of 0.25 ± 0.26 mm), thus supporting the assumption that calibration remains stable during the experiment. In the time period studied, the 8-camera setup revealed a mean tracking error of 0.25 mm (including a miscalibrated camera). Miscalibrated camera pairs generated a mean tracking error of 1.14 mm, whereas in calibrated pairs the mean tracking error was 0.57 mm. This difference demonstrated that the loss of accuracy caused by a miscalibration is constant over time. The remaining variability in tracking error

could be due to the intrinsic noise of the system caused by temperature variations or mounting vibrations, which could alter calibration parameters over time.

In the accuracy study using the robotic scenario, the 8-camera spatial configuration showed a percentile 99 tracking error of 0.08 mm (Table 3.3) and a mean rms value of 1.08 mm inside the whole working volume (300 × 500 × 400 mm). This value represents the pure accuracy of the system when occlusions and miscalibrations are not present. The results showed that tracking error was dependent on the number of occluded cameras (Fig. 3.12 and Table 3.3). We would like to point out that this trend also depends on the size of the working volume: the smaller the working volume, the lower the tracking error, even when occlusions are present. This is consistent with the working volume design, where the outer part of the volume is covered by a lower number of sensors leading to larger errors at the volume edges [62], [93]. Note that when occlusions affect the system, outer parts could be tracked by a reduced number of cameras or even not tracked. In [93], the authors emphasized the importance of the spatial dependency of the tracking error, showing that Polaris system errors are higher at the upper right corners of its working volume and generally increase with the distance from the cameras. This effect is depicted in Figure 3.11 and Table 3.3, where the robustness of the multicamera system is demonstrated. A percentile 99 tracking error was always below 0.11 mm for up to 5 occluded cameras. However, mean rms tracking error values for the occluded cases studied showed much higher values (Table 3.3). This effect means that occlusions produce a higher number of tracking error outliers instead of a significant loss of accuracy inside the working volume. Consequently, occlusions during tracking are important and should be taken into account when OptiTrack is used for an IGS navigation scenario. In particular, our results demonstrate the relevance of an appropriately designed working volume to ensure that tracking is robust against occlusions.

When a miscalibration is detected, we suggest disconnecting the miscalibrated camera if a new calibration cannot be performed (i.e., owing to surgical or time restrictions). This solution would result in a lower number of cameras; however, it would ensure that the system does not contain any miscalibrated camera that could deteriorate the accuracy expected. Naturally, when time and clinical restrictions are not limiting factors, repeating system calibration would be a better option for maintaining the maximum number of cameras and thus ensuring better accuracy. Even so, in results from the calibration reliability study (Figure 3.10 and Table 3.2), where a camera was

miscalibrated on purpose, the reported error (mean tracking error 0.25 ± 0.26 mm) for a single marker was similar to the error reported for the calibrated system with no occlusions in the robotic scenario (mean tracking error, 0.24 mm), thus supporting the capability of multicamera optical trackers to face miscalibrations and demonstrating the feasibility of its clinical application in a fixed configuration inside the OR.

The use of tracked tools (rigid bodies) demonstrated an improvement in location accuracy (Fig. 3.13). As expected, multimarker tools reduced tracking error by an order of magnitude in all the tools studied (Table 3.4). It is also noteworthy that the spatial distribution of the tool's optical markers affected tracking accuracy. In fact, the Polaris pointer demonstrated higher accuracy (0.0501 ± 0.0001 mm tracking error) than the IOERT applicator (0.0527 ± 0.0001 mm tracking error) or the in-house pointer (mean tracking error of 0.0593 ± 0.0338 mm). Tracking error dependency on the spatial distribution of markers has been assessed for some tools [98], [108], thus demonstrating the importance of designing optimal rigid bodies for optically tracked surgical tools. In our case, the design of the IOERT applicator and the custom pointer must be revised to reduce tracking error during guidance. One possible explanation for the lower accuracy of the in-house pointer is the number of markers of the rigid body. When this number is high, the distance between them should be higher to avoid marker-to-marker occlusions. Such occlusions could impede detection of the marker by the optical sensors, thus leading to loss of accuracy. Intuitively, when fewer cameras are used, this effect could be more pronounced. Nevertheless, we would like to point out that the differences in the tracking accuracy of the tools are below ~0.01 mm (Table 3.4), which is negligible for our application purposes, namely, positioning of the IOERT collimator. In this study, all the tools were calibrated following the geometrical specifications. However, in several applications a pivoting calibration is needed. In [62], authors study this issue using a similar multicamera system. They demonstrate that the tool calibration improves the accuracy if the pivoting is performed at the center of the system working volume since it is tracked by the maximum number of optical sensors.

During the calibration assessments, we caused miscalibrations by rotating the cameras from their mounting screw. In that sense, we only evaluated geometrical miscalibration along the screw direction: this is not illustrative of all the possible cases. However, when a multicamera optical tracker is installed, the

screw is the unsteadiest part of the fastening setup, is prone to knocks, and represents the principal cause of miscalibration in the IOERT OR scenario.

Our study is limited by the spatial configuration of the cameras and the number of cameras used, which may not be suitable for other applications. We used 8 Flex 13 cameras surrounding the whole patient area as the working volume. However, given the large number of possible spatial configurations of the multicamera optical tracker, a more in-depth evaluation would prove cumbersome. A possible approach to overcome this limitation could be to perform simulations using the camera pair accuracy reported for different spatial configurations. Nonetheless, the OR setup we studied covers a wide range of IGS applications, since it was installed in a real clinical environment and could therefore be comparable to other possible scenarios. Furthermore, results for the temporal reliability of calibration, together with the proposed miscalibration detection protocol, corroborate the feasibility of using an OptiTrack tracker inside a real OR. As for the reliability of calibration time, one factor limiting accuracy is the illumination of the working volume. During the navigation in the OR, the lighting could be modified at the surgeon's request, and system calibration could be affected by lurking reflections, which were not studied here. We suggest performing the calibration and the navigation under similar lighting conditions. Nevertheless, this issue warrants further evaluation.

The main original contribution of this study is the analysis of space-dependent accuracy in occlusions. When an occlusion occurs during tracking, the system is expected to compensate by using the remaining cameras (system redundancy). In such cases, this compensation reduced the accuracy of the system. In fact, for a higher number of occluded cameras the accuracy of the system decreases (Table 3.3). For the OR setup, when a camera is occluded, the working volume is expected to be reduced because of its initial design. Furthermore, the occlusions affect the cameras that are placed at the corners, thus leading to a reduction in working volume. It is clear that there is a tradeoff between the number of cameras used (spatial redundancy in occlusions) and the size of the working volume. For an application with a low risk of occlusion, the working volume could be larger for a given number of cameras. However, applications that present a high risk of occlusion (such as IOERT) should reduce the working volume in favor of camera redundancy to avoid a marked loss of accuracy or increase the number of cameras used. Nevertheless, according to the results, this key issue could deteriorate the navigation solution for multicamera optical trackers and should be studied for each specific navigation environment in terms of accuracy and risk of occlusion.

The initial IOERT radiation field is usually designed to include a 3-5–cm margin beyond the tumor bed in order to reduce the risk of metastatic spread [16]. The 8-camera setup we studied demonstrated reasonable accuracy for the positioning of the IOERT radiation cone. Even though the tracker was subject to a substantial number of occlusions, the tracking error for a single marker proved to be below 0.11 mm (Table 3.3). However, the accuracy results for the tools tracked (Table 3.4) indicate that tracking error is expected to be reduced (Fig. 3.13). In a preliminary study, we demonstrated the feasibility of using OptiTrack (V100:R2 camera model) for applicator guidance (tracking error < 2 mm) during IOERT with a CT scanner as the gold standard [54]. This study broadens our preliminary results in that it uses a newer camera model and completes our assessment of the system.

In summary, the OptiTrack 8-camera optical tracker was evaluated for miscalibration sensitivity, accuracy, camera occlusions and tool detection using a feasible clinical setup. The system is suitably accurate for IGS navigation, improves redundancy and allows larger working volumes. Our study adds to the results of a similar OptiTrack system in [100], where the dynamic and static characteristics of an 8-camera V100R2 OptiTrack model were evaluated. We believe that our assessment and the validated miscalibration protocol are important contributions to the IGS community, where the choice of the tracker for surgical applications is critical and knowledge of system accuracy under situations of camera occlusion is mandatory during IGS navigation assessments.

4

Line Based Registration

4.1 Introduction

As described in the introduction, image-to-world registration is a critical step of a IGI system, since it estimates the geometrical correspondence between the tracker and the medical imaging studies and thus enables the surgical instruments navigation. In the literature, image-to-world registration is found with two different approaches: fiducial based or fiducial-free. The former uses markers that are attached to the patient's body while the later uses devices such surface scanners or time of flight (ToF) cameras for the acquisition of position data from the patient's anatomy [64], [69], [70].

One of the main differences between both approaches is that fiducial-based registration preserves the knowledge of the fiducial-to-fiducial correspondence while the fiducial-free approach does not. The iterative closest point (ICP) algorithm is a common solution when the point cloud must be matched with no knowledge of named correspondence.

The original ICP algorithm [71] is an iterative implementation comprising two steps: matching and minimization. In each iteration, the algorithm first estimates the correspondence between points using the Euclidean distance metric. Once that correspondence is established, a second minimization step estimates the registration parameters that best map every point from the source to the target point cloud in the least squares sense. Each iteration repeats the process, re-estimates the point-to-point correspondence and updates the resulting registration parameters until convergence, that is, a predefined minimum distance metric or a maximum number of iterations is reached. This algorithm has been extended by many authors in order to overcome the known limitations of ICP [70], [72]–[74].

The original ICP algorithm assumes that on noisy position data, added fiducial localization error (FLE) follows an isotropic Gaussian distribution, but this is not always true in real applications [70]. When devices such as laser scanners or time of flight (ToF) cameras are used, FLE anisotropy becomes more relevant, driving estimation of the ICP transformation towards an erroneous result. In order to overcome this limitation, Maier-Hein et al. presented the anisotropic ICP algorithm (AICP) in [70]. The authors introduced a penalty term based on the FLE distribution during both the matching and the minimization steps of the original ICP. Directions with lower FLE are assigned more weight during distance computation according to the anisotropic distribution of FLE. An alternative approach to ICP in [109] uses three data sources with different resolutions and estimates the registration parameters by adding a modelling step during the first ICP iteration. The aim of this modelling step is to filter outliers through the random sample consensus (RANSAC) algorithm [110] before estimation of registration parameters. However, not all variants of the ICP algorithm are based on the two-step schema (matching and minimization). In [111], the authors propose a probabilistic approach named coherent point drift (CPD), considering the alignment of two point clouds as a probability density estimation problem. Target points are used as centroids of a Gaussian mixture model (GMM), and source points are registered by maximizing the likelihood that they belong to the established target GMM. Registration and GMM parameters are computed using the expectation-maximization (EM) algorithm [112].

4.2 Objective

In the present study, we propose a new registration algorithm, line-based registration (LBR), which uses line-shaped fiducials to estimate registration parameters. LBR combines the advantages of landmark-based and fiducial-free registration approaches. We used line-shaped fiducials as landmarks, thus preserving fiducial-to-fiducial correspondence and increasing the amount of position data points acquired from each fiducial. The rigid transformation matrix is estimated by means of a modelling step that takes advantage of a priori knowledge of the fiducial shape. A complete simulation-based evaluation of the LBR algorithm was performed in order to compare the accuracy and robustness of LBR with those of the classic ICP, AICP [70] and coherent point drift (CPD) [111].

4.3 Material and Methods

4.3.1 Rationale for LBR

The registration approach we propose is based on line-shaped fiducials, which make it possible to find the spatial correspondence for the tracker and the image. Since it uses lines (one-dimensional geometrical structures) instead of points (zero-dimensional), the amount of data collected for registration increases substantially with respect to classic point-based approaches. The advantage of this strategy is that the fiducial-to-fiducial correspondence data is maintained while redundancy increases. Correspondence information is used by LBR to initialize the registration and avoid any user interaction. Furthermore, the LBR algorithm takes advantage of data redundancy by introducing a fiducial-based statistical model during the estimation of registration parameters. Initialization,

statistical modelling of the line-shaped fiducials and the registration approach are described in the following sections.

4.3.2 Detailed description of the LBR algorithm

LBR comprises three distinct blocks: fiducial modelling, initialization and statistically enhanced ICP registration. These blocks work together to estimate the transformation that maps source and target fiducial positions. Each block is described in detail below.

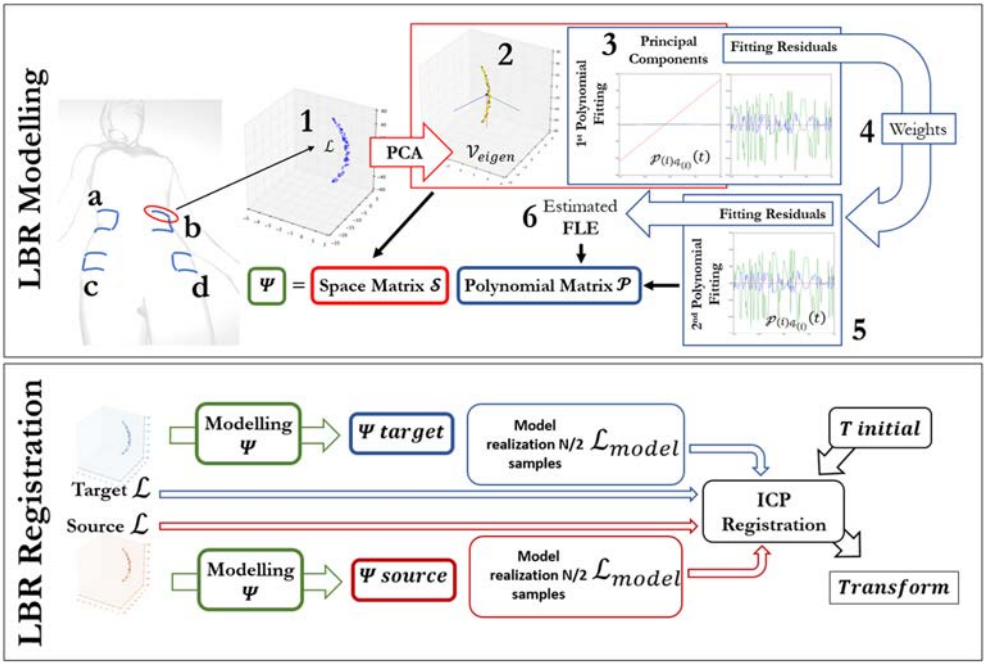

Figure 4.1: Schemas for Line Based Registration (LBR) fiducial modelling (upper panel) and registration (lower panel**). (a, b, c, d)** Line fiducials placed over a patient. **(1)** Line point-cloud. **(2)** PCA and eigenvectors. **(3)** Principal components of a line point-cloud and residuals from a first polynomial fitting.

Fiducial Modelling

Fiducial modelling takes advantage of the line-shape of the fiducial. As stated above, we use LBR to estimate image-to-world registration for navigation of the collimator that delivers the radiation to the patient during IOERT. In this particular application, it is necessary to register an optical tracker to a preoperative CT image of the patient in order to guide the placement of the collimator during the procedure. We propose to use metallic line-shaped fiducials (i.e., metallic wires), since they can be localized by thresholding the CT scan in the image coordinate system and by means of an optically tracked pointer in the tracker coordinate system. Fiducials are placed over the patient's skin before a CT scan is acquired with the patient in the surgical position (Fig. 4.1 a, b, c, d). They are then bent so that their shape adapts to the patient's body surface. The number of points collected in a CT image for a single line is ~100. In order to reduce the acquisition time, we also acquire 100 localization points along each complete fiducial in the tracker space using a tracked pointer.

Each line localization is composed of N (100) three-dimensional points in each geometric space. During acquisition, FLE is unavoidably added to the true position data. The LBR's modelling block fits each fiducial data item to a three-dimensional polynomial curve model by means of principal component analysis (PCA). This step, which is similar to that described in [109], filters outliers and reduces any further effect of FLE on the estimation of registration parameters by introducing shape knowledge during the modelling step. Note that the same modelling step is applied independently to each line fiducial.

Let $\mathcal{L}$ be the fiducial point cloud data with N collected points (Fig 4.1-1). For each wire, the centroid c is computed and used to center the point cloud coordinates of the line, thus yielding $\mathcal{L}_{c[3\ \mathrm{x}\ \mathrm{N}]}$ (Eq. 4.1 and Eq. 4.2).

$$\mathcal{L} = [\boldsymbol{x}_n] = \begin{bmatrix} x_1 & \cdots & x_N \\ y_1 & \cdots & y_N \\ z_1 & \cdots & z_N \end{bmatrix}_{[3\ x\ N]} \tag{4.1}$$

$$\boldsymbol{c} = \begin{bmatrix} c_x \\ c_y \\ c_z \end{bmatrix}_{[3\ x\ 1]} \tag{4.2}$$

PCA is then performed for the centered point cloud, and eigenvectors are computed (Fig 4.1-2).

Let $\mathcal{V}_{eigen}$ be the eigenvectors of the centered line point cloud $\mathcal{L}_c$ (Eq. 3)

$$\mathcal{V}_{eigen\,[3\ x\ 3]} = [\boldsymbol{v}_1 \quad \boldsymbol{v}_2 \quad \boldsymbol{v}_3] = \begin{bmatrix} v_{1x} & v_{2x} & v_{3x} \\ v_{1y} & v_{2y} & v_{3y} \\ v_{1z} & v_{2z} & v_{3z} \end{bmatrix}_{[3\ x\ 3]} \tag{4.3},$$

where $\boldsymbol{v}_i$ is the i-th eigenvector. We can project $\mathcal{L}$ onto $\mathcal{V}$ and extract the principal components (Fig 4.1-3) of $\mathcal{L}_c$ as shown in (Eq. 4.4)

$$\mathcal{L}_{PC\,[3\ x\ N]} = \mathcal{V}^{\mathrm{T}}_{eigen\,[3\ \mathrm{x}\ 3]} \cdot \mathcal{L}_{c[3\ \mathrm{x}\ \mathrm{N}]} = [\tilde{\ell}_1 \quad \tilde{\ell}_2 \quad \tilde{\ell}_3\ ]^{\mathrm{T}} \tag{4.4},$$

where $\mathcal{L}_{PC}$ are the principal components of the fiducial point cloud.

When points from a fiducial are acquired, either using the tracker or by segmenting the fiducial from the CT image, the point cloud $\mathcal{L}$ might not be sorted from the first to the last edge point. Therefore, the first component is sorted from lower to higher values and other components are sorted equally (Eq. 4.5).

$$\mathcal{L}_{PC-Sort} = [sort(\tilde{\boldsymbol{\ell}}_1, \boldsymbol{\ell}_s) \quad sort(\tilde{\boldsymbol{\ell}}_2, \boldsymbol{\ell}_s) \quad sort(\tilde{\boldsymbol{\ell}}_3, \boldsymbol{\ell}_s)]^T = [\tilde{\boldsymbol{\ell}}_{1s} \quad \tilde{\boldsymbol{\ell}}_{2s} \quad \tilde{\boldsymbol{\ell}}_{3s}]^T \tag{4.5}$$

$\boldsymbol{\ell}_s$ is the sorted first component, the function $sort(a, b)$ reorganizes the values in vector a according to the values of vector b in ascending order and $\tilde{\boldsymbol{\ell}}_{(i)s}$ is the i-th sorted component.

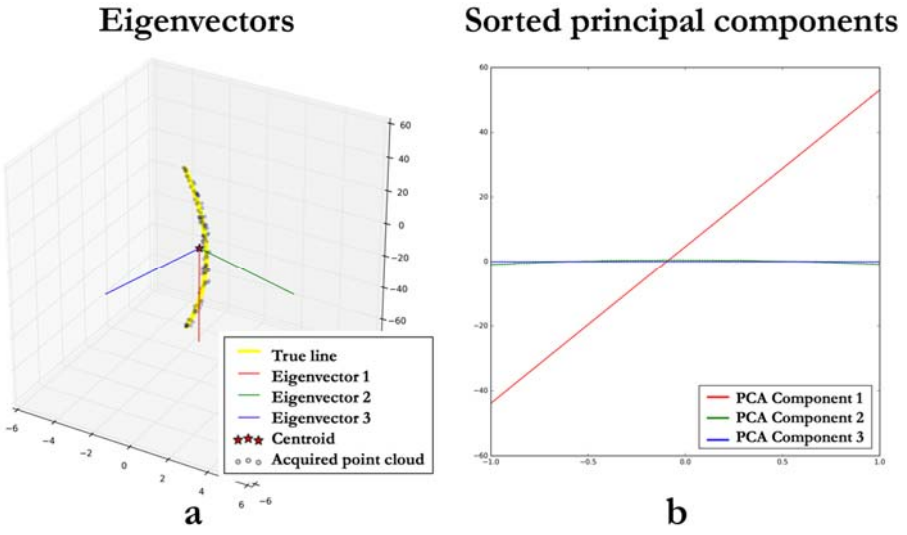

Figure 4.2: Example of an acquired point cloud line and PCA. **(a)** 3D point cloud, eigenvectors and centroid of the data. **(b)** Sorted principal components of the point cloud.

Figure 4.2 (a) shows an example acquisition of a fiducial point cloud (100 points), while Fig. 4.2 (b) displays the values of the principal components of the point cloud obtained after projecting onto $\mathcal{V}_{eigen}$ and sorting the values accordingly (Eq. 4.4 and 4.5). The first principal component is very close to a straight line (Fig. 4.2 b, red), while the second and third components show some small curvature. In general, fiducials bend when they are placed on the patient's body. This bending is translated into second and third principal component curvatures.

Each sorted component of $\mathcal{L}_{PC-Sort}$ (Eq. 4.5) is fitted to a polynomial curve (Fig 4.1-3). Let the fitting polynomial of order q be $\mathcal{p}_q(\mathrm{t})$ (Eq. 4.6)

$$\mathcal{p}_q(t) = \sum_{r=0}^{q} a_r \cdot t^r, \qquad t \in [-1,1] \tag{4.6}$$

where a_r are the coefficients of the polynomial and t the independent variable.

For each sorted component i, a polynomial model that fits $\tilde{\boldsymbol{\ell}}_{(i)\mathrm{s}}$ in the least squares sense is computed as (Eq. 4.7)

$$\mathcal{p}_{(i)q_{(i)}}(t) = \sum_{r=0}^{q_{(i)}} a_{(i)r} \cdot t^r = \tilde{\boldsymbol{\ell}}_{(i)\mathrm{s}} + \varepsilon_{(i)}, \qquad t \in [-1,1] \tag{4.7}$$

where i refers to the i-th component, $q_{(i)}$ to the order of the fitting polynomial of the i-th component, $a_{(i)r}$ to the coefficients, $\varepsilon_{(i)}$ to the fitting residuals and t to the independent variable. After a first fitting computation, residuals are used as inverted weights on a second fitting step (Fig. 4.1-5) of the same order $q_{(\mathrm{i})}$. The aim of this step is to compensate for outliers (Fig 4.1-4).

Depending on their anatomical location, fiducial can present more complex three-dimensional shapes. Nonetheless, the curvature of fiducials is expected to be small, since they are placed along the patient's skin and far enough from the surgical area. Large $q_{(\mathrm{i})}$ values would enable the model to adapt to more general three-dimensional curves. If we select a suitable polynomial order $q_{(i)}$, second polynomial-fitting residuals could be used to estimate anisotropic $\mathrm{FLE}_{\mathrm{rms}}$ (root mean square value of FLE). In particular, LBR estimates $\mathrm{FLE}_{\mathrm{rms}}$ from the covariance matrix Σ_{rms} of the residuals (Fig. 4.1-6).

Let $\Gamma_{[3\,x\,N]}$ be the residual matrix comprising the N residuals from one fiducial point cloud after modelling. Notice that LBR uses residuals from the second fitting polynomial step for estimation of FLE (Eq. 4.8)

$$\Gamma = \left[\boldsymbol{\varepsilon}_{i,j}\right]_{[3\ x\ N]} = \begin{bmatrix} \varepsilon_{1,1} & \cdots & \varepsilon_{1,N} \\ \varepsilon_{2,1} & \cdots & \varepsilon_{2,N} \\ \varepsilon_{3,1} & \cdots & \varepsilon_{3,N} \end{bmatrix}_{[3\ x\ N]} \quad \textbf{(4.8).}$$

If the covariance matrix is (Eq. 4.9)

$$\Sigma_{rms\ [3\ x\ 3]} = \Gamma \cdot \Gamma^T = \begin{bmatrix} \sigma_1^2 & \sigma_1\sigma_2 & \sigma_1\sigma_3 \\ \sigma_1\sigma_2 & \sigma_2^2 & \sigma_2\sigma_3 \\ \sigma_1\sigma_3 & \sigma_2\sigma_3 & \sigma_3^2 \end{bmatrix} \quad \textbf{(4.9),}$$

we can estimate the anisotropic FLE_{rms} as a three-dimensional Gaussian random process of zero mean and standard deviation $[\sigma_1, \sigma_2, \sigma_3]$ (Eq. 4.10)

$$FLE \sim \aleph\,(\mu = [0,0,0], std = [\sigma_1, \sigma_2, \sigma_3]\,) \quad \textbf{(4.10),}$$

where $\aleph\,(\mu, std)$ is a normal distribution centered at μ with a standard deviation of std.

Using the fitting polynomials and the estimated FLE_{rms}, we define the probabilistic model of the fiducial as (Eq. 4.11)

$$\underbrace{\mathcal{L}}_{model}(t) = \begin{bmatrix} \boldsymbol{v}_1 \cdot \mathcal{p}_{1q_1}(t) \\ \boldsymbol{v}_2 \cdot \mathcal{p}_{2q_2}(t) \\ \boldsymbol{v}_3 \cdot \mathcal{p}_{3q_3}(t) \end{bmatrix} + \boldsymbol{c} + \aleph\,(\mu = [0,0,0], std = k \cdot [\sigma_1, \sigma_2, \sigma_3]\,)\,, t \in [-1,1] \quad \textbf{(4.11),}$$

where $\boldsymbol{v}_{(i)}$ are the eigenvectors of the centered point cloud, $\mathcal{p}_{(i)q_{(i)}}(t)$ the fitting polynomials, $\boldsymbol{c}$ the centroid and $\aleph$ the random process defined in (Eq. 4.10). Note that the factor k regularized the statistical modelled FLE contribution, while $q_{(i)}$ controls the expected fiducial shape. For our application, we selected a value of $k = 0.125$ and $q_{(i)} = 2$. Depending on the specific tracker accuracy, k may need to be adjusted.

The model can be written in a closed form using homogeneous coordinates and decoupling the dependence on parameter t as (Eq. 4.12)

$$\underbrace{\mathcal{L}}_{model} = \begin{bmatrix} \mathcal{V}_{eigen\,[3\,x\,3]} & \boldsymbol{c}_{[3\,x\,1]} \\ 0_{[1\,x\,3]} & 1_{[1\,x\,1]} \end{bmatrix} \cdot \begin{bmatrix} \aleph(\mathcal{p}_{1q_1}, k \cdot \sigma_1) \\ \aleph(\mathcal{p}_{2q_2}, k \cdot \sigma_2) \\ \aleph(\mathcal{p}_{3q_3}, k \cdot \sigma_3) \\ 1 \end{bmatrix} = \mathcal{S} \cdot \mathcal{P} \qquad \textbf{(4.12),}$$

$$= \Psi$$

where $\mathcal{V}_{\mathbf{eigen}}$ is a matrix containing the eigenvectors in columns, $\boldsymbol{c}$ the wire centroid, $\mathcal{S}$ the so-called space matrix and $\mathcal{P}$ the polynomial matrix containing the fitting polynomial coefficients and the statistical modelling of FLE. We called Ψ the model matrix. Note that a different model matrix Ψ is obtained for each acquired fiducial point cloud.

The modelling process is completed for each fiducial point cloud in both image and tracker geometrical spaces. Note that the same data in both spaces are related ideally (null FLE) by

$$\Psi_{Tracker} = {}_{Image}T^{Tracker} \cdot \Psi_{Image} \qquad \textbf{(4.13),}$$

where $\Psi_{\mathbf{Tracker}}$ is the model matrix in the tracker coordinate system, $\Psi_{\mathbf{Image}}$ the model matrix in the image coordinate system and ${}_{\mathbf{Image}}\mathbf{T}^{\mathbf{Tracker}}$ the rigid image-to-tracker transformation. In fact, under idealistic conditions, $\mathcal{P}_{\mathbf{Image}} \equiv \mathcal{P}_{\mathbf{Tracker}}$, because polynomial fitting is performed on a PCA basis. Therefore,

$$\mathcal{S}_{Tracker} = {}_{Image}T^{Tracker} \cdot \mathcal{S}_{Image} \quad \textbf{(4.14).}$$

However, due to the FLE, the computation of Ψ is not optimal; thus, Eq. 4.14 is not always fulfilled.

An extra processing step is included to account for the fact that computing PCA could produce a differently oriented $\mathcal{V}$ basis. PCA does not provide a unique orientation for the components for a given input in $\mathbb{R}^3$ space. To overcome this problem and preserve the same orientation during modelling for fiducial point clouds in both spaces (image and tracker), target fiducials' point clouds modelling is performed first. Then, since fiducial-to-fiducial correspondence is known, PCA of the source point cloud is reoriented for all possible orientations of $\mathcal{V}_{\mathbf{eigen}}$. For each orientation, a different polynomial matrix is computed. The target fiducial polynomial matrix is compared with each of the computed source polynomial matrices. Since, ideally, $\mathcal{P}_{\mathbf{Target}} \equiv \mathcal{P}_{\mathbf{Source}}$ for a given line, the PCA orientation that minimizes the difference between matrices $\left\|\mathcal{P}_{\mathbf{Target}} - \mathcal{P}_{\mathbf{Source}}\right\|_2$ is the orientation selected for the source model.

Initialization of registration and model-driven registration

The initialization process is performed in two steps. First a fast point-based registration using the centroid of each fiducial approximates the rigid transformation. If the number of fiducials is greater than three, the centroid of each acquired fiducial point cloud is computed in both coordinate systems, and a rigid point-based registration is performed to initialize the second registration step. For this purpose, the code provided in [113] is used for point-based registration. If the number of fiducials is two, the end-points of each one are registered. Finally, if the registration uses a unique fiducial, then the two end points and centroid are registered. In a second step, ICP registration is computed using the point-based preregistered input data described above.

In order to estimate the registration parameters after initialization, a realization of the model Ψ is generated using the probabilistic model described in (Eq. 4.12) for each line. The number of points generated for this purpose is

half of the input points for each acquired fiducial point cloud. Note that if the number of points generated using the model grows, the registration will be driven mainly by the modeling step. Choosing half of the input points as the number of points generated provides a good compromise between relying only on the modelling step or depending on the original noisy points. The model-based points and the input data points generated are then registered using the classical ICP algorithm (Fig. 4.1, bottom panel).

4.3.3 Simulations and evaluation methods

We carried out an extensive number of simulations to evaluate the outcome of the algorithm proposed and compare results with those of classic ICP [71], AICP [70] and CPD [111]. We used the public code from [73] for the classic ICP algorithm, MATLAB (Matlab 6.1, The MathWorks Inc., Natick, MA, 2000) to code AICP according to [70] and the code available in [114] for CPD registration. The methods were compared in terms of the number of fiducials, the anisotropy on FLE, the FLE standard deviation and the ratio of the number of points in the source to the number of targets for each line.

In each simulated registration problem, a fixed number of fiducials ($N_{fiducials}$) was simulated in the source (world) space with 12 cm length. Fiducials were placed around a simulated target volume (patient's abdomen), which was simulated with a radius of 30 ± 0.5 cm (mean ± std), in much the same way they are usually placed in a real application. An example of simulated fiducials ($N_{fiducials}$ = 12) is depicted in Fig. 4.1 a, b, c and d.

To simulate the target (image) points, source fiducial point clouds were rigidly transformed. The transformation on each simulated case was randomly composed of a Gaussian distributed translation of 10.0 ± 2.0 mm (mean ± std) on each axis and an equally distributed random rotation angle in the range of [0-360] degrees on a random rotation axis. This transformation is saved for each simulated case as the gold standard. Once target points are transformed, a three-dimensional Gaussian isotropic zero-mean noise of 10^{-4} mm standard deviation is added to the target point cloud. This noise simulated the small FLE found on the patient's CT scan when fiducial localization is recorded for registration purposes and is related to the CT voxel size. On the other hand, source data were perturbed using a three-dimensional Gaussian isotropic zero-mean noise with controlled standard deviation (FLE_{std}). This perturbation noise will simulate the FLE produced by the tracker acquisition.

In order to study the effect of FLE anisotropy on the outcome of each algorithm studied, we simulated two different anisotropy values (Eq. 4.15)

$$FLE_{std} = [std_x,\ std_x,\ \boldsymbol{F_A} \cdot std_z] \quad \textbf{(4.15)},$$

where FLE_{std} is the standard deviation of the three-dimensional Gaussian simulated FLE and $\boldsymbol{F_A}$ a factor that controls FLE anisotropy on the z axis for the point cloud.

Parameter	Values Studied				
$N_{fiducials}$	3		6		12
FLE_{std}	0.02	0.04	0.10	0.25	0.50
N_{source}/N_{target}	0.25	0.50	0.75		1.00
$\boldsymbol{F_A}$	1 (isotropic)		2 (anisotropic)		

Table 4.1: Simulation parameters for LBR assessment.

We were also interested in the robustness of the registration algorithms under lack of input data. In order to study such cases, we randomly sampled each source fiducial point cloud using a lower number of points than the target point cloud ($100 \cdot N_{source}$ / N_{target}). We performed 500 repetitions for each combination of parameter values (see Table 4.1).

Each simulated dataset was registered using AICP, ICP, CPD and LBR, and an estimation of the gold standard registration matrix was obtained. Note that in order to perform a fair comparison, AICP, ICP and CPD were initialized by the centroid-based registration matrix estimated using the initialization step of LBR algorithm.

The registration of each algorithm was evaluated by means of two different metrics. On the one hand, we compared ICP, AICP, CPD and LBR results to

the gold standard transformation using the 'strength' metric (Eq. 4.16) [115], [116]. The strength of a rigid transformation matrix is defined as (Eq. 4.16)

$$S(T_{[4x4]}) = \sqrt{l^2 + \left(\frac{\theta}{\alpha}\right)^2} \quad \textbf{(4.16),}$$

where α represents a scaling factor between the translation and rotation contributions, l is the length of the translation and θ the rotation angle. Using this definition, two transformation matrices can be compared using the strength distance metric defined in [116] as (Eq. 4.17)

$$Strength\ Distance\ (T_{gs}, T_i) = \frac{S\left(T_{gs}T_i^{-1}\right) + S\left(T_{gs}^{-1}T_i\right)}{2} \quad \textbf{(4.17),}$$

where T_{gs} is the gold standard and T_i the transformation compared. Note that a small value in the strength distance means that transformations are closer. For evaluation purposes, we used $\alpha = 2.632$ according to [115] based on l and θ in mm and degrees, respectively.

On the other hand, for each simulation, we also measured the TRE value of each method (ICP, AICP, CPD and LBR) on a point grid cube of 30 x 30 x 30 cm sampled at 10 x 10 x 10 points. This cube was placed at the centroid of the target volume. Note that TRE is spatially dependent and is calculated as (Eq. 4.18)

$$TRE(\boldsymbol{x}) = \|\mathcal{T}_{Gold\ Standard}\langle \boldsymbol{x} \rangle - \mathcal{T}_{Method}\langle \boldsymbol{x} \rangle\|_2^2, \quad \boldsymbol{x} \in \boldsymbol{\Omega} \quad \textbf{(4.18),}$$

where $\mathcal{T}_{Gold\ Standard}\langle \boldsymbol{x} \rangle$ is the point transformed using the gold standard transformation, $\mathcal{T}_{Method}\langle \boldsymbol{x} \rangle$ the point transformed using the evaluated method on each case and $\boldsymbol{\Omega}$ is the cube (target volume).

In order to quantify the improvement in TRE obtained when LBR was applied, we calculated the TRE difference (between each registration algorithm tested and LBR) on each target point of the cube. On each simulation, we computed the percentage of points in the volume of interest where the TRE difference was higher and lower than a given threshold. Finally, the improvement in the outcome of LBR ($M_{Algorithm}$) was computed as a percentage metric (Eq. 4.19)

$$M_{Algorithm} = 100 \cdot \frac{\sum_{x}^{\Omega}[(TRE_{Algorithm}\langle x \rangle - TRE_{LBR}\langle x \rangle) > \boldsymbol{th}] - \sum_{x}^{\Omega}[(TRE_{Algorithm}\langle x \rangle - TRE_{LBR}\langle x \rangle) < \boldsymbol{th}]}{N} \quad \textbf{(4.19),}$$

where $\sum_{x}^{\Omega}[c]$ is the number of points in the target volume ($\boldsymbol{\Omega}$) that fulfill the condition c, N is the total number of points inside $\boldsymbol{\Omega}$ (10 x 10 x 10) and $Algorithm$ refers to ICP, AICP and CPD. Note that the metric described in Eq. 4.18 is positive when LBR is better on a larger zone of the target volume and negative in cases where the algorithm evaluated results in a better registration than LBR. This metric takes into account the spatial distribution of TRE for each algorithm and thus summarizes the outcome of the algorithms compared inside the complete target volume and not only on the centroid.

We studied the metric $M_{Algorithm}$ for TRE threshold values of 10^{-4}, 10^{-3}, 10^{-2}, 10^{-1}, 0, 1, 1.25, 1.5, 1.75, 2, 2.5 and 3 mm. Note that the higher the threshold, the more restrictive the metric is when considering TRE differences. This is important, since small differences in TRE values could be insignificant depending on the application. However, greater differences (higher threshold) could lead to a significant difference in the outcome of registration.

The two metrics described were used on each simulation. For each parameter shown in Table 4.1, the mean and 95% confidence interval of the mean were computed in order to depict metric-to-parameter dependency.

4.4 Results

Figure 4.3 shows the mean strength distance (Eq. 4.17) for each algorithm to the gold standard transformation. LBR showed the lowest values of all the parameters studied. In Fig. 4.3 a, the algorithms showed a metric dependency on the number of fiducials used, where a higher number favored better registration for all the algorithms evaluated. This result was expected, since the number of points available for registration is higher (high redundancy) when more fiducials are used. A similar trend was observed for the factor that controls the number of source-target points (Fig. 4.3 b): the higher the number of points on both clouds, the lower the transformation distance for all algorithms.

With respect to the simulated tracker noise, the outcome of AICP, ICP and LBR depended on the value of FLE (Fig. 4.3 c). However, CPD did not show this dependence, probably because CPD is a pure probabilistic method that simultaneously estimates the target noise and registration parameters that could compensate for FLE. Nonetheless, CPD values of strength distance were higher in all cases than those of AICP, ICP or LBR. Finally, the values of the strength metric for all methods are shown for the two anisotropy values studied (Fig. 4.3 d). As expected, AICP performed better than ICP and had a lower metric than the gold standard. For CPD, we can see how the algorithm is able to maintain similar values independently of anisotropy, although again with a poorer outcome than the other algorithms. LBR yielded the best results of all the algorithms evaluated.

Figure 4.4 shows the results for the metric of Eq. 4.19 (see Material and Method section 4.2) and for the factors studied. LBR yielded a positive improvement for each combination of parameters and TRE threshold. Notice also that for all the graphs depicted, when the threshold grows, the outcome of the algorithms—in comparison with LBR—tends toward 0%, thus indicating that the number of points inside the simulated volume of interest where LBR performed better (worse) than the other algorithms is reduced (increased). Note that the difference in TRE between the methods is limited by the maximum TRE found in the evaluation volume of interest for each simulation. For threshold values close to that maximum, the difference in points tends toward 0% because the number of points where LBR performs better (worse) also tends toward zero.

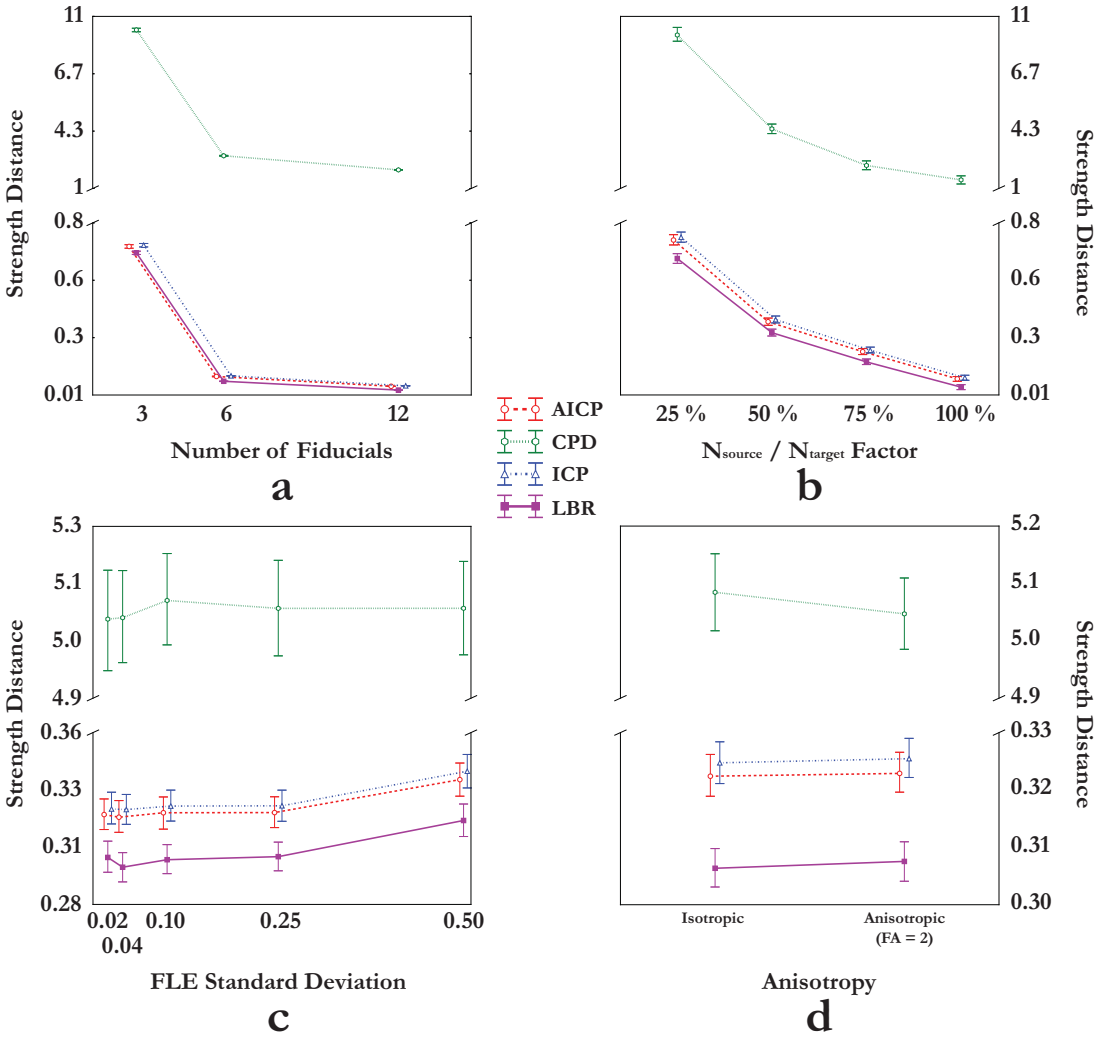

Figure 4.3: Mean strength distance (Eq. 17) and 95% confidence interval for each method (CPD, AICP, ICP and LBR) against the parameters studied: **(a)** Number of fiducials used for registration, **(b)** ratio of number of sources used to number of target points, **(c)** simulated tracker noise or FLE and **(d)** simulated factor of anisotropy.

Figure 4.4: Percentage improvement in TRE volume (mean and 95% confidence interval) of LBR over ICP, AICP and CPD for the different TRE thresholds and factors values studied: first row **(a, b, c)**, number of fiducials simulated, second row **(d, e, f)**, ratio of number of sources to number of target points, third row **(g, h, i)**, FLE simulated noise and fourth row **(j, k, l)**, anisotropy.

As for the number of fiducials (Fig. 4.4 first row), the outcome of the algorithms assessed was closer to that of LBR when the number of fiducials increased. This observation is also consistent with the results shown in Figure 4.3, where the methods yielded lower values for the distance to the gold standard when a higher number of fiducials was used for registration. In this case, similar results were observed for AICP and ICP, with AICP being the most competitive algorithm compared with LBR.

4.5 Discussion and Conclusion

Our new line-based approach for image-to-world registration combines the main advantages of fiducial-based and fiducial-free registration approaches, namely, data redundancy and geometric correspondence. The algorithm we propose, LBR, makes it possible to estimate rigid registration parameters. Our algorithm models data from each fiducial in order to tackle FLE, uses correspondence data to perform the initial registration and estimates registration parameters using a computed statistical model of fiducials.

The strategy presented reduces tracker acquisition time inside the operating room. However, it requires fiducial segmentation in the image space in order to collect the point cloud data. This segmentation could be made by simple thresholding of the CT image, since the fiducials proposed are made of high-density material (metal).

We assessed the LBR algorithm using simulations that enabled us to study the effect of various parameters on registration outcome, such as the number of fiducials, ratio of the number of sources to the number of targets, tracker-induced FLE and FLE anisotropy of the data acquired. Comparison of the outcome of LBR with the results of the classic ICP, AICP and CPD algorithms revealed TRE to be lower with LBR than with ICP, AICP or CPD for most of the target points studied. Outcome was evaluated using the strength distance of the algorithms and gold standard transformation matrices and with TRE inside a volume of interest.

The dependency of each parameter is shown in detail in Fig. 4.3 and Fig. 4.4. Strength distance (Eq. 4.17) and the TRE-based outcome metric (Eq. 4.19) demonstrated the robustness and accuracy of our approach. In most cases, LBR showed lower TRE ($< 10^{-1}$ mm) on more than ~15% of the target volume. For lower TRE differences (< 1.0 mm), results were always better for LBR than for

the other algorithms. AICP and ICP yielded similar results for the parameters analyzed and for the simulated registration problems. However, if we focus on anisotropic FLE results (Fig. 4.4 j, k - blue line), AICP performed better than ICP, while ICP yielded similar results for isotropic and anisotropic cases. These small differences in both algorithms could be due to the spatial distribution of the point cloud. Simulated lines were placed around the volume of interest using separated point clouds (one for each simulated fiducial), thus favoring the behavior of ICP, which produces results only ~3% lower than AICP for anisotropic FLE registration problems.

The number of fiducials used is a major issue that is closely related to the amount of data collected for registration. LBR showed the best results when 12 fiducials were used for registration. Such a low number of lines could be acquired over a short period, thus ensuring both fast registration and a fair TRE value. However, this parameter seems to limit the favorable outcome of CPD, which showed a marked difference against LBR for all the cases studied (Fig. 4.4 c, f, i, l). TRE threshold dependency is consistent, since all graphs showed lower values of improvement in LBR for higher threshold values. However, differences are quite high, with improvement values >35% for all the factors and thresholds. CPD is a point cloud registration method (see Introduction section 4.1) and depends on a three-dimensional GMM with the number of components equal to the number of target points. In fact, the centroids (mean estimate) of components correspond to the target points. Source points are classified by maximizing the likelihood of belonging to the target mixture model. When the number of samples to be classified is smaller than the number of parameters estimated (isotropic FLE components and registration parameters), GMM could lead to a poor solution [117]. As CPD is model-based, it is expected that for higher values of FLE, a low number of points collected could lead to a poor estimation of GMM parameters. In all of the cases we studied, the number of target points used was 100. CPD was designed to register point clouds with a large number of points. The proposed number of collected points in source and target fiducials might not be appropriate for estimation of the GMM and registration parameters. However, our objective was to study the outcome of registration algorithms in our application of interest. Increasing the number of points acquired would lead to an increase in acquisition time, thus extending the required registration time more than would be desirable during surgery.

In all the simulations performed, LBR significantly improved the accuracy of our image-to-world registration approach. Our results also confirm the robustness of the method against parameters such as different numbers of lines,

anisotropic FLE, data subsampling and distance to the geometric center of fiducials. Given this improvement in accuracy and robustness over previous algorithms, we consider that LBR is an important contribution to image-guided procedures. The potential impact of this work on the field of image-guided interventions is high, since image-to-world registration is a key component of these procedures.

5

Integration of Free-Hand 3D Ultrasound and Mobile C-Arm Cone-Beam CT: Feasibility and Characterization for Real-Time Guidance of Needle Insertion

5.1 Introduction

Accurate placement of a needle or probe is a common requirement in minimally invasive interventions, pain management and drug delivery. In brachytherapy, for example, radioactive seeds need to be precisely placed within the patient to ensure correct delivery of the planned dose distribution to the tumor volume [118]. Various ablation techniques rely on similar accurate placement of therapeutic probes within the target – e.g., radiofrequency ablation (RFA) and cryotherapy [119]. Accurate placement of the needle / probe is therefore important to achieve the clinical objective and avoid complications such as infection [120], hemorrhage, pain or pneumothorax [121].

Interventional imaging systems are widely used to assist clinicians during needle insertion and improve safety and accuracy of several procedures [40],

[118], [122]. Two-dimensional ultrasound is commonly used to provide real-time imaging at a relatively low cost [123]–[125]. Example low-cost ultrasound systems include those produced by Interson (Pleasanton USA), Wallach Surgical Devices (Trumbull CT USA), and American 3B Scientific (Tucker Georgia USA), offering a diversity of designs adapted to specific applications, such as vascular drug delivery or percutaneous biopsy. However, manufacturers usually offer limited information regarding the imaging performance characteristics. Hence, selecting a low-cost system suitable to a particular task requires a rigorous technical assessment. Specifically, real-time ultrasound visualization of the needle position and orientation relative to surrounding anatomy can be helpful in facilitating needle guidance [126] [127]; however, safe and accurate needle placement requires sufficient spatial resolution for accurate targeting, contrast resolution for visualization of the target of interest (e.g., cyst or vessel), and enough image depth for the anatomical site of interest. On the other hand, in the field of IOERT the use of US imaging during breast interventions helps clinicians to ensure the correct placement of the protection used to avoid irradiating the ribs or the heart and assess the treatment depth [34], [83], [84]. However, this technique is not suitable for dose distribution estimation which limits its possibilities for IOERT procedure re-planning.

Registering anatomical information from high-resolution 3D preoperative imaging such as computed tomography (CT) or magnetic resonance imaging (MRI) to the intraoperative scene could improve localization accuracy in such interventions. These imaging techniques provide soft-tissue contrast and high spatial resolution with a large 3D field of view; for example, CT guidance of RFA was shown to achieve probe localization error <3 mm [128]. Furthermore, CT imaging could be used in the IOERT context for accurate dose delivery estimation [85]–[87]. However, these modalities show strong cost limitations and require special room space and radiation considerations. In [129], the authors present a cone-beam CT (CBCT) and fluoroscopy system capable of guiding needle-based interventions including vertebroplasty, RFA of large lung tumors, and lung biopsies. Such work demonstrates the benefits of intraoperative CBCT with respect to radiation dose reduction, as it required only a single CBCT at the beginning of the procedure showing a mean overall targeting error of 3.7 ± 2.3 mm [129]. Some needle-based applications, such as high-dose-rate (HDR) brachytherapy where –needles are introduced into the patient anatomy to place the radiation seeds- would benefit an anatomically updated CBCT image both for seed placement guidance and as a necessary component for customizing treatment dose distribution [130]. In [131], authors evaluated the feasibility of

using a C-arm to acquire images during IOERT in order to calculate a 3D dose distribution based on individual patient anatomy, which is not possible on US images. Although intraoperative 3D imaging provided rich anatomical context, as the authors discuss, the lack of real-time imaging during needle placement carries the potential for inaccurate target localization due to respiratory motion and anatomical deformation [132]–[136].

Recent improvements in the cost, image quality, and flexibility in low-cost ultrasound imaging systems along with the increasing availability of mobile C-arm CBCT motivates a multi-modality imaging approach. The combination of ultrasound and mobile C-arm CBCT could provide up-to-date anatomical visualization and allow precise localization of interventional tools registered through surgical tracking systems and/or image registration [137].

5.2 Objective

The objective of this work is to present the initial development of an integrated ultrasound-CBCT system for image-guided needle interventions, combining a surgical navigation system, with a low-cost transducer for real-time free-hand ultrasound and a mobile C-arm for CBCT. The ultrasound probe used in this study was the Interson Vascular Access Probe VC 7.5 MHz (Interson, Pleasanton CA), and the work includes assessment of ultrasound imaging performance characteristics – to our knowledge, the first reported assessment for this device. We also integrated the probe with the TREK navigation platform [137] via the manufacturer's software development kit (SDK) and the PLUS library [138]. The mobile C-arm was a previously reported [139]–[142] prototype capable of fluoroscopy and CBCT. The performance of ultrasound-CBCT registration was investigated in three simulated needle guidance scenarios in phantoms emulating vascular access, abdominal tumor ablation, and lumbar puncture procedures.

5.3 Material and Methods

5.3.1 Ultrasound Imaging Performance

An Interson Vascular Access Probe VC 7.5 MHz (Interson, Pleasanton CA) (Fig. 5.1 a) was used as the basis for ultrasound-CBCT integration for image-guided needle insertion. This low-cost probe allows imaging at three frequencies (5, 7.5 and 12 MHz) with a manufacturer-specified depth range from 5 to 100 mm. The focal point is specified to be 20 mm from the transducer, and the scan sector has a 60° aperture. The probe can be operated simply via a single USB connection to a tablet, laptop, or workstation without an extra power supply. As detailed below, the ultrasound probe was assessed in terms of its imaging performance characteristics, geometric accuracy of surgical tracking and image registration with CBCT.

Ultrasound Image Quality

Image quality of the ultrasound system was assessed in terms of spatial resolution and contrast-to-noise ratio (CNR) measured at different probe frequency settings and as a function of depth in the field of view (FOV). To evaluate spatial resolution, we used the phantom shown in Fig. 5.1 c, constructed using a 3D printer (and polylactic acid material) and consisting of four walls with holes placed at different heights similar to the calibration phantom described in [143]. Nylon wires of 0.5 mm diameter were spatially separated by 5 mm (Fig. 5.1 b). An example ultrasound image is shown in Fig. 5.1 b, where the intersections of the wires and the ultrasound image plane are detected. These intersections were localized and fit to a bivariate Gaussian (Eq. 5.1) as follows:

$$\mathrm{G}(x,y) = \frac{1}{2\pi\sigma_1\sigma_2}\exp(-[a(x-\mu_1)^2 - 2b(x-\mu_1)(y-\mu_2) + c(y-\mu_2)^2])$$

$$a = \frac{cos^2\alpha}{2\sigma_1^2} + \frac{sin^2\alpha}{2\sigma_2^2}$$

$$b = -\frac{\sin 2\alpha}{4\sigma_1^2} + \frac{\sin 2\alpha}{4\sigma_2^2} \qquad \textbf{(5.1),}$$

$$c = \frac{sin^2\alpha}{2\sigma_1^2} + \frac{cos^2\alpha}{2\sigma_2^2}$$

where μ_1, μ_2 localizes the centroid (corresponding to the voxel with maximum image intensity μ_X, μ_Y), σ_1 and σ_2 are the standard deviation of the Gaussian, and $|\alpha| < \frac{\pi}{3}$ is the angle between the centre line of the ultrasound image plane and the line that pass through the point at which the point spread function (PSF) is measured and the probe sensor. The two-dimensional PSF was estimated in both directions (σ_1 and σ_2) as the full-width at half-maximum FWHM $= 2\sqrt{2 \ln 2}\,(\sigma_1, \sigma_2)$ .For each intersection we estimated σ_1, σ_2, and α as shown in Fig. 5.1 d, e.

We acquired 200 image planes with the ultrasound probe held in a static passive arm for each combination of the operating frequencies (5, 7.5, and 12 MHz) and depths (50, 60, 80, 100 and 120 mm) at a constant frame rate of 5 fps. The σ_1, σ_2, and α parameters were evaluated for each case as a function of position in the FOV.

To measure the CNR we constructed a phantom that emulated a soft tissue background with blood vessels as shown in Fig 5.3 a. Gelatin and cylindrical pasta were used to mimic the properties of soft-tissue and blood vessels, respectively. Simulated vessels were placed at varying depth within an otherwise uniform simulated soft-tissue background. The CNR in ultrasound images was measured in terms of the contrast between the simulated vessels and the background as a function of depth using regions of interest (ROI) containing the simulated vessel and background with a 5×5 pixel size. CNR was computed from each ROI as:

$$\text{CNR} = 2\frac{\mu_v - \mu_{bg}}{\sigma_v + \sigma_{bg}} \qquad \textbf{(5.2),}$$

where μ_v is the mean intensity value of the simulated vessel wall, μ_{bg} is the mean intensity value of the background, σ_v is the standard deviation of voxel values in the vessel wall, and σ_{bg} is the standard deviation of voxels in the background. For each measurement, we acquired 500 ultrasound images at 5 fps at operating frequencies of 5, 7.5 and 12 MHz.

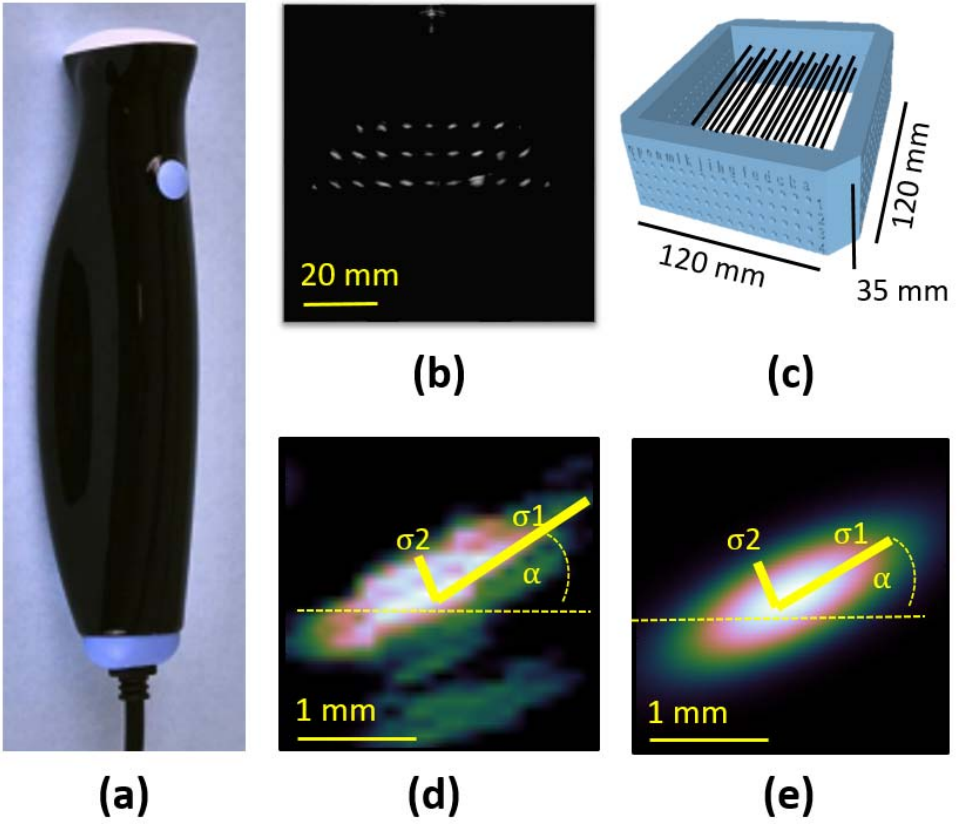

Figure 5.1: Ultrasound probe and PSF assessment. **(a)** Interson 7.5 MHz ultrasound probe (Interson, Pleasanton USA). **(b)** Example ultrasound image of the wire phantom. **(c)** 3D model of the wire phantom used for PSF assessment. **(d)** Example image showing the intersection of a wire with the ultrasound image plane. **(e)** Gaussian fit and parameters for the image shown in **(d)**.

Ultrasound Calibration

The ultrasound probe was calibrated in terms of spatial location and timing of the acquisition. Temporal and spatial calibration of the tracked ultrasound probe is necessary for free-hand 3D ultrasound imaging (via image mosaic) and surgical navigation [138]. Temporal calibration estimates the time lag between acquisition of the ultrasound images and the pose information read from a

surgical tracking system, thereby allowing synchronization of the ultrasound and tracking systems. Spatial calibration is then used to estimate the transformation ($^{P}T_{U}$) from the ultrasound image plane (labelled U in Fig. 5.2 c) to the tracked rigid body used to localize the probe (labelled P in Fig. 5.2 c). In Fig. 5.2 c all related transformations are depicted, where each transformation, $^{B}T_{A}$, is a transformation from 'A' to 'B' frames. Using $^{P}T_{U}$, the ultrasound image plane localized in the tracker coordinate system can be calculated as

$$\langle {}^{T}T_{U} \rangle = {}^{T}T_{P}\, {}^{P}T_{U} \qquad \textbf{(5.3),}$$

where $^{T}T_{P}$ is the pose of the rigid-body probe (P) in the tracker frame (T), and $\langle {}^{T}T_{U} \rangle$ is the estimated transformation from the ultrasound image to the tracker geometric frame.

The PLUS open-source software toolkit [138] – originally developed for ultrasound-guided interventions – was used to integrate the Interson software development kit (SDK) with the TREK surgical tracking and navigation platform [137], using essential functions for tracked ultrasound, such as spatial calibration, ultrasound image acquisition, free-hand 3D ultrasound volume imaging via mosaic (referred to as "mosaicking").

The calibration transformation ($^{P}T_{U}$) was obtained from imaging a calibration phantom via a tracked ultrasound. In this work, we employed the calibration 'fCal 2.0 Phantom' proposed by PLUS authors [138] for 100–120 mm depth ultrasound image settings. The calibration phantom was formed using nine lengths of nylon line whose relative spatial positions are known. A description of the phantom and a printable 3D model can be obtained from the public web documentation for the PLUS library [138]. The calibration transformation ($^{P}T_{U}$) is estimated by the algorithm presented in [144] that extracts the pose of the wire intersection within image planes and minimizes the in-plane error (IPE), computed as the least-square difference of the detected and expected intersections of the wires and the ultrasound image plane.

$$\text{IPE} = \sum_{i=1}^{N_i} \sum_{j=1}^{N_w} \left\| u_{x_{ij}} - u_{w_{ij}} \right\|^2 \quad \textbf{(5.4)},$$

where $u_{x_{ij}}$ is the detected intersection between the jth wire and the ith ultrasound image, and $u_{w_{ij}}$ is the expected intersection position of the jth wire with the computed image plane.

The aim of the calibration assessment presented below was to determine the minimum number of image planes (N_i) required for an accurate spatial calibration of the ultrasound probe. We performed 10 repeated spatial calibrations using different number of ultrasound plane images (100, 150, 200, 250, 500 and 750). For evaluation, we acquired an extra set of images (20% of the number of calibration images) and measured the average IPE on this extra set.

5.3.2 Ultrasound and C-Arm Cone-Beam CT Integration

The integration of ultrasound image acquisition and C-arm CBCT was implemented using the *TREK* imaging and surgical navigation platform [137]. *TREK* is based primarily on two software packages: cisst (Johns Hopkins University, Baltimore MD) [145] and *3DSlicer* (Brigham and Women's Hospital, Boston MA) [146] allowing intraoperative CBCT and image guidance [137]. In this work, we contributed two main software developments: (1) *TREK* functionality was expanded to perform ultrasound imaging by means of the PLUS toolkit, and (2) a dedicated module was created for ultrasound imaging that permits control of the acquisition parameters (i.e., operating probe depth and frequency), loading of tracker calibration files (calibration transformation), and custom ultrasound scanner functionalities (i.e., last-image-hold, changing modes, and FOV settings). The *Plus* toolkit interfaces to the probe using the manufacturer's SDK and a software wrapper that permits the *Plus* library to call SDK functions. However, this wrapper does not allow real-time ultrasound image acquisition nor changing ultrasound acquisition parameters. This work contributed such functionality to the *Plus* toolkit and can be found in the most recent version of the code contribution to the wrapper in [147].

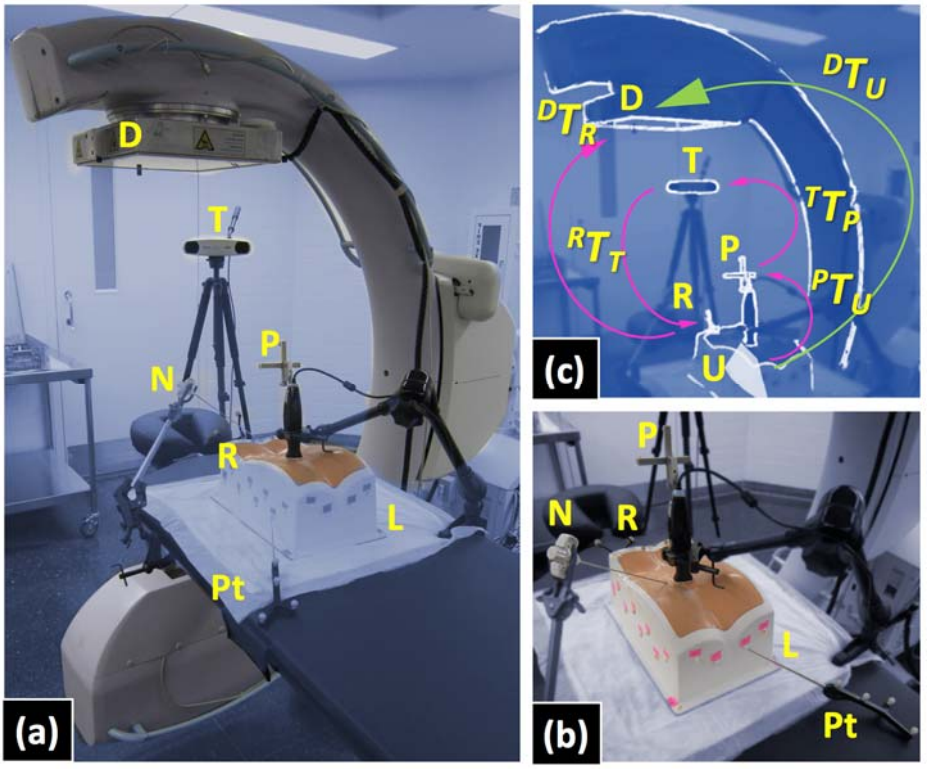

Figure 5.2: Experimental setup for free-hand 3D ultrasound imaging with C-Arm CBCT and surgical tracking for guidance of needle placement in a lumbar phantom (panels **a** and **b**). Panel **(c)** shows pertinent coordinate transformations for needle guidance. System components include: C-Arm flat-panel detector **(D)**, Polaris Vicra tracker **(T)**, ultrasound probe with attached rigid body for tracking **(P)**, lumbar phantom **(L)**, phantom tracking reference marker **(R)**, Polaris pointer used for divot localization **(Pt)**, surgical needle **(N)** and ultrasound image plane **(U)**.

The C-arm imaging platform was the prototype mobile isocentric C-arm for intraoperative CBCT shown in Fig. 5.2 (D, a modified PowerMobil, Siemens, Erlangen, Germany, as described in [95], [148]–[150]) equipped with a flat-panel detector (PaxScan 3030 +, 1536 × 1536 pixels at 194 μm pitch), Varian Imaging Products, Palo Alto, CA. The C-arm is able to rotate about the operating room (OR) table covering a total angular range of ~178° and operates in pulsed-

fluoroscopic mode allowing 3D CBCT volume reconstruction with a ~20×20×20 cm3 FOV. The ultrasound-CBCT system can be used with other probes that are supported by *Plus* and may be tailored to other specific clinical applications.

An experimental setup was devised to evaluate the feasibility and integration of the system (Fig. 5.2). We placed the mobile C-arm (Fig. 5.2, D) tableside in a laboratory OR. We placed an optical tracker (Polaris Vicra, Mississauga Canada) (Fig. 5.2, T) ~1.5 m from the operating table, allowing C-arm rotation and line-of-sight to the tracked elements (i.e., ultrasound probe, assessment phantoms and a pointer). The ultrasound probe was temporally and spatially calibrated (using 500 calibration frames) before experimental assessment with a mean IPE (in-plane error) of ~1.2 mm.

Experiments employed three phantoms: a custom soft-tissue (gelatin) simulated vessel phantom (described before, Fig. 5.3 a), an abdominal phantom (Image-guided Abdominal Biopsy Phantom, Model 071A, CIRS, Norfolk, Virginia, USA) with simulated spherical tumors of varying density (Fig. 5.3 b), and a lumbar spine phantom (Lumbar Training Phantom, Model 034, CIRS, Norfolk, Virginia, USA) containing simulated bone, cerebrospinal fluid, and soft tissues (Fig. 5.3 c). Fiducial divots (Fig. 5.3, Dv) were placed on the surface of each phantom to register the free-hand ultrasound and CBCT images via point-based registration. Two rigid needles of 22-gauge (Fig. 5.2 and 5.3, N) were

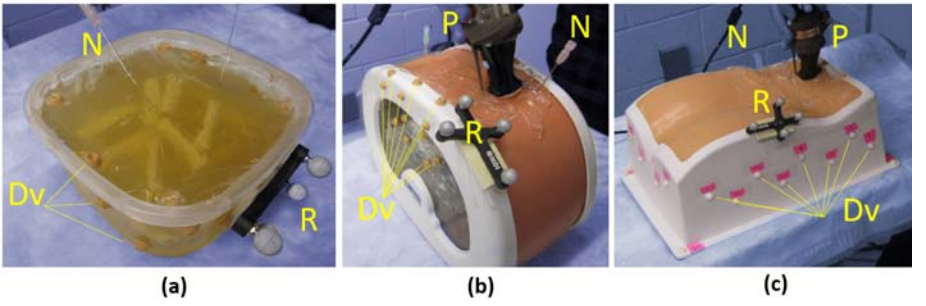

Figure 5.3: Validation phantoms: vessel phantom **(a)**, abdominal soft-tissue phantom **(b)** and lumbar phantom **(c)**. Attached optical tracked reference frame **(R)**, inserted surgical needles **(N)**, registration 3D printed divots **(Dv)** and ultrasound probe during acquisition **(P)**.

inserted at different locations within the CBCT FOV, targeting an interior vessel (~0.5 cm diameter), simulated tumor (~1 cm diameter), and facet joint (~0.5 cm width) in the three phantoms, respectively, in order to simulate three needle-based procedures (drug delivery, tumor ablation, and lumbar puncture).

The experimental workflow consisted of the following steps: (1) the 3D fiducial locations were measured using a tracked pointer (Fig. 5.2, Pt) in the tracker geometric space, which coincides with the US free-hand space after calibration; (2) three free-hand 3D ultrasound images were acquired following initial CBCT; (3) US- and CBCT- guided procedure simulation (needle insertion); and (4) acquisition of CBCT and three free-hand 3D ultrasound images (for each phantom study) at the end of the procedure with needles at target locations inside a given phantom.

Fiducial divots were segmented in the first CBCT image as reference and localized in the tracker coordinate frame using a tracked pointer tool (Fig. 5.2, Pt). Localization in both frames were registered using point-based registration to obtain the registration matrix ${}^{D}T_{R}$ (Fig. 5.2 c) that relates CBCT and tracker frames. Using ${}^{D}T_{R}$ and ${}^{P}T_{U}$ we estimated the transformation between CBCT and free-hand 3D ultrasound as:

$$\langle {}^{D}T_{U} \rangle = {}^{D}T_{R}\, {}^{R}T_{T}\, {}^{T}T_{P}\, {}^{P}T_{U} \qquad \textbf{(5.5)}$$

The geometric point-based registration accuracy was evaluated in terms of fiducial registration error (FRE) and target registration error (TRE). FRE was measured for each registration as:

$$\langle \mathrm{FRE} \rangle = \sqrt{\sum_{i=1}^{N_{\mathrm{divots}}} \left\| x_{\mathrm{Tracker}(i)} - x_{\mathrm{CBCT}(i)} \right\|^{2}} \qquad \textbf{(5.6),}$$

where $x_{\mathrm{Tracker}(i)}$ and $x_{\mathrm{CBCT}(i)}$ are the pose of the ith divot in the tracker (free-hand 3D ultrasound image) and in the CBCT image frames, respectively. N_{divots} is the number of divots used for each study (20, 13, and 23 in the vessel,

abdomen, and lumbar, respectively). Estimation of TRE was performed by localizing the inserted needle tip in free-hand 3D ultrasound and CBCT images manually by three users that were familiar with CT and US manual segmentation. For each registration the TRE was estimated as:

$$\langle \mathrm{TRE} \rangle = \sum_{i=1}^{3} \sum_{j=1}^{2} \left\| y_{3\mathrm{DUS}(i,j)} - y_{\mathrm{CBCT}(i,j)} \right\| \qquad \textbf{(5.7)},$$

where $y_{3\mathrm{DUS}(i,j)}$ and $y_{\mathrm{CBCT}(i,j)}$ are the pose of the localized jth needle tip in the acquired ith 3D ultrasound and CBCT image respectively.

5.3.3 Image-based registration assessment

Image-based registration could further improve registration accuracy, and enable compensation for misalignment caused by patient motion during the procedure. However, it requires a robust image similarity metric suitable for ultrasound-CBCT image registration. Challenges associated with such images and similarity metrics include: the need for a fast performance; untracked (void) regions within 3D ultrasound volume acquired via mosaicking of tracked 2D ultrasound; and limitations of ultrasound imaging in the context of gas-filled regions and/or bony structures. Registration of C-arm CBCT with other 3D imaging modalities has been previously reported and is the subject of ongoing work [151]–[153]. Ultrasound-CT registration has also been investigated in, for example, [154] and [155], where authors addressed the limitation of ultrasound in scanning bony structures by surface-based registration techniques. The authors simulated ultrasound images from the CT scans to perform the registration in liver and kidney applications in [156]. An example of image-based registration is described in [157] in which 2D ultrasound image planes were registered to CT volumes employing the cross correlation as similarity metric.

To investigate the feasibility of ultrasound-CBCT image registration in application to needle interventions, we implemented and assessed three classes of image similarity metric that could support such integration, including Normalized Mutual Information (NMI)

$$\text{NMI} = \frac{H(F) + H(u(M,p))}{H(F,u(M,p))} \quad \textbf{(5.8),}$$

where $H(F)$ is the entropy of fixed image, $H(u(M,p))$ is the entropy of the moving image under a deformation u with transformation parameters p, and $H(F,u(M,p))$ is the joint entropy of images F and M. We also investigated performance using Normalized Cross Correlation (NCC)

$$\text{NCC} = \frac{\sum_x F(x) * M(x\ + u(x,p))}{\sqrt{\sum_x F(x)^2 * M(x\ + u(x,p))^2}} \quad \textbf{(5.9),}$$

where x is a voxel in the fixed image F, M is the moving image, and $u\ (x,p)$ is the deformation of x depending on the transform parameters p. Finally, we measured the similarity of F and M using a Huber distance [158] between their modality-independent neighborhood descriptors (MIND) [159]. An element of a MIND descriptor $S(I,x,y)$ is given by

$$S(I,x,y) = \exp\left(-\frac{SSD(x,y)}{\sigma^2}\right) \qquad x,y\ \in N \quad \textbf{(5.10),}$$

where I is the image, σ^2 is an estimate of the local variance at x, SSD is the sum of square differences, and N is the neighborhood over which the descriptor is calculated for a patch centered at x.

We defined a ROI of ~40×30×30 mm^3 inside the vessel phantom containing two whole vessels in order to evaluate the image-based metrics on a volume scanned by the free-hand 3D ultrasound imaging method described above. We randomly perturbed the ultrasound ROI volume from the tracker-

based registration solution by a rigid transformation (translation and rotation) according to a Gaussian distribution:

$$G(x) = \frac{1}{\sigma\sqrt{2\pi}} e^{\frac{-(x-\mu)^2}{2\sigma^2}} \quad \textbf{(5.11),}$$

where μ is the mean value (or perturbation factor) and $\sigma = 0.1$ is the standard deviation. We varied the perturbation factor over the μ range [-3,3] (mm and degrees for translation and rotation, respectively) in steps of 0.1. For each perturbation, we performed 100 trials with 6 random parameters corresponding to the 6 degrees of freedom of a rigid transformation.

Image-based registration performance was assessed in terms of TRE as well as the objective function (NCC, NMI, and MIND Huber distance) directly as a function of perturbation factor. The registration result was visualized by overlaying the gradient of the CBCT volume (moving target image) with the free-hand 3D ultrasound (fixed source image).

5.4 Results

5.4.1 Ultrasound Imaging Performance

The PSF for different frequency and depth is showed in Fig. 4a. An example of the PSF parameters [standard deviation in both directions (σ_1 ,σ_2) and angle (α)] for the case of 7.5 MHz frequency and 80 mm depth is depicted in Fig. 5.4 b–d. The PSF was reduced (sharper) in the lateral direction for higher frequencies and almost constant in the ultrasound pulse propagation direction, consistent with the dependence of depth resolution on duration of the ultrasound pulse (independent of depth and frequency). Also notice in Fig. 5.4 b (σ_1 map) that the minimum measured σ_1 is found at ~2 cm depth, which corresponds to the probe focal point according to manufacturer's specifications. The computed α map was consistent with the direction of the ultrasound pulse through the image plane. Overall, we see FWHM that is fairly constant ($FWHM_2$

~0.3 mm) in the lateral direction and steeply degrading with depth ($FWHM_1$ ~1.0–5.5 mm) in the depth direction over the depth ranges 20–100 mm.

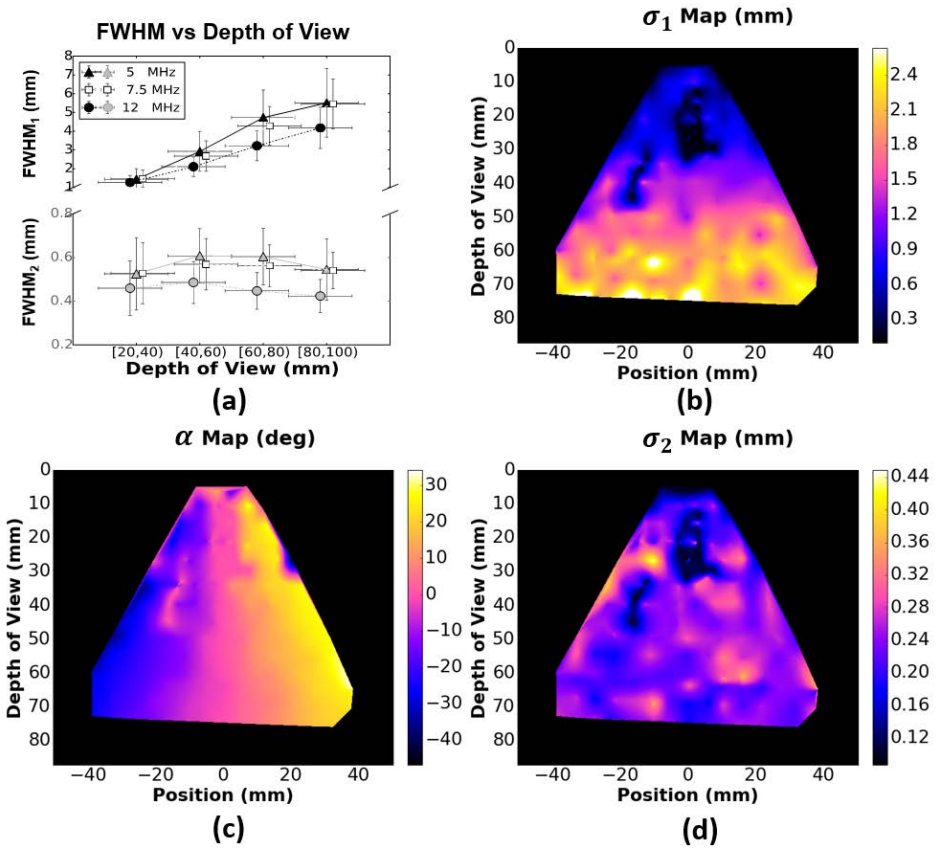

Figure 5.4: Ultrasound image spatial resolution. **(a)** FWHM of the Point Spread Function (PSF) for different frequencies as a function of depth of view. **(b)** Measured PSF width at 7.5 MHz and maximum depth of 80 mm in the direction *perpendicular* to sound wave propagation. **(c)** Angle between the two-dimensional fitting Gaussian model with respect to horizontal. **(d)** Measured PSF width in the direction *parallel* to sound wave propagation direction.

The CNR measured at different frequencies as a function of depth is shown in Fig. 5.5. The CNR decreases by more than a factor of 2 over the depth of field and is highest at the lowest frequency settings (Fig. 5.5 a). This degradation is also shown in the example ultrasound image of the vessel phantom (Fig. 5.5

b) where CNR decreases along the length of the vessel wall as the ultrasound wave is attenuated at increased depth in tissue. Broadening of the lateral component of the PSF width at increased depth is also evident.

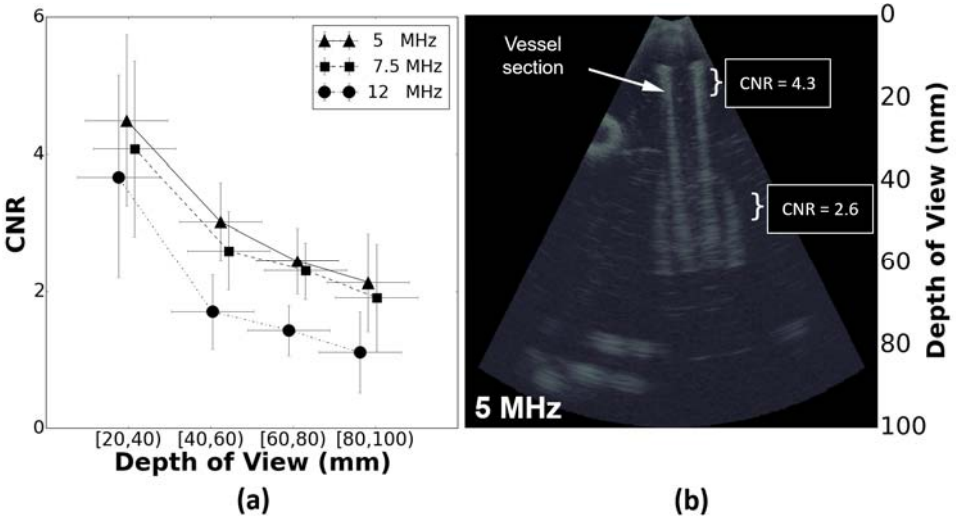

Figure 5.5: Contrast resolution measurements for the ultrasound imaging system. **(a)** Mean and standard deviation in CNR for different frequencies as a function of depth. **(b)** Example ultrasound image of the vessel phantom acquired at 5 MHz and maximum depth of 100 mm.

Results for the ultrasound calibration assessment are presented in Fig 5.6. The IPE distribution is presented as a function of the number of frames used in the calibration, showing the degradation in IPE when the number of calibration images is small (<150). Using more than 500 frames for calibration does not seem to lead to lower IPE, and the minimum IPE is limited by the image resolution for greater than ~300 frames. In Fig. 5.6 b a volumetric rendering of the vessel phantom is shown to illustrate the capability of the system to produce free-hand 3D ultrasound volumes when a correct calibration is achieved.

5.4.2 Ultrasound and C-Arm Cone-Beam CT Integration

The TREK navigation system updated via the PLUS software library for ultrasound integration was used to evaluate the combined ultrasound-CBCT system. Functionality included: connecting the probe to the system, loading

calibration parameters, and allowing free-hand 3D ultrasound imaging. In Fig. 5.7 results for FRE and TRE (at the needle tip) are shown. The FRE (mean ± standard deviation) was 1.1 ± 0.5 mm for the vessel phantom, 1.3 ± 0.4 mm for the abdomen phantom, and (0.9 ± 0.3) mm for the lumbar phantom, consistent with the registration accuracy of the tracker. TRE at the needle tip was 2.3 ± 0.3 mm for the vessel phantom, 3.0 ± 0.4 mm for the abdomen phantom, and 2.1 ± 0.6 mm for the lumbar phantom.

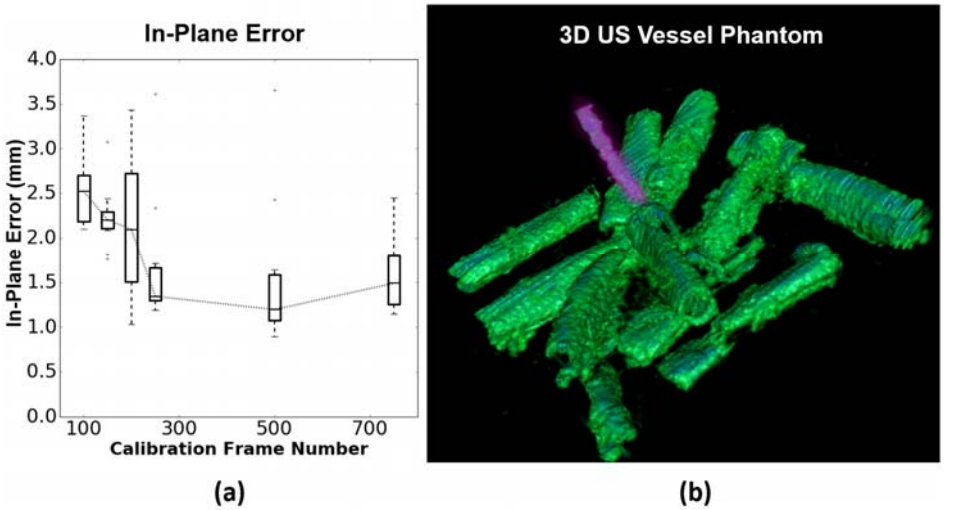

Figure 5.6: Registration accuracy. **(a)** In-plane error during probe-to-tracker calibration as a function of the number of collected calibration frames. **(b)** Volumetric rendering of the vessel phantom 3D ultrasound image showing the simulated vessels **(green)** and the inserted surgical needle **(purple)**.

Fig. 5.8 shows the ultrasound-CBCT registered images in the vicinity of the needle for the three cases evaluated: vessel, abdomen, and lumbar phantom. The registered images illustrate the utility of combined ultrasound and CBCT – the former providing real-time visualization, and the latter providing high-quality 3D imaging of soft-tissue and bone. In Fig. 5.8 (a, d, g) a slice of the vessel phantom image is shown, where the needle is clearly visible within the simulated tissue and the CBCT provides high soft tissue contrast showing the inner part of the vessels. In Fig. 5.8 b, the needle tip for the abdominal phantom case is conspicuous in the ultrasound plane (where the needle is seen to miss the simulated tumor). Finally, in Fig. 5.8 (c, f, i) the ultrasound image shows the edge

of the spine, while CBCT shows the complete bone structure and is exemplary of the potential benefit in combining both modalities – i.e., ultrasound performing real-time guidance and CBCT depicting the needle path inside the bone, where US contrast is limited by the technique.

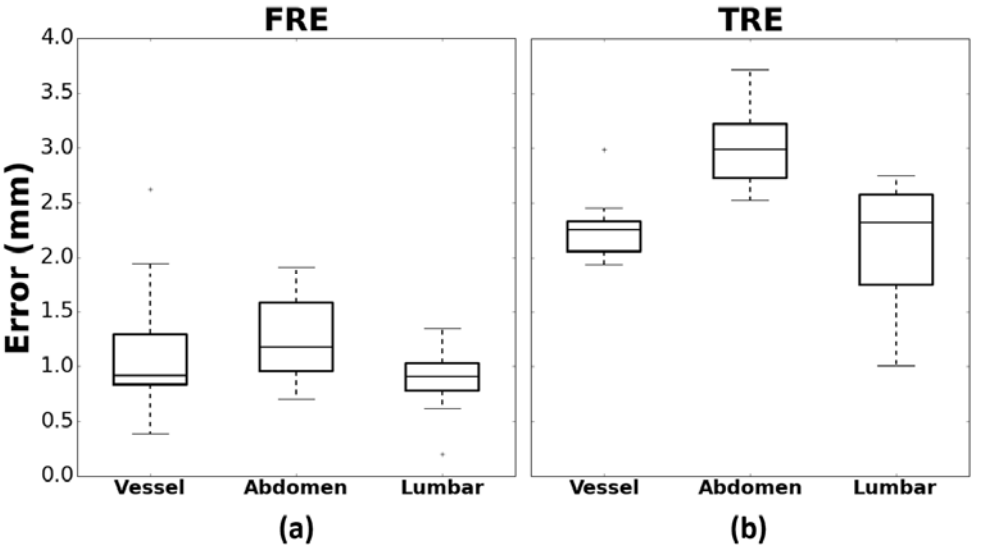

Figure 5.7: Geometric accuracy of ultrasound-CBCT integration. **(a)** Fiducial Registration Error (FRE). **(b)** Target Registration Error (TRE), calculated at the needle tip for the vessel and abdomen phantoms and at the intersection of the needle with bone for the lumbar phantom.

5.4.3 Image-based registration assessment

Results of the image-based registration are showed in Fig. 5.9, demonstrating that registration was feasible even with a low-cost ultrasound probe with limited image quality. Each of the similarity metrics maximizes at a solution that is within 1 mm and 1 degree of the tracker-based registration solution. Similarly, TRE is minimized at approximately the same solution. Errors in the localization of the needle tip during TRE estimation could cause the higher values of TRE in this example case (i.e., minimum TRE ~3.0-3.5 mm in Fig. 5.9 compared to ~2.0 -3.0 mm in Fig. 5.7). Note that a perturbation factor of 0 also introduces random transformations. In cases studied, the NMI and MIND-Huber similarity metrics performed similar TRE minimum values, supporting

their potential suitability for this multi-modality registration problem. The results are likely dependent on anatomical site and require validation in clinical image data, which is the subject of future work beyond this feasibility study.

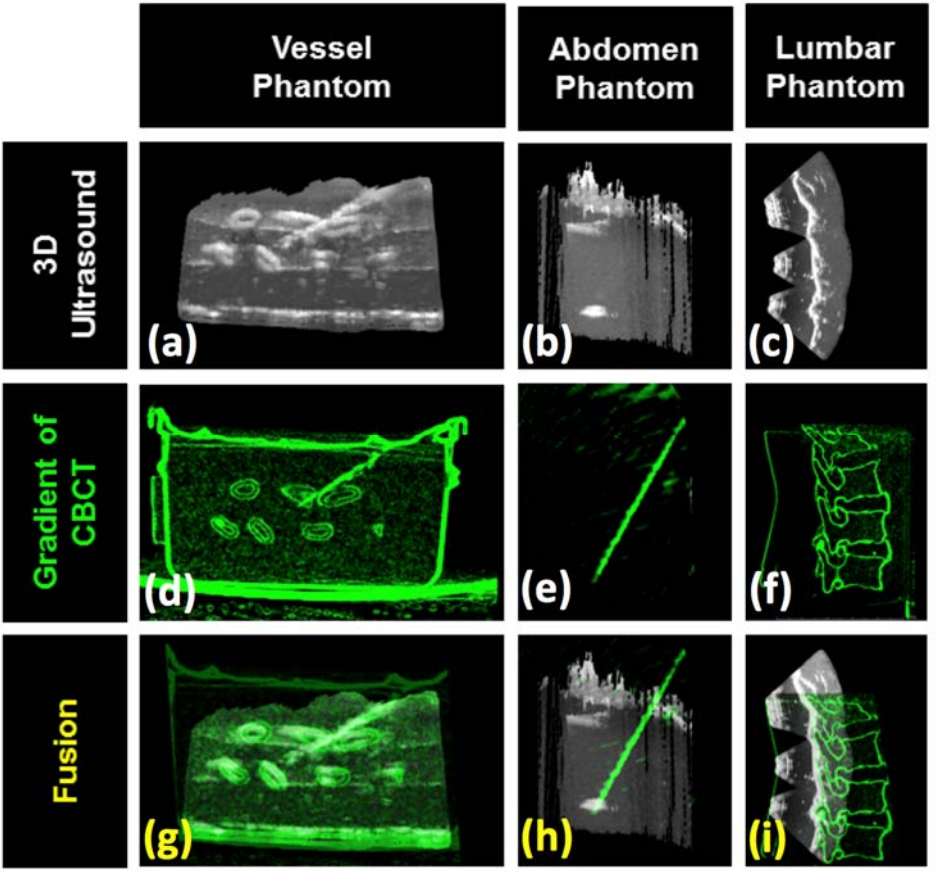

Figure 5.8: Registration of free-hand 3D ultrasound with CBCT using fiducial-based registration. **(a-c)** Ultrasound image, **(d-f)** gradient of CBCT image, and **(g-i)** fusion of free-hand 3D ultrasound and CBCT gradient image for the Vessel, Abdomen, and Lumbar phantoms.

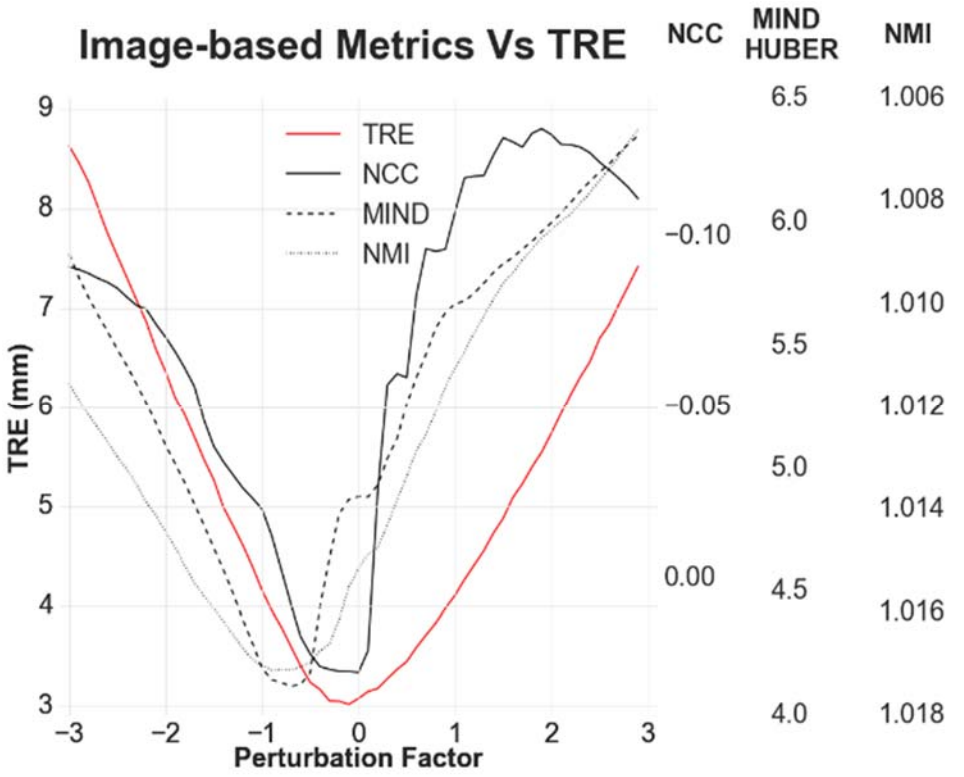

Figure 5.9: Image-based registration of 3D ultrasound and CBCT. The (target registration error) TRE was measured as a function of Perturbation Factor, minimizing at the transformation taken as reference "truth." Three similarity metrics (NCC [normalized cross correlation], NMI [normalized mutual information], and MIND-Huber [modality-independent neighborhood descriptors]) are each minimized within ~1 mm and ~1° of the reference.

5.5 Discussion and Conclusion

This Chapter presented the first image quality assessment for the Interson Vascular Access Probe VC 7.5 MHz and initial implementation of an integrated ultrasound-CBCT system for image-guided needle interventions. The low-cost ultrasound system showed modest image quality in terms of CNR and spatial

resolution (PSF) and could be suitable for a variety of needle interventions within ~20–60 mm depth of the surface. Examples include superficial interventions such as arterial blood and thyroid biopsies, or obstetrics applications [160] that could benefit from the competitive price and convenience of the system. Its small size, USB power supply, and low price could be suitable for environments with limited access to high-end imaging technology.

Development and feasibility of a free-hand 3D ultrasound imaging system registered with mobile C-arm CBCT was demonstrated. In the vessel phantom experiment, the system was able to track needle insertion in real-time due to ultrasound imaging that could be verified to hit the vessel target using CBCT. In the lumbar puncture experiment, the needle could be tracked to the surface of the spine using ultrasound, and the utility of the integrated system was evident in combination with CBCT capability to visualize the position of the needle in bone (see Fig. 5.8 i).The advantages of such US-CBCT integration is not limited to the potential clinical applications subject to the constraints of the US image quality characteristics of the Interson probe assessed in this study and could facilitate multi-modal image guidance capability to a wide variety of needle interventions with other suitable, higher-end US systems.

Needle-tip localization accuracy was ~2.1–3.0 mm (TRE) via the integrated ultrasound-CBCT system using fiducial-based registration. A limitation of this feasibility study is that we employed only two needles and only one insertion per phantom. However, we do not expect strong variability in TRE across the region of interest investigated in this work, given the fairly high number of registration fiducials (divots) surrounding the ROI [68]. This fairly high TRE was attributed primarily to the limited spatial resolution and CNR of the ultrasound probe that somewhat compromised the spatial calibration. The basic concept for ultrasound-CBCT system integration implemented here is compatible (without requiring additional development) with higher-end ultrasound systems with improved functionality and image quality, which would presumably enhance the ultrasound-to-tracker calibration and image-based registration.

Fiducials were placed surrounding the target on each case with different spatial distribution. It is known that TRE depends on the distribution of fiducials around the target. The better the target is covered by fiducials the smaller is the expected TRE [68]. In the three studied cases, we found similar FRE values for each case (Fig. 5.7 a). However, due to the target spatial differences for each case (vessel, tumor and spine), TRE was found different. Furthermore, TRE also depends in part on the image quality (for both the observer-based truth

definition and – for registration-based approaches – for the registration accuracy). The three phantoms presented distinct challenges with respect to both ultrasound and cone-beam CT image quality, and the TRE varies accordingly. We would like to point that the acquisition of the 3DUS image using the probe introduces some deformations on the phantom surface. Depending on factors such as pressure, material elasticity or target depth, produced deformations could bias the TRE.

Image-based registration results suggest that similarity metrics such as NCC or MIND-Huber are suitable objective functions for registration of these modalities. Image-based registration demonstrated estimated TRE < 4 mm for scenarios in which soft tissue was visible in both modalities and FOV was reasonably well covered by both modalities (i.e., ultrasound mosaicking holes were minimized). For the needle guidance task in these scenarios, initial work employed a rigid registration model; however, soft-tissue deformations due to the needle and/or ultrasound probe can be expected and warrants future investigation of nonrigid registration approaches – e.g., B-spline [161] or Demons [162], [163] transformations. On the other hand, surface-based registration schemes could be also feasible in the US-CBCT registration context. Such strategies require a surface detection/segmentation processing (or surface markers) of both modalities in advance. A commercial example is the ClearGuide system (Clear Guide Medical, Baltimore, MD, USA). This image preprocessing, together with the found US imaging quality characteristics of the studied low-cost probe could become an important issue during the registration performance that should be study properly and it was not the aim of the presented image-based registration section. Despite that, our results demonstrate feasibility for ultrasound-CBCT image-based registration and motivate future work in which the tracker is used for construction of the free-hand 3D ultrasound volumes (and optionally for registration initialization), and accurate registration is performed via image-based or surface registration approaches. Regarding the future research on automatic image-based registration, animal studies could be an important element to overcome the limitation of using phantoms and study realistic the images and deformation patterns. Nevertheless, we think that the reported research provides an important point of reference (comparison) for future work on automatic CT-to-ultrasound registration algorithms.

The *TREK* software architecture provided a flexible platform for development of modules for integrating the *Plus* library with CBCT and surgical tracking. This work presented an integrated platform for needle guidance

combining available open-source software tools and SDKs. Particular improvements to the *Plus* toolkit were implemented regarding the ultrasound probe interface, including online tuning of acquisition parameters during the procedure, thereby allowing more convenient tuning of image probe parameters that affect image quality.

The feasibility of integrated free-hand 3D ultrasound and mobile C-arm CBCT was demonstrated in phantom studies in scenarios emulating needle-based registration based on a low-cost ultrasound probe. The broad availability of low-cost ultrasound imaging systems with streamlined integration with fluoroscopy and CBCT could improve performance and safety in a variety of needle-based interventions.

6

Mobile Accelerator Guidance during docking steps in IOERT Procedures using an Optical Tracker

6.1 Introduction

Dedicated linear accelerators appeared in late 1990s as units that can be moved into the OR with the aim of improving the IOERT availability and obviating the need of patient's transfer during surgery. These devices produce the electron beam that will be delivered to the tumor bed. The alignment of the radiation applicator and the linear accelerator is a critical task for IOERT procedures [36] because the applicator could deviate from its current position during docking, thus altering the distribution of the delivered dose.

Docking techniques can be classified into hard and soft docking. The former (used for example by the NOVAC-7 and LIAC systems) connects directly the applicator to the linear accelerator gantry while the later decouples both elements. Usually, the time needed for the docking procedure can take up to ~14 min [37]. Some systems such as Mobetron provide aid techniques that help during the gantry and applicator alignment demonstrating a slight reduction of docking time of ~5 min.

Docking is time-consuming owing to two main factors: safety requirements and the limited degrees of freedom (DoF) of the gantry. Commercial mobile accelerators are not isocentric per se [21], thus making docking a cumbersome task for the operators in the OR. In fact, in some cases, and because of the limitations of the OR for movement of the mobile accelerator, some applicator positions/orientations are unreachable. In these cases, the patient's bed is usually moved closer to the mobile unit or placement of the applicator is modified by the oncologist.

Consequently, new techniques are required to guide docking of the applicator for mobile accelerators that improve safety and speed of the procedure, reduce anesthesia time for the patient and avoid unreachable positions. The oncology department at Hospital Gregorio Marañón (Madrid, Spain) performs IOERT regularly in a non-dedicated OR using Sordina's LIAC (Fig. 6.1). Once the applicator is correctly positioned, hard docking (see Introduction section 1.1.3) is performed by technicians and oncologists based on their experience. The mobile unit has five DoFs: gantry rotation angle, tilt angle, height, translational shift and wheel rotation. It is attached to the radiation collimator using a hard docking technique. The two-rotation axes of the gantry intersect at a point outside the collimator axis, thus making the docking procedure poorly intuitive in many cases. This limitation results in a docking time up to 15 minutes depending on the location of the tumor, even for trained technicians [79].

6.2 Objective

The objective of this study was to present a navigation solution based on optical tracking for the guidance of the docking process that is expected to improve safety and reduce procedure time. The solution presented, which tracks the applicator localization inside the OR, computes the movements that the mobile linear accelerator should perform to align the applicator and the radiation gantry and warns the oncologist if the setup is unreachable by the available DoFs. The following sections describe each component of the system: the mobile linear accelerator, the optical tracker (that locates the IOERT applicator in real time), the calibration process and the docking navigation workflow. The navigation system was implemented using an in-house software application to guide the technician during the docking procedure. The feasibility of the

proposed approach was tested on three cases emulating real clinical scenarios, where docking time was recorded for evaluation purposes.

6.3 Material and Methods

6.3.1 Mobile linear accelerator: description and kinematics

The IOERT accelerator used in our institution is a LIAC 12 device (Sordina, Aprilia, Italy), which can work at nominal energies of 4, 6, 8, 10 and 12 MeV. Its flatness is ≤ 9% for the most commonly used applicators (4, 5, 6, 7, 8, 9 and 10 cm diameter), and the dose rate (measured using the 10 cm diameter applicators) is 3-20 Gy/min. The physical dimensions of the mobile unit (Figure 6.1 b) are 180 x 76 x 210 cm with 400 kg weight.

LIAC has five DoFs (Figure 5.1 b-1, -2, -3, -4, -5): base shift (Fig 6.1 b-1), base rotation (Fig. 6.1 b-2), gantry rotation (Fig. 6.1 b-3), gantry height (Fig. 6.1 b-4) and gantry tilt (Fig. 6.1 b-5). When an IOERT procedure is performed, only the mobile unit is moved into the OR during surgery, and the hard docking technique is used. By manipulating the remote control (Fig. 6.1b), the user can perform the docking process. LIAC can move the complete mobile unit (Fig. 6.1 b) by shifting and rotating the base (Fig. 6.1-1 and -2) with no restrictions. However, the gantry's movements (Fig. 6.1, 3-5) are limited (Figure 6.1 c).

The Denavit-Hartenberg (DH) convention [164] is widely used in the literature to describe the kinematics of robotic arms. DH associates each DoF with a single joint, which is defined by a transformation that depends on a unique parameter (q). Robotic arms are defined as a chain of joints. Depending on the joint type (rotation or shift), the parameter (q) that defines the position of the joint is measured in degrees (rotation) or meters (shift) with respect to its outset

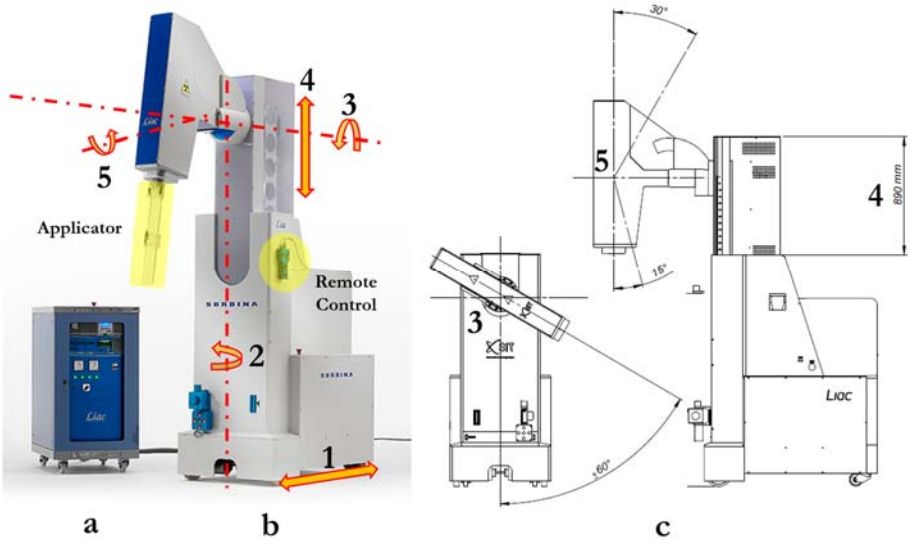

Figure 6.1: LIAC 12 (Sordina, Aprilia, Italy). **(a)** Control unit. **(b)** Mobile unit. Degrees of freedom: **(1)** base shift, **(2)** base rotation, **(3)** gantry rotation, **(4)** gantry height and **(5)** gantry tilt. **(c)** Gantry movement limits. In yellow highlight: Radiation applicator and remote control. (Images courtesy of Sordina).

position. To define the kinematics of a complete chain of joints (i.e., robotic arm), the DH nomenclature starts from the basis that it is fixed in space (where the robotic arm is attached) and defines the associated transformation to the first joint. This transformation depends on the control parameter (q, rotation or shift) that characterizes its movement and relates the base and joint coordinate systems by the transformation ${}^{Joint_1}T_{Base}(q_1)$. The next joint is then defined by a new transformation that depends on another unique parameter (q_2). This transformation relates the current and the previous joint coordinate systems (${}^{Joint_2}T_{Joint_1}(q_2)$). The process is repeated for each joint of the robotic arm. Using this notation, the end-joint coordinate system (i.e., robotic arm tip) is related to the base's coordinate system by the product in (Eq 6.1):

$$^{Joint_N}T_{Base}(\boldsymbol{q}) = \prod_{i=0}^{N} {}^{N-i}T_{N-1-i}[q_{N-i}] \quad \textbf{(5.1)},$$

where $^{Joint_N}T_{Base}(\boldsymbol{q})$ is the transformation that relates the coordinate system of the base and the last joint of the robotic arm and depends on the vector $\boldsymbol{q} = [q_1, \dots, q_N]$, N is the number of total joints, q_j the joint parameter (rotation angle/shift) of the j-th joint and $^{j}T_{j-1}[q_j]$ relates the joint (j) and $(j-1)$ coordinate systems when the joint is at the position defined by q_j. Note that for $q_i = 0.0,\ i \in [1, N]$ (i.e., outset position) the transformation $^{Joint_N}T_{Base}$ relates the base coordinate system to the robotic arm tip.

In kinematic terms, LIAC can be considered a robotic arm with 5 degrees of freedom. Following the DH convention, we can describe the complete kinematic chain of the accelerator using 5 joints, 1 for each DoF. However, the kinematic chain of the LIAC gantry is attached to the base of the mobile unit (Fig. 6.1 b), which is also mobile. To represent this mobility in DH nomenclature, we added two auxiliary joints to the defined kinematic chain as in Fig. 6.2 (i.e., Joints 1 and 2). Thus, we summarize the movement of the LIAC as a base rotation restricted to ± 45º (Joint 1, parameter q_1), a base shift restricted to ± 0.3 m (Joint 2, parameter q_2), a second base rotation restricted to ± 45º (Joint 3, parameter q_3), a second base shift restricted to ± 0.3 m (Joint 4, parameter q_4), gantry height restricted to 0-0.89 m (Joint 5, parameter q_5), gantry rotation restricted ± 60º (Joint 6, parameter q_6) and gantry tilt rotation restricted to –30º to 15º (Joint 7, parameter q_7) (Fig. 6.2). Note that the last 3 joints are restricted to LIAC specifications (Fig. 6.1 c). From this DH characterization standpoint, the accelerator can perform seven movements to reach the target orientation and location (i.e., IOERT applicator position), and complete the docking process.

Joints 1-4 represent the freedom of movement of the mobile unit. The LIAC installed in our OR can only be moved over a 2 m^2 surface owing to the restriction imposed by the OR ceiling height (in order to prevent collisions). When a patient is going to be irradiated, the applicator is positioned over the tumor bed and fixed to the OR bed. The surgical bed is then moved closer to the LIAC's reaching volume—without collisions—for docking. In our case, we limited the movements of these joints to ±45º for the base rotation (Joints 1 and

3) and ±0.3 m for the base shift (Joints 2 and 4). This moving restriction ensures that the LIAC is confined to operate in the safety volume (collision-free) of the OR. Note that for an OR of a different size, these parameters could be adapted accordingly.

Using the DH characterization described above, the location of the gantry with respect to the outset position is completely defined by the parameter q_i when the LIAC is moved for docking. The transformation that relates both

a

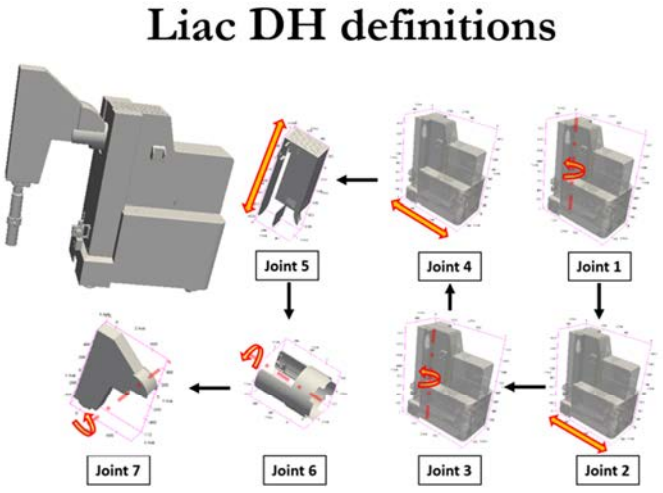

b

	Joint 1	Joint 2	Joint 3	Joint 4	Joint 5	Joint 6	Joint 7
Rotation Z	$0º + q_1$	90º	$0º + q_3$	0º	0º	$0º + q_6$	$-90º + q_7$
Traslation Z	0	$0 + q_2$	0	$0 + q_4$	$0 + q_5$	d_1 (1.325 m)	d_2 (0.3 m)
Traslation X	0	0	0	0	0	0	0
Rotation X	0º	90º	-90º	90º	-90º	90º	-90º
Minimum	-45º	-0.3 m	-45º	-0.3 m	0	-60º	-30º
Maximum	45º	0.3 m	45º	0.3 m	0.89 m	60º	15º
	Extra joint for convenience		Current Liac Joints				

Figure 6.2: Denavit-Hartenberg parameters for the Sordina LIAC 12 device. **(a)** Defined Joints and movements for the kinematic chain. **(b)** Table of D-H parameters **(q_i)** and limits of each joint.

coordinate systems (outset position and accelerator gantry) can be computed using DH definitions as in Eq. 6.1 (Fig. 6.3 f) under restrictions from Table 6.1.

Once Joints 1-4 are fixed, the gantry's DoF (Joints 5-7) restrict the possible docking orientations. Therefore, in a typical operation, some docking arrangements are not possible unless the mobile unit or the patient is appropriately reoriented. Note that this is one of the main factors that increases docking time in common usage.

Figure 6.3 (f) shows all the geometric transformations involved in the navigation solution. The transformation ${}^{L}T_{G}$ (Fig. 6.3 f) relates the position of the gantry (Fig. 6.3 f, 'G') geometrically with respect to the accelerator base (Fig. 6.3 f, 'L'). Note that ${}^{L}T_{G} = {}^{G}T_{L}^{-1}$. According to DH parameters, ${}^{L}T_{G}$ (Fig. 6.3 f) depends on the parameter $\boldsymbol{q}$ and is completely defined (Eq. 6.2).

$$ {}^{L}T_{G} = {}^{L}T_{G}(\boldsymbol{q}) \qquad \textbf{(6.2)} $$

6.3.2 Optical tracker and navigation setup

We used the OptiTrack V120:Duo optical tracker (NaturalPoint, OR, USA) (Fig. 6.3 a) to track the applicator (Fig. 6.3 d-a). We also used other system elements, such as the navigation calibration tool (Fig. 6.3 c). This system has two cameras embedded in a body measuring 279 × 51 × 41 mm. Each camera has an image resolution of 640 × 480 and a pixel size of 6 × 6 μm and can work at a frame rate in the range of 30-120 frames per second (fps). Each camera has a 3.5-mm lens (M12), F#2.0, with a horizontal field of view (FoV) of 47 degrees, a vertical FoV of 43 degrees and an 800 nm infrared (IR) long pass filter. Cameras illuminate the scene with a light-emitting diode (LED) ring composed of 26 adjustable LEDs at a wavelength of 850 nm. The system calculates the position of the passive retro-reflective markers (Fig. 3b), which are small spheres coated with IR-reflective material. Several marker diameter sizes are offered by the manufacturer depending on the specific application requirements. In this study, we used an 11.5 mm diameter marker from NaturalPoint (7/16" hard model [60]) for all experimental setups because this is the recommended size for the OR tracking volume studied. It is also important to note that all the tracked tools for this study were built using the same marker size.

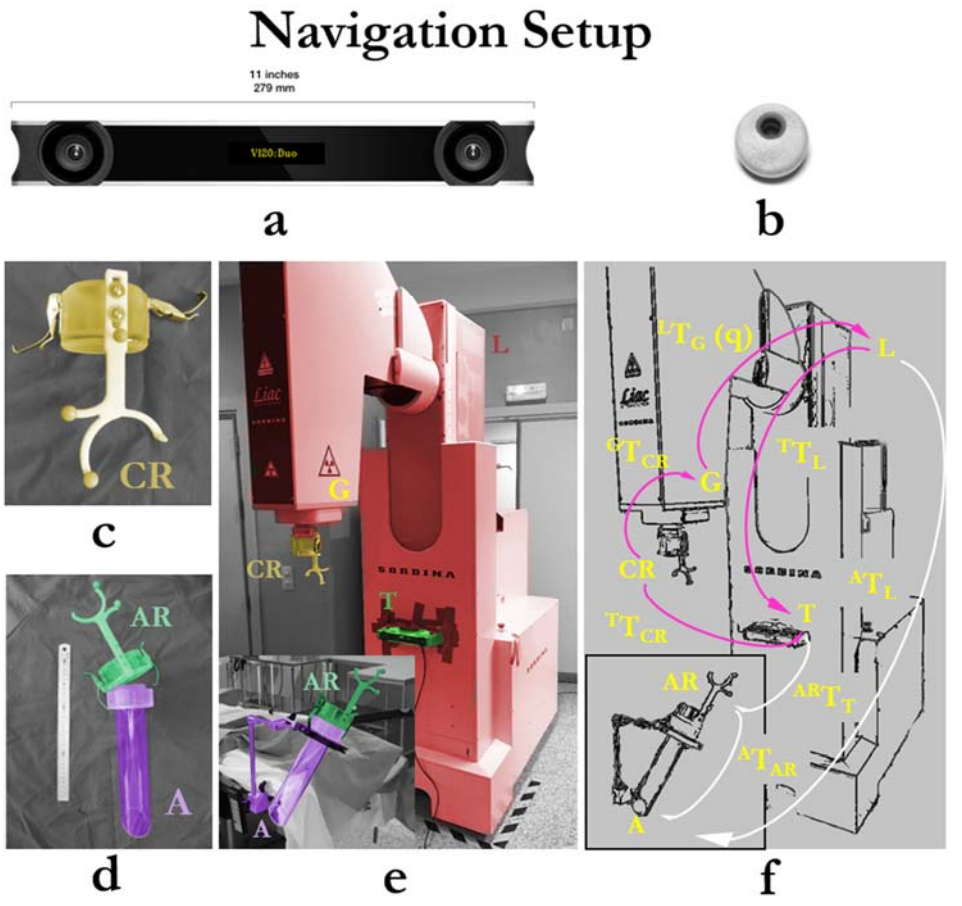

Figure 6.3: Experimental setup for IOERT docking navigation. **(a)** OptiTrack V120:Duo [60]. **(b)** Reflective marker. **(c)** Calibration tool and associated tracking rigid-body **(CR)**. **(d)** IOERT applicator **(A)** and associated tracking rigid body **(AR)**. **(e)** Complete navigation set-up: **(G)** accelerator gantry, **(CR)** calibration rigid-body tool, **(T)** tracker, **(AR)** applicator rigid body, **(A)** IOERT applicator and Sordina LIAC **(L)**. **(f)** Pertinent coordinate transformations of the docking navigation setup.

The position of the tracked tools was obtained in real time using a forward projection approach [107] and acquired using the manufacturer's application programming interface (API). Reflective markers are positioned in a unique geometry known as a rigid body (an unmistakable shape for any orientation) that is identified by the cameras in order to determine the tool's position and orientation. The simplest rigid body must be composed of at least 3 reflective markers whose distances and angles are fixed with respect to each other.

The tracker was attached to the mobile unit (Fig. 6.3 e 'T') in a fixed position. We placed the tracker in the front part of the accelerator in order to track calibration (Fig. 6.3 c and 6.3 d, 'CR') and the IOERT applicator rigid bodies (Fig. 6.3 d and 6.3 e, 'AR'). Placing the tracking system at the position shown enables the clear line-of-sight requirement of optical tracking for this application to be satisfied, owing to the limited FOV characteristics of the tracker. Note that the tracker is attached to the base of the mobile unit. Therefore, when the base is driven, the optical tracker is moved jointly since both elements are attached together. The main idea for navigation is to track the treatment applicator localization (Fig. 6.3 d, 'A') using the attached rigid body (Fig. 6.3 d and 6.3 e, 'AR'). The inverse kinematics of the mobile accelerator (Section 6.2.1) is then solved, and the docking parameters ($\boldsymbol{q}$) are computed to align the LIAC's gantry and the radiation applicator under safe conditions, including speed constraints and avoidance of collisions.

6.3.3 Navigation system calibration

In order to obtain the transformation ${}^{T}T_{L}$ (Fig. 6.3 f), which relates the tracker (Fig. 6.3 f, 'T') and LIAC accelerator base (Fig. 6.3, 'L') coordinate systems, a calibration step has to be performed prior to navigation. We used a custom-designed calibration tool composed of three retro-reflective markers and attached to the LIAC gantry (Fig. 6.3 c, 'CR') for this purpose. Since the calibration tool is fixed to the gantry, the transformation ${}^{G}T_{CR}$ (Fig. 6.3 f) is known and constant. The tracker provides the gantry location as ${}^{G}T_{T} = {}^{G}T_{CR} \cdot \left({}^{T}T_{CR}\right)^{-1}$ (Fig. 6.3 f) in the tracker coordinate system.

Before calibration, the LIAC is moved to the outset position ($q_i = 0.0,\ i \in [1,7]$). The calibration process consists of three tracking acquisitions. First, (1) we gather the localization of the gantry (${}^{G}T_{T}$) at the LIAC outset position. Then, (2) we rotate the gantry (joint 7) from –60º to 60º and record its trajectory.

Finally, (3) we return to the outset position and record the gantry location while only Joint 5 (gantry height) is moved from 0 to 0.89 m. For the outset gantry location, we record 1000 samples, whereas for the calibration trajectories of Joints 7 and 5, we record tracking data at the tracker's maximum frame rate by moving the joints at maximum (and constant) speed.

We then estimate the center of the gantry coordinate system in the tracker coordinate system as the mean of the acquired location samples at the outset position (1). This central location populates the last column of the transformation ${}^{T}\boldsymbol{T}_{L}$ (Fig. 6.3 f). Orientation is extracted using two trajectory acquisitions, namely, rotation and height shift of the gantry (2 & 3). Note that both acquisitions are in perpendicular planes. The normal vectors to the planes define two axes of the gantry coordinate system—$\boldsymbol{x}$ and $\boldsymbol{y}$. The third axis of rotation ($\boldsymbol{z}$) is computed based on the cross product following right-handed geometry notation ($\boldsymbol{x} \times \boldsymbol{y} = \boldsymbol{z}$). Vectors $\boldsymbol{x}$, $\boldsymbol{y}$ and $\boldsymbol{z}$ populate the orientation matrix of ${}^{T}\boldsymbol{T}_{L}$ (Fig. 6.3 f). When the calibration process is finished, the transformation ${}^{T}\boldsymbol{T}_{L}$ (Fig. 6.3 f) is fully estimated and can be used to compute the location of the applicator with respect to the accelerator coordinate system by ${}^{A}\boldsymbol{T}_{L}$ (Fig. 6.3 f).

6.3.4 Docking navigation

After a calibration tool (Fig. 6.2 c and 6.2 d, 'CR') is used to estimate ${}^{T}\boldsymbol{T}_{L}$ (Fig. 6.3 f), the proposed navigation set-up is ready to assist in the docking procedure. First, the applicator (Fig. 6.3 d, 'A') is fixed to the tumor bed, and the patient's bed is moved closer to the accelerator (safety area in the OR). Then, the applicator rigid body (Fig. 6.3 d, 'AR') is attached to the fixed IOERT applicator (Fig. 6.3 d, 'A'). Note that this rigid body needs to be sterilized for use during the procedure. The transformation ${}^{A}\boldsymbol{T}_{AR}$ is known and relates the applicator (Fig. 6.3 d, 'A') to the attached rigid body (Fig. 6.3 d, 'AR').

The tracker (Fig. 6.3 e, 'T') locates the position of the applicator (Fig. 6.3 f, 'A') as (Eq. 6.4):

$$ {}^{A}T_{T} = {}^{A}T_{AR} \cdot {}^{AR}T_{T} \quad \textbf{(6.4)} $$

We compute the position of the applicator (Fig. 6.3 f, 'A') in the accelerator (Fig. 6.3 f, 'L') coordinate system using the calibration matrix ${}^{T}T_{L}$ (Fig. 6.3 f), as shown in (Eq. 6.5):

$$ {}^{A}T_{L} = {}^{A}T_{T} \cdot {}^{T}T_{L} = {}^{A}T_{AR} \cdot {}^{AR}T_{T} \cdot {}^{T}T_{L} \quad \textbf{(6.5)} $$

The objective of docking is to move the LIAC ($\boldsymbol{q}$) to fulfill the condition of (Eq. 6.6), where the applicator and gantry coordinate systems are coinciding.

$$ {}^{A}T_{L} \equiv {}^{G}T_{L}(\boldsymbol{q}) \quad \textbf{(6.6)} $$

In mathematical terms, the docking problem can be written as a minimization problem (Eq. 6.7) using the navigation set-up proposed, as follows:

$$ \boldsymbol{q} = [q_1, q_2, q_3, q_4, q_5, q_6, q_7] $$

$$ \min_{\boldsymbol{q}} \left\| {}^{A}T_{L} - {}^{G}T_{L}(\boldsymbol{q}) \right\|_{M} \; such\ as\ q_i \in [min_i, max_i], i \in [1,7] \quad \textbf{(6.7),} $$

where $\boldsymbol{q}$ are the accelerator moving parameters, $[min_i, max_i]$ the limits of parameter q_i (Table 6.1) and M a metric that measures the transformation differences.

Solving the problem of Eq. 6.7 produces the optimal docking accelerator parameters. We used the L_2 norm as the metric (M) and the Sequential Least SQuares Programming optimization algorithm (SLSQP) to estimate the docking parameters [165].

Given the limits of the accelerator DoF, the solution to Eq. 6.7 could not produce an ideal match (i.e., Eq. 6.6). In order to quantify the docking error of the solution obtained, we estimated position and rotation error of the given solution. The position error measures the Euclidean distance of the solution obtained and the current applicator position at the center of the applicator bevel. The rotation error measures the difference in the angle on the applicator longitudinal axis. These parameters are given to the radiation oncologist before the docking procedure. If the errors are too large, the physician could decide in advance to orient the patient's bed differently and/or move it closer to the LIAC in order to estimate new docking parameters with a lower error (better accuracy). It is important to note that, since the points the gantry can reach are unknown in routine practice, for those cases where the gantry cannot reach the position, docking has to be repeated after moving the patient's bed, thus increasing docking time. Hence, providing the oncologist with this valuable information prior to the docking procedure could save time.

6.3.5 Software application

We integrated the navigation system into a software application that connects all the necessary elements and provides a user interface. This integration was implemented using the *TREK* imaging and surgical navigation platform [137], where a specific software module was implemented to perform the calibration and the docking guidance. *TREK* is based primarily on *3DSlicer* (Brigham and Women's Hospital, Boston, MA, USA) [146].

NaturalPoint provides an application programming interface (API) that makes it possible to control the tracker system. However, controlling the tracker hardware directly using the API is not suitable for clinical applications, where robust error handling is critical for appropriate correction of system error [166]. We used the *BiiGOptitrack* library [167] to interface with the tracker and collect the tracking information. This library follows the tracking interface standard defined by the *OpenIGTLink* protocol [168], thus enabling connection to the tracker, tool management and safe recovery from errors during tracking acquisition [166]. The PLUS toolkit [138], which was upgraded to work with

NaturalPoint trackers by means of the *BiiGOptitrack* library [167], was used to interface the user module and the tracker.

Figure 6.4 shows the module developed for guidance of docking with the LIAC. The application has two main tabs, namely, calibration and guidance (Fig. 6.4 a and 6.4 b, respectively). In the former, the user can connect the optical

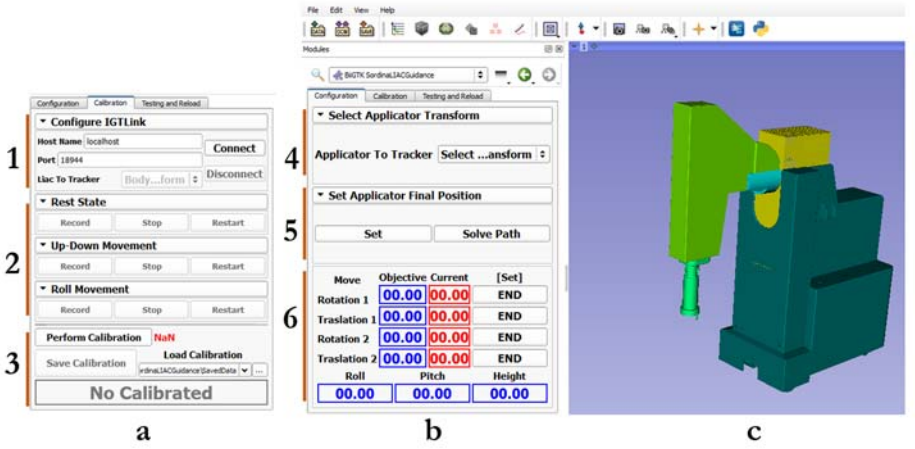

Figure 6.4: IOERT LIAC docking navigation application. **(a)** Calibration interface, **(1)** OpenIGTLink connection configuration, **(2)** calibration acquisition interface and **(3)** calibration load/save interface. **(b)** Docking navigation panel: **(4)** tracker transformation selector, **(5)** applicator tracking settings and **(6)** accelerator kinematic guidance interface. **(c)** 3D model of LIAC and target applicator position showing the final docking set-up.

tracker using the *OpenIGTLink* protocol parameters (host and port) in order to start collecting tracking data (Fig. 6.4 a, '1') from the tracker. Once the calibration tool (Fig. 6.3 c) has been attached to the accelerator gantry, the three calibration acquisitions can be controlled using the 'Record', 'Stop' and 'Restart' buttons on the user interface (Fig 6.4 a, '2'). Finally, when calibration acquisition is finished, the user presses the Perform Calibration button (Fig. 6.4 a, '3') to estimate the transformation ${}^{T}T_{L}$ (Fig. 6.3 f). The calibration can be saved to a file for future use or loaded from a previous calibration as long as the tracker maintains the same attachment position over the accelerator. The user is

informed that the calibration has been performed via a message at the bottom of the calibration panel.

The configuration panel (Fig. 6.4 b) is used to guide the technician during docking of the IOERT applicator. The selector in (Fig. 6.4 b, '4') sets the transformation associated with the tracked applicator tool (Fig. 6.3 d, 'AR'), i.e., ${}^{T}\boldsymbol{T}_{AR}$ (Fig. 6.3 f). Once the transformation is selected, a red applicator 3D model is shown in the visualization panel (Fig. 6.4 c). The location of this 3D model is updated in real-time by showing the location of the applicator with respect to the 3D accelerator model, which is also shown on the visualization panel (Fig. 6.4 c).

Once the oncologist has defined the site of treatment for the applicator and this is fixed to the patient's bed, the Set button is pressed (Fig. 6.4 b, '5'). The software then saves the (objective) applicator location. Optimal docking parameters ($\boldsymbol{q}$) are estimated after pressing the button Solve Path (Fig. 6.4 b, '5') and shown in the user interface (Fig. 6.4 b, '6' blue column, Objective). The applicator rotation and position error estimates are given to the oncologist for decision making. The technician can then use the remote control of the mobile unit (Fig. 6.1 b) and follow the computed docking parameters.

Since remote controls do not provide the current base positions (q_1, q_2, q_3, q_4), the software estimates and shows them in the user interface for guidance purposes (Fig. 6.4 b, '6'). When the user starts to move Joint 1 of the LIAC, the rotation value is updated. This information can be used to reach the objective (blue) joint orientation. Once computed position of Joint 1 is reached, the user must press the END button (Fig. 6.4 b, '6') and perform the following moves (Joints 2 to 4). The computed estimates of the gantry moves are shown on the bottom part of the panel (Fig. 6.4 b, '6'). Again, the technician needs to set the gantry orientation using the mobile unit remote control according to the values shown.

6.3.6 Evaluation of docking navigation

We measured the docking time for normal clinical IOERT treatments over one month in our dedicated OR. Specifically, we measured the time interval between when the applicator is fixed to the patient's bed until final docking.

We also ran an experimental setup using the navigation software in the OR in which we emulated three clinical cases (left breast, right breast and rectal cancer) by fixing the applicator to the bed in different orientations. The applicator was positioned based on the experience of a qualified radiotherapist. We calibrated the system following the workflow described above and estimated the docking parameters using the software application. A skilled IOERT technician controlled the accelerator movements following the application parameters with no other guidance, and a clinician evaluated the suitability of docking.

Localization	Docking Time
Rectum	05:50 min
Rectum	05:20 min
Rectum	05:40 min
Right Breast	09:40 min
Left Breast	06:30 min
Rectum	06:00 min
Right Breast	18:00 min *
Testicles	08:00 min
Right Breast	13:00 min *
Mean	**8:26** min

Table 6.1: Docking time at Hospital General Universitario Gregorio Marañón (Madrid, Spain) for different cases and locations. **(*)** Cases considered extremely time-consuming.

6.4 Results

Table 6.1 shows the docking times recorded in the OR for IOERT procedures over one month at Hospital General Universitario Gregorio Marañón (Madrid, Spain). As we can see, the mean time of 8:26 min shows that docking is a time-consuming task. Note the particular cases where the time is much higher than the others (Table 6.1, red). According to the physicians, such cases, which are right breast interventions, are particularly complicated owing to

the spatial limitations of the OR. As detailed above, LIAC could not be moved freely because it was restricted by ceiling height. Right breast cases usually require critical applicator arrangements that often lead to unreachable docking arrangements by the accelerator, with the result that the patient must be moved closer or even reoriented, thus increasing docking time considerably (see Table 6.1).

Table 6.2 shows the docking time for the three simulated cases. Using our navigation system, the maximum docking time was below 5 minutes, which is shorter than all the clinical cases recorded in Table 6.1. In all cases, the computing time for optimal docking parameters was < 20 s. In one case (right breast, Table 6.1), the docking error calculated was too large (> 15º applicator axis) owing to an unreachable orientation. This case was recalculated using our

Localization	Docking Time
Rectum	03:20 min
Right Breast	04:10 min
Left Breast	03:30 min
Mean	**3:40** min

Table 6.2: Docking time for simulated clinical cases using the navigation system.

software after moving the patient (and the fixed applicator) closer to the accelerator. For all of the cases tested, the docking parameters were estimated correctly, and the technician performed the docking using the navigation panel with no major issues. As an example of docking performance using our navigation solution, Figure 6.5 shows the alignment of the applicator (Fig. 6.5 b) and the gantry (Fig. 6.5 a) for the simulated case of rectal cancer.

6.5 Discussion and Conclusion

We present a navigation solution based on optical tracking as a guide for docking that improves safety and reduces procedure time. To our knowledge,

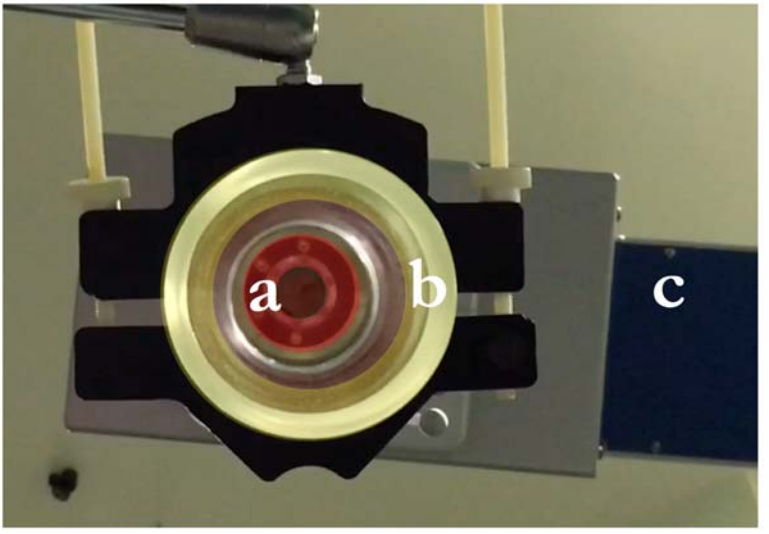

Figure 6.5: Docking as seen from the applicator bevel. **(a)** Sordina LIAC gantry. **(b)** Applicator fixed to the patient's bed simulating the location of rectal cancer. **(c)** Sordina LIAC head.

this is the first docking navigation system for mobile linear accelerators. Our solution, which is able to track the applicator location inside the OR, computes the movements needed for the LIAC mobile unit to correctly align the applicator and the radiation gantry. In case the set-up is unreachable because of DoF limitations, the system can notify the user to save procedure time, thus improving performance of IOERT. Note that it can also be applied to other linear accelerators or even for soft docking guidance. However, it requires specific tools such as the rigid-bodies attached to the applicator (which need to be adapted to each applicator size or linear accelerator model) and a previous system calibration.

We would like to point out that the docking navigator presented could be built together with the mobile accelerator unit in order to reduce calibration time. It could also be adapted to any specific movement limitations in the OR. This

paper presents a proof of concept to demonstrate the feasibility of using an optical tracker for guiding the docking task. A key limitation of this system is the user's reliance on the control of the accelerator's DoF. The movements of the mobile unit are not controlled by stepper motors. Hence, they cannot reliably locate the mobile unit arrangement. In this study, we resolved this drawback by computing the accelerator position (Joints 1-4) with respect to the IOERT applicator location using the optical tracker. However, this solution could be inaccurate for guidance, because possible errors could accumulate during the drive of the first joints (1-4), thus leading to a loss of accuracy during the last docking moves (Joints 5-7). Introducing stepper motors or encoders for feedback on linear and angular position could overcome this limitation, since placement of the mobile unit would be used by the navigation system to guide the user towards optimal estimates of rotations and shifts.

Many studies in the literature have followed a similar approach (by combining trackers and robots) in various clinical applications to overcome limitations in accuracy due to human-to-machine interactions. In [169], the authors presented an optically guided positioning system designed to improve the accuracy of patient location. They demonstrated an improvement in the accuracy of patient location relative to the linear accelerator able to detect and correct errors introduced by the conventional couch-mounted systems. A robotically assisted prostate brachytherapy system was presented in [170]. That solution combined transrectal ultrasound and a spatially coregistered robot integrated with the brachytherapy treatment planning system for guiding placement of radioactive seeds. Another example can be seen in the robot-assisted fracture manipulation system developed by [171], where a robotic manipulator connected to bone fractures was able to assist surgeons treating broken bones. Finally, similar gantry-target alignment problems have already been addressed in external radiotherapy by application of tracking techniques in linear accelerators such as TrueBeam (Varian Medical Systems, Palo Alto, CA, USA) and Elekta Infinity (Elekta AB, Stockholm, Sweden). These systems use tracking information to guarantee that the prescribed radiation dose is correctly delivered to the tissues by ensuring correct placement of the patient (position and orientation) over the accelerator bed. These examples support the use of optical tracking guidance to improve the accuracy of other radiotherapy procedures such as IOERT.

We previously described a navigation system adapted to IOERT procedures that is currently installed in Hospital Gregorio Marañón [54], [59], [172]. The solution we present here complements those results by focusing on

the guidance of docking while minimizing procedure time. In fact, both solutions could be connected to the IOERT treatment planning system, thus improving automation of IOERT procedures. Such an approach could overcome human data transmission errors and make it possible to monitor potential mistakes in human actions (risk factors previously identified in [173]), thus improving quality control in these interventions.

The system we present safeguards against OR limitations (ceiling), calculates the optimal DoF arrangement of the accelerator and reduces docking time. These benefits, which are shown in our limited trial results, have encouraged us to confirm them through further study in clinical cases in the near future. We think that the docking navigator we present is an important contribution to the IOERT community, where docking is critical for reducing surgical time, ensuring patient safety and guaranteeing that the treatment administered follows the prescription of the radiotherapist.

7

Image-guided Navigation for Intraoperative Electron Radiation Therapy

7.1 Introduction

Several authors have studied the surgical workflow of IOERT focusing on the process optimization and risk factors evaluation [27], [28], [32]. IOERT performance is noticeably based on the radiation oncologist experience who must decide a considerable number of parameters *in situ*. This promoted the development of IOERT-specific treatment planning systems (TPS) to optimize the procedure and minimize the stress in the OR during the radiation parameters selection [33], [174]. However, the delivered dose could differ from the one planned since a validation process is not available during the procedure. Furthermore, updating the parameters is necessary in the case of in situ surgical findings (e.g. modification of the applicator size when the surgical incision is smaller than that predicted preoperatively). In that case, updated settings must be entered into the TPS to recalculate the radiation dose distribution according to the revised treatment –which increases the surgical time.

Image-guided approaches could overcome the TPS limitation for the assessment of the planned treatment and/or dose distribution recalculation *in*

situ. If the positioning of the radiation collimator with respect to the patient's anatomy is known, the planned procedure could be validated or re-planned in the OR [28].

In [54], we reported an image-guided system (navigator) designed to assist oncologists during the applicator placement. The system showed a high accuracy for the applicator positioning (accuracy < 2 mm (mean error of the bevel center) and 2 degrees in orientation (mean error of the bevel axis and the longitudinal axis) that was found acceptable for the clinical IOERT application –where radiation margins are 2-4 cm surrounding the tumor [28]. Nevertheless, the incorporation of a navigator in the IOERT workflow implies several processes such as tracker calibration, positioning accuracy verification and image-to-tracker registration that must be performed prior to and during the procedure. A multidisciplinary and well-trained staff, the clear definition of the procedure and the identification of responsibilities are key factors for a successful IOERT treatment [27]. The clinical implementation of the navigation system in the IOERT process must thus be studied in detail in a clinical context. We therefore set out a clinical evaluation of the IOERT navigation workflow to complement the feasibility assessment of our solution [54].

7.2 Objective

The objectives of this Chapter are to describe the installation setup of the navigation system, evaluate the implementation feasibility in an IOERT-dedicated OR, identify potential limitations in the upgraded IOERT workflow and report the first clinical experience using this system. For that purpose, our navigation system was tested in twelve different IOERT procedures in which no clinical decisions were made based on the navigation component.

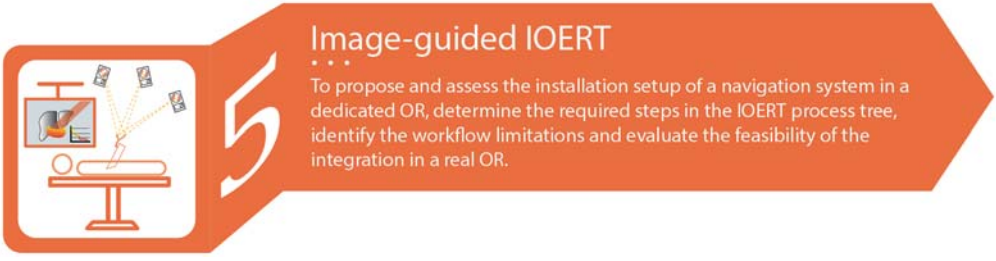

7.3 Material and Methods

7.3.1 Image-guided IOERT: navigation setup

The navigation system consists of the components depicted in Figure 7.1: the optical tracker and tools, the visualization screens and the control computer.

We used the Optitrack [60] tracker evaluated in Chapter 3, for the localization of objects in space, similar to other systems such as fusionTrack (Atracsys Inc., Puidoux, Switzerland) or Polaris (NDI Inc., Ontario, Canada).

The installed multicamera optical tracker consists of eight Flex13 cameras (Fig. 7.1 e) that are arranged around the patient bed on the OR ceiling (Fig. 7.1 a, working volume) and connected to a USB hub which is controlled by the

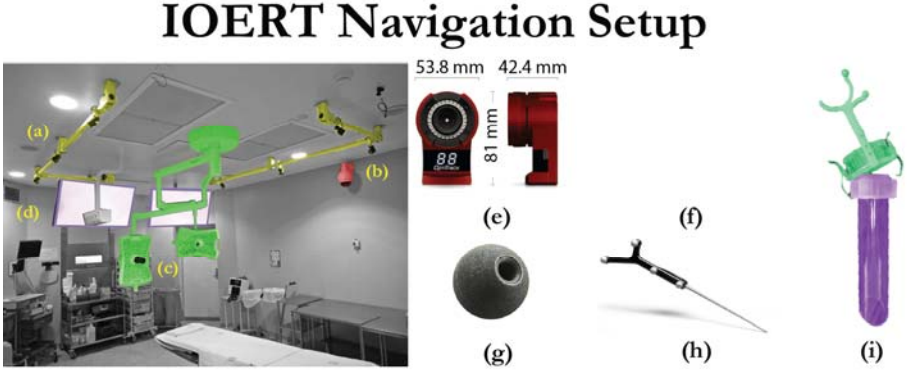

Figure 7.1: OR scenario: Distribution of cameras in Hospital Gregorio Marañón (Madrid) used for navigating the IOERT applicator. **(a)** Mounting structure with eight Flex13 tracking cameras. **(b)** Recording video camera. **(c)** Surgical lamps. **(d)** Navigation screens. **(e)** Optitrack Flex13 camera (NaturalPoint Inc., Corvallis, OR, USA). **(f)** Optiwand calibration tool **(g)** Reflective marker with 11.5 mm radius. **(h)** Rigid-body pointer tool (NDI, Ontario, Canada). **(i)** IOERT applicator **(purple)** and tracking rigid-body **(green)**.

manufacturer's software. We designed a rigid-body (Fig. 7.1 i) that is attached to the head of the applicator and consist of four passive retro-reflective markers (small spheres coated with IR-reflective material, Fig. 7.1 g). The tracker obtains the real-time position and orientation of the applicator by calculating the position of each marker. The navigation system can be used to guide the oncologist during applicator positioning following preoperative planning. Thus, the applicator is tracked in the OR and compared to the planned localization in real-time. The attachment is sterilized with ethylene oxide before its use in a clinical setting.

A CT scan of the patient is acquired before every procedure in the same body position as the one expected during surgery. A registration step is required to align the CT image study with the true patient structures. Line-shaped fiducials placed on the patient's skin are used as references for the registration process. The pose of these landmarks is identified in the CT image and localized with a tracked pointer (Fig. 7.1 h). The rigid registration parameters are estimated from these datasets using the LBR algorithm [175].

Finally, we also installed two surveillance cameras (Fig. 7.1 b) to ensure patient safety during radiation and for documentation. Two large screens are also part of the set up allowing the display of the applicator position with respect to the patient's preoperative CT scan. This facilitates applicator placement over the tumor bed and verification of the planned dose distribution. The navigation system can update the localization of the applicator in real-time in the TPS and allows the oncologist to recalculate the delivered dose distribution when the applicator position is different from the planned one. The navigation setup is completed by the computer (placed in an OR attached room) that controls the tracker, the navigation software, the two screens and runs the TPS.

7.3.2 Image.guided IOERT process tree

The upgraded IOERT process tree, including the navigation, is depicted in Figure 7.2. Yellow and blue-framed processes correspond to the navigation setup and the standard IOERT procedure, respectively. The green-framed step was added for feasibility assessment purposes [27].

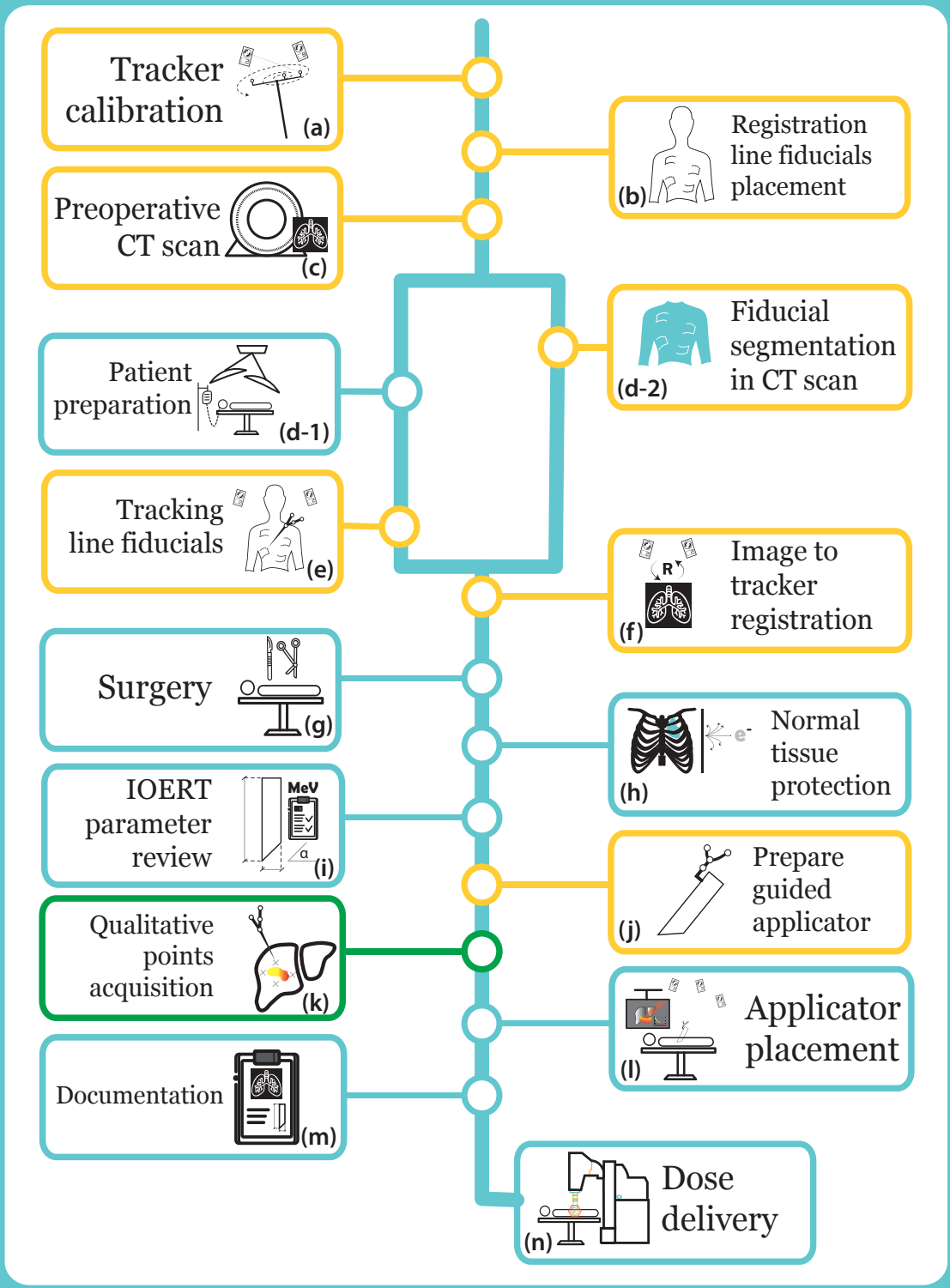

Figure 7.2: Processes involved in the navigation protocol. In blue: processes related to conventional treatment delivery and verification. In yellow: processes related to the navigation protocol. In green: evaluation of the navigation protocol.

First, a calibration of the tracker (Fig. 7.2 a) is performed to ensure proper tracking accuracy. The optical tracker requires a calibration process for every single application that is performed prior to any other use of the OR. Then (Fig. 7.2 b) the line-shaped fiducials are attached to the patient's skin surrounding the expected surgical area and (Fig. 7.2 c) a CT scan is acquired in surgical position. The patient is moved to the OR (Fig. 7.2 d-1) and the registration fiducials are localized in the tracker space using the pointer tool (Fig. 7.1h and Fig. 7.2 e). At the same time, fiducials are also localized (Fig. 7.2 d-2) in the geometric space derived from the CT image. When all positions of the registration fiducials have been collected from the image and the tracker spaces, the registration transformation is estimated (Fig. 7.2 f). Then, tumor removal surgery (Fig. 7.2 g) is performed. When the tumor bed is ready for radiation delivery, normal tissues are protected (if needed) (Fig. 7.2 h) and IOERT parameters are reviewed (Fig. 7.2 i). Before applicator positioning, the sterile tracking rigid-body (Fig. 7.1 i) is attached to the applicator (Fig. 7.2 j). Then, the position of the applicator is tracked and displayed on the navigation screens installed in the OR (Fig. 7.1 d). The oncologist uses the pointer tool (Fig. 7.1 h) to acquire the location of the edges of the tumor bed for evaluation purposes (Fig. 7.2 k). Finally, the applicator is placed over the tumor bed (Fig. 7.2 l) and fixed to the surgical bed in a steady position. The procedure is documented (Fig. 2 m) and the linear accelerator is introduced into the OR to perform the docking and the treatment dose-delivery (Fig. 7.2 n).

Furthermore, we designed a survey to evaluate the level of satisfaction of the surgical team with the navigation solution, the improvement to the routine clinical practice and the effect of the patient's CT image, displayed on the installed OR screens, during the procedure. We surveyed nurses, radiation oncologists, surgeons and the linear accelerator technicians. Moreover, we asked them to identify possible procedure complications derived from the navigation workflow steps (Fig. 7.2, yellow).

7.4 Results

From July 2013 to February 2014, twelve cancer patients were included in the evaluation of the navigation protocol. Primaries were: gastro-esophageal cancer (3), retroperitoneal sarcoma (2), colon-cecal (1), rectal (2), oligorecurrent ovary (1), breast cancer (1), chondrosarcoma (1) and sacral chordoma (1). Anatomical sites from surgical approach were: thoracic cavity (3), upper

abdomen (3), pelvic cavity (3) and semi-deep-sited tumors (non-cavity sites) (3). A summary of the lesions localization is depicted in (Fig. 7.3). Table 7.1 summarizes the clinical and IOERT treatment parameters for each case. Each selected patient was treated by a different surgical and oncological team to include a wide variety of experts during the evaluation of the navigation system.

The CT acquisition, image to patient registration and applicator navigation steps were performed in the twelve clinical cases. The duration of the standard IOERT procedure was increased by approximately 15 min using Navigation (10 min. for registration purposes and 5 min. for the navigation feasibility assessment). In all cases, the applicator position over the tumor bed was displayed on the screens and verified by the radiation oncologist, matching the

		IOERT Treatment related parameters			
Surgical Approach	**Clinical Parameters**	**Applicator Size (cm)**	**Applicator Bevel (deg)**	**Energy (MeV)**	**Total Dose (cGy)**
Intra thoracic	Distal esophagus (cT3Nx)	5	30	10	1000
	Distal esophagus **(*)** (cT3Nx)	6	45	12	1250
	Gastro-esophageal junction **(*)** (cT2N1)	5	30	8	1200
Intra abdominal (Upper)	Retroperitoneal sarcoma (13 × 12 × 7 cm primary)	*No IOERT: no malignancy*			
	Retroperitoneal sarcoma (13 × 12 × 5 cm recurrent)	10	30	10	1250
	Colon-cecal (pT4pN1)	8	0	6	1250
Intra abdominal (Pelvic)	Rectal cancer (cT2cN1)	8	15	6	1250
	Rectal cancer **(*)** (cT3cN1)	5	45	10	1250
	Oligorecurrent ovary (Ø 3 cm)	7	15	8	1500
Semi-deep seated	Breast (cT1cNx)	5	15	6	1000
	Chondrosarcoma inguinal	7	30	8	1250
	Sacral chordoma	15	45	10	1500

Table 7.1: IOERT and clinical parameters of each tested procedure **(*)** Cases where the size of the tumor bed was measured using the navigation setup and the tracked pointer for further analysis.

pre-planned IOERT procedure without any additional complications for the surgical team. Furthermore, the complete navigation protocol was documented with pictures and videos for further analysis of each procedure (Fig. 7.2).

The size of the tumor bed was measured (Table 7.2) using the tracked pointer (Fig. 7.2 k) and compared to the chosen applicator size in three different cases (Table 7.1 **(*)**) for evaluation purposes. Summarized results are shown in Table 7.2, showing a similar tumor bed size of ~3 cm × 3 cm on each case. The chosen applicator diameter for each case was different. However, the size of the

treatment radiation beam was similar due to the prescribed applicator bevel angle.

Surgical Approach	Clinical Parameters		IOERT Treatment related parameters: Applicator Size (cm)	IOERT Treatment related parameters: Applicator Bevel (deg)	Tumor Bed Size: Longitudinal (cm)	Tumor Bed Size: Axial (cm)
Intra thoracic	Distal esophagus	(cT3Nx)	6	45	3.30	3.30
	Gastro-esophageal junction	(cT2N1)	5	30	3.13	3.02
Intra abdominal (Pelvic)	Rectal cancer	(cT2cN1)	8	15	3.17	3.20

Table 7.2: Used applicator size and bevel angle compared to the tumor bed size measured using the navigation system for the three evaluation cases.

Figure 7.4 summarizes the results from the evaluation survey. The most appreciated enhancement of the navigation system by all the evaluated team members was the displayed CT image of the patient. Also, note that most of the evaluations were positive with the proposed navigator, (i.e., an improvement to the everyday clinical practice and a positive level of satisfaction). Regarding the complications, the surveyed professionals reported the following issues: the need for surgical team training using the navigator (oncologists), the increased surgical time (surgeons and nurses), the need for accuracy measurements of the applicator placement (oncologists) and the need for a larger OR (nurses). On the other hand, no patient risk or additional surgical complications were encountered during any of the interventions.

Figure 7.5 shows three examples of the performed IOERT navigation. This figure depicts the complexity of the IOERT environment which demands the involvement of a large multidisciplinary team. In (Fig. 7.5 a, b and c) a retroperitoneal sarcoma was treated. Figure 7.5 (a) shows the real-time applicator position provided by the navigation system on the TPS screen. Figure 7.5 (d, e and f) show three other cases involving different surgical and oncological teams.

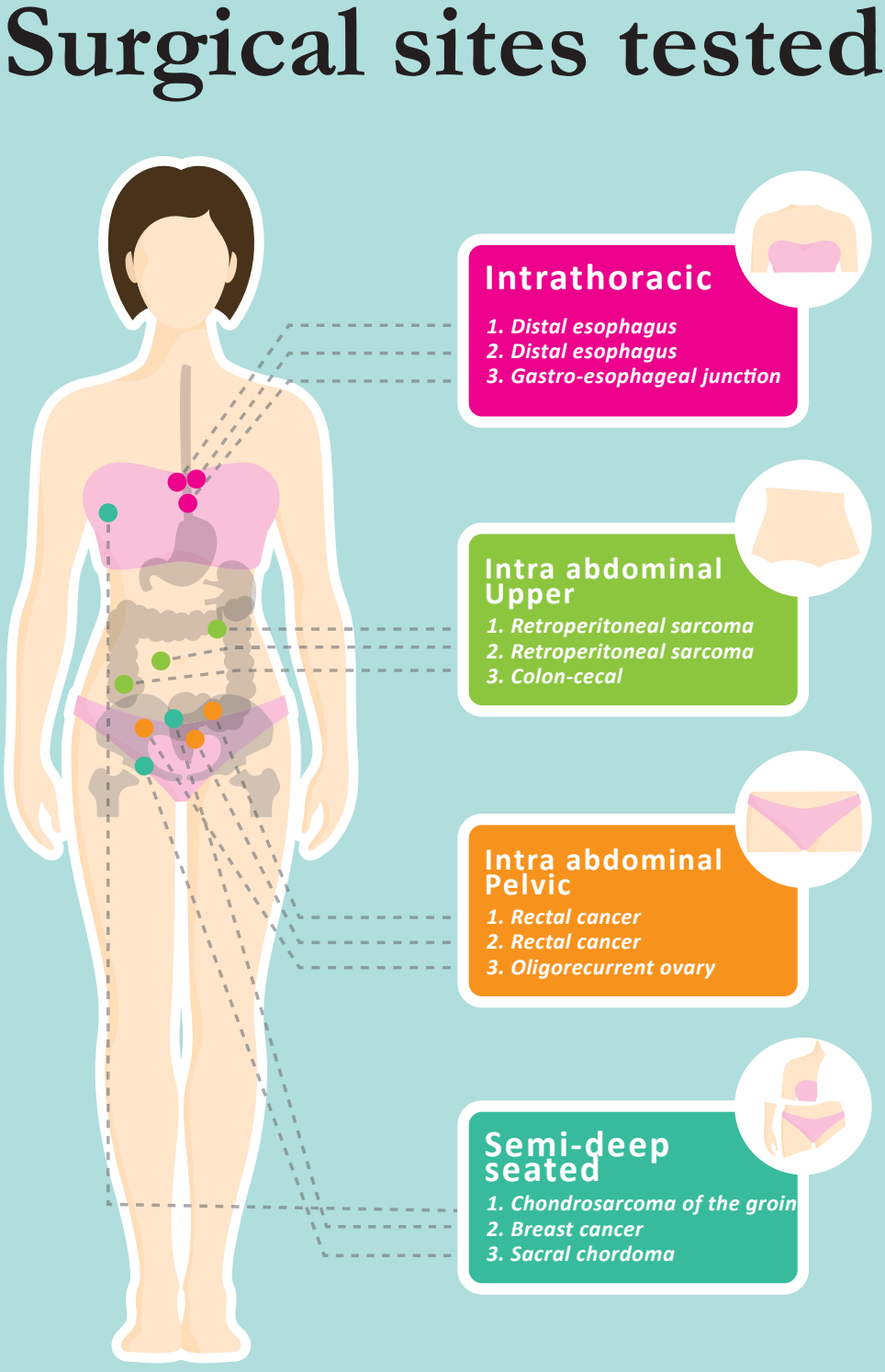

Figure 7.3: Surgical sites and cancer types of the patients who were included in the evaluation of the navigation protocol.

Satisfaction Survey

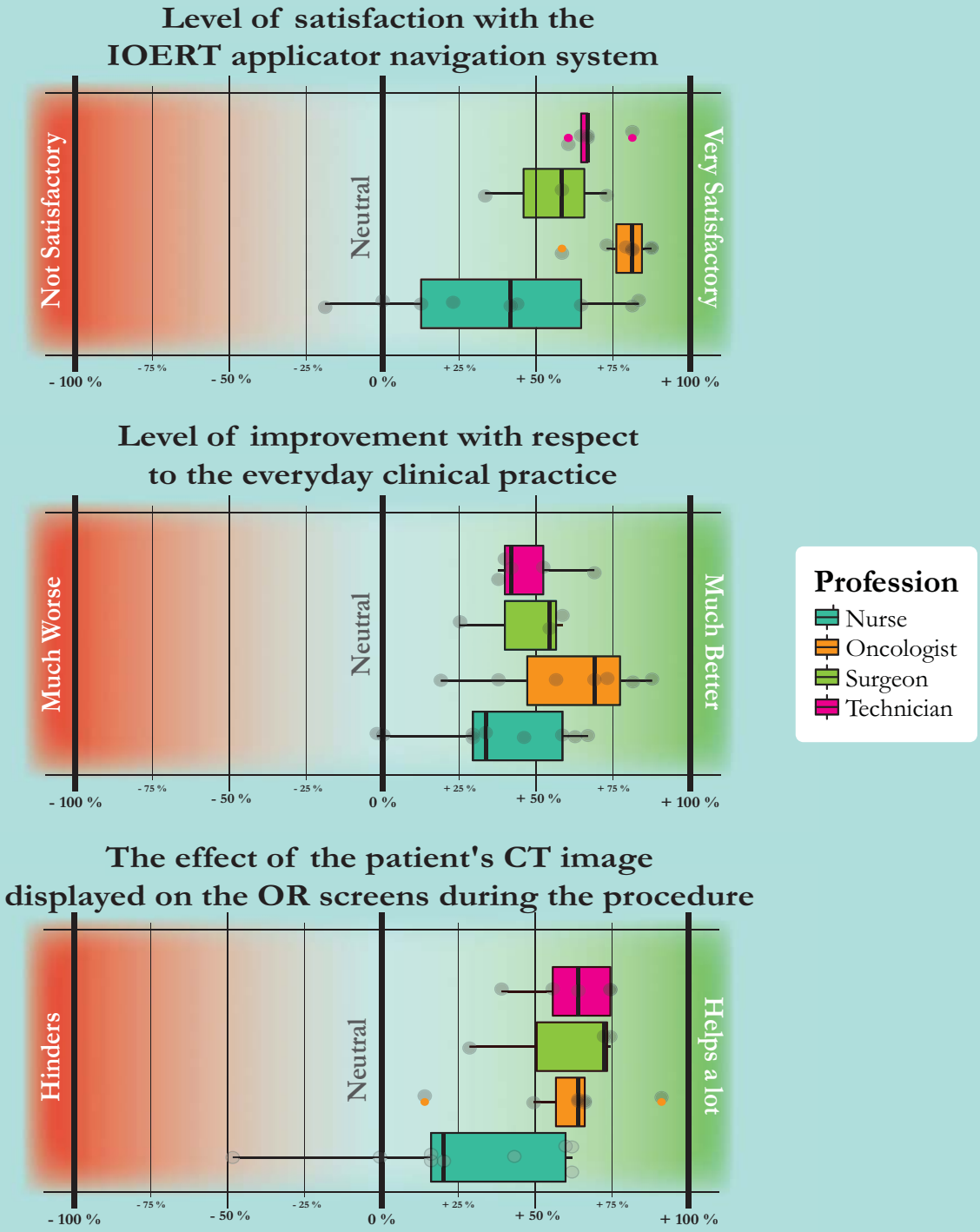

Figure 7.4: Satisfaction of the IOERT team (nurses, oncologists, surgeons and radiation technicians) with the image-guided solution.

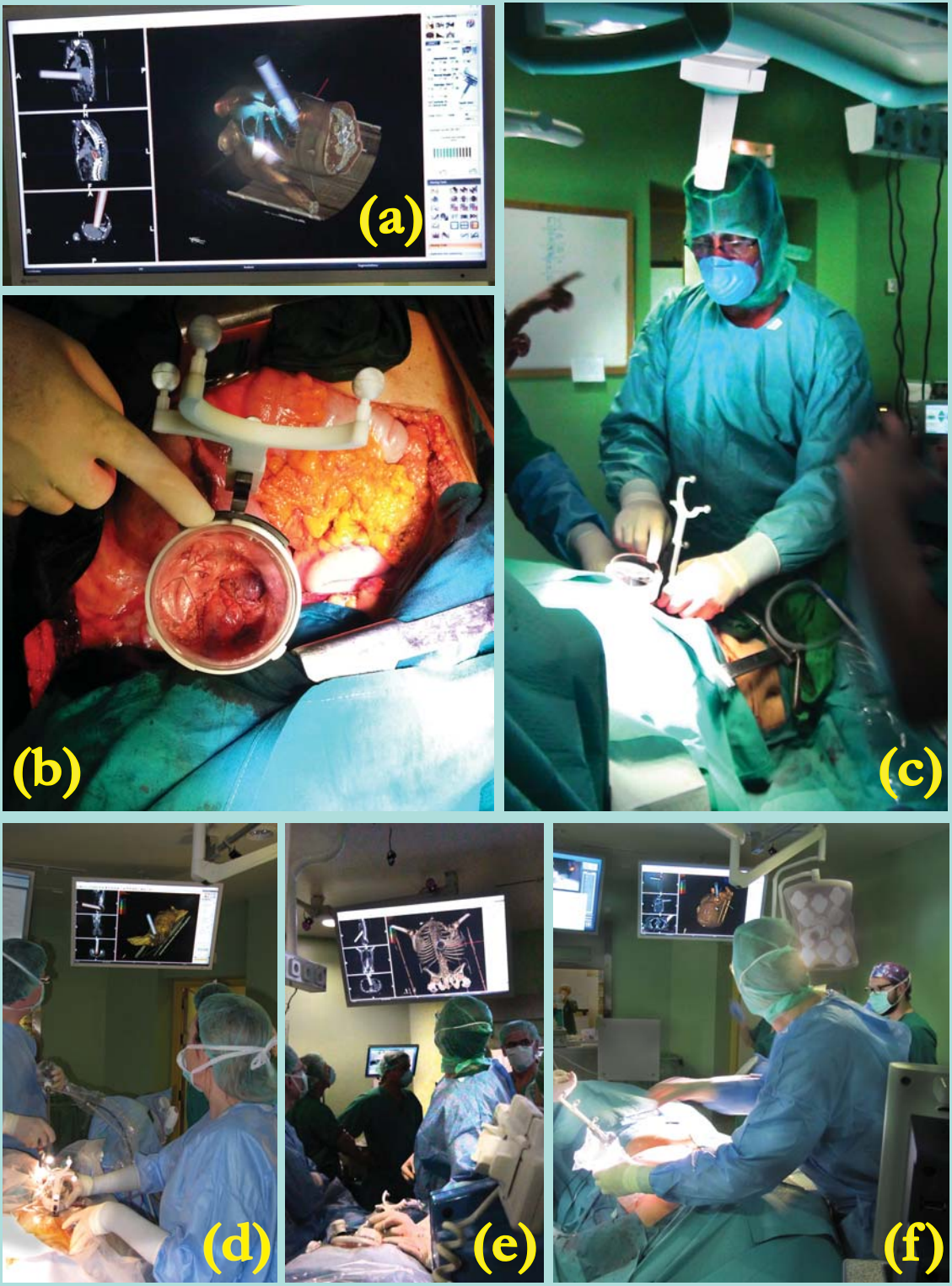

Figure 7.5: Example of the image-guided IOERT procedures performed. Retroperitoneal sarcoma: **(a)** treatment planning system showing the guided collimator, **(b)** applicator placed over the tumor bed and **(c)** radiation oncologist positioning the image-guided applicator. **(d)** Rectal cancer. **(e)** Gastro-esophageal junction. **(f)** Breast cancer.

7.5 Discussion and Conclusion

We presented a navigation protocol based on optical tracking for the support of IOERT procedures during the applicator placement in order to follow the planned treatment. To the best of our knowledge, this is the first reported experience of clinical IOERT navigation procedures using a mobile unit inside an OR. The protocol demonstrated to be feasible in a clinical environment adding ~15 min to the standard procedure time. Furthermore, no safety risks for the patient or additional complications for the surgical team were found during the clinical evaluation.

The IOERT tracking environment is prone to occlusions due to the many involved agents during the procedure. However, the proposed navigation system based on a multicamera optical tracker demonstrated robustness given the tested working volume while maintaining the tracking capabilities during all the assessed operations. In some cases, we found that the movement of the surgical lamps during surgery needs to be limited to avoid collisions with the tracker cameras that would spoil the tracker calibration.

From a clinical standpoint, the procedure was found to be safe and feasible. Important ways to improve the navigator implantation during clinical practices were related to the training of the surgical team and the need of a larger OR. Also, the clinical team reported the need for system accuracy measurements in real-time. Showing difference metrics from the planned to the true guided applicator position could overcome this limitation. However, regarding our objective for a first assessment of the system, the surgeons and oncologists did not report any limitation during the included IOERT workflow. Of utmost importance, the anatomical information presented on the navigation screens was found very helpful by the clinicians during surgery and applicator positioning (Fig. 7.4).

An important limitation of the navigation system is the increased duration (~15 min) of the surgery, and the need for a presurgical CT scan of the patient. The CT scan must be acquired in surgical body position because that is required for tracker-to-patient registration. However, it is also necessary for the treatment planning since dose estimation is based on the anatomical structures position with respect to the applicator position [176]. Also, note that IOERT is a multidisciplinary procedure, where surgeons and oncologist work closely to adapt the course of action to the patient and the pathology. The possibility of planning the procedure prior to the surgery under this collaboration may lead to

a reduction of uncertainty during the dose delivery that could be beneficial to the clinical approach. Finally, when the oncologist needs to modify the treatment parameters, the applicator position provided by the navigator would allow the recalculation of the dose distribution *in situ*. This could help clinicians to adapt the procedure. [28]. Moreover, surveyed professionals reported a positive effect of displaying this CT image during the procedure. All these advantages would justify the acquisition of an IOERT pre-operative CT scan.

Another limitation detected is the localization of the registration fiducials at surgical time. If the registration is performed at the beginning of the procedure, a risk of misregistration due to any surgical bed movement exists. However, if localization is obtained just before the guidance, the sterility of surgical area could be compromised. This limitation can be overcome using a tracked reference tool attached to the patient's anatomy. However, this reference should be adapted to every single procedure in terms of the surgical area or involved anatomical structures, which may not be trivial. This instigates further investigation of the registration methodology. While it seems that using line-shaped fiducials reduces the acquisition time in the OR, alternative registration approaches must be explored to preserve the sterile conditions while preserving accuracy. Other tracking techniques such as surface scanning could be a solution [166], [177].

From a technical standpoint, we designed a suitable and safe wiring installation over the OR's ceiling connecting all the navigation elements such as the control computer, the tracker, surveillance recording cameras and the navigation screens. This approach safeguards the sterile conditions of the OR, clears the space for surgical operation and can be reproduced in any similar IOERT dedicated OR.

The IOERT navigation system demonstrated to be clinically feasible, showing the applicator localization over the patient scan and enabling the recalculation of the estimated dose distribution *in situ*. We assessed the system feasibility and reported no complications in twelve clinical cases with different anatomical localizations and involving distinct surgical teams. The proposed navigation system addresses the applicator placement uncertainty issue and provides valuable data for the IOERT community. Furthermore, the presented work also raises important considerations for the true implementation of a navigation system into the IOERT complex environment such as the need for the surgical team training, or the implementation of real-time accuracy metrics to advice the clinicians.

8

Discussion and Conclusion

8.1 Discussion

Even though IOERT has been clinically applied only during the last three decades, the promising results from clinical studies and the scientific evidence in the literature [178] validate this technique for the treatment of a wide variety of cancer types. Nowadays, IOERT is noticeably based on the experience of the radiation oncologist who must decide a considerable number of parameters in situ (i.e., field size, beam energy, protections, applicator specifications). Technological progresses including the appearance of IOERT-specific treatment planning systems (TPS) and mobile linear accelerators have facilitated the implantation of IOERT programs in a great number of hospitals around the globe. IOERT TPS has enabled physicians to optimize the procedure in advance and minimize the stress during parameter selection inside the OR. Finally, availability of a mobile linear accelerator avoids transferring the patient to a dedicated radiation room. These examples reflect the strong connection of technology enhancement and IOERT procedures. However, these advances also introduce new challenges in the IOERT process that should be addressed for an accurate and safe dose delivery to the patient. For instance, the IOERT radiation collimator placement over the tumor bed requires a validation methodology to ensure correct delivery of the prescribed dose distribution previously planned in the TPS. The main objective of this Thesis was to explore technological and procedural alternatives to improve the IOERT outcome.

In this context, we focused our research on three IOERT limitations identified in the literature: applicator positioning over the tumor bed, docking of the linear accelerator gantry with the applicator, and validation of the prescribed dose delivery [16], [27], [28], [35], [75]. Image-guided techniques are being widely used in the EBRT field for several applications such as patient setup verification, radiation-beam gating by respiratory motion and assessment of brachytherapy seed placement [43]–[48]. In this work, we employed image-guided techniques to construct a guidance framework adapted to IOERT procedures.

We developed the first IOERT-specific navigation system to help during the radiation applicator placement task inside the OR. For that purpose, we studied a multicamera optical tracker in terms of accuracy and reliability considering the particular requirements of IOERT clinical environment such as a large working volume. We proposed an image-to-tracker registration algorithm that improves current alternatives in terms of speed and accuracy. We explored intraoperative imaging techniques such US and CBCT C-arm to enhance navigation with updated information during surgery. Furthermore, we developed a guidance system for driving the mobile linear accelerators reducing time and increasing safety of the docking task. Finally, we investigated possible drawbacks during a potential technological transfer of the navigation system to a true clinical environment. We would like to remark the multidisciplinary aspect of this Thesis. Every member of the IOERT surgical team was involved in the presented research work with the aim of identifying possible limitations and gathering relevant information that may facilitate the technological transfer of this work to the true clinical practice.

The introduction of navigation into the IOERT workflow requires an upgrade of the clinical protocol with specific processes such as the acquisition of a preoperative CT scan in surgical position for dose delivery estimation, the registration of the tracker to the patient's anatomy or the verification of the tracking reliability during the procedure for quality assurance. However, from an IGI standpoint, IOERT OR is a very complex scenario due to occlusions, space limitations, involved equipment and the great variety of target localizations.

Our results confirmed the robustness against occlusions of the chosen tracker (OptiTrack), very important issue in this type of environments. We found that occlusions affect the tracking error distribution inside the working volume increasing the number of outliers. This points out the importance of a well stablished methodology for the evaluation of multicamera optical trackers

that must consider the three-dimensional dependency of the tracking error on the spatial configuration of the sensors. This error is not equally distributed inside the working volume. However, the flexibility of the spatial configuration of the cameras makes this tracker appropriate for any OR demanding a large working volume. Regarding the system accuracy, OptiTrack demonstrated a tracking error of 0.24 ± 1.05 mm (mean ± std) for the positioning of a single reflecting marker which was found fair for the IOERT application –where margins are 2-4 cm surrounding the tumor bed to be irradiated [28]. Furthermore, we considered the system calibration in a clinical environment and proved that any miscalibration can be detected thanks to the high sensitivity of the tracker. We think that this characteristic —typical of multicamera optical trackers- must be taken into consideration when assessing this system in any surgical environment for safety reasons. Our evaluation was the first one reported in the literature using a robot as gold standard for this tracker, for which limited experience is found in the literature with IGI applications [54], [57], [59]; however, we established important considerations for future evaluation of multicamera optical trackers.

Regarding the investigation of intraoperative imaging for IOERT guidance, we assessed a multimodal image-guided system that combines the 3D US and the CBCT C-arm imaging techniques. In this context, the introduction of a tracker permits the acquisition of 3D US which may be easily interpreted for the correct placement of needles inside the anatomical structures. It is known that there are commercially available 3D probes, but they are expensive and usually dedicated for diagnostic purposes. Note also that the introduction of tracking in this context facilitates the fusion of more information sources such as the preoperative CT scan —where the IOERT dose delivery is planned-, the position of the applicator or intraoperative imaging data, such as the evaluated CBCT C-arm. This latter modality could be used for recalculating the dose estimation according to possible anatomical changes during surgery. Although the achieved divot-based registration performance showed elevated TRE values (TRE ~ 3 mm), we also explored the potential use of image-based techniques that demonstrated its feasibility for solving this problem in future applications. In fact, metrics such as NCC or NMI could be combined to provide a fair registration accuracy in the IOERT surgical context.

Image-to-world registration is one of the main error sources during IGI applications. Common registration algorithms for IGI are based on point fiducials and applied to rigid structures such as bones or skull where IGI are more widespread. However, for applications where the field of interest is larger

and/or the number of possible anatomical localizations is bigger, a general registration solution is not trivial. In that sense, we proposed and validated a new registration algorithm for line-shaped fiducials that decreases the acquisition time during surgery and improves the accuracy of the registration. The proposed registration algorithm (LBR) demonstrated a better performance in comparison to ICP, AICP and CPD alternatives. For the studied volume of interest, we found twelve fiducials to provide a fair registration performance. LBR demonstrated to be robust against FLE and anisotropy which ensures an adequate outcome for the proposed IOERT navigation system. Furthermore, we assessed the registration in the region of interest instead of in a single point, pointing out the importance of the revision of the evaluation methodology of registration algorithms for IGI applications. In that sense, we measured TRE with its spatial dependency and provide a summary metric for further comparisons in the literature.

With respect to mobile linear accelerator docking, we identified the driving process as a problematic issue in commercially available devices. Radiation technicians at Hospital Gregorio Marañón call attention to this cumbersome task when using the studied device (LIAC 12, Sordina, Italy) in the OR. In the literature, this issue has been addressed for devices with soft-docking techniques [22], [36], [38], [39]. However, this is the first work that deals with this problem for devices that use hard-docking techniques. The solution proposed in this Thesis for docking aid demonstrated its feasibility and a reduction in the time required during our experiments compared to the manual driving procedure. Our docking-navigation solution requires an initial calibration process. Nevertheless, for an effective installation in the true IOERT environment this calibration could be performed in advance by the manufacturer to avoid further error during docking aid. Furthermore, the introduction of stepper motors in a future design of the mobile LINAC could increase the accuracy and automatize the docking process.

All the contributions presented in this Thesis demonstrated its feasibility and good performance in the IOERT context. However, installation of the navigation system in a real OR brings technical concerns such as the physical installation of the required navigation components that we also addressed. We described the cabling, screens, tracker and control computer installation of the navigation system pointing out the importance of sterilization in this environment and demonstrating the feasibility using the IOERT navigation system in a real OR.

One main concern for IGI is the presentation of guidance information to the clinicians. This Thesis emphasized the importance of informing the clinicians about the different error sources that contribute to the final accuracy of the navigation system such as the registration or the tracker. Since the clinician is the maximum responsible of the procedure, we think that this information is crucial during any IGI application. Quantitative measurements of error and uncertainty must be provided for a reliable use of navigation system and should be included during clinical trials in regards to the accepted error margins for every specific application. For the proposed navigation system, a possible solution could use augmented reality to enhance the physician experience during surgery. Some authors use sound signals to inform the user about the distance of tracked tools from certain surgical targets [179], [180]. That approach could improve the guidance of the applicator positioning in combination with the guidance screens for dose-delivery presentation in the IOERT OR framework.

Because of the multidisciplinary aspect of IOERT, we also evaluated the navigation system in a clinical context and questioned all the members of the surgical team: radiation oncologists, surgeons, nurses and radiation technicians. Most users agreed on a positive evaluation of the navigation system in terms of guidance help during the procedure. However, the surgical nurses team reported the need for a larger OR and their concerns about sterilization issues for a clinical navigation system installation.

Limitations of the presented work include the revision of the design of the rigid-body for the applicator tracking. Results showed that the tracking accuracy was lower for our design than for the rest of tested tools. To address this issue, some authors proposed optimal methodologies for rigid-body design; however, the size of the applicator is different on each case and a solution for all cases should be deeply studied. On the other hand, the registration performance also presents some constrains such as the tissue deformation during surgery. LBR was proposed for rigid-based registration which is not adequate for handling large deformations of the registered geometries. Our work was made under the assumption of small changes in the tumor bed after the resection —where the true dose is delivered- expected to be constant along the surgery. However, small motions in nearby soft tissues or respiration could increase the uncertainty of the guidance. Surface scanners or intraoperative imaging (US or CBCT C-arms) could solve this issue updating the patient's anatomy in the TPS. However, the combination (registration) of this information with the preoperative IOERT plan should be studied in detail in order to propose an accurate solution.

Finally, the main contributions and conclusions of this work are summarized in the following section.

8.2 Conclusions

The OptiTrack 8-camera optical tracker was evaluated in terms of miscalibration sensitivity, accuracy, camera occlusions and tool detection in a feasible clinical setup that covers a wide range of IGS applications and scenarios.

- The system accuracy is suitable for IGS navigation [with a percentile 99 tracking error of 0.08 mm inside the whole working volume (300 × 500 × 400 mm)]
- An appropriate working volume design is needed to ensure an occlusion-robust IGS tracking due to the dependence of system accuracy on occlusions.
- The tracked tools' rigid bodies pattern affects the localization accuracy of the tools
- Miscalibration sensitivity of the system is high [~30 mm/deg and the maximum rotation threshold was 0.16 ± 0.09 degrees].
- Calibration reliability is stable over 5 consecutive days in a controlled tracking environment [tracking error of 0.25 ± 0.26 mm]
- The proposed miscalibration detection protocol for multicamera optical trackers is feasible for clinical uses and satisfies the requirements of automaticity and speed of IGS applications.

◊

We proposed and validated a new algorithm, line-based registration (LBR) that increases redundancy and reduces tracker acquisition time for image-to-world registration.

- The LBR algorithm has a lower TRE [TRE < 10^{-1} mm on more than ~15% of the target volume] than ICP, AICP and CPD and the best performance when using 12 line-shaped fiducials.

◊

We demonstrated the feasibility of integrated free-hand 3D ultrasound and mobile C-arm CBCT for needle-based procedures in phantom studies using a low-cost US probe.

- The integrated US-CBCT system has a needle-tip localization accuracy < 3.0 mm using fiducial- and image-based registration.
- We presented the first image quality assessment for the Interson Vascular Access Probe VC 7.5 MHz showing a fair performance for needle-based interventions up to ~60 mm depth of the surface.

◊

We presented the first navigation solution based on optical tracking that computes the movements needed for the LIAC mobile unit to correctly align the applicator and the radiation gantry during the docking process.

- The docking navigation system improves safety, reduces procedure time and is feasible for clinical scenarios.
- Mean docking time using the presented system is 3:40 min in a clinical scenario
- The developed user interface software performs the calibration and docking guidance successfully.

◊

We proposed the first IOERT navigation system based on optical tracking and demonstrated its feasibility in twelve clinical cases with different anatomical localizations and involving distinct surgical teams.

- The navigation system safeguards the sterile conditions of the OR, clears the space for surgical operation and can be reproduced in any similar IOERT dedicated OR.
- The navigation protocol adds ~15 min to the standard IOERT procedure time.
- The designed wiring installation that connects all the navigation elements in the OR is suitable and safe for clinical use.
- Major concerns of the IOERT surgical team are: need for larger OR, sterilization and training.
- The grand majority of involved IOERT surgical teams agreed on a positive evaluation of the navigation system in terms of guidance help during the procedure.

8.3 Possible future lines of research derived from the present work

Several possible lines for future improvements of the work presented here still remain open:

- Optimization of the spatial arrangement of the OptiTrack cameras in a surgical environment considering factors such as: the size of the OR, the surgical devices (lamps and anesthesia support) and development of a continuous miscalibration protocol in order to ensure the maximum tracking accuracy during all the operation.
- Investigate a feasible methodology for the optimal design of optically tracked tools.
- Improve LBR algorithm to address anatomical deformations and their effect on the registration performance for IOERT procedures in terms of dose distribution deviations.
- Explore intraoperative imaging techniques such as 3D-US and surface scanning in the IOERT context to update surgical information into the TPS for dose distribution estimation during surgery.

9

Software contributions summary

This Chapter describes the most important software contributions that were developed during this thesis. The first part is related to the integration of the multicamera optical tracker (OptiTrack) with the most known open-source platforms for image-guided applications in the literature. The second part focuses on the user interface applications within the *3DSlicer* framework (Brigham and Women's Hospital, Boston MA) [146]. Finally, the third part summarizes miscellaneous contributions to the open source community developed in the context of this PhD Thesis.

9.1 Optitrack tracker integration for image-guided applications

NaturalPoint [60] trackers include different solutions depending on the end application. For multicamera optical tracking, Flex, Prime and Slim camera series are offered. These systems need a calibration regarding the spatial configuration of the cameras in the working volume. V120:Trio and V120:Duo models offer compact tracking solutions that do not require a calibration step but have a limited tracking volume.

OptiTrack is controlled by *Motive* optical motion capture software which can communicate to the Unreal [181] and Unity [182] engines. However, for developing specific applications for which raw tracking information is required, NaturalPoint provides an API (Application Programming Interface) in the form of already compiled **C++** and **C#** libraries –only for Windows™ systems. In particular, image-guided applications require specific software functions and processes in order to provide a safe tracking environment for surgical use. OptiTrack's API does not currently provide this safe support.

The research community demands open-source software tools that improve accessibility, usability and reproducibility of novel methods and algorithms. This permits fair comparisons among new and stablished methodologies and promotes the validation of new developed software. Nowadays, this philosophy is encouraged by the increasing number of journals that demand open-source code and data [183]–[185]. Specifically, IGI applications have strongly benefited from this tendency. Several software platforms and frameworks have been developed that include most of the classic and newest methods and algorithms and solve particular IGI requirements (e.g., support of complex clinical workflows, integration of different kinds of hardware and data, real-time processing of data, high robustness).

The most known IGI software platforms are: Medical Imaging Interaction Toolkit (*MITK*, German Cancer Research Center, Heidelberg, Germany) [186], [187], *3DSlicer* (Brigham and Women's Hospital, Boston MA) [146], Public software Library for UltraSound imaging research (*Plus*) [138] and Image-Guided Surgery Toolkit (*IGSTK)* [188]. These platforms can connect to most available commercial trackers (optical, magnetic and inertial) making IGI application development easier and faster than doing it from scratch. However, newer trackers like OptiTrack are currently not supported by those frameworks, complicating the research of IGI applications using this tracking system.

In this thesis, the studied IOERT tracking environment motivated the use of OptiTrack multicamera optical tracker because of its specifications. Thus, given the previously mentioned advantages of open-source tools, NaturalPoint API was integrated with these frameworks. The following sections describe each software integration to add OptiTrack support to *MITK*, *3DSlicer*, *Plus* and *IGSTK*.

9.1.1 BiiGOptitrack library

OpenIGTLink (Brigham and Women's Hospital, Boston MA) [168] provides a standardized mechanism for communication among computers and devices in operating rooms for wide variety of IGT applications. It aims to provide a plug-and-play unified real-time communications (URTC) in ORs for image-guided interventions, where imagers, sensors, surgical robots, and computers from different vendors work cooperatively. This URTC will ensure a seamless data flow among those components and enable a closed-loop process of planning, control, delivery, and feedback. *OpenIGTLink* is suitable for both industrial and academic developers and provides a reference implementation of the protocol as a `C/C++` library.

One key concern when trying to control a tracker hardware for clinical applications is the error handling necessary to provide software recovery methodologies for patient' safety reasons. Hence, the *BiiGOptitrack* library [167] was developed to interface with the manufacturer's API for any potential surgical applications. *BiiGOptitrack* follows the standard tracking interface defined by the *OpenIGTLink* protocol and allows the tracker connection, tracked tools management and safe error recovery during tracking acquisition. The library is based on Insight Toolkit (*ITK*) [189] for the thread and object management and is composed of two main classes: `OptitrackTool` and `OptitrackTracker`. The former represents any tracked object in the applications while the latter includes tracker specific functionalities such as calibration file loading and camera settings (illumination, thresholding and exposure parameters).

9.1.2 MITK Integration

The Medical Imaging Interaction Toolkit (*MITK*) [186] is a free open-source development environment for medical image processing created by the German Cancer Research Center (DKFZ, Heidelberg, Germany). *MITK* combines the Insight Toolkit (*ITK*) [189] and the Visualization Toolkit (*VTK*) [190] with an application framework. As a toolkit, *MITK* offers features that are relevant for the development of IGI software: handling and processing medical imaging data, concepts for processing of tracking data and support of commercial tracking devices. The tracking layer offers an interface for tracking and holds classes with established connection to tracking devices. Supported trackers are: Polaris (Northern Digital Inc.), Aurora (Northern Digital Inc.),

MicronTracker (Claron Technologies) and Microbird (Ascension Technology Corporation). In this work, the implementation of the necessary classes for the inclusion of OptiTrack trackers into the *MITK* navigation layer was also developed for *MITK* users and uploaded to the public *MITK* repository.

9.1.3 Plus Integration

The Public software Library for UltraSound imaging research (*Plus*) [138] is an open-source software toolkit for data acquisition, pre-processing, and calibration for navigated image-guided interventions developed by the Laboratory for Percutaneous Surgery (PerkLab) at Queen's University (Ontario, Canada). *Plus* was originally developed for ultrasound-guided interventions and it contains all essential functions for implementing tracked ultrasound systems, but it is now widely used in many types of IGI applications reported in the literature, even when no US support is necessary. *Plus* supports generic tracking devices and inertial sensor units such as Aurora, MicronTracker, Polaris or Phidget sensors (Phidgets Inc., Alberta, Canada). Implementation for the support of the OptiTrack system was also developed for this toolkit adding two extra classes and defining the specific configuration files for easy use.

9.1.4 IGSTK Integration

The Image-Guided Surgery Toolkit (*IGSTK*) [188] is a high-level, component-based framework that provides a common functionality for image-guided surgery applications. The framework is a set of high-level components integrated with low-level open source software libraries and APIs from hardware vendors. *IGSTK* is supported by Kitware (New York, USA) [191], company that builds their own open-source platforms and provides flexible software products. For instance, the *ITK* [189] and *VTK* [190] toolkits that are widely used in the medical imaging and IGI research community are coded by Kitware.

The cornerstone of *IGSTK* [188] is robustness. *IGSTK* provides the following high-level functionalities: the ability to read and display medical images, including CT and MRI in DICOM format; an interface for common tracking hardware (e.g., Aurora from NDI); a general user interface (GUI) and visualization capabilities, including four-quadrant view (axial, sagittal, coronal, and 3D) and multi-slice axial view (from 1 x 1 to many by many, such as 10 x 10); point-based registration; and robust common internal software services for

logging, exception-handling, and problem resolution. In this context, enabling support for OptiTrack tracker within the *IGSTK* framework was also an important contribution of this thesis, making NaturalPoint's trackers accessible to the wider research IGI community.

9.2 *3DSlicer* Modules

3DSlicer [146] is an open-source software platform for medical image informatics, image processing, and three-dimensional visualization. Build through support from the National Institutes of Health and worldwide developer community, Slicer brings powerful cross-platform processing tools to physicians, researchers and the general public. The major developers are Kitware and the PerkLab amongst others. Specifically, *SlicerIGT* is an extension of *3DSlicer* for IGI procedures that allows the connection with tracker devices through *Plus* library or *IGSTK*.

Two modules were implemented in the *3DSlicer* framework in order to provide a user interface to two main contributions of this thesis. On one hand, we developed a module for the Interson US probe (Interson VC 7.5 MHz, Pleasanton CA) connection, described in Chapter 5. On the other hand, the proposed solution for the docking of a linear accelerator aid was implemented as another *3DSlicer* module (Chapter 6).

9.3 Line Based Registration Algorithm

Python [192] is a high-level programming language for general-purpose programming released for the first time in 1991. This language is based on interpreters so it can run in almost any existing operating system. CPython, the core implementation of Python, is open-source and is managed by the non-profit Python Software Foundation. Nowadays, Python has become one of the most extensively used languages in the research community. This is mainly due to the extensive set of libraries that deal with frequently occurring problems such as optimization, data visualization, data processing and statistics.

The proposed and validated LBR registration algorithm (Chapter 4) was implemented using the *Scipy* [193], *Matplotlib* [194], *Pandas* [195] and *Numpy* [196] packages (Python libraries). This code is made available for the community

following the philosophy of open-source based research in order to provide an easy and comprehensible manner of using the proposed registration algorithm.

9.4 Others

9.4.1 Python OpenIGTLink

An additional contribution of this thesis is the development of a Python package that provides the implementation of the standardized *OpenIGTLink* protocol for sending and receiving tracking information through different computers. This library can be used for testing purposes (e.g., when the user has no access to a true tracker and needs to simulate a running tracking system connected to the *Plus* library). Note that this package can also simulate potential tracking errors. Consequently, the user can isolate the software development for different software modules of a navigation system. Thereby, enhancing the performance and reducing the time needed during the testing phase –which is very important for IGI navigation systems. It is also made available for the research community through a github repository [197].

9.4.2 Interson Probe Wrapper

In Chapter 5, an Interson Vascular Access Probe VC 7.5 MHz (Interson, Pleasanton CA) (Fig. 5.1 a) was used for the US-CBCT integration. The Plus toolkit was used to interface the probe with the manufacturer's SDK (Software Development Kit). Internally, Plus uses a software wrapper that permits the Plus toolkit (**C++**) to call the probe's SDK functions (**C#**) [147]. However, this wrapper does not allow real-time acquisition of ultrasound images. This work contributed such functionality to the wrapper and can be found in the most recent version of the code in [147].

10
Publications

10.1 Related to this thesis

10.1.1 Articles in peer-reviewed journals

[10.1.1.1] E. **Marinetto**, A. Uneri, T. de Silva, S. Reaungamornrat, W. Zbijewski, A. Sisniega, S. Vogt, G. Kleinszig, J. Pascau and J. H. Siewedsen, "Integration of free-hand 3D ultrasound and mobile C-arm cone-bean CT: Feasibility and characterization for real-time guidance of needle insertion," Computerized Medical Imaging and Graphics., **2017**

[10.1.1.2] E. **Marinetto**, V. García-Vázquez, F. A. Calvo, M. Muñoz, F. J. Serrano, M. Desco and J. Pascau, "Image-guided Navigation for Intraoperative electron radiation therapy. Pilot clinical study," Int. J. Radiation Oncology, Biology, Physics., **2017** [**Under review**. Submitted 11th Apr 2017]

[10.1.1.3] E. **Marinetto**, D. García-Mato, A. García, S. Martínez, M. Desco and J. Pascau, "Multicamera optical tracker assessment for computer aided surgery applications," IEEE Transactions on Automation Science and Engineering., **2017** [**Under review**. Submitted 21st Feb 2017]

[10.1.1.4] E. **Marinetto**, J. G. Victores, M. García-Sevilla, M. Muñoz, F. A. Calvo, C. Balaguer, M. Desco and J. Pascau, "Mobile accelerator guidance during docking steps in IOERT procedures using an optical tracker," Medical Physics. **2017** [**Under Review**. Submitted 22nd Feb 2017]

[10.1.1.5] E. **Marinetto**, J. F. P. J. Abascal, J. M. Mateos, M. Desco and J. Pascau, "Line-Based Registration. A new image-to-world registration strategy for image-guided interventions," Medical and Biological Engineering and Computing. **2017** [**Under Review**. Submitted 9th Feb 2017]

[10.1.1.6] V. García-Vázquez, E. **Marinetto**, P. Guerra, M. F. Valdivieso-Casique, F. A. Calvo, E. Alvarado-Vásquez, C. V. Sole, K. G. Vosburgh, M. Desco, and J. Pascau, "Assessment of intraoperative 3D imaging alternatives for IOERT dose estimation," Z. Med. Phys., **2016**.

[10.1.1.7] M. Brudfors, V. García-Vázquez, B. Sesé-Lucio, E. **Marinetto**, M. Desco, and J. Pascau, "ConoSurf: Open-source 3D scanning system based on a conoscopic holography device for acquiring surgical surfaces," Int. J. Med. Robot. Comput. Assist. Surg., Nov. **2016**.

[10.1.1.8] M. F. Valdivieso-Casique, R. Rodríguez, S. Rodríguez-Bescós, D. Lardíes, P. Guerra, M. J. Ledesma, A. Santos, P. Ibáñez, M. Vidal, J. M. Udías, M. A. Otaduy, J. A. Calama, J. López-Tarjuelo, J. A. Santos-Miranda, M. Desco, V. García-Vázquez, E. **Marinetto**, J. Pascau, F. Calvo, and C. Illana, "RADIANCE-A planning software for intra-operative radiation therapy," Transl. Cancer Res., vol. 4, no. 2, **2015**.

[10.1.1.9] F. Calvo, E. **Marinetto**, V. García-Vázquez, J. A. Santos-Miranda, C. V Sole, M. Desco, and J. Pascau, "PO-0927: Stereotactic image-guided intraoperative electron irradiation: proof of concept and clinical feasibility," Radiother. Oncol., no. 111, p. S117, **2014**.

[10.1.1.10] V. García-Vázquez, E. **Marinetto**, J. A. Santos-Miranda, F. A. Calvo, M. Desco, and J. Pascau, "Feasibility of integrating a multi-camera optical tracking system in intra-operative electron radiation therapy scenarios," Phys. Med. Biol., vol. 58, no. 24, pp. 8769–8782, **2013**.

10.1.2 International Conferences

[10.1.2.1] E. **Marinetto**, J. G. Vitores, M. García-Sevilla, M. Muñoz, F. A. Calvo, M. Desco, and J. Pascau, "Docking guidance of a mobile accelerator

using an optical tracker for IOERT procedures: Feasibility study," in International Conference on Computer Assited Radiology and Surgery, **2017**.

[10.1.2.2] E. **Marinetto**, A. Uneri, T. De Silva, S. Reaungamornrat, W. Zbijewski, G. Kleinszig, J. P. Wolinsky, Z. L. Gokaslan, J. Pascau, and J. H. Siewerdsen, "Intraoperative Fusion of 3D Ultrasound and a C-Arm Cone Beam CT: Feasibility and Characterization for Real-time Guidance of needle insertion," in International Conference on Computer Assisted Radiology and Surgery, **2015**.

[10.1.2.3] E. **Marinetto**, J. F. P. J. Abascal, J. M. Mateos, M. Desco, and J. Pascau, "Initial Evaluation of a New Line-Based Approach for Image-To-World Registration in Image-Guided Interventions," in International Conference on Computer Assisted Radiology and Surgery, **2015**.

[10.1.2.4] S. S. Goswami, J. E. Ortuño Fisac, G. Wollny, V. García-Vázquez, E. **Marinetto**, A. Santos Lleó, J. Pascau, and M. J. Ledesma Carbayo, "A new workflow for image guided intraoperative radiotherapy using fluoroscopy based pose tracking," in International Conference on Computer Assisted Radiology and Surgery, 2015, 24/06/**2015**., vol. 10, no. Suppl 1, pp. S201–S203.

[10.1.2.5] V. García-Vázquez, E. **Marinetto**, P. Guerra, M. F. Valdivieso, F. A. Calvo, E. Alvarado-Vásquez, J. A. Santos-Miranda, C. V Solé, M. Desco, and J. Pascau, "Alternatives for intraoperative imaging in IOERT," in International Conference on Computer Assisted Radiology and Surgery, 2015, 24/06/**2015**., vol. 10, no. Suppl 1, pp. S38–S39.

[10.1.2.6] E. **Marinetto**, V. García-Vázquez, J. A. Santos-Miranda, F. Calvo, M. Valdivieso, C. Illana, M. Desco, and J. Pascau, "Optical Tracking System Integration into IORT Treatment Planning System," in Mediterranean Conference on Medical and Biological Engineering and Computing, 2014, 25/09/**2013**., vol. 25–28 sept, pp. 37–40.

[10.1.2.7] F.A. Calvo, E. **Marinetto**, V. García-Vázquez, J.A. Santos-Miranda, C. Solé, M. Desco, "Stereotactic image-guided intraoperative electron irradiation: proof of concept and clinical feasibility," in ESTRO, **2014**, vol. 1802, p. S117.

[10.1.2.8] V. García-Vázquez, E. **Marinetto**, F. A. Calvo, E. Alvarado, J. A. Santos-Miranda, M. Desco, and J. Pascau, "Evaluation of

intraoperative imaging alternatives for IOERT," in 8th International Conference of Intraoperative Radiotherapy (ISIORT), 2014, 25/09/**2014**., vol. 25–27 sept.

[10.1.2.9] E. **Marinetto**, V. García-Vázquez, J. A. Santos-Miranda, F. A. Calvo, M. Desco, and J. Pascau, "Image-guided intraoperative electron irradiation: clinical set-up and feasibility," in 8th International Conference of Intraoperative Radiotherapy (ISIORT), 2014, 25/09/**2014**., vol. 25–27 sept.

[10.1.2.10] E. **Marinetto**, V. García-Vázquez, J. A. Santos-Miranda, M. Desco, and J. Pascau, "Positioning wire landmarks for image-guided intraoperative radiotherapy: an evaluation study," in International Conference on Computer Assisted Radiology and Surgery, **2013**.

[10.1.2.11] E. **Marinetto**, I. Balsa-Lozano, J. Lansdown, J. A. A. Santos-Miranda, M. Valdivieso, M. Desco, and J. Pascau, "Semi-automatic Segmentation of Sacrum in Computer Tomography Studies for Intraoperative Radiation Therapy," in Mediterranean Conference on Medical and Biological Engineering and Computing, 2013, 25/09/**2013**., vol. 25–28 sept, pp. 344–347.

[10.1.2.12] V. García-Vázquez, E. **Marinetto**, J. A. Santos-Miranda, F. Calvo, L. Camacho-Márquez, C. Illana, M. Desco, J. Pascau, "Toward real scenario in intra-operative electron radiation therapy," in International Conference on Computer Assited Radiology and Surgery, 2012, 27/06/**2012**., vol. 27–30 jun, no. Suppl 1, pp. S64--S65.

[10.1.2.13] J. Pascau, J. Santos-Miranda, C. González San-Segundo, C. Illana, M. Valdivieso, V. García-Vázquez, E. **Marinetto**, F. Calvo, and M. Desco, "Intraoperative Imaging in IOERT Sarcoma Treatment: Initial Experience in two Clinical Cases," International Journal of Radiation Oncology*Biology*Physics, vol. 2–6 oct, no. 2. Estados Unidos de América, Miami Beach, Florida, p. S90, **2011**.

10.1.3 National Conferences

[10.1.3.1] D. García-Mato, E. **Marinetto**, L. Sanz-Díaz, M. Desco, and J. Pascau, "Optimización del protocolo de calibración para sistemas de posicionamiento ópticos multicámara," in Congreso Anual de la Sociedad Española de Ingeniería Biomédica, 2015, 04/11/**2015**., vol. 4–6 nov, pp. 414–417.

[10.1.3.2] E. **Marinetto**, V. García-Vázquez, J. A. Santos-Miranda, F. A. Calvo, L. Sanz-Díaz, C. V Solé, M. Desco, J. Pascau, "Radioterapia Intraoperatoria Guiada por Imagen: entorno clínico y viabilidad," in Congreso Anual de la Sociedad Española de Ingeniería Biomédica, 2014, 26/11/**2014**., vol. 26–28 nov, p. s.p. (4 pp).

[10.1.3.3] E. **Marinetto**, V. García-Vázquez, J. A. Santos-Miranda, F. A. Calvo, A. Camacho-Márquez, M. Desco, J. Pascau, "Estudio de la Viabilidad de la Integración de un Sistema de Posicionamiento Óptico en el Entorno de la Radioterapia Intraoperatoria," in Libro de actas del XXIX Congreso Anual de la Sociedad Española de Ingeniería Biomédica (CASEIB), 2011, 14/12/**2011**., vol. 14 dic, pp. 307–310.

10.2 Other Publications

10.2.1 Articles in peer-reviewed journals

[10.2.1.1] Q. Cao, M. Brehler, A. Sisniega, E. **Marinetto**, A. Zyazin, I. Peters, J. Stayman, J. Yorkston, J. Siewerdsen, and W. Zbijewski, "WE-AB-207A-01: BEST IN PHYSICS (IMAGING): High-Resolution Cone-Beam CT of the Extremities and Cancellous Bone Architecture with a CMOS Detector," Med. Phys., vol. 43, no. 6, pp. 3797–3797, Jun. **2016**.

[10.2.1.2] K. Martínez, S. K. Madsen, A. A. Joshi, S. H. Joshi, F. J. Román, J. Villalon-Reina, M. Burgaleta, S. Karama, J. Janssen, E. **Marinetto**, M. Desco, P. M. Thompson, and R. Colom, "Reproducibility of brain-cognition relationships using three cortical surface-based protocols: An exhaustive analysis based on cortical thickness," Hum. Brain Mapp., vol. 36, no. 8, pp. 3227–3245, **2015**.

[10.2.1.3] J. F. P.-J. Abascal, P. Montesinos, E. **Marinetto**, J. Pascau, and M. Desco, "Comparison of total variation with a motion estimation based compressed sensing approach for self-gated cardiac cine MRI in small animal studies.," PLoS One, vol. 9, no. 10, p. e110594, **2014**.

[10.2.1.4] A. García, M. M. M. Erenas, E. **Marinetto**, C. A. Abad, I. de Orbe-Paya, A. J. Palma, and L. F. Capitán-Vallvey, "Mobile phone platform

as portable chemical analyzer," Sensors Actuators B Chem., vol. 156, no. 1, pp. 350–359, Aug. **2011**.

10.2.2 International Conferences

[10.2.2.1] M. Brehler, E. **Marinetto**, Q. Cao, A. Sisniega, J. W. Stayman, J. Yorkston, S. Demehri, J. H. Siewerdsen, and W. Zbijewski, "Quantitative Assessment of Trabecular Bone Microarchitecture Using High-Resolution Extremities Cone-Beam CT," in Radiological Society of North America 2016 Scientific Assembly and Annual Meeting, **2016**.

[10.2.2.2] E. **Marinetto**, M. Brehler, A. Sisniega, Q. Cao, J. W. Stayman, J. Yorkston, J. H. Siewerdsen, and W. Zbijewski, "Quantification of bone microarchitecture in ultra-high resolution extremities cone-beam CT with a CMOS detector and compensation of patient motion," in International Conference on Computer Assisted Radiology and Surgery, **2016**.

[10.2.2.3] J. F. P.-J. Abascal, P. Montesinos, E. **Marinetto**, J. Pascau, J. J. J. Vaquero, M. Desco, "A Prior-Based Image Variation (PRIVA) Approach Applied to Motion-Based Compressed Sensing Cardiac Cine MRI," in Mediterranean Conference on Medical and Biological Engineering and Computing, 2013, 25/09/**2013**., vol. 25–28 sept, pp. 233–236.

[10.2.2.4] M. Abella, J. F. P.-J. Abascal, E. **Marinetto**, J. J. Vaquero, M. Desco, J. F. Pérez-Juste Abascal, E. Marinetto, J. J. Vaquero, and M. Desco, "Novel 4D image reconstruction for dynamic X-ray computed tomography in slow rotating scanners," in Proceedings IEEE Nuclear Science Symposium & Medical Imaging Conference, 2014, 08/11/**2014**., vol. 8–15 nov, p. s.p. (3 pp).

10.2.3 National Conferences

[10.2.3.1] N. Sánchez, E. **Marinetto**, M. Desco, and J. Pascau, "Segmentación automática de tejido cerebral en imagen preclínica," in Congreso Anual de la Sociedad Española de Ingeniería Biomédica, **2012**, p. s.p.

[10.2.3.2] E. **Marinetto**, M. Desco, P. Montesinos, and J. Pascau, "Corrección de artefacto de inhomogeneidad en imágenes de resonancia magnética de pequeños animales," in Congreso Anual de la Sociedad Española de Ingeniería Biomédica, 2010, 24/11/**2010**., vol. 24–26 nov, p. 125.

11

References

[1] J. H. Breasted and University of Chicago. Oriental Institute., *The Edwin Smith surgical papyrus, published in facsimile and hieroglyphic transliteration with translation and commentary in two volumes*. University of Chicago, Oriental Institute, 1930.

[2] R. P. Feldman and J. T. Goodrich, "The Edwin Smith Surgical Papyrus," *Child's Nerv. Syst.*, vol. 15, no. 6–7, pp. 281–284, 1999.

[3] American Cancer Society, "The History of Cancer," *Cancer*, 2011.

[4] R. W. Moss, *Galen on Cancer*. 2004.

[5] S. M. Lodish H, Berka A, Matsudaira P, Kaiser C, Krieger M, "Molecular Cell Biology- Lodish," in *Biologia celular y Molecular*, 2008, pp. 924–930.

[6] B. W. Stewart and C. P. Wild, *World Cancer Report 2014*. 2014.

[7] P. Denoix, "Enquete permanent dans les centres anticancereaux," *Bull Inst Nat Hyg*, vol. 1, pp. 70–5, 1946.

[8] C. V. Sole, *PhD Thesis: Valor pronóstico de la radioterapia externa en el tratamiento multidisciplinar de pacientes con cáncer oligo-recurrente loco-regional*. 2015.

[9] L. L. Gunderson, C. G. Willett, F. A. Calvo, and L. B. Harrison, *Intraoperative Irradiation: Techniques and Results*. Springer, 2011.

[10] Y. Niibe and K. Hayakawa, "Oligometastases and Oligo-recurrence: The New Era of Cancer Therapy," *Jpn. J. Clin. Oncol.*, vol. 40, no. 2, pp. 107–111, Feb. 2010.

[11] M. G. Haddock, R. C. Miller, H. Nelson, J. H. Pemberton, E. J. Dozois, S. R. Alberts, and L. L. Gunderson, "Combined modality therapy including intraoperative electron irradiation for locally recurrent colorectal cancer," *Int. J. Radiat. Oncol. Biol. Phys.*, vol. 79, no. 1, pp. 143–150, 2011.

[12] X. Chen and S. T. C. Wong, "Cancer Theranostics: An Introduction," *Cancer Theranostics*, pp. 3–8, 2014.

[13] C. Washington and D. Leaver, *Principles and practice of radiation therapy*. Elsevier - Health Sciences Division, 2015.

[14] I. Rosenberg, "Radiation Oncology Physics: A Handbook for Teachers and Students," *Br. J. Cancer*, vol. 98, p. 1020, 2008.

[15] L. Van De Voorde, L. Delrue, M. van Eijkeren, and G. De Meerleer, "Radiotherapy and surgery-An indispensable duo in the treatment of retroperitoneal sarcoma," *Cancer*, vol. 117, no. 19, pp. 4355–4364, Oct. 2011.

[16] F. A. Calvo, R. M. Meirino, and R. Orecchia, "Intraoperative radiation therapy first part: rationale and techniques," *Crit. Rev. Oncol. Hematol.*, vol. 59, no. 2, p. 106, Aug. 2006.

[17] F. K. Storm and D. M. Mahvi, "Diagnosis and management of retroperitoneal soft-tissue sarcoma," *Ann. Surg.*, vol. 214, no. 1, pp. 2–10, Jul. 1991.

[18] M. G. del Carmen, J. F. McIntyre, and A. Goodman, "The role of intraoperative radiation therapy (IORT) in the treatment of locally advanced gynecologic malignancies," *Oncologist*, vol. 5, no. 1, pp. 18–25, 2000.

[19] K. S. Hu, W. E. Enker, and L. B. Harrison, "High-dose-rate intraoperative irradiation: Current status and future directions," *Semin. Radiat. Oncol.*, vol. 12, no. 1, pp. 62–80, Jan. 2002.

[20] F. Casas, F. Ferrer, and F. A. Calvo, "European historical note of intraoperative radiation therapy (IORT): a case report from 1905," *Radiother. Oncol.*, vol. 43, no. 3, p. 323, Jun. 1997.

[21] A. S. Beddar, P. J. Biggs, S. Chang, G. A. Ezzell, B. A. Faddegon, F. W. Hensley, and M. D. Mills, "Intraoperative radiation therapy using mobile electron linear accelerators: report of AAPM Radiation Therapy Committee Task Group No. 72," *Med. Phys.*, vol. 33, no. 5, p. 1476, May

2006.

[22] H. Chandriah, "Mobetron, Health Technology Assessment Section (MaHTAS)," 2010.

[23] J. S. Vaidya, M. Baum, J. S. Tobias, S. Morgan, and D. D'Souza, "The novel technique of delivering targeted intraoperative radiotherapy (Targit) for early breast cancer," *Eur. J. Surg. Oncol.*, vol. 28, no. 4, p. 447, Jun. 2002.

[24] F. A. Calvo, "Intra-operative radiotherapy: a developmental technique for loco-regional intensification of cancer treatment," *Pathol. Biol. (Paris).*, vol. 39, no. 9, p. 883, Nov. 1992.

[25] A. Ruano-Ravina, R. Almazán Ortega, and F. Guedea, "Intraoperative radiotherapy in pancreatic cancer: A systematic review," *Radiother. Oncol.*, vol. 87, no. 3, pp. 318–325, Jun. 2008.

[26] F. A. Calvo, R. M. Meirino, and R. Orecchia, "Intraoperative radiation therapy. Part 2. Clinical results," *Critical Reviews in Oncology/Hematology*, vol. 59, no. 2. pp. 116–127, Aug-2006.

[27] M. Ciocca, M.-C. C. Cantone, I. Veronese, F. Cattani, G. Pedroli, S. Molinelli, V. Vitolo, and R. Orecchia, "Application of failure mode and effects analysis to intraoperative radiation therapy using mobile electron linear accelerators," *Int J Radiat Oncol Biol Phys*, vol. 82, no. 2, pp. e305-11, Feb. 2012.

[28] F. W. Hensley, "Present state and issues in IORT Physics," *Radiat. Oncol.*, vol. 12, no. 1, p. 37, Dec. 2017.

[29] J. E. Tepper, L. L. Gunderson, A. L. Goldson, T. J. Kinsella, W. U. Shipley, W. F. Sindelar, W. C. Wood, and J. K. Martin, "Quality control parameters of intraoperative radiation therapy," *Int. J. Radiat. Oncol.*, vol. 12, no. 9, pp. 1687–1695, 1986.

[30] A. S. Beddar, M. L. Kubu, M. A. Domanovic, R. J. Ellis, T. J. Kinsella, and C. H. Sibata, "A new approach to intraoperative radiation therapy," *Assoc. Perioper. Regist. Nurses journal, J.*, vol. 74, no. 4, pp. 500–505, 2001.

[31] V. E. Kouloulias, P. M. Poortmans, J. Bernier, J. C. Horiot, K. A. Johansson, B. Davis, F. Godson, G. Garavaglia, M. Pierart, and E. Van Der Schueren, "The Quality Assurance programme of the Radiotherapy Group of the European Organization for Research and Treatment of Cancer (EORTC): A critical appraisal of 20 years of continuous efforts,"

European Journal of Cancer, vol. 39, no. 4. pp. 430–437, 2003.

[32] J. López-Tarjuelo, A. Bouché-Babiloni, A. Santos-Serra, V. Morillo-Macías, F. A. Calvo, Y. Kubyshin, and C. Ferrer-Albiach, "Failure mode and effect analysis oriented to risk-reduction interventions in intraoperative electron radiation therapy: The specific impact of patient transportation, automation, and treatment planning availability," *Radiother. Oncol.*, vol. 113, no. 2, pp. 283–289, 2014.

[33] M. F. Valdivieso-Casique, R. Rodríguez, S. Rodríguez-Bescós, D. Lardíes, P. Guerra, M. J. Ledesma, A. Santos, P. Ibáñez, M. Vidal, J. M. Udías, M. A. Otaduy, J. A. Calama, J. López-Tarjuelo, J. A. Santos-Miranda, M. Desco, V. García-Vázquez, E. Marinetto, J. Pascau, F. A. Calvo, and C. Illana, "RADIANCE-A planning software for intra-operative radiation therapy," *Transl. Cancer Res.*, vol. 4, no. 2, 2015.

[34] R. Reitsamer, F. Sedlmayer, M. Kopp, G. Kametriser, C. Menzel, S. Glueck, O. Nairz, H. Deutschmann, F. Merz, and F. Peintinger, "Concepts and techniques of intraoperative radiotherapy (IORT) for breast cancer," *Breast Cancer*, vol. 15, no. 1, pp. 40–46, Jan. 2008.

[35] U. Veronesi, R. Orecchia, A. Luini, G. Gatti, M. Intra, S. Zurrida, G. Ivaldi, G. Tosi, M. Ciocca, A. Tosoni, and F. De Lucia, "A preliminary report of intraoperative radiotherapy (IORT) in limited-stage breast cancers that are conservatively treated," *Eur. J. Cancer*, vol. 37, no. 17, pp. 2178–2183, 2001.

[36] P. Björk, T. Knöös, P. Nilsson, and K. Larsson, "Design and dosimetry characteristics of a soft-docking system for intraoperative radiation therapy.," *Int. J. Radiat. Oncol. Biol. Phys.*, vol. 47, no. 2, pp. 527–33, May 2000.

[37] A. S. Beddar, M. A. Domanovic, M. Lou Kubu, R. J. Ellis, C. H. Sibata, and T. J. Kinsella, "Mobile Linear Accelerators for Intraoperative Radiation Therapy," *Assoc. Perioper. Regist. Nurses journal, J.*, vol. 74, no. 5, pp. 700–705, Nov. 2001.

[38] J. R. Palta and N. Suntharalingam, "A non-docking intraoperative electron beam applicator system," *Int. J. Radiat. Oncol. Biol. Phys.*, vol. 17, no. 2, pp. 411–417, Aug. 1989.

[39] D. Jones, E. Taylor, J. Travaglini, and S. Vermeulen, "A non-contacting intraoperative electron cone apparatus," *Int. J. Radiat. Oncol. Biol. Phys.*, vol. 16, no. 6, pp. 1643–1647, Jun. 1989.

[40] T. M. Peters, K. Cleary, and T. M. Peters, *Image-guided interventions: technology review and clinical applications*, vol. 12, no. 1. Annual Reviews, 2010.

[41] V. R. Ramakrishnan and T. T. Kingdom, "Does Image-Guided Surgery Reduce Complications?," *Otolaryngol. Clin. North Am.*, vol. 48, no. 5, pp. 851–859, 2015.

[42] B. C. Odisio and M. J. Wallace, "Image-Guided Interventions in Oncology," *Surg. Oncol. Clin. N. Am.*, vol. 23, no. 4, pp. 937–955, 2014.

[43] M. F. Spadea, G. Baroni, M. Riboldi, B. Tagaste, C. Garibaldi, R. Orecchia, and A. Pedotti, "Patient set-up verification by infrared optical localization and body surface sensing in breast radiation therapy," *Radiother. Oncol.*, vol. 79, no. 2, pp. 170–178, May 2006.

[44] K. M. Langen, T. R. Willoughby, S. L. Meeks, A. Santhanam, A. Cunningham, L. Levine, and P. A. Kupelian, "Observations on Real-Time Prostate Gland Motion Using Electromagnetic Tracking," *Int. J. Radiat. Oncol.*, vol. 71, no. 4, pp. 1084–1090, 2008.

[45] R. L. Smith, K. Lechleiter, K. Malinowski, D. M. Shepard, D. J. Housley, M. Afghan, J. Newell, J. Petersen, B. Sargent, and P. Parikh, "Evaluation of Linear Accelerator Gating With Real-Time Electromagnetic Tracking," *Int. J. Radiat. Oncol.*, vol. 74, no. 3, pp. 920–927, 2009.

[46] M. R. Alnowami and S. K. Hagi, "The battle against respiration-induced organ motion in external beam radiotherapy," *Saudi Med. J.*, vol. 35, no. 7, pp. 651–662, 2014.

[47] C. K. Glide-Hurst and I. J. Chetty, "Improving radiotherapy planning, delivery accuracy, and normal tissue sparing using cutting edge technologies," *J. Thorac. Dis.*, vol. 6, no. 4, pp. 303–318, 2014.

[48] Y. Watanabe and L. L. Anderson, "A system for nonradiographic source localization and real-time planning of intraoperative high dose rate brachytherapy," *Med. Phys.*, vol. 24, no. 12, pp. 2014–2023, Dec. 1997.

[49] V. Horsley and R. H. Clarke, "The Structure and Functions of the Cerebellum examined by a new Method.," *Brain*, vol. 31, no. 1, pp. 45–124, 1908.

[50] R. L. Galloway, Jr., C. A. E. II, J. T. Lewis, and R. J. Maciunas, "Image display and surgical visualization in interactive image-guided neurosurgery," *Opt. Eng.*, vol. 32, no. 8, p. 1955, 1993.

[51] R. J. Maciunas, R. L. Galloway Jr., J. M. Fitzpatrick, V. R. Mandava, C. A. Edwards, and G. S. Allen, "A Universal System for Interactive Image-Directed Neurosurgery," *Stereotact. Funct. Neurosurg.*, vol. 58, no. 1–4, pp. 108–113, Sep. 1992.

[52] E. M. Friets, J. W. Strohbehn, J. F. Hatch, and D. W. Roberts, "A frameless stereotaxic operating microscope for neurosurgery," *IEEE Trans. Biomed. Eng.*, vol. 36, no. 6, pp. 608–617, Jun. 1989.

[53] D. W. Roberts, J. W. Strohbehn, J. F. Hatch, W. Murray, and H. Keti 'enberger, "A frameless stereotaxic integration of computerized tomographic imaging and the operating microscope," *J Neurosurg*, vol. 65, no. 4, pp. 545–549, Oct. 1986.

[54] V. García-Vázquez, E. Marinetto, J. A. Santos-Miranda, F. A. Calvo, M. Desco, and J. Pascau, "Feasibility of integrating a multi-camera optical tracking system in intra-operative electron radiation therapy scenarios," *Phys. Med. Biol.*, vol. 58, no. 24, pp. 8769–8782, 2013.

[55] T. Peters and K. Cleary, *Image-guided interventions: Technology and applications*. 2008.

[56] N. C. Atuegwu and R. L. Galloway, "Volumetric characterization of the Aurora magnetic tracker system for image-guided transorbital endoscopic procedures," *Phys. Med. Biol.*, vol. 53, no. 16, pp. 4355–4368, Aug. 2008.

[57] T. Sielhorst, M. Bauer, O. Wenisch, G. Klinker, and N. Navab, "Online estimation of the target registration error for n-ocular optical tracking systems.," *Med. Image Comput. Comput. Assist. Interv.*, vol. 10, pp. 652–659, 2007.

[58] B. Li, L. Zhang, H. Sun, J. Yuan, S. G. F. Shen, and X. Wang, "A novel method of computer aided orthognathic surgery using individual CAD/CAM templates: a combination of osteotomy and repositioning guides," *Br. J. Oral Maxillofac. Surg.*, vol. 51, no. 8, p. 239, Dec. 2013.

[59] E. Marinetto, V. García-Vázquez, J. A. Santos-Miranda, F. Calvo, M. Valdivieso, C. Illana, M. Desco, and J. Pascau, "Optical Tracking System Integration into IORT Treatment Planning System," in *Mediterranean Conference on Medical and Biological Engineering and Computing*, 2014, 25/09/2013., vol. 25–28 sept, pp. 37–40.

[60] "NaturalPoint, Inc. - Optical Tracking Solutions, Corvallis, OR, USA."

[Online]. Available: http://naturalpoint.com/. [Accessed: 01-Mar-2017].

[61] F. Ioakeimidou, A. Olwal, A. Nordberg, and H. Von Holst, "3D visualization and interaction with spatiotemporal X-ray data to minimize radiation in image-guided surgery," in *IEEE Symposium on Computer-Based Medical Systems*, 2011, pp. 1–6.

[62] Z. Min, D. Zhu, and M. Q.-H. Meng, "Accuracy assessment of an N-ocular motion capture system for surgical tool tip tracking using pivot calibration," in *IEEE International Conference on Information and Automation (ICIA)*, 2016, pp. 1630–1634.

[63] S. J. Obst, R. Newsham-West, and R. S. Barrett, "In vivo measurement of human achilles tendon morphology using freehand 3-D ultrasound," *Ultrasound Med. Biol.*, vol. 40, no. 1, pp. 62–70, Jan. 2014.

[64] J. M. Fitzpatrick, "The role of registration in accurate surgical guidance," in *Institution of Mechanical Engineers*, 2010, vol. 224, no. 5, pp. 607–622.

[65] D. L. G. Hill, P. G. Batchelor, M. Holden, and D. J. Hawkes, "Medical Image Registration," *Phys. Med. Biol.*, vol. 46, no. 3, p. 392, Mar. 2001.

[66] B. V. Dasarathy, "Medical image fusion: A survey of the state of the art," *Inf. Fusion*, vol. 19, pp. 4–19, 2014.

[67] J. M. Fitzpatrick, "Fiducial registration error and target registration error are uncorrelated," *Proc. SPIE*, vol. 7261, pp. 726102-726102–12, 2009.

[68] J. M. Fitzpatrick, J. B. West, and C. R. Maurer, "Predicting error in rigid-body point-based registration," *IEEE Trans. Med. Imaging*, vol. 17, pp. 694–702, 1998.

[69] Y. Fan, D. Jiang, M. Wang, and Z. Song, "A new markerless patient-to-image registration method using a portable 3D scanner," *Med. Phys.*, vol. 41, no. 10, Oct. 2014.

[70] L. Maier-Hein, A. M. Franz, T. R. dos Santos, M. Schmidt, M. Fangerau, H.-P. Meinzer, and J. M. Fitzpatrick, "Convergent iterative closest-point algorithm to accomodate anisotropic and inhomogenous localization error," *IEEE Trans. Pattern Anal. Mach. Intell.*, vol. 34, no. 8, p. 1520, Aug. 2012.

[71] P. J. Besl and H. D. McKay, "A method for registration of 3-D shapes," *IEEE Trans. Pattern Anal. Mach. Intell.*, vol. 14, no. 2, pp. 239–256, 1992.

[72] S. Bouaziz, A. Tagliasacchi, and M. Pauly, "Sparse Iterative Closest Point," *Comput. Graph. Forum*, vol. 32, no. 5, pp. 113–123, Aug. 2013.

[73] D. J. Kroon, "Finite Iterative Closest Point," *http://www.mathworks.com/matlabcentral/fileexchange/24301-finite-iterative-closest-point*, 2009. [Online]. Available: http://www.mathworks.com/matlabcentral/fileexchange/24301-finite-iterative-closest-point. [Accessed: 08-Jun-2014].

[74] M. Levoy and S. Rusinkiewicz, "Efficient variants of the ICP algorithm," in *hird International Conference on 3-D Digital Imaging and Modeling*, 2001, pp. 145–152.

[75] F. A. Calvo, "Intraoperative irradiation: precision medicine for quality cancer control promotion," *Radiat. Oncol.*, vol. 12, no. 1, p. 36, Dec. 2017.

[76] J. R. Palta, P. J. Biggs, J. D. Hazle, M. S. Huq, R. A. Dahl, T. G. Ochran, J. Soen, R. R. Dobelbower, and E. C. McCullough, "Intraoperative electron beam radiation therapy: Technique, dosimetry, and dose specification: Report of task force 48 of the radiation therapy committee, American Association of Physicists in Medicine," *Int. J. Radiat. Oncol. Biol. Phys.*, vol. 33, no. 3, pp. 725–746, Oct. 1995.

[77] A. S. Beddar and S. Krishnan, "Intraoperative radiotherapy using a mobile electron LINAC: a retroperitoneal sarcoma case," *J. Appl. Clin. Med. Phys.*, vol. 6, no. 3, pp. 95–107, 2005.

[78] A. Rosi and V. Viti, "Guidelines for quality assurance in intra-operative radiation therapy (English version). Rapporti ISTISAN 03/1 EN Istituto Superiore di Sanità (Viale Regina Elena, 299 - 00161 Roma)," 2003.

[79] M. Carlson, J. Hessler, S. Grzetic, and N. Gupta, "Dosimetric Evaluation of Soft Docking Sensitivity On An INTRAOP Mobetron IORT Device," *Med. Phys.*, vol. 42, no. 6, p. 3407, Jun. 2015.

[80] M. Pimpinella, D. Mihailescu, a S. Guerra, and R. F. Laitano, "Dosimetric characteristics of electron beams produced by a mobile accelerator for IORT," *Phys. Med. Biol.*, vol. 52, no. 20, pp. 6197–6214, 2007.

[81] L. Paul, P.-L. Docquier, O. Cartiaux, O. Cornu, C. Delloye, and X. Banse, "Selection of massive bone allografts using shape-matching 3-dimensional registration," *Acta Orthop.*, vol. 81, no. 2, pp. 250–255, 2010.

[82] E. G. Shaw, C. R. Blackwell, E. C. McCullough, and L. L. Gunderson,

"Matching intraoperative electron-beam fields: dosimetric and clinical considerations.," *Int. J. Radiat. Oncol. Biol. Phys.*, vol. 13, no. 9, p. 1303, Sep. 1987.

[83] F. Sedlmayer, R. Reitsamer, C. Fussl, I. Ziegler, F. Zehentmayr, H. Deutschmann, P. Kopp, and G. Fastner, "Boost IORT in Breast Cancer: Body of Evidence," *Int. J. Breast Cancer*, vol. 2014, pp. 1–6, 2014.

[84] F. Sedlmayer, F. Zehentmayr, and G. Fastner, "Partial breast re-irradiation for local recurrence of breast carcinoma: Benefit and long term side effects," *The Breast*, vol. 22, pp. S141–S146, Aug. 2013.

[85] D. A. Jaffray, J. H. Siewerdsen, J. W. Wong, and A. A. Martinez, "Flat-panel cone-beam computed tomography for image-guided radiation therapy," *Int. J. Radiat. Oncol. Biol. Phys.*, vol. 53, no. 5, pp. 1337–1349, 2002.

[86] G. X. Ding, D. M. Duggan, and C. W. Coffey, "Accurate patient dosimetry of kilovoltage cone-beam CT in radiation therapy," *Med. Phys.*, vol. 35, no. 3, pp. 1135–1144, Feb. 2008.

[87] S. Yoo and F. F. Yin, "Dosimetric feasibility of cone-beam CT-based treatment planning compared to CT-based treatment planning," *Int. J. Radiat. Oncol. Biol. Phys.*, vol. 66, no. 5, pp. 1553–1561, 2006.

[88] C.-Y. Chang, B. Lange, M. Zhang, S. Koenig, P. Requejo, N. Somboon, A. Sawchuk, and A. Rizzo, "Towards Pervasive Physical Rehabilitation Using Microsoft Kinect," in *International Conference on Pervasive Computing Technologies for Healthcare*, 2012.

[89] C. Zhu and W. Sheng, "Realtime human daily activity recognition through fusion of motion and location data," in *IEEE International Conference on Information and Automation*, 2010, pp. 846–851.

[90] B. Spanlang, J.-M. Normand, E. Giannopoulos, and M. Slater, "A first person avatar system with haptic feedback," in *ACM Symposium on Virtual Reality Software and Technology*, 2010, p. 47.

[91] D. Webster and O. Celik, "Experimental evaluation of Microsoft Kinect's accuracy and capture rate for stroke rehabilitation applications," in *IEEE Haptics Symposium, HAPTICS*, 2014, pp. 455–460.

[92] R. Khadem, C. C. Yeh, M. Sadeghi-Tehrani, M. R. Bax, J. A. Johnson, J. N. Welch, E. P. Wilkinson, and R. Shahidi, "Comparative tracking error analysis of five different optical tracking systems," *Comput. Aided Surg.*, vol.

5, no. 2, pp. 98–107, 2000.

[93] A. D. Wiles, D. G. Thompson, and D. D. Frantz, "Accuracy assessment and interpretation for optical tracking systems," in *International Society for optics and photonic. (SPIE) Medical Imaging 2004: Visualizations, Image-guided Precedures and Display*, 2004, vol. 5367, pp. 421–432.

[94] R. Tranberg, *PhD Thesis. Analysis of body motions based on optical markers applications*. 2010.

[95] H. Dang, Y. Otake, S. Schafer, J. W. Stayman, G. Kleinszig, and J. H. Siewerdsen, "Robust methods for automatic image-to-world registration in cone-beam CT interventional guidance," *Med. Phys.*, vol. 39, no. 10, p. 6484, Oct. 2012.

[96] J. B. West, J. M. Fitzpatrick, S. A. Toms, C. R. Maurer, and R. J. Maciunas, "Fiducial point placement and the accuracy of point-based, rigid body registration," *Neurosurgery*, vol. 48, pp. 810-816-817, 2001.

[97] L. Davis, F. G. Hamza-lup, and J. P. Rolland, "A Method for Designing Marker-Based Tracking Probes College of Optics and Photonics," in *International Symposium on Mixed and Augmented Reality*, 2004, pp. 120–129.

[98] T. Pintaric and H. Kaufmann, "A rigid-body target design methodology for optical pose-tracking systems," in *ACM symposium on Virtual reality software and technology*, 2008, pp. 73–76.

[99] W. Birkfellner, F. Watzinger, F. Wanschitz, R. Ewers, and H. Bergmann, "Calibration of tracking systems in a surgical environment," *IEEE Trans. Med. Imaging*, vol. 17, no. 5, pp. 737–742, 1998.

[100] J. D. Kertis, J. M. Fritz, J. T. Long, and G. F. Harris, "Static and Dynamic Calibration of an Eight-Camera Optical System for Human Motion Analysis," *Crit. Rev. Phys. Rehabil. Med.*, vol. 22, no. 1–4, pp. 49–59, 2010.

[101] J. Kertis, *Master's Thesis: Biomechanical Evaluation of an Optical System for Quantitative Human Motion Analysis*. 2012.

[102] D. D. Frantz, A. D. Wiles, S. E. Leis, and S. R. Kirsch, "Accuracy assessment protocols for electromagnetic tracking systems," *Phys. Med. Biol.*, vol. 48, no. 14, pp. 2241–2251, Jul. 2003.

[103] J. Hummel, M. Figl, W. Birkfellner, M. R. Bax, R. Shahidi, C. R. Maurer, and H. Bergmann, "Evaluation of a new electromagnetic tracking system using a standardized assessment protocol," *Phys. Med. Biol.*, vol. 51, no. 10,

pp. N205–N210, May 2006.

[104] R. Rohling, P. Munger, J. M. Hollerbach, and T. Peters, "Comparison of Relative Accuracy Between a Mechanical and an Optical Position Tracker for Image-Guided Neurosurgery," *Comput. Aided Surg.*, vol. 1, no. 1, pp. 30–34, Jan. 1995.

[105] Y. Ehara, H. Fujimoto, S. Miyazaki, M. Mochimaru, S. Tanaka, and S. Yamamoto, "Comparison of the performance of 3D camera systems II," *Gait Posture*, vol. 5, no. 3, pp. 251–255, Jun. 1997.

[106] C. NDI Inc., Waterloo, Ontario, "Polaris Specifications," 2016. [Online]. Available: http://www.ndigital.com/medical/products/polaris-family/#specifications. [Accessed: 03-Mar-2017].

[107] R. Hartley and A. Zisserman, "Multiple View Geometry in Computer Vision," *Robotica*, vol. 23, no. 2, pp. 271–271, Mar. 2005.

[108] J. B. West and C. R. Maurer, "Designing Optically Tracked Instruments for Image-Guided Surgery," *IEEE Trans. Med. Imaging*, vol. 23, no. 5, pp. 533–545, May 2004.

[109] T. Ridene and F. Goulette, "Registration of fixed-and-mobile- based terrestrial Laser data sets with DSM," in *IEEE International Symposium on Computational Intelligence in Robotics and Automation - (CIRA)*, 2009, pp. 375–380.

[110] M. Fischler and R. Bolles, "Random sample consensus: a paradigm for model fitting with applications to image analysis and automated cartography," *ACM Symp. Virtual Real. Softw. Technol.*, vol. 24, no. 6, 1981.

[111] A. Myronenko and X. Song, "Point set registration: coherent point drift," *IEEE Trans. Pattern Anal. Mach. Intell.*, vol. 32, no. 12, p. 2262, Dec. 2010.

[112] T. K. Moon, "The expectation-maximization algorithm," *IEEE Signal Process. Mag.*, vol. 13, no. 6, pp. 47–60, 1996.

[113] R. Balachandran and J. M. Fitzpatrick, "Iterative solution for rigid-body point-based registration with anisotropic weighting," 2009, p. 72613D.

[114] A. Myronenko, "Point set registration: CPD." [Online]. Available: https://sites.google.com/site/myronenko/research/cpd. [Accessed: 11-Nov-2014].

[115] R. P. Paul, *Robot manipulators: mathematics, programming, and control: the computer*

control of robot manipulators. Richard Paul, 1981.

[116] P. Gendron, S. Lemieux, and F. Major, "Quantitative analysis of nucleic acid three-dimensional structures," *J. Mol. Biol.*, vol. 308, no. 5, p. 919, May 2001.

[117] R. M. Neal and G. E. Hinton, "A View of the Em Algorithm that Justifies Incremental, Sparse, and other Variants," in *Learning in Graphical Models*, Dordrecht: Springer Netherlands, 1998, pp. 355–368.

[118] G. Koukourakis, N. Kelekis, V. Armonis, and V. Kouloulias, "Brachytherapy for prostate cancer: a systematic review," *Adv. Urol.*, p. 327945, Jan. 2009.

[119] L. Tiong and G. J. Maddern, "Systematic review and meta-analysis of survival and disease recurrence after radiofrequency ablation for hepatocellular carcinoma," *Br. J. Surg.*, vol. 98, no. 9, p. 1210, Sep. 2011.

[120] J. K. Rudzinski and J. Kawakami, "Incidence of infectious complications following transrectal ultrasound-guided prostate biopsy in Calgary, Alberta, Canada: A retrospective population-based analysis," *Can. Urol. Assoc. J.*, vol. 8, no. 5–6, pp. E301-5, May 2014.

[121] T. Boskovic, J. Stanic, S. Pena-Karan, P. Zarogoulidis, K. Drevelegas, N. Katsikogiannis, N. Machairiotis, A. Mpakas, K. Tsakiridis, G. Kesisis, T. Tsiouda, I. Kougioumtzi, S. Arikas, and K. Zarogoulidis, "Pneumothorax after transthoracic needle biopsy of lung lesions under CT guidance," *J. Thorac. Dis.*, vol. 6 Suppl 1, pp. S99–S107, Mar. 2014.

[122] K. Chin, A. Perlas, V. Chan, and R. Brull, "Needle Visualization in Ultrasound-Guided Regional Anesthesia: Challenges and Solutions," *Reg. Anesth. Pain Med.*, vol. 33, no. 6, pp. 532–544, Nov. 2008.

[123] M. Lamperti, A. R. Bodenham, M. Pittiruti, M. Blaivas, J. G. Augoustides, M. Elbarbary, T. Pirotte, D. Karakitsos, J. LeDonne, S. Doniger, G. Scoppettuolo, D. Feller-Kopman, W. Schummer, R. Biffi, E. Desruennes, L. A. Melniker, and S. T. Verghese, "International evidence-based recommendations on ultrasound-guided vascular access," *Intensive Care Med.*, vol. 38, no. 7, pp. 1105–1117, 2012.

[124] S. F. Coquia, L. C. Chu, and U. M. Hamper, "The role of sonography in thyroid cancer," *Radiologic Clinics of North America*, vol. 52, no. 6. pp. 1283–1294, 2014.

[125] M. Fingerman, J. G. Benonis, and G. Martin, "A practical guide to commonly performed ultrasound-guided peripheral-nerve blocks," *Curr. Opin. Anaesthesiol.*, vol. 22, no. 5, pp. 600–607, 2009.

[126] C. Nolsøe, L. Nielsen, S. Torp-Pedersen, and H. H. Holm, "Major complications and deaths due to interventional ultrasonography: a review of 8000 cases," *J. Clin. ultrasound*, vol. 18, no. 3, pp. 179–84, 1990.

[127] Y. Zhu, D. Magee, R. Ratnalingam, and D. Kessel, "A training system for ultrasound-guided needle insertion procedures," in *Medical image computing and computer-assisted intervention: MICCAI*, 2007, vol. 10, no. Pt 1, pp. 566–74.

[128] L. Maier-Hein, A. Tekbas, A. Seitel, F. Pianka, S. A. Müller, S. Satzl, S. Schawo, B. Radeleff, R. Tetzlaff, A. M. Franz, B. P. Müller-Stich, I. Wolf, H.-U. Kauczor, B. M. Schmied, and H.-P. Meinzer, "In vivo accuracy assessment of a needle-based navigation system for CT-guided radiofrequency ablation of the liver," *Med. Phys.*, vol. 35, no. 12, pp. 5385–96, Dec. 2008.

[129] Z. Yaniv, P. Cheng, E. Wilson, T. Popa, D. Lindisch, E. Campos-Nanez, H. Abeledo, V. Watson, K. Cleary, and F. Banovac, "Needle-based interventions with the image-guided surgery toolkit (IGSTK): from phantoms to clinical trials," *IEEE Trans. Biomed. Eng.*, vol. 57, no. 4, p. 922, Apr. 2010.

[130] S. L. Showalter, G. Petroni, D. M. Trifiletti, B. Libby, A. T. Schroen, D. R. Brenin, P. Dalal, M. Smolkin, K. A. Reardon, and T. N. Showalter, "A novel form of breast intraoperative radiation therapy with CT-guided high-dose-rate brachytherapy: results of a prospective phase 1 clinical trial," *Int. J. Radiat. Oncol. Biol. Phys.*, vol. 96, no. 1, pp. 46–54, Sep. 2016.

[131] F. Roeder, O. Schramm, C. Timke, G. Habl, M. C. Tanner, and P. E. Huber, "Postplanning of a three-dimensional dose distribution for intraoperative electron radiation therapy (IOERT) using intraoperative C-arm based 3D-imaging – a phantom study," in *Int J CARS, 5 (Suppl. 1*, 2010, pp. S71–S72.

[132] Y. Chan, J. H. Siewerdsen, M. A. Rafferty, D. J. Moseley, D. A. Jaffray, and J. C. Irish, "Cone-beam computed tomography on a mobile C-arm: novel intraoperative imaging technology for guidance of head and neck surgery," *J. Otolaryngol. Head Neck Surg.*, vol. 37, no. 1, pp. 81–90, Feb. 2008.

[133] A. Khoury, J. H. Siewerdsen, C. M. Whyne, M. J. Daly, H. J. Kreder, D. J. Moseley, and D. A. Jaffray, "Intraoperative cone-beam CT for image-guided tibial plateau fracture reduction," *Comput. Aided Surg.*, vol. 12, no. 4, pp. 195–207, Jul. 2007.

[134] G. Bachar, J. H. Siewerdsen, M. J. Daly, D. A. Jaffray, and J. C. Irish, "Image quality and localization accuracy in C-arm tomosynthesis-guided head and neck surgery," *Med. Phys.*, vol. 34, no. 12, p. 4664, Dec. 2007.

[135] E. Barker, K. Trimble, H. Chan, J. Ramsden, S. Nithiananthan, A. James, G. Bachar, M. Daly, J. Irish, and J. Siewerdsen, "Intraoperative use of cone-beam computed tomography in a cadaveric ossified cochlea model," *Otolaryngol. Head. Neck Surg.*, vol. 140, no. 5, pp. 697–702, May 2009.

[136] S. Lee, G. L. Gallia, D. D. Reh, S. Schafer, A. Uneri, D. J. Mirota, S. Nithiananthan, Y. Otake, J. W. Stayman, W. Zbijewski, and J. H. Siewerdsen, "Intraoperative C-arm cone-beam computed tomography: quantitative analysis of surgical performance in skull base surgery," *Laryngoscope*, vol. 122, no. 9, p. 1925, Sep. 2012.

[137] A. Uneri, S. Schafer, D. J. Mirota, S. Nithiananthan, Y. Otake, R. H. Taylor, G. L. Gallia, A. J. Khanna, S. Lee, D. D. Reh, and J. H. Siewerdsen, "TREK: an integrated system architecture for intraoperative cone-beam CT-guided surgery," *Int. J. Comput. Assist. Radiol. Surg.*, vol. 7, no. 1, p. 159, Jan. 2012.

[138] A. Lasso, T. Heffter, A. Rankin, C. Pinter, T. Ungi, and G. Fichtinger, "PLUS: open-source toolkit for ultrasound-guided intervention systems," *IEEE Trans. Biomed. Eng.*, pp. 1–11, 2014.

[139] M. J. Daly, J. H. Siewerdsen, Y. B. Cho, D. A. Jaffray, and J. C. Irish, "Geometric calibration of a mobile C-arm for intraoperative cone-beam CT.," *Med. Phys.*, vol. 35, no. 5, pp. 2124–36, May 2008.

[140] S. Schafer, S. Nithiananthan, D. J. Mirota, A. Uneri, J. W. Stayman, W. Zbijewski, C. Schmidgunst, G. Kleinszig, A. J. Khanna, and J. H. Siewerdsena, "Mobile C-arm cone-beam CT for guidance of spine surgery: image quality, radiation dose, and integration with interventional guidance," *Med. Phys.*, vol. 38, no. 8, p. 4563, Aug. 2011.

[141] S. Schafer, J. W. Stayman, W. Zbijewski, C. Schmidgunst, G. Kleinszig, J. H. Siewerdsen, J. W. Stayman, W. Zbijewski, C. Schmidgunst, G. Kleinszig, and J. H. Siewerdsen, "Antiscatter grids in mobile C-arm cone-

beam CT: effect on image quality and dose," *Med. Phys.*, vol. 39, no. 1, p. 153, Jan. 2012.

[142] K. Wermker, J. Kleinheinz, S. Jung, and D. Dirksen, "Soft tissue response and facial symmetry after orthognathic surgery," *J. Craniomaxillofac. Surg.*, Jan. 2014.

[143] H. Neshat, D. W. Cool, K. Barker, L. Gardi, N. Kakani, and A. Fenster, "A 3D ultrasound scanning system for image guided liver interventions," *Med. Phys.*, vol. 40, no. 11, p. 112903, Nov. 2013.

[144] G. Carbajal, A. Lasso, A. Gómez, and G. Fichtinger, "Improving N-wire phantom-based freehand ultrasound calibration," *Int. J. Comput. Assist. Radiol. Surg.*, vol. 8, no. 6, p. 1063, Nov. 2013.

[145] A. Deguet, R. Kumar, R. Taylor, and P. Kazanzides, "The cisst libraries for computer assisted intervention systems," *MIDAS J. Syst. Arch. Comput. Assist. Interv.*, pp. 1–8, 2008.

[146] S. Pieper, M. Halle, and R. Kikinis, "3D Slicer," *IEEE Int. Symp. Biomed. Imaging Nano to Macro*, vol. 2, pp. 632–635, 2004.

[147] Kitware Inc., "IntersonSDKCxx," *IntersonSDKCxx*. [Online]. Available: https://github.com/KitwareMedical/IntersonSDKCxx.

[148] J. H. Siewerdsen, D. J. Moseley, S. Burch, S. K. Bisland, A. Bogaards, B. C. Wilson, and D. A. Jaffray, "Volume CT with a flat-panel detector on a mobile, isocentric C-arm: pre-clinical investigation in guidance of minimally invasive surgery," *Med. Phys.*, vol. 32, no. 1, pp. 241–54, Jan. 2005.

[149] A. S. Wang, J. W. Stayman, Y. Otake, G. Kleinszig, S. Vogt, G. L. Gallia, A. J. Khanna, and J. H. Siewerdsen, "Soft-tissue imaging with C-arm cone-beam CT using statistical reconstruction," *Phys. Med. Biol.*, vol. 59, no. 4, p. 1005, Feb. 2014.

[150] N. M. Hamming, M. J. Daly, J. C. Irish, and J. H. Siewerdsen, "Automatic image-to-world registration based on x-ray projections in cone-beam CT-guided interventions," *Med. Phys.*, vol. 36, no. 5, p. 1800, May 2009.

[151] S. Nithiananthan, S. Schafer, D. J. Mirota, J. W. Stayman, W. Zbijewski, D. D. Reh, G. L. Gallia, and J. H. Siewerdsen, "Extra-dimensional Demons: a method for incorporating missing tissue in deformable image registration," *Med. Phys.*, vol. 39, no. 9, p. 5718, Sep. 2012.

[152] S. Reaungamornrat, W. P. Liu, A. S. Wang, Y. Otake, S. Nithiananthan, A. Uneri, S. Schafer, E. Tryggestad, J. Richmon, J. M. Sorger, J. H. Siewerdsen, and R. H. Taylor, "Deformable image registration for cone-beam CT guided transoral robotic base-of-tongue surgery," *Phys. Med. Biol.*, vol. 58, no. 14, p. 4951, Jul. 2013.

[153] A. Uneri, S. Nithiananthan, S. Schafer, Y. Otake, J. W. Stayman, G. Kleinszig, M. S. Sussman, J. L. Prince, and J. H. Siewerdsen, "Deformable registration of the inflated and deflated lung in cone-beam CT-guided thoracic surgery: initial investigation of a combined model- and image-driven approach," *Med. Phys.*, vol. 40, no. 1, Jan. 2013.

[154] B. Brendel, S. Winter, a. Rick, M. Stockheim, and H. Ermert, "Registration of 3D CT and ultrasound datasets of the spine using bone structures," *Comput. Aided Surg.*, vol. 7, no. 3, pp. 146–155, Jan. 2002.

[155] D. M. Muratore, J. H. Russ, B. M. Dawant, and R. L. Galloway, "Three-dimensional image registration of phantom vertebrae for image-guided surgery: a preliminary study," *Comput. Aided Surg.*, vol. 7, no. 6, p. 342, Jan. 2002.

[156] W. Wein, S. Brunke, A. Khamene, M. R. Callstrom, and N. Navab, "Automatic CT-ultrasound registration for diagnostic imaging and image-guided intervention," *Med. Image Anal.*, vol. 12, no. 5, pp. 577–585, Oct. 2008.

[157] C. X. B. Yan, B. Goulet, D. Tampieri, and D. L. Collins, "Ultrasound-CT registration of vertebrae without reconstruction," *Int. J. Comput. Assist. Radiol. Surg.*, vol. 7, no. 6, pp. 901–909, 2012.

[158] P. J. Huber, "Robust Estimation of a Location Parameter," *Ann. Math. Stat.*, vol. 35, no. 1, pp. 73–101, Mar. 1964.

[159] M. P. Heinrich, M. Jenkinson, B. W. Papiez, S. M. Brady, J. A. Schnabel, B. W. Papież, S. M. Brady, and J. A. Schnabel, "Towards Realtime Multimodal Fusion for Image-Guided Interventions Using Self-similarities," *Med. Image Comput. Comput. Interv. – MICCAI*, vol. 8149 LNCS, pp. 187–194, 2013.

[160] D. V. Surbek, A. Young, E. Danzer, A. Schoeberlein, L. Dudler, and W. Holzgreve, "Ultrasound-guided stem cell sampling from the early ovine fetus for prenatal ex vivo gene therapy," *Am. J. Obstet. Gynecol.*, vol. 187, no. 4, pp. 960–963, Oct. 2002.

[161] D. Rueckert, L. I. Sonoda, C. Hayes, D. L. G. Hill, M. O. Leach, and D. J. Hawkes, "Nonrigid registration using free-form deformations: application to breast MR images," *IEEE Trans. Med. Imaging*, vol. 18, no. 8, pp. 712–721, 1999.

[162] T. Vercauteren, X. Pennec, A. Perchant, and N. Ayache, "Diffeomorphic demons: Efficient non-parametric image registration," *Neuroimage*, vol. 45, no. 1, pp. S61–S72, 2009.

[163] S. Nithiananthan, S. Schafer, A. Uneri, D. J. Mirota, J. W. Stayman, W. Zbijewski, K. K. Brock, M. J. Daly, H. Chan, J. C. Irish, and J. H. Siewerdsen, "Demons deformable registration of CT and cone-beam CT using an iterative intensity matching approach," *Med. Phys.*, vol. 38, no. 4, p. 1785, 2011.

[164] R. S. Hartenberg and J. Denavit, *Kinematic synthesis of linkages*. McGraw-Hill, 1964.

[165] D. Kraft, "On Converting Optimal Control Problems into Nonlinear Programming Problems," in *Computational Mathematical Programming*, Berlin, Heidelberg: Springer Berlin Heidelberg, 1985, pp. 261–280.

[166] M. Brudfors, V. García-Vázquez, B. Sesé-Lucio, E. Marinetto, M. Desco, and J. Pascau, "ConoSurf: Open-source 3D scanning system based on a conoscopic holography device for acquiring surgical surfaces," *Int. J. Med. Robot. Comput. Assist. Surg.*, Nov. 2016.

[167] E. Marinetto, "BiiGOptitrack Library," 2015. [Online]. Available: http://github.com/HGGM-LIM/BiiGOptitrack.

[168] J. Tokuda, G. S. Fischer, X. Papademetris, Z. Yaniv, L. Ibanez, P. Cheng, H. Liu, J. Blevins, J. Arata, A. J. Golby, T. Kapur, S. Pieper, E. C. Burdette, G. Fichtinger, C. M. Tempany, and N. Hata, "OpenIGTLink: An open network protocol for image-guided therapy environment," *Int. J. Med. Robot. Comput. Assist. Surg.*, vol. 5, no. 4, pp. 423–434, Dec. 2009.

[169] S. L. Meeks, F. J. Bova, W. A. Friedman, J. M. Buatti, R. D. Moore, and W. M. Mendenhall, "IRLED-Based Patient Localization for Linac Radiosurgery," *Int. J. Radiat. Oncol.*, vol. 41, no. 2, pp. 433–439, 1998.

[170] G. Fichtinger, J. P. Fiene, C. W. Kennedy, G. Kronreif, I. Iordachita, D. Y. Song, E. C. Burdette, and P. Kazanzides, "Robotic assistance for ultrasound-guided prostate brachytherapy," *Med. Image Anal.*, vol. 12, no.

5, pp. 535–545, Oct. 2008.

[171] G. Dagnino, I. Georgilas, P. Tarassoli, R. Atkins, and S. Dogramadzi, "Intra-operative 3D imaging system for robot-assisted fracture manipulation," in *International Conference of the IEEE Engineering in Medicine and Biology Society, EMBS*, 2015, vol. 2015–Novem, pp. 9–12.

[172] F. A. Calvo, E. Marinetto, V. García-Vázquez, J. A. Santos-Miranda, C. V Sole, M. Desco, and J. Pascau, "Stereotactic image-guided intraoperative electron irradiation: proof of concept and clinical feasibility," *Radiother. Oncol.*, vol. 1802, no. 111, p. S117, 2014.

[173] J. López-Tarjuelo, A. Bouché-Babiloni, A. Santos-Serra, V. Morillo-Macías, F. A. Calvo, Y. Kubyshin, and C. Ferrer-Albiach, "Failure mode and effect analysis oriented to risk-reduction interventions in intraoperative electron radiation therapy: The specific impact of patient transportation, automation, and treatment planning availability," *Radiother. Oncol.*, vol. 113, no. 2, pp. 283–289, 2014.

[174] J. Pascau, J. A. Santos Miranda, F. A. Calvo, A. Bouché, V. Morillo, C. González-San Segundo, C. Ferrer, J. López Tarjuelo, and M. Desco, "An Innovative Tool for Intraoperative Electron Beam Radiotherapy Simulation and Planning: Description and Initial Evaluation by Radiation Oncologists," *Int. J. Radiat. Oncol.*, vol. 83, no. 2, pp. e287–e295, 2012.

[175] E. Marinetto, V. García-Vázquez, J. A. Santos-Miranda, M. Desco, and J. Pascau, "Positioning wire landmarks for image-guided intraoperative radiotherapy: an evaluation study," in *International Conference on Computer Assisted Radiology and Surgery*, 2013.

[176] V. García-Vázquez, E. Marinetto, P. Guerra, M. F. Valdivieso-Casique, F. A. Calvo, E. Alvarado-Vásquez, C. V. Sole, K. G. Vosburgh, M. Desco, and J. Pascau, "Assessment of intraoperative 3D imaging alternatives for IOERT dose estimation," *Zeitschrift fur Medizinische Physik*, 2016.

[177] Y. Nakajima, T. Dohi, T. Sasama, Y. Momoi, N. Sugano, Y. Tamura, Sung-hwan Lim, I. Sakuma, M. Mitsuishi, T. Koyama, K. Yonenobu, S. Ohashi, M. Bessho, and I. Ohnishi, "Surgical tool alignment guidance by drawing two cross-sectional laser-beam planes," *IEEE Trans. Biomed. Eng.*, vol. 60, no. 6, pp. 1467–1476, Jun. 2013.

[178] C. V. Sole, F. A. Calvo, C. Ferrer, J. Pascau, and H. Marsiglia, "Bibliometrics of intraoperative radiotherapy," *Strahlentherapie und Onkol.*,

vol. 190, no. 12, pp. 1111–1116, Nov. 2014.

[179] D. Black, C. Hansen, A. Nabavi, R. Kikinis, and H. Hahn, "A Survey of auditory display in image-guided interventions," *Int. J. Comput. Assist. Radiol. Surg.*, pp. 1–12, Mar. 2017.

[180] D. Black, J. Hettig, M. Luz, C. Hansen, R. Kikinis, and H. Hahn, "Auditory feedback to support image-guided medical needle placement," *Int. J. Comput. Assist. Radiol. Surg.*, pp. 1–9, Feb. 2017.

[181] Epic Games, "What is Unreal Engine 4," 2015. [Online]. Available: https://www.unrealengine.com/what-is-unreal-engine-4. [Accessed: 24-Feb-2017].

[182] Unity, "Unity - Game Engine," 2005. [Online]. Available: https://unity3d.com/es/. [Accessed: 24-Feb-2017].

[183] T. Ungi, A. Lasso, and G. Fichtinger, "Open-source platforms for navigated image-guided interventions," *Medical Image Analysis*, vol. 33, pp. 181–186, 2016.

[184] E. von Hippel and G. von Krogh, "Open Source Software and the 'Private-Collective' Innovation Model: Issues for Organization Science," *Organ. Sci.*, vol. 14, no. 2, pp. 209–223, Apr. 2003.

[185] E. Von Hippel, "The Promise of Research on Open Source Software," *Inst. Oper. Res. Manag. Sci.*, vol. 52, no. 7, pp. 975–983, Jul. 2006.

[186] I. Wolf, M. Vetter, I. Wegner, T. Böttger, M. Nolden, M. Schöbinger, M. Hastenteufel, T. Kunert, and H. P. Meinzer, "The medical imaging interaction toolkit," *Med. Image Anal.*, vol. 9, no. 6, pp. 594–604, Dec. 2005.

[187] M. Nolden, S. Zelzer, A. Seitel, D. Wald, M. Müller, A. M. Franz, D. Maleike, M. Fangerau, M. Baumhauer, L. Maier-Hein, K. H. Maier-Hein, H.-P. Meinzer, and I. Wolf, "The Medical Imaging Interaction Toolkit: challenges and advances : 10 years of open-source development," *Int. J. Comput. Assist. Radiol. Surg.*, vol. 8, no. 4, p. 607, Jul. 2013.

[188] K. Gary, L. Ibáñez, S. Aylward, D. Gobbi, M. B. Blake, and K. Cleary, "IGSTK: An open source Software Toolkit for Image-Guided surgery," *Open Source*, vol. 39, no. 4, pp. 46–53, Apr. 2006.

[189] Insight Consortium, "ITK - Segmentation & Registration Toolkit," *Open Source*, 2012. [Online]. Available: https://itk.org/. [Accessed: 24-Feb-

2017].

[190] B. Lorensen, W. Schroeder, and K. Martin, "VTK - The Visualization Toolkit," *Open Source*, 2016. [Online]. Available: http://www.vtk.org/. [Accessed: 24-Feb-2017].

[191] "Kitware, Inc. | Open-source Platforms, Advanced Research Solutions." [Online]. Available: https://www.kitware.com/. [Accessed: 24-Feb-2017].

[192] Python Software Foundation, "Python.org," 2016. [Online]. Available: https://www.python.org/. [Accessed: 24-Feb-2017].

[193] T. E. Oliphant, "SciPy: Open source scientific tools for Python," *Comput. Sci. Eng.*, vol. 9, pp. 10–20, 2007.

[194] J. Hunter and M. Droettboom, "matplotlib," in *The Architecture of Open Source Applications*, vol. 2, no. Volume 2, 2014, pp. 1–14.

[195] W. McKinney and P. D. Team, "Pandas - Powerful Python Data Analysis Toolkit," *Pandas - Powerful Python Data Anal. Toolkit*, p. 1625, 2015.

[196] N. Community, "NumPy Reference," 2011.

[197] E. Marinetto, "OpenIGTLink Python"

(https://github.com/nenetto/OpenIGTLink)

[198] "Novac 11 - Sordina Iort Technologies." [Online]. Available: http://www.soiort.com/en/solutions-eng/novac-11-eng/. [Accessed: 06-Mar-2017].

[199] "Liac 12 MeV - Sordina Iort Technologies." [Online]. Available: http://www.soiort.com/en/solutions-eng/liac-12-mev-eng/. [Accessed: 06-Mar-2017].

[200] "Atracsys." [Online]. Available: https://atracsys.com/web/. [Accessed: 06-Mar-2017].

12

Extra Material

Following pages summarized the main Chapters (3 to 7) with the main results and contributions.

Multicamera Optical Tracker Assessment for Computer Aided Surgery Applications

3

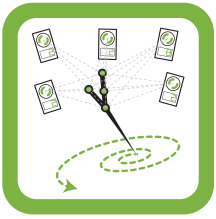

OBJECTIVE

To evaluate a commercial multicamera optical tracker in terms of accuracy, sensitivity to miscalibration, camera occlusions and detection of tools using a feasible surgical setup; and propose an automatic miscalibration detection protocol that satisfies the IOERT requirements of automaticity and speed

MATERIAL & METHODS

We studied the tracking accuracy of the 8-camera Optitrack tracker using a robotic arm (~µm precision) as the gold standard, a single reflective marker (avoiding the use of tracked tools) and various tracked objects while the system was being installed in a real operating room. We also propose and validate a protocol to detect miscalibration of the system in terms of sensitivity and temporal reliability

RESULTS

The estimated Tracking Error sensitivity to miscalibration was 29.92 mm/deg using a two camera system. The proposed miscalibration protocol is able to distinguish miscalibrated cameras automatically. Calibration was stable during 5 consecutive days in the OR environment. Occlusions can affect the tracking accuracy of the system. The use of tracked tools increases the accuracy and the different distribution could affect the system performance

CONCLUSION

Our results provide valuable information for future surgical applications of this tracking approach in terms of tracking volume design, miscalibration detection and tracking accuracy.- The assessment we present and the validated miscalibration protocol are important contributions to image-guided surgery, where the choice of the tracker is critical and the knowledge of the accuracy in situations of camera occlusion is mandatory during assessment of navigation

RESULTS

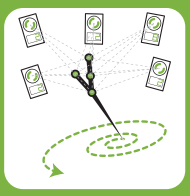

Miscalibration sensitivity

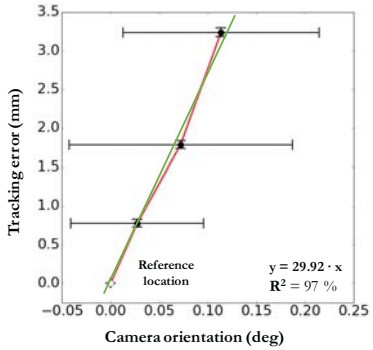

Tools accuracy

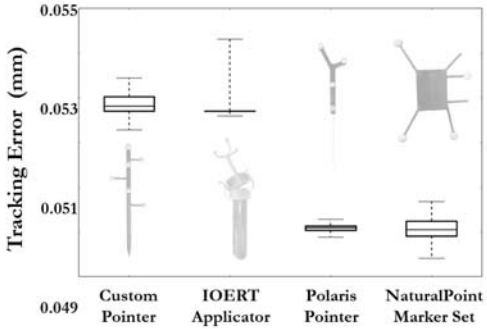

Miscalibration protocol

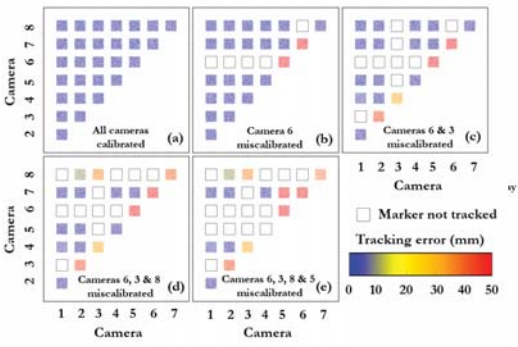

Temporal reliability

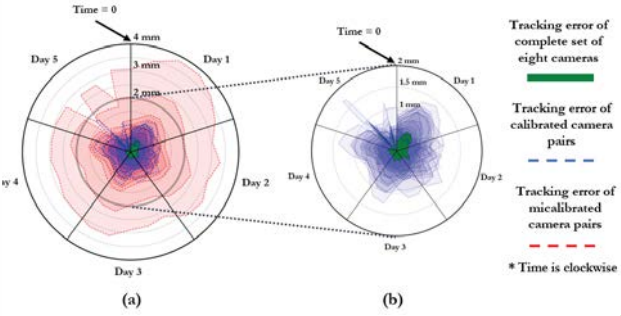

Occlusions & Accuracy

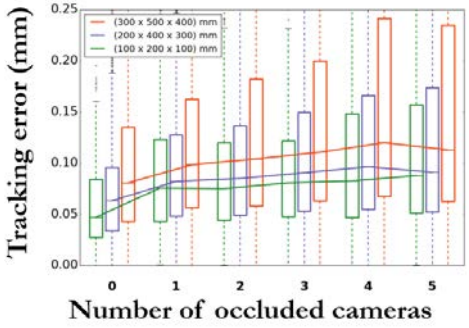

Number of Occluded Cameras	Tracking Error (mm)						
	Central Statistics			Percentiles			
	Mean	Standard Deviation	Mean rms	50	75	95	99
5	1.65	5.07	5.33	0.11	0.11	0.11	0.11
4	1.18	2.99	3.21	0.12	0.12	0.12	0.12
3	0.94	2.49	2.66	0.11	0.11	0.11	0.11
2	0.82	2.31	2.45	0.10	0.10	0.10	0.10
1	0.55	1.84	1.92	0.10	0.10	0.10	0.10
0	0.24	1.05	1.08	0.08	0.08	0.08	0.08

Line Based Registration

A new image-to-world registration strategy for image-guided interventions

4

OBJECTIVE

To develop a new robust, accurate and fast image-to-world alternative approach for image-guided interventions

MATERIAL & METHODS

The transformation is obtained using a previous modelling step based on knowledge of fiducial shape. This study presents a complete simulation-based evaluation of our algorithm in order to compare its accuracy and robustness with those of a classic iterative closest point (ICP) algorithm, anisotropic ICP (a modified version that exploits anisotropic fiducial localization error) and coherent point drift (a statistical registration method based on Gaussian mixture models)

RESULTS

The LBR algorithm has a lower TRE [TRE < 10-1 mm on more than ~15% of the target volume] than ICP, AICP and CPD and the best performance when using 12 line-shaped fiducials.

CONCLUSION

The algorithm proposed significantly improved the accuracy of registration in all our simulations in terms of target registration error inside the target volume. Our results also confirm the robustness of the method against parameters such as the different number of fiducials used or fiducial localization error

RESULTS

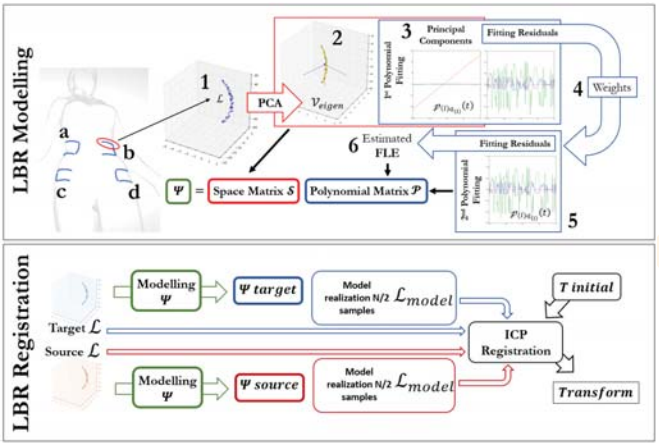

LBR Algorithm

Mean strength distance (Eq. 4.17) and 95% confidence interval for each method (CPD, AICP, ICP and LBR) against the parameters studied: (a) Number of fiducials used for registration, (b) ratio of number of sources used to number of target points, (c) simulated tracker noise or FLE and (d) simulated factor of anisotropy

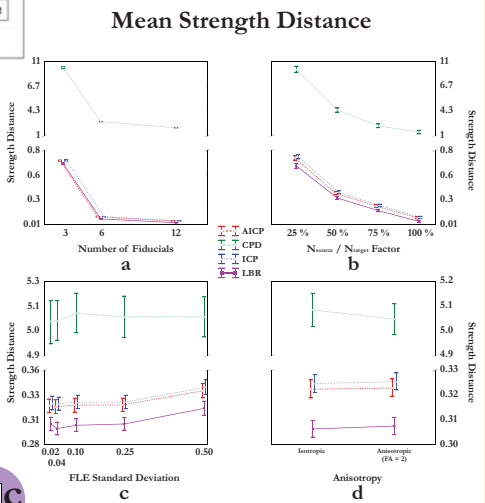

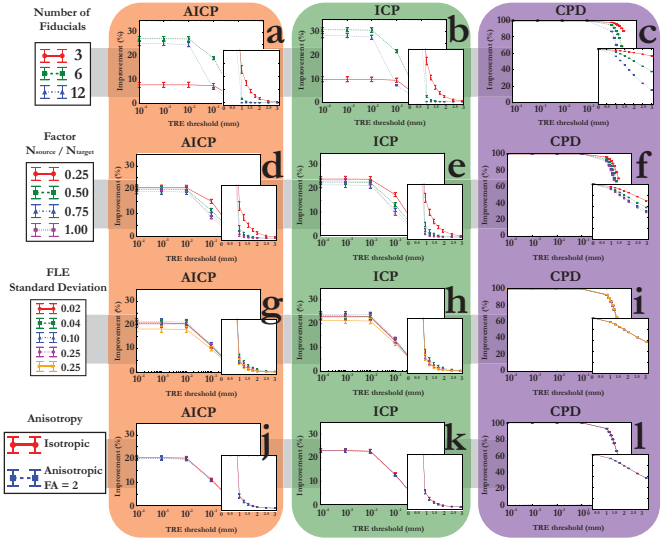

Percentage improvement in TRE volume (mean and 95% confidence interval) of LBR over ICP, AICP and CPD for the different TRE thresholds and factors values studied: first row (a, b, c), number of fiducials simulated, second row (d, e, f), ratio of number of sources to number of target points, third row (g, h, i), FLE simulated noise and fourth row (j, k, l), anisotropy

Integration of Free-Hand 3D Ultrasound and Mobile C-Arm Cone-Beam CT

Feasibility and Characterization for Real-Time Guidance of Needle Insertion

5

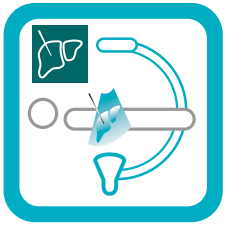

OBJECTIVE

To study the integration of a commercial low-cost ultrasound transducer and cone beam CT C-arm for image-guided interventions that combines surgical navigation and to explore registration techniques for both modalities.

MATERIAL & METHODS

We assessed the ultrasound probe imaging performance characteristics and integrated the probe with the TREK navigation system via probe SDK and PLUS library.
Feasibility of integrated free-hand 3D ultrasound and mobile C-Arm CBCT is demonstrated in phantom studies in scenarios emulating needle-based registration based on a low-cost ultrasound probe

RESULTS

Needle-tip localization accuracy was ~2.1–3.0 mm (target registration error) via the integrated system using fiducial-based registration. The low-cost ultrasound system showed modest image quality in terms of contrast-to-noise ratio and spatial resolution

CONCLUSION

The feasibility of integrated free-hand 3D ultrasound and mobile C-arm CBCT was demonstrated in phantom studies in scenarios emulating needle-based registration based on a low-cost ultrasound probe. The broad availability of low-cost ultrasound imaging systems with streamlined integration with fluoroscopy and CBCT could improve performance and safety in a variety of needle-based interventions

RESULTS

3DUS & C-arm CBCT Integration

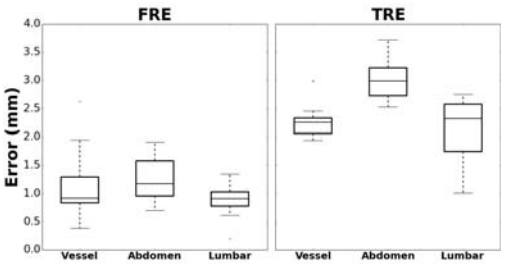

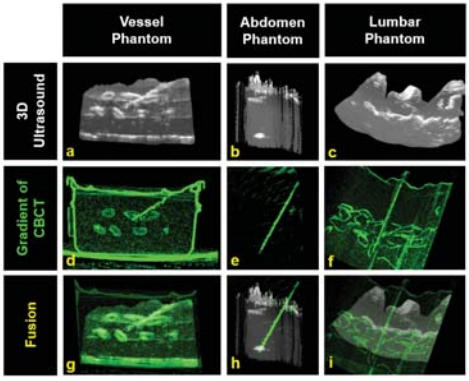

FWHM and CNR of the Interson VC 7.5 probe

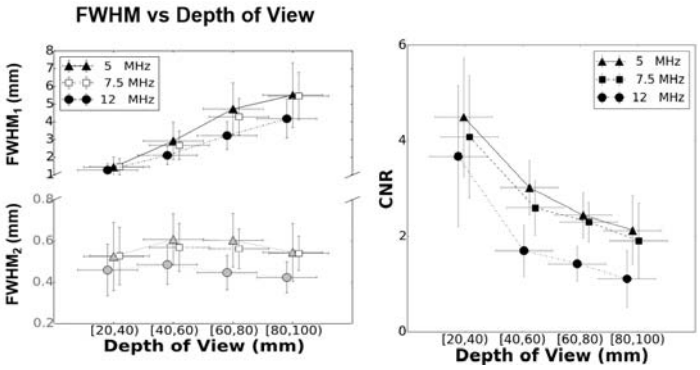

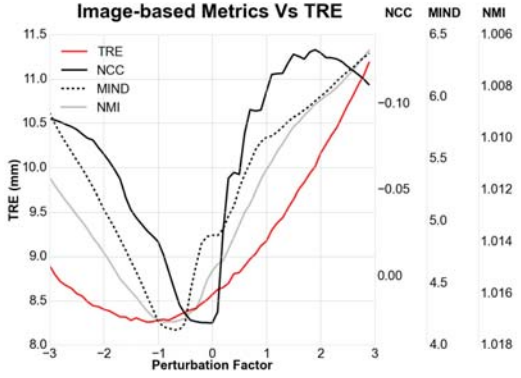

Image-based registration of 3D ultrasound and CBCT. The TRE was measured as a function of Perturbation Factor, minimizing at the transformation taken as reference "truth." Three similarity metrics (NCC, NMI, and MIND-Huber) are each minimized within ~1 mm and ~1° of the reference

Docking of a Mobile Accelerator in IOERT Procedures: Guidance Usingan Optical Tracker

Feasibility Study

6

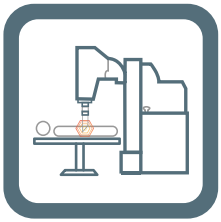

OBJECTIVE

To develop a navigation solution based on optical tracking for the docking of the mobile linear accelerator to the radiation applicator, improving safety and reducing procedure time

MATERIAL & METHODS

We used an optical tracker attached to the mobile linear accelerator in order to track the prescribed localization of the radiation collimator inside the operating room. Using this information, the integrated navigation system was developed to compute the movements that the mobile linear accelerator has to perform to align the applicator and the radiation gantry; and warns the physician if docking is unrealizable according to the available degrees of freedom of the mobile linear accelerator. Furthermore, we integrated the navigation system into a software application that connects all the necessary functioning elements and provides a user interface for the tracker calibration and docking guidance

RESULTS

The system was able to safeguard against the spatial limitations of the operating room, calculate the optimal arrangement of the accelerator and reduce the docking time in experimental setups

CONCLUSION

The system could be used to guide docking with any commercial linear accelerator. We believe that the docking navigator we present is a major contribution to IOERT, where docking is critical when attempting to reduce surgical time, ensure patient safety and guarantee that the treatment administered follows the radiation oncologist's prescription

RESULTS

a

b

c

d

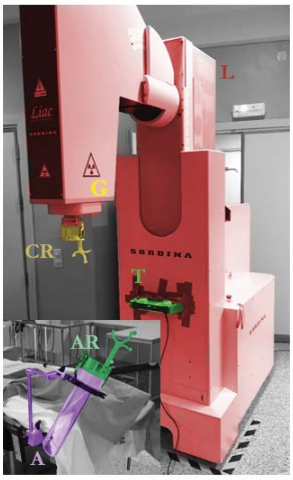

e

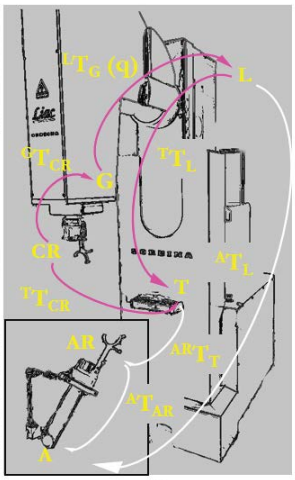

f

Experimental setup for IOERT docking navigation. (a) OptiTrack V120:Duo (b) Reflective marker. (c) Calibration tool and associated tracking rigid-body (CR). (d) IOERT applicator (A) and associated tracking rigid body (AR). (e) Complete navigation set-up: (G) accelerator gantry, (CR) calibration rigid-body tool, (T) tracker, (AR) applicator rigid body, (A) IOERT applicator and Sordina LIAC (L). (f) Pertinent coordinate transformations of the docking navigation setup

Docking time for simulated clinical cases using the navigation system

Localization	Docking Time
Rectum	03:20 min
Right Breast	04:10 min
Left Breast	03:30 min
Mean	**3:40** min

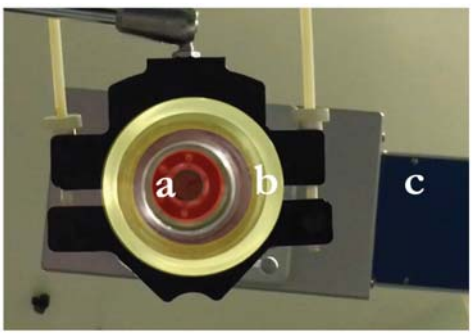

Docking as seen from the applicator bevel. (a) Sordina LIAC gantry. (b) Applicator fixed to the patient's bed simulating the location of rectal cancer. (c) Sordina LIAC head

Image-guided Navigation for IORT
First pilot clinical study

7

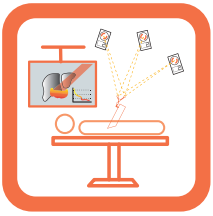

OBJECTIVE

To propose and assess the installation setup of a navigation system in a dedicated OR, determine the required steps in the IOERT process tree, identify the workflow limitations and evaluate the feasibility of the integration in a real OR

MATERIAL & METHODS

We assessed the system feasibility in twelve clinical cases in different anatomical localizations and by different surgical teams

RESULTS

The protocol demonstrated to be feasible for the clinical environment adding ~15 min to the procedure. The anatomical information presented on the navigation screens was found very helpful by the clinicians during surgery, applicator positioning and recalculation of the delivered dose. Moreover, no safety risks or added limitations were found during the evaluation

CONCLUSION

Up to our knowledge, this is the first reported experience on clinical IOERT navigation. The presented solution is an important contribution to the IOERT community where effort shout be taken to reduce uncertainty and provide valuable reports that may help improve the quality of the procedure and contribute to prove evidence of the therapeutic benefits of IOERT

RESULTS

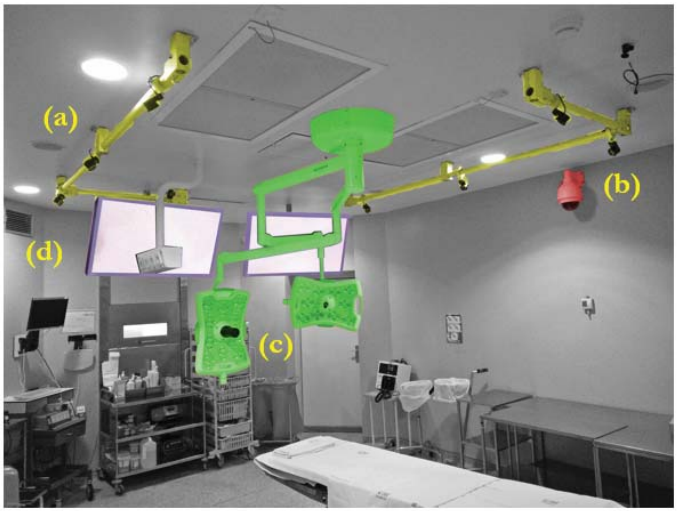

OR scenario: Distribution of cameras in Gregorio Marañón Hospital (Madrid) used for navigating IOERT applicator. (a) Mounting tracker structure with eight Flex13 tracking cameras. (b) Recording video camera. (c) Surgical lamps. (d) Navigation screens

Surgical sites and cancer types of the patients that were included in the evaluation of the navigation protocol

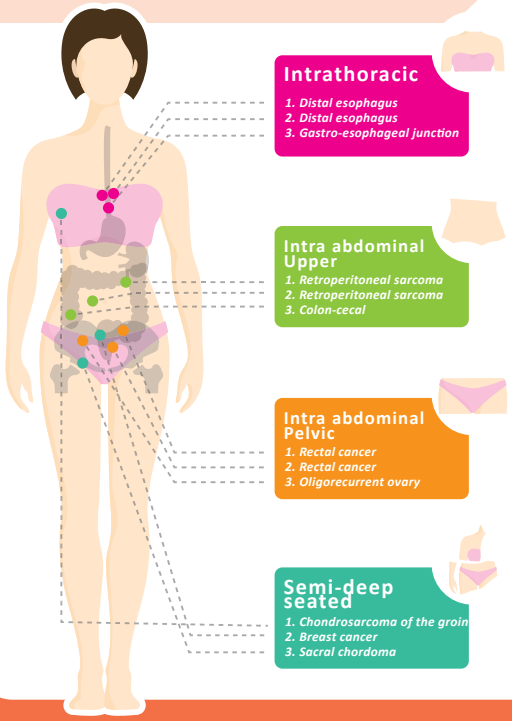

Example of the performed image-guided IOERT procedures. Retroperitoneal sarcoma

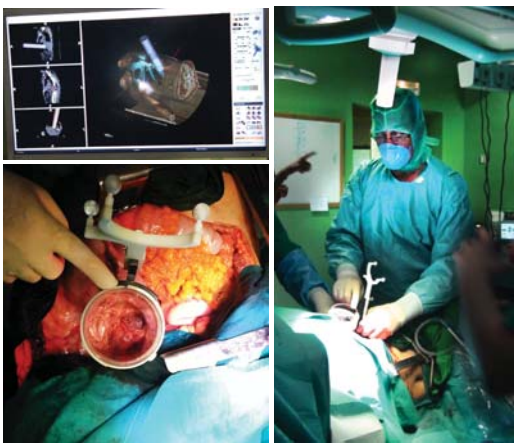

شكراً أبي